

© Copyright 2000  
Teodora Rutar Shuman

**NOX AND CO FORMATION FOR LEAN-PREMIXED METHANE-AIR COMBUSTION  
IN A JET-STIRRED REACTOR OPERATED AT ELEVATED PRESSURE**

**BY**

**TEODORA RUTAR SHUMAN**

A dissertation submitted in partial fulfillment of the  
requirements for the degree of

Doctor of Philosophy

University of Washington

2000

Program Authorized to Offer Degree: Mechanical Engineering

University of Washington

Graduate School

This is to certify that I have examined this copy of a doctoral dissertation by

Teodora Rutar Shuman

and have found that it is complete and satisfactory in all respects,  
and that any and all revisions required by the final  
examining committee have been made.

Chair of Supervisory Committee:

---

Philip C. Malte

Reading Committee:

---

Philip C. Malte

---

John C. Kramlich

---

George Kosàly

Date:

---

In presenting this dissertation in partial fulfillment of the requirements for the Doctoral degree at the University of Washington, I agree that the Library shall make its copies freely available for inspection. I further agree that extensive copying of the dissertation is allowable only for scholarly purposes, consistent with "fair use" as prescribed in the U.S. Copyright Law. Requests for copying or reproduction of this dissertation may be referred to Bell and Howell Information and Learning, 300 North Zeeb Road, P.O. Box 1346, Ann Arbor, MI 48106-1346, to whom the author has granted "the right to reproduce and sell (a) copies of the manuscript in microform and/or (b) printed copies of the manuscript made from microform."

Signature \_\_\_\_\_

Date \_\_\_\_\_

University of Washington

Abstract

NO<sub>x</sub> AND CO FORMATION FOR LEAN-PREMIXED METHANE-AIR COMBUSTION IN A JET-STIRRED REACTOR OPERATED AT ELEVATED PRESSURE

BY TEODORA RUTAR SHUMAN

Chairperson of the Supervisory Committee

Professor Philip C. Malte

Department of Mechanical Engineering

The coupling between NO<sub>x</sub> formation chemistry and the mixing/transport environment is of critical importance to the design of lean-premixed gas turbine combustors, but is poorly understood. In the present dissertation, this problem is addressed via the study of NO<sub>x</sub> formation in a high-pressure jet-stirred reactor operating on lean-premixed methane/air. These experiments focus on the effects of residence time (0.5-4.0 ms), pressure (6.5, 4.7, and 3.0 atm), and inlet temperature (344-573 K). The combustion temperature varies from 1815±5 K at the lowest residence times to 1910±30 K at the highest residence times. The NO<sub>x</sub> is lowest at intermediate residence times, reaching higher values at the extremes. Increasing pressure and inlet temperature tend to reduce NO<sub>x</sub> concentrations. Concentration profiling in the reactor suggests two general environments: (1) a highly non-equilibrium reaction zone defined by high CO concentrations, and (2) a post-flame environment. The NO<sub>x</sub> formation is concentrated in the region of strongly non-equilibrium combustion chemistry. The Damköhler number is

$0.06 \leq Da \leq 1$ , and the ratio of turbulent intensity to laminar burning velocity is  $28 \leq u'/S_L \leq 356$ , indicating the combustion occurs in the high intensity, chemical rate limiting regime. The results are interpreted using a two-environment, detailed chemistry model in which the size and structure of the flame environment are established by matching the measured data. This approach is independently verified using premixed turbulent flame thickness/velocity correlations. The modeling suggests NO<sub>x</sub> formation is controlled by both the specific conditions in the non-equilibrium zone and by the size of the zone. Since both these features are influenced by the experimental parameters, a highly non-linear scenario emerges with implications for minimizing NO<sub>x</sub> via combustor design. The modeling also suggests the unique case of well-stirred combustion for NO<sub>x</sub> at elevated pressure is obtained at low residence time conditions.

## TABLE OF CONTENTS

<b>LIST OF FIGURES</b>	<b>v</b>
<b>LIST OF TABLES</b>	<b>xii</b>
<b>CHAPTER 1</b>	
<b>PROBLEM STATEMENT AND OBJECTIVES</b>	<b>1</b>
1.1 Problem Statement	1
1.2 Overview of Future Trends in the Gas Turbine Industry	3
1.3 NO <sub>x</sub> , CO and Other Emissions from Lean-Premixed Natural Gas Fired Gas Turbine Combustors	4
1.4 Objectives of the Current Study	7
1.4.1 Stirred Reactor Experiments	7
1.4.2 Data Interpretation	11
1.5 Contributions of the Current Study	14
<b>CHAPTER 2</b>	
<b>PARAMETERS INFLUENCING NO<sub>x</sub> AND CO EMISSIONS FROM NATURAL GAS-FIRED LEAN-PREMIXED GAS TURBINE COMBUSTORS</b>	<b>16</b>
2.1 Overview	16
2.2 Fuel Type	16
2.3 Chemistry of NO <sub>x</sub> and CO Formation in Natural-Gas Fired Gas Turbine Engine Combustors	18
2.4 NO <sub>x</sub> and CO Formation: Spatial Characteristics in a Gas Turbine Engine Combustor	21
2.5 Fuel/Air Equivalence Ratio	23
2.6 Combustion Temperature	24

2.7 Combustor Residence Time	26
2.8 Degree of Premixing	28
2.9 Combustion Pressure	29
2.10 Inlet Air Temperature	30
2.11 Summary of Chapter 2	32

### **CHAPTER 3**

#### **HIGH-PRESSURE JET STIRRED REACTOR MEASUREMENTS: EXPERIMENTAL**

<b>METHODS AND RESULTS</b>	<b>34</b>
3.1 Introduction	34
3.2 Experimental Setup	35
3.3 Gas Temperature	46
3.3.1 HP-JSR Gas Temperature Measurements Using R-Type Thermocouples	47
3.3.2 Optical Pyrometer Wall Temperature Measurements	48
3.3.3 Inlet Gas Temperature Measurements with a K-type Thermocouple	51
3.3.4 HP-JSR Gas Temperature Calculation	53
3.4 Experimental Results and Discussion	60
3.4.1 Residence Time and Pressure Effect on NO <sub>x</sub> Formation for Unheated Inlet Experiments	60
3.4.1.1 NO <sub>x</sub> , CO and Hydrocarbon Profiles for Unheated Inlet Experiments	63
3.4.2 Residence Time and Pressure Effect on NO <sub>x</sub> Formation for Preheated Inlet Experiments	72
3.4.2.1 NO <sub>x</sub> and CO Profiles for Preheated Inlet Experiments	75
3.4.3 Nitrous Oxide Measurements	79
3.5 Conceptual Data Interpretation	80
3.5.1 A Concept for Residence Time Effect on NO <sub>x</sub> Formation in the HP-JSR	80
3.5.2 Pressure Effect on NO <sub>x</sub> Formation in the HP-JSR	85
3.5.3 Inlet Temperature Effect in HP-JSR	85

3.6 Summary of Major Experimental Findings	91
<b>CHAPTER 4</b>	
<b>MODEL DEVELOPMENT, RESULTS AND DISCUSSION</b>	<b>93</b>
4.1 Introduction	93
4.2 Model Development	94
4.2.1 Calculation of Turbulent Flame Characteristics	94
4.2.1.1 Defining the HP-JSR Operating Regime in Turbulent Combustion Terms	94
4.2.1.2 Calculation of Turbulent Burning Velocity	107
4.2.1.3 Calculation of Turbulent Flame Thickness	112
4.2.2 Two-PSR Model	117
4.3 Comparison of Turbulent Flame Thickness Model to Chemical Reactor Model	135
4.3.1 Determination of the Size of the Flame	135
4.4 Chemical Kinetic Results	138
4.4.1 Kinetics of NO <sub>x</sub> Formation in Single-PSR (Short Residence Time) Cases	139
4.4.2 Kinetics of NO <sub>x</sub> Formation in Two-PSR (Long Residence Time) Cases	150
4.5 Summary of Modeling Results	162
<b>CHAPTER 5</b>	
<b>CONCLUSIONS AND RECOMMENDATIONS</b>	<b>164</b>
5.1 Conclusions	164
5.2 Recommendations	167

<b>CHAPTER 6</b>	
<b>DESIGN CONCEPT FOR A LEAN-PREMIXED COMBUSTOR WITH A TIME-OPTIMIZED</b>	
<b>FLAME CAVITY</b>	<b>169</b>
6.1 Background	169
6.2 Application to Lean-Premixed Gas Turbine Combustors	172
<b>LIST OF REFERENCES</b>	<b>178</b>
<b>APPENDIX A</b>	
<b>EXPERIMENTAL DATA</b>	<b>186</b>
<b>APPENDIX B</b>	
<b>HP-JSR GAS TEMPERATURE CALCULATIONS</b>	<b>196</b>
<b>APPENDIX C</b>	
<b>PREMIXED TURBULENT COMBUSTION CALCULATIONS</b>	<b>206</b>
<b>APPENDIX D</b>	
<b>CHEMICAL KINETIC MODELING DATA</b>	<b>209</b>

## LIST OF FIGURES

Figure 2.1 Schematic of a lean-premixed combustor can.....	22
Figure 2.2 Published lean-premixed natural gas NO <sub>x</sub> experimental data .....	25
Figure 3.1 High-pressure jet-stirred reactor experimental system.....	36
Figure 3.2 Schematic of the jet-stirred reactor cavity.....	38
Figure 3.3 Schematic of the probe (units are mm).....	40
Figure 3.4 A schematic of the heat transfer within the HP-JSR .....	49
Figure 3.6 Measured inlet temperature versus residence time for 6.5, 4.7 and 3.0 atm runs in HP-JSR operated at 1800 K measured reactor gas temperature .....	52
Figure 3.7 HP-JSR temperature measurements and calculations for 6.5 atm data .....	55
Figure 3.8 HP-JSR temperature measurements and calculations for 4.7 atm data .....	59
Figure 3.9 HP-JSR temperature measurements and calculations for 3.0 atm data. ....	60
Figure 3.10 NO <sub>x</sub> versus residence time at 6.5, 4.7 and 3.0 atm for unheated inlet. Measured temperature is $1803 \pm 5$ K.....	62
Figure 3.11 Corrected measured NO <sub>x</sub> data at 3.0 and 6.5 atm for unheated inlet. Corrected values correspond to a reactor temperature of 1820 K .....	63
Figure 3.12 CO [%, dry, as measured] profiles in the HP-JSR at 6.5 atm, no preheat and 0.5, 1.0, 1.5, 2.0, 2.5 and 3.5 ms overall reactor residence times .....	65
Figure 3.13 NO <sub>x</sub> [ppmv, dry, as measured] profiles in the HP-JSR at 6.5 atm, no preheat and 0.5, 1.0, 1.5, 2.0, 2.5 and 3.5 ms overall reactor residence times.....	65
Figure 3.14 CO+CO <sub>2</sub> [%, dry, as measured] profiles in the HP-JSR at 6.5 atm, no preheat and 0.5, 1.0, 1.5, 2.0, 2.5 and 3.5 ms overall reactor residence times.....	66
Figure 3.15 O <sub>2</sub> [%, dry, as measured] profiles in the HP-JSR at 6.5 atm, no preheat and 0.5, 1.0, 1.5, 2.0, 2.5 and 3.5 ms overall reactor residence times .....	67
Figure 3.16 CO [%, dry, as measured] profiles in the HP-JSR at 4.7 atm, no preheat and 1.0, 1.5, 2.0, 2.5, 3.0 and 3.5 ms overall reactor residence times .....	69
Figure 3.17 NO <sub>x</sub> [ppmv, dry, as measured] profiles in the HP-JSR at 4.7 atm, no preheat and 1.0, 1.5, 2.0, 2.5, 3.0 and 3.5 ms overall reactor residence times.....	69

Figure 3.18 Hydrocarbon [ppmv, dry, as measured] profiles in the HP-JSR at 4.7 atm, no preheat and 0.8 ms overall reactor residence times .....	70
Figure 3.19 CO [% , dry, as measured] profiles in the HP-JSR at 3.0 atm, no preheat and 1.0, 1.5, 2.0, 2.5, 3.0 and 3.5 ms overall reactor residence times .....	71
Figure 3.20 NOx [ppmv, dry, as measured] profiles in the HP-JSR at 3.0 atm, no preheat and 1.0, 1.5, 2.0, 2.5, 3.0 and 3.5 ms overall reactor residence times.....	72
Figure 3.21 NOx versus residence time at 6.5, 4.7 and 3.0 atm for inlet preheated to 573 K. Measured temperature is $1803 \pm 5$ K.....	73
Figure 3.22 Corrected measured NOx data at 3.0 and 6.5 atm for inlet preheated to 573 K. Corrected values correspond to a reactor temperature of 1820 K.....	74
Figure 3.23 CO [% , dry, as measured] profiles in the HP-JSR at 6.5 atm, 573 K preheat and 0.75, 0.9, 1.2, 1.5, 2.1 and 4.0 ms overall reactor residence times.....	76
Figure 3.24 NOx [ppmv, dry, as measured] profiles in the HP-JSR at 6.5 atm, 573 K preheat and 0.75, 0.9, 1.2, 1.5, 2.1 and 4.0 ms overall reactor residence times.....	76
Figure 3.25 CO [% , dry, as measured] profiles in the HP-JSR at 4.7 atm, 573 K preheat and 0.9, 1.0, and 1.5 ms overall reactor residence times.....	78
Figure 3.26 NOx [ppmv, dry, as measured] profiles in the HP-JSR at 4.7 atm, 573 K preheat and 0.9, 1.0, and 1.5 ms overall reactor residence times.....	78
Figure 3.27 N <sub>2</sub> O versus residence time at 6.5, 4.7 and 3.0 atm for unheated inlet and inlet preheated to 573 K. Measured temperature is $1803 \pm 5$ K .....	79
Figure 3.28a NOx data at 6.5 atm corrected to a constant temperature of 1820 K. Two linear curve-fits are used. One for data in the 0.5 to 2.5 ms range, and the other for the data in the 2.5 ms to 4.0 ms range.....	84
Figure 3.28b Function f, calculated using Eq. (3.6) and the power law, versus residence time .....	84
Figure 3.29 Effect of preheat on NOx [ppmv, wet] at 6.5 atm and 1800 K measured temperature in HP-JSR .....	87

Figure 3.30 Effect of preheat on NO <sub>x</sub> [ppmv, wet] at 3.0 atm and 1800 K measured temperature in HP-JSR .....	89
Figure 3.31 Comparison of CO [%, dry, as measured] profiles in the HP-JSR at 6.5 atm, for unpreheat cases at 0.89 and 1.5 ms and preheated cases at 0.75, 0.89 and 1.5 ms overall reactor residence times .....	90
Figure 4.1 Important parameters characterizing turbulent premixed combustion. (Abraham et al., 1985.) Operation of the HP-JSR at the minimum and maximum residence times are identified for following conditions: 6.5 atm (circles), 3.0 atm (diamonds), 6.5 atm at 573 K inlet temperature (squares), and 3.0 atm at 573 K inlet temperature (triangles).....	96
Figure 4.2 Turbulence intensity, $u'$ , plotted versus residence time for three pressures and for unheated and heated (573 K) inlets .....	98
Figure 4.3 Laminar flame speed versus residence time for three pressures and for unheated and heated (573 K) inlets.....	100
Figure 4.4 Calculated thermal diffusivity versus residence time for three pressures and for unheated and heated (573 K) inlets .....	101
Figure 4.5 Laminar flame thickness versus residence time for three pressures and for unheated and heated (573 K) inlets.....	102
Figure 4.6 Kolmogorov scale versus residence time for three pressures and for unheated and heated (573 K) inlets.....	103
Figure 4.7 Damköhler number versus residence time .....	104
Figure 4.8 Turbulent Reynolds number versus residence time.....	105
Figure 4.9 Turbulent burning velocity versus residence time for three pressures and for unheated and heated (573 K) inlets.....	109
Figure 4.10 Non-dimensionalized burning velocity ( $S_T/S_L$ ) versus $u'Da^{0.5}/S_L$ .....	110
Figure 4.11 Ratio of turbulent and laminar burning velocities versus ratio of turbulent intensity and laminar burning velocity .....	111

Figure 4.12 Chemical time versus residence time for three pressures and for unheated and heated (573 K) inlets .....	112
Figure 4.13 Turbulent flame thickness versus residence time for three pressures and for unheated and heated (573 K) inlets .....	114
Figure 4.14 Sketch of flame geometry .....	115
Figure 4.15 Conceptual model for two-PSR model .....	120
Figure 4.16 Schematic of the two-PSR model .....	120
Figure 4.17 CO and NO exiting PSR2 in PFR+PSR1+PSR2 reactor setup, using GRI 3.0 Mech. at 0.5 ms, 6.5 atm and no preheat conditions. The two arrows indicate experimentally measured values of CO and NOx.....	122
Figure 4.18 CO and NO exiting PSR2 in PFR+PSR1+PSR2 reactor setup, using GRI 3.0 Mech. at 4.0 ms, 6.5 atm and no preheat conditions. The two arrows indicate experimentally measured values of CO and NOx.....	123
Figure 4.19 NOx conversion or formation rate versus volume ratio in two-PSR model	124
Figure 4.20 CO and NO exiting PSR2 in PFR+PSR1+PSR2 reactor setup, using GRI 3.0 Mech. at 1.5 and 2.0 ms, 6.5 atm and no preheat conditions. The arrows indicate experimentally measured values of CO and NOx.....	126
Figure 4.21 Volume ratio corresponding to the best match between the measured and modeled data versus reactor residence time for the three pressures and no preheat	129
Figure 4.22 Volume ratio corresponding to the best match between the measured and modeled data versus reactor residence time for the three pressures and 573 K preheat.....	129
Figure 4.23 NOx data compared to the results obtained using two-PSR model for unheated cases.....	130
Figure 4.24 CO data compared to the results obtained using two-PSR model for unheated cases.....	130
Figure 4.25 NOx data compared to the results obtained using two-PSR model for 573 K preheat cases .....	131

Figure 4.26 CO data compared to the results obtained using two-PSR model for 573 K preheat cases .....	131
Figure 4.27 Ratio of PSR1 volume to the total volume ( $V_{psr1}/V_t$ ), corresponding to the best match between the measured and modeled data, and ratio of flame volume to the total volume ( $V_{flame}/V_t$ ), estimated by turbulent premix combustion correlations, plotted versus reactor residence time. The pressures are 6.5 and 3.0 atm and there is no preheat.....	136
Figure 4.28 Ratio of PSR1 volume to the total volume ( $V_{psr1}/V_t$ ), corresponding to the best match between the measured and modeled data, and ratio of flame volume to the total volume ( $V_{flame}/V_t$ ), estimated by turbulent premix combustion correlations, plotted versus reactor residence time. The pressures are 6.5, 4.7 and 3.0 atm and reactants are preheated to 573 K .....	137
Figure 4.29 Percent of the NO formed by each of the four pathways in a single-PSR at 6.5 atm and without preheat.....	141
Figure 4.30 Percent of the NO formed by each of the four pathways in a single-PSR at 6.5 atm with 573K preheat.....	141
Figure 4.31 Percent of the NO formed by each of the four pathways in a single-PSR at 4.7 atm without preheat.....	142
Figure 4.32 Percent of the NO formed by each of the four pathways in a single-PSR at 3.0 atm without preheat.....	142
Figure 4.33 Concentration of CH radical versus reactor residence time for single-PSR cases .....	145
Figure 4.34 Concentration of O-atom versus reactor residence time for the single-PSR cases .....	146
Figure 4.35 Absolute value of the NO formed by each of the four pathways in a single-PSR at 6.5 atm and without preheat. Also shown is the sum of the NO <sub>x</sub> formed by the four pathways, the NO from the PSR output (NO model) and the measured NO <sub>x</sub> .....	148

Figure 4.36 Absolute value of the NO formed by each of the four pathways in a single-PSR at 6.5 atm and 573 K preheat. Also shown is the sum of the NO <sub>x</sub> formed by the four pathways, the NO from the PSR output (NO model) and the measured NO <sub>x</sub> .....	149
Figure 4.37 Absolute value of the NO formed by each of the four pathways in a single-PSR at 4.7 atm and without preheat. Also shown is the sum of the NO <sub>x</sub> formed by the four pathways, the NO from the PSR output (NO model) and the measured NO <sub>x</sub> .....	149
Figure 4.38 Absolute value of the NO formed by each of the four pathways in a single-PSR at 3.0 atm and without preheat. Also shown is the sum of the NO <sub>x</sub> formed by the four pathways, the NO from the PSR output (NO model) and the measured NO <sub>x</sub> .....	150
Figure 4.39 Percent of the NO formed by each of the four pathways in the PSR2 at 6.5 atm without preheat.....	154
Figure 4.40 Percent of the NO formed by each of the four pathways in the PSR2 at 6.5 atm with 573 K preheat.....	154
Figure 4.41 Percent of the NO formed by each of the four pathways in the PSR2 at 4.7 atm without preheat.....	155
Figure 4.42 Percent of the NO formed by each of the four pathways in the PSR2 at 3.0 atm without preheat.....	155
Figure 4.43 NO <sub>x</sub> formation rate versus overall residence time for three pressures with unheated inlet and for 6.5 atm and inlet preheated to 573 K. For residence times at 2.0 ms and above, the values correspond to the rates in corresponding PSR1 .....	157
Figure 4.44 Percent of the NO formed by each of the four pathways in PSR1 at 6.5 atm without preheat.....	158
Figure 4.45 Percent of the NO formed by each of the four pathways in PSR1 at 6.5 atm with 573 K preheat.....	158

Figure 4.46 Percent of the NO formed by each of the four pathways in PSR1 at 4.0 atm without preheat.....	159
Figure 4.47 Percent of the NO formed by each of the four pathways in PSR1 at 3.0 atm without preheat.....	159
Figure 6.1 Conceptual design of the circular Time-Optimized Flame Cavity (TOFC) positioned above single premixed fuel-air nozzle in a lean-premixed combustor primary zone .....	177
Figure A.1 GC calibration data and best-fit functions for C <sub>2</sub> H <sub>4</sub> , C <sub>2</sub> H <sub>6</sub> , and CH <sub>4</sub> . .....	194
Figure B.1 Radiation resistance network.....	202
Figure B.2 HP-JSR temperature measurements and calculations for 6.5 atm data and inlet gases preheated to 573 K .....	202
Figure B.3 HP-JSR temperature measurements and calculations for 4.7 atm data and inlet gases preheated to 573 K .....	203
Figure B.4 HP-JSR temperature measurements and calculations for 3.0 atm data and inlet gases preheated to 573 K .....	203
Figure D.1 O-atom concentration versus PSR residence time.....	211
Figure D.2 CH-radical concentration versus PSR residence time .....	211

## LIST OF TABLES

Table 3.1 Measured pyrometer temperatures [ $^{\circ}\text{C}$ ]	50
Table 3.2 6.5 atm data at 3.0 and 0.88 ms. Unheated inlet and 573 K data are compared	87
Table 4.1 Free radical concentrations [ppmv, wet] in PSR1 and PSR2 at 6.5 atm at 0.5 ms and no preheat conditions.	125
Table 4.2 Numerical results for single-PSR model. ([ppmw] denotes [ppmv, wet].)	143
Table 4.3a Numerical results for two-PSR model (for 6.5 atm). ([ppmw] denotes [ppmv, wet].)	152
Table 4.3b Numerical results for two-PSR model (for 4.7 and 3.0 atm). ([ppmw] denotes [ppmv, wet].)	153

## ACKNOWLEDGMENTS

I would like to acknowledge Professor Philip C. Malte, for being my friend as much as my faculty advisor throughout the course of my graduate studies. His outstanding devotion and ability to help me on numerous occasions have provided an unprecedented support.

I would also like to acknowledge:

Professor John C. Kramlich, for being a good friend and for spending countless hours coaching me to become both a better researcher and a better teacher;

Professor George Kosàly, for cheering me up with comments that only us Europeans could enjoy;

Professor David T. Pratt, for being a great mentor during my days as a teaching assistant;

Dr. David G. Nicol, for spending hours helping me with computer-related issues;

David C. Horning, for training me to use the high-pressure jet-stirred reactor facility at the Mechanical Engineering Department.

Thank you Simonida, for being the best person, and, hence, the best sister imaginable.

Thank you Brandon, for your unconditional generosity that has empowered me to complete my studies. Thank you for the rational romanticism that is the essence of our life.

## **DEDICATION**

Mom tati – od koga sam nasledila mudrost, strpljenje i neiscrpni optimizam

Mojoj mami – od koje sam nasledila upornost, snagu i spartanski nacin zivota

To my father, from whom I have inherited wisdom, patience, and inexhaustible optimism

To my mother, from whom I have inherited persistence, strength, and Spartan lifestyle

## CHAPTER 1

### PROBLEM STATEMENT AND OBJECTIVES

#### *1.1 Problem Statement*

Growing environmental concerns are influencing power producers to reduce emissions of harmful substances into the environment. The ultimate goal is to develop technologies with "zero emissions". The present research has direct application to gas turbine combustor technology, which has not yet reached the goal of ultra low NO<sub>x</sub> (oxides of nitrogen) emissions due to the unresolved complexity of the competition between the processes controlling NO<sub>x</sub> formation in flames.

NO<sub>x</sub> formation in flames is a result of many competing factors, such as the type of fuel, the fuel-air equivalence ratio, the degree of fuel-air premixing, the flame pressure, the inlet air temperature, the residence time in the flame zone and post-flame zone, the flow velocity, and mixing within the combustor. These factors can be summarized as thermodynamical, chemical and fluid mechanical. This significantly increases the complexity of understanding exactly what controls NO<sub>x</sub> formation in a given system.

Experimental data sometimes show opposite trends in the behavior with some variables, an indication of the complexity of the trade-off between the various fundamental processes controlling NO<sub>x</sub> formation. One clear example is the dependency of NO<sub>x</sub> on the combustor pressure. The NO<sub>x</sub> can be found in the literature to increase, decrease or remain unchanged when pressure in the combustor is increased. This behavior appears to be system specific.

An objective of the present research is to fill the gap in the existing understanding by finding correlations for NO<sub>x</sub> formation with pressure, with residence time in the flame and post-flame zones, and with inlet gas temperature. The carbon monoxide (CO) is also studied because of its close correlation with NO<sub>x</sub> formation, and because it is an important pollutant in its own right. The present research assumes the following: (1) NO<sub>x</sub> formation in flames is complex and in need of further insight and understanding; (2) the most effective control of NO<sub>x</sub> emissions is by prevention of NO<sub>x</sub> formation rather than by post-combustor denitrification; and (3) CO emissions control depends on the sufficient residence time and temperature in the post-flame zone.

The present research consists of two parts:

1. Experiments in a high-pressure jet-stirred reactor (HP-JSR) conducted at gas turbine combustor temperatures using methane fuel.
2. Interpretation of the NO<sub>x</sub> and CO data using premixed turbulent combustion correlations and chemical reactor modeling.

This study, together with previous studies by Steele (1995) and Bengtsson et al. (1998), aids the optimization of parameters for obtaining low NO<sub>x</sub> as well as low CO emissions from lean-premixed gas turbine combustors fired on natural gas. Suggesting optimal parameters for emissions control to gas turbine combustor manufacturers allows them to adequately modify their combustor designs to meet ultra low emission requirements. This work combines previously conflicting results of effects of pressure and inlet temperature on NO<sub>x</sub> into homogeneous conclusions regarding emission control in lean-premixed, methane-air flames.

## ***1.2 Overview of Future Trends in the Gas Turbine Industry***

Advanced gas turbine engine cycles for power generation are developing in two directions:

1. Improving the design of existing gas turbines to be used in simple cycle (Brayton) machines or combined with the steam cycle (Rankine) for production of electricity in combined-cycle machines, where Brayton is the topping and Rankine is the bottoming cycle, or for the co-generation of process heat and steam with electricity.
2. Developing new technologies for power generation that can use gas turbines to improve efficiency. An example is the combination of a gas turbine engine with high-pressure fuel cells. In this case, fuel cells operate at high efficiency due to the high pressures obtained from the compressor of a gas turbine engine.

These directions will most likely overlap, but the one which will become predominant in future power generation will be determined by many factors, both technical and socio-economic. One of the most important technical (or scientific) factors is the impact on the environment. Natural gas fired gas turbines and combined cycle plants have very low emissions relative to other power generating technologies, but they have not reached the ultimate goal of "zero emissions". They are projected to capture 47% of the international and 75-85% of the US electric power generation market in the next decade (Touchstone, 1996). This is believed to be due to their low capital cost, short installation times, reliability and availability, high combined cycle efficiency, relatively low environmental impact and the availability of cheap natural gas (Touchstone, 1996; Kuehn, 1995). For example, the Westinghouse 501G engine, with 230 MW output and combined cycle

efficiency of 58% when fired with natural gas, is designed to produce NO<sub>x</sub> of less than 25 ppmv, dry (15% O<sub>2</sub>), CO of less than 10 ppmv and unburned hydrocarbons (UHC) of less than 10 ppmv (Southall and McQuiggan, 1995). The Asea Brown Boveri (ABB) engines GT24 (60 Hz, 165 MW) and GT26 (50 Hz, 240 MW) also share a combined cycle efficiency of 58% and NO<sub>x</sub> emissions of less than 25 ppmv, dry (15% O<sub>2</sub>) (Farmer, 1993).

The US Department of Energy is sponsoring the development of high efficiency technology in order to satisfy its 1992 "Earth Summit" pledge to reduce CO<sub>2</sub> emissions. The result is that many new, advanced systems have been developed for intermediate load power plants, and most of these new systems incorporate a natural or reformed gas fired gas turbine.

The projected development of gas turbine technology, the emerging competitive technologies, such as gas turbines with fuel cells or with catalytic combustors, and the "zero emissions" goal are putting a considerable amount of pressure on resolving the NO<sub>x</sub> issue.

### ***1.3 NO<sub>x</sub>, CO and Other Emissions from Lean-Premixed Natural Gas Fired Gas Turbine Combustors***

Nitric oxide (NO) and nitrogen dioxide (NO<sub>2</sub>), commonly referred to as NO<sub>x</sub> (=NO + NO<sub>2</sub>), are a serious threat to the environment for the following reasons (Sloss et al., 1992):

1. They are one of the two major reactants of photochemical smog,

2. They are poisonous to humans,
3. They are constituents of acid rain and dust, and
4. They destroy the stratospheric ozone layer.

The role of NO<sub>x</sub> in photochemical smog production is pronounced in regions with low winds and low precipitation. Many NO<sub>x</sub> regulations are, therefore, localized and can be as low as 3-5 ppmv for gas turbines in certain parts of California, due to its extreme smog problem. The adverse effect of NO<sub>x</sub> on human health is manifested primarily through the diminished function of lungs, as well as other internal organs. NO<sub>x</sub> also has been found to have a carcinogenic effect. NO<sub>x</sub> forms acidic compounds that are found in acid rain and dust, which are known to deteriorate soil, flora and fauna. In addition, NO<sub>x</sub> affects man-made structures through corrosion and erosion. Pollution from NO<sub>x</sub> emitted from land-based combustion sources acts locally (photochemical smog and toxicity) and regionally (photochemical smog and acid rain). Therefore, it does not contribute to stratospheric ozone layer depletion unless it forms in the stratosphere from nitrous oxide, N<sub>2</sub>O, emitted by a land-based source.

Land based, lean premixed gas turbines fired on natural gas have lower pollutant emissions than other commercially used electric power generating technologies based on combustion. The lean-premixed (LP) gas turbine engines commercially operating today have reached NO<sub>x</sub> levels of 25 ppmv, dry (15% O<sub>2</sub>) or less. Thermal power plants operating on coal are still struggling with NO<sub>x</sub> emissions of a few to several hundred ppm's.

Carbon monoxide, CO, a poisonous gas, has a low emission, since most gas turbine combustors permit CO burnout. However, because of reduced flame temperature, LP combustors tend to emit somewhat greater CO levels than conventional diffusion flame combustors. Newest lean-premixed combustor technologies are reaching CO levels of about 10 ppmv in the exhaust.

The emission of carbon dioxide, CO<sub>2</sub>, the major greenhouse gas emitted from combustion sources, is low per unit of electricity produced, compared to other fossil fuel systems, for two reasons: (1) high combined cycle thermal efficiencies, and (2) dry products of combustion of coal usually have more than twice the CO<sub>2</sub> of dry natural gas combustion products, due to high carbon content of coal.

Nitrous oxide, N<sub>2</sub>O, another greenhouse gas, and a stratospheric ozone layer depleting gas, has very low emissions (a few ppm) from gas turbine engines, due to the high combustion temperatures, which favor N<sub>2</sub>O destruction and relaxation to the low equilibrium concentrations.

Unburned hydrocarbons, UHC, are products of incomplete combustion of fuels. Newest lean-premixed combustor technologies are reaching UHC levels of 10 ppmv or less in the exhaust.

Water, H<sub>2</sub>O, emitted from combustion sources represents only a minor portion of the overall water content in the atmosphere, so this contribution does not influence the established atmospheric cycles or the global warming.

## ***1.4 Objectives of the Current Study***

The objectives of this study have been summarized in Section 1.1 as a two-stage study: the stirred reactor experiments and the data interpretation. A detailed overview of each stage is provided below.

### ***1.4.1 Stirred Reactor Experiments***

The highest rates of formation of NO<sub>x</sub> occur in the flame zone because it is filled with high concentrations of free radicals. Thus, experiments are conducted in a laboratory setup that simulates the highly non-equilibrium, radical rich environment that prevails in the flame zone. This flame zone is spread-out to allow more accessible probing. A jet stirred reactor (JSR) developed at the University of Washington (Thornton, 1987, and Steele, 1995), gives a high mixing-intensity flame environment that has been successfully used in the past for the study of NO<sub>x</sub> emitted from the lean-premixed combustion. The high pressure version of the reactor is termed the high-pressure jet stirred reactor, HP-JSR, and it has been successfully used by Steele (1995) to simulate the lean premixed combustor flame zone and immediate post-flame zone. This HP-JSR system, with a few modifications, is used in the present study, and is operated between 3.0 and 6.5 atm. The essential difference of the present research to that of Steele (1995) is the use of very short residence times, allowing the HP-JSR to approach well-stirred behavior.

Well-stirred behavior is defined as a condition where the temperature and species concentrations are spatially uniform and time steady in the time-mean values or

measurements. Sampling of the gas in the present work records the time-mean concentrations, and indicates approximately well-stirred behavior in the HP-JSR operated at short residence time. The perfectly-stirred reactor (PSR) is defined as a spatially uniform and time steady reactor for temperatures and species concentrations. Both the well-stirred reactor condition (WSR) and the PSR theory are extensively used in the present study. The WSR is used to describe specific experimental conditions, and the PSR is used in the modeling of the experimental results.

The experiments explore the following important parameters:

1. NO<sub>x</sub> versus pressure, for 3.0, 4.7 and 6.5 atm, at 1800 to 1940 K reactor gas temperature. The pressure of 6.5 atm corresponds to the maximum pressure possible for the HP-JSR system.
2. NO<sub>x</sub> versus residence time, from 0.5 to 4.0 ms, at 3.0, 4.7 and 6.5 atm pressure, and about 1800 to 1940 K reactor gas temperature. The residence time of 0.5 ms corresponds to the maximum mass flow rate possible for the HP-JSR system, while 4.0 ms corresponds to a fairly long combustion time by gas turbine engine “standards” and permits a system pressure drop similar to that of the gas turbine combustor (< 5%).
3. NO<sub>x</sub> versus inlet air temperature, i.e., preheat temperature. The unheated inlet temperature is approximately 373 K due to back-heat from the reactor and heated inlet temperature is approximately 573 K. The pressure is 3.0, 4.7 and 6.5 atm, the

residence time 0.5 to 4.0 ms, and combustion reactor gas temperature is 1800 to 1940 K.

The combustion temperature for the study, 1800 to 1940 K, is selected to correspond with the highest combustion temperatures at which the LP combustors operate. This means that the results of this study give highest NO<sub>x</sub>, since any lower temperature will yield less NO<sub>x</sub>, with all other parameters unchanged. This is important when considering the NO<sub>x</sub> emissions because the goal is to keep them low, and thus, this work provides an upper limit for NO<sub>x</sub> emissions in LP combustion.

The three pressure levels of 3.0, 4.7 and 6.5 atm were selected to provide a reasonable range of pressures within the capabilities of the HP-JSR system. However, pressures in land-based gas turbine engines are in the 10 to 40 atm range. An argument that the results from this study can be applied to the higher pressures of gas turbine engine conditions is given in previous work. As the pressure of the LP combustion process increases, two phenomena occur:

1. Chemical kinetic modeling assuming a PSR shows the NO<sub>x</sub> leveling off with pressure above a pressure of 5-to-10 atm (Nicol, 1995).
2. Chemical kinetic modeling assuming a PSR followed by a PFR or assuming a freely propagating laminar flame shows the relaxation rate of the O-atom increasing with increasing pressure (Nicol, 1995). Thus, as the pressure increases, the region of super-equilibrium O-atom, and thus the region having a high formation rate of NO<sub>x</sub> shrinks, leading to a reduced NO<sub>x</sub> emission.

The end result is that NO<sub>x</sub> emission appears to be most sensitive to pressure in the 1 to 5 atm range. This scenario is consistent with Bengtsson et al. (1998), who have studied NO<sub>x</sub> formation in jet-stirred reactors at pressures up to 20 atm, and have seen that the measured-NO<sub>x</sub> decrease with pressure is significantly more pronounced at pressures below 5 atm.

The range of residence times, between 0.5 and 4.0 ms, is selected to cover as wide a range of flow rates as possible. At 0.5 ms, the HP-JSR approaches well-stirred behavior for NO<sub>x</sub> formation, whereas at 4.0 ms, the combustion field is significantly different so that a distinct flame zone and post-flame zone are formed. Operation at the intermediate residence times, though more difficult to interpret, is closer to actual engine conditions. Operation at the long residence times is useful to establish a low-mixing rate limit.

Two inlet temperature levels are studied in order to discern the effect of preheat on NO<sub>x</sub>: one at about 373 K, and the other at approximately 573 K. Preheat occurs naturally in gas turbines due to the temperature increase across the compressor.

The data obtained in this study show new trends. For example, thermal NO<sub>x</sub> is a linear function of the residence time (Heywood, 1988, eq. 11.11, p. 575) if the NO<sub>x</sub> concentration remains sufficiently low to prevent significant reverse reaction within the Zeldovich pathway. Additionally, Steele (1995) found a linear dependency of NO<sub>x</sub> on residence time for lean-premixed combustion in an atmospheric pressure JSR. However, results of the present study show that NO<sub>x</sub> decreases from a maximum value at 0.5 ms to a minimum value at 2.0-2.5 ms (for pressures of 4.7 and 6.5 atm). Then, the NO<sub>x</sub> increases again as the maximum residence time of 4.0 ms is approached. Also,

depending on the residence time, NO<sub>x</sub> can decrease or behave neutrally with respect to pressure. Finally, high inlet temperature generally lowers the NO<sub>x</sub>, an effect especially manifested at the very short residence times. The present data help to explain the conflicting trends observed in the industrial data, which are detailed in Chapter 2.

Both the fluid mechanics and the chemical kinetics influence the experimentally observed trends. That is, NO<sub>x</sub> emissions are a consequence of size of the flame and the post-flame zone, the temperature, the stoichiometry, the pressure, and the inlet temperature. Premixed turbulent combustion correlations and chemical reactor modeling are used as tools for explaining the experimental data.

The experimental results suggest a possible modification for the gas turbine combustor primary zone that should result in reduced emissions. The proposal for this modification is given in Chapter 6. In addition, the present work also applies to widely used swirl stabilized combustors because it explains fundamentals of NO<sub>x</sub> formation.

#### ***1.4.2 Data Interpretation***

The NO<sub>x</sub> emissions depend on the time gases spend in the flame and the post-flame zone, and on the rates of the NO<sub>x</sub> formation in both zones. The objective of data interpretation is to estimate these times and rates by using existing computer codes.

Several computer codes were considered as tools for interpretation of the experimental data, namely:

1. Computational fluid dynamics (CFD),

2. The University of Washington partially-stirred reactor model (PaSR) named the finite-rate mixing model (FMM), and
3. The University of Washington chemical reactor model (CRM).

The three approaches are shown in decreasing order of fluid mechanical complexity, and increasing order of chemical reaction mechanism complexity. These approaches are ranked for today's stage of computer capabilities.

The CFD codes use either  $k$ - $\epsilon$  or Reynolds stress closure methods to model Reynolds stresses in the momentum equation. Although this simplifies the fluid mechanics, it significantly reduces the run-times and, at the same time, gives a useful, practical result for the flowfield. The chemistry modeling in the CFD codes is, however, limited to a few reactions and a few species. Thus, CFD is not used because the present work requires full chemistry modeling.

The PaSR or FMM involves finite rates of micromixing and macromixing of the reactor gas content. The code available at the University of Washington was written by Tonouchi (1996). It uses the Jain-Spalding model for finite-rate macromixing and coalescence dispersion or interaction-by-exchange-with-the-mean models for finite-rate micromixing. The FMM code can incorporate reduced chemical kinetic mechanisms, but due to computational limitations full chemistry is not easily accommodated by this model. Breidenthal et al. (1990) concluded that the rate-limiting process in mixing via jets in confined volumes is the large-eddy rotation. Therefore, micromixing effects are secondary. Bengtsson et al. (1998) came to a similar conclusion after a study using the

PaSR to model JSR emissions, where they found that micromixing has a minor influence on NO<sub>x</sub> and CO levels.

The CRM consists of one or more reactors, which are made up of combinations of (1) the zero-dimensional perfectly stirred reactor (PSR) and (2) the one-dimensional plug flow reactor (PFR). The model incorporates full chemical kinetic mechanisms, but fluid mechanics is greatly simplified. Steele (1995) and Bengtsson (1998) had success in modeling their high-pressure lean premixed methane jet-stirred reactor data as two PSR's in series. The CRM code runs two PSR's in series almost instantaneously on today's computers, thus it represents a convenient tool for kinetic interpretation of the data.

Full kinetic interpretation of the NO<sub>x</sub> data is essential for flames and immediate post-flame zones. Therefore, CRM is used in the present work. However, since CRM cannot predict any fluid mechanics in the reactor, an additional approach had to be taken to estimate the type of flame and its volume. This approach consists of applying existing premixed turbulent combustion correlations to compute flame thickness and length, and, based on that, to estimate the volume of the flame. The result of this approach is a flame that encompasses the entire reactor volume at short residence times. However, the flame volume sharply decreases at intermediate residence times (between 1 and 2 ms) and becomes less than 10% reactor volume at large residence times.

The CRM configurations used are a single-PSR or two-PSR's in series, operated at experimental conditions. The PSR sizes are determined by matching CRM output to the experimentally measured NO<sub>x</sub> and CO. The results show that the HP-JSR is well simulated as a PSR for NO<sub>x</sub> formation at the short residence times. At larger residence

times, greater than approximately 1.5 ms, the data are best matched by the two-PSR model. The first PSR represents the flame zone because of the high concentrations of free radicals, and its volume is up to 10% of the full reactor volume. The second PSR represents the post-flame zone, and also corresponds to the recirculation zone of the HP-JSR. The two-PSR model results imply that the flame resides in a small part of the reactor volume, and that the rest is filled by hot, but less reactive gas.

It is notable that the results obtained by two independent approaches, i.e., by matching the data with CRM, and by premixed turbulent correlations, give similar solutions for the sizes of the flame and the post-flame zones. This increases confidence in the NO<sub>x</sub> calculations done with the CRM.

### ***1.5 Contributions of the Current Study***

The contributions of this study are the following:

1. Measurements for residence times below about 1.0 ms show the NO<sub>x</sub> forming behavior in high-pressure, high-intensity, lean-premixed combustion of methane approaches the well-stirred condition. Such measurements are thought to be unique.
2. The measurements and their interpretation by chemical reactor modeling provide a comprehensive study of pressure, residence time, and inlet temperature effects at elevated pressures in jet-stirred reactors. Interpretation leads to phenomenological understanding of how the features governing NO<sub>x</sub> formation respond to the imposed parameters. Consequently, this study is unique in its attempt to link the NO<sub>x</sub> emissions to the size of the confined distributed flame. The sizing of the high-

intensity flame zone via turbulent flame correlations provides an a priori means of establishing the CRM configuration without the need for experimental measurements.

## CHAPTER 2

# PARAMETERS INFLUENCING NO<sub>x</sub> AND CO EMISSIONS FROM NATURAL GAS-FIRED LEAN-PREMIKED GAS TURBINE COMBUSTORS

### *2.1 Overview*

Chapter 2 is designed to explain major parameters influencing NO<sub>x</sub> and CO formation in natural gas-fired lean-premixed gas turbine combustors. Each section explains one of the parameters and its contribution to pollutant formation, reviews the literature and previous research, and explains how the present work contributes to the understanding of the influence of that parameter on NO<sub>x</sub> and CO emissions. In addition, Sections 2.3 and 2.4 give an overview of NO<sub>x</sub> and CO formation chemistry and the spatial location of reaction zones in natural gas-fired lean-premixed gas turbine engine combustors.

### *2.2 Fuel Type*

Natural gas has replaced liquid fuels (crude oil derivatives) as the most commonly used fuel in new gas turbines for power generation. This is because natural gas has satisfactory supply sources, it burns homogeneously, it has lower pollutant emissions than liquid fuels, and natural gas cost differential has decreased relative to traditional gas turbine fuels. Natural gas-fired burners form and emit less NO<sub>x</sub> than oil-fired burners for two reasons: (1) unlike oil, natural gas contains no fuel bound nitrogen, which is easily

converted to NO<sub>x</sub> during combustion; (2) in combustion of natural gas, the fuel and air are premixed prior to entering the combustor, (which avoids generation of stoichiometric interfaces), so combustion tends to occur at local fuel-lean and lower temperature conditions. Conversely, oil has to be fully vaporized prior to premixing, and then premixed to achieve the same effectiveness. Since this is difficult to properly control, oil burns in fuel-richer pockets, often even under stoichiometric conditions, which form substantially more NO<sub>x</sub>.

Although natural gas, or methane, is the only fuel used in this study, it should be mentioned that alternate fuels are also burned in some gas turbine engines. The most common alternate fuel is a natural gas of lower methane concentration, and higher condensable hydrocarbons level. Pockets of condensable hydrocarbons (mostly higher order alkanes) may be randomly pushed into the combustor through the premixer, causing a sudden increase of the primary zone temperature and, therefore, an increase in NO<sub>x</sub> emissions. These hot spots can also cause hardware damage. A fuel projected for the future is synthetic gas, i.e. a mixture of carbon monoxide (CO), hydrogen (H<sub>2</sub>), carbon dioxide (CO<sub>2</sub>), water (H<sub>2</sub>O), and nitrogen (N<sub>2</sub>). This gas has a lower heating value than natural gas, but has the advantage of generally good burning. It opens the opportunity for coal (through gasification) to be indirectly used for firing gas turbines. This is of value for regions where coal is abundant, and natural gas supplies are limited.

Natural gas is extracted from the ground through wells connected to a pipeline (equipped with compressors) that transports the gas to the consumer. Addition of water or oil (sprayed into the gas to keep it “moist”) and air leaks during suction from the wells

alter the original gas composition (Combustion Engineering, 1981). Therefore, the gas composition must be verified prior to reaching the consumer. The primary component of the natural gas is methane, CH<sub>4</sub>. Although most of the gases contain more than 80% methane, its concentration can go as low as 10%, and the heating value varies accordingly. The secondary component of natural gas is ethane, C<sub>2</sub>H<sub>6</sub>. Other common constituents are N<sub>2</sub>, CO<sub>2</sub>, C<sub>2</sub>H<sub>4</sub>, C<sub>3</sub>H<sub>8</sub>, C<sub>4</sub>H<sub>10</sub>, C<sub>5</sub>H<sub>12</sub> (Combustion Engineering, 1981).

Experiments in this study are conducted with high-pressure bottles of natural gas (with high methane content). Pure methane (>99%) is also used in the experiments, and is confirmed to produce the same amount of NO<sub>x</sub> as the natural gas. The modeling of the experimental data is done assuming pure methane.

### ***2.3 Chemistry of NO<sub>x</sub> and CO Formation in Natural-Gas Fired Gas Turbine Engine Combustors***

The only source of nitrogen for NO<sub>x</sub> formation in methane-air combustion is the combustion air, which contains almost 79% nitrogen, N<sub>2</sub>, by volume.

The GRI 3.0 (Smith et al., 1999) chemical kinetic mechanism has been used to study the main pathways for NO<sub>x</sub> formation under lean premixed combustion of methane. These are Zeldovich, nitrous oxide, prompt, and NNH pathways.

The following reactions make up the Zeldovich pathway:



This work distinguishes the Zeldovich from the thermal pathway, which is a special case of the Zeldovich mechanism. In the Zeldovich pathway, the initial reaction (2.1) is formed by super-equilibrium O-atom, whereas, in the thermal pathway the O-atom is at local equilibrium. Also, other relevant species, such as the H-atom, OH-radical and O<sub>2</sub> are at nonequilibrium concentrations in the Zeldovich pathway and at equilibrium levels in the thermal pathway. The Zeldovich pathway is extremely temperature sensitive. At high combustion temperatures, i.e., in the vicinity of 2000 K and above, it dominates other pathways. However, at lower temperatures, which are characteristic for lean-premixed methane-air combustion, the Zeldovich pathway is comparable to the contribution of the other three pathways.

The following reactions make up the nitrous oxide pathway:



The N<sub>2</sub>O is formed in reaction (2.4), which is the initiation reaction. NO is mainly formed via reaction (2.5), but also forms by reactions (2.7) and (2.9). It should be noted that NH formed via reaction (2.7) oxidizes into NO, adding to the overall NO production.

The prompt pathway is initialized by the following reaction:



The CH radical is formed via the hydrocarbon destruction pathway  $\text{CH}_4 \rightarrow \text{CH}_3 \rightarrow \text{CH}_2 \rightarrow \text{CH}$ , and exists in the early parts of the flame for a very short period of time. Hydrogen cyanide (HCN) and N-atom formed through reaction (2.10) are rapidly oxidized to NO.

The following reactions constitute the NNH pathway (Harrington et al., 1996):



The NNH is a short-living radical. It is formed via reaction (2.11), and leads to NO via reaction (2.12). The NH formed via reaction 2.12 oxidizes into NO, adding to the overall NO production. Bozzelli et al. (1994) first introduced this pathway and have pointed out that it is important at combustion temperatures.

The NO formed by the above pathways can, at lower temperatures, oxidize to  $\text{NO}_2$ , mainly by reaction (2.13) below.



The results of this work are presented as  $\text{NO}_x = \text{NO} + \text{NO}_2$ .

Carbon monoxide forms as an intermediate product of the series of hydrocarbon oxidation reactions. If given sufficient time, CO is oxidized to  $\text{CO}_2$ . The CO levels measured in the high-pressure jet-stirred reactor are rather high, (a few hundred ppmv to above 1%), indicating that CO does not have sufficient time to oxidize to  $\text{CO}_2$ .

## ***2.4 NO<sub>x</sub> and CO Formation: Spatial Characteristics in a Gas Turbine Engine Combustor***

A schematic of a gas turbine engine combustor is shown in Figure 2.1, which also depicts the characteristic zones within the combustor. These combustion zones are based on a CFD solution of a gas-turbine test combustor by Hamer and Roby (1997). The solution was generated with the Star-CD program (a commercial CFD code) and a global mechanism, developed by Nicol et al. (1999). The global mechanism contains three reactions for methane oxidation and two for NO<sub>x</sub> formation. The CFD generates a solution for the flow field, the temperature, and the concentration of species, such as CH<sub>4</sub>, CO and NO<sub>x</sub>. The three thick arrows in Figure 2.1 show flow direction for the bulk of the gas. The farthestmost upstream arrow shows the combustion air and fuel entering into the combustor through the pre-mixer. After entering the combustor, the air and fuel pass through the flame, burn, and the resulting combustion products flow towards the exit, as shown with the final two arrows. However, some of the flow remains in the combustor longer because it is trapped in one of the two recirculation zones shown in the figure, i.e., the dome and the on-axis recirculation zones. The dome recirculation zone is the coldest combustor zone because it contains combustion products and the cold dome cooling air. The on-axis recirculation zone is the hottest in the entire combustor because it contains undiluted combustion products. The dome and the liner cooling air, depicted in Figure 2.1, is added to the combustor for film-cooling of the walls.

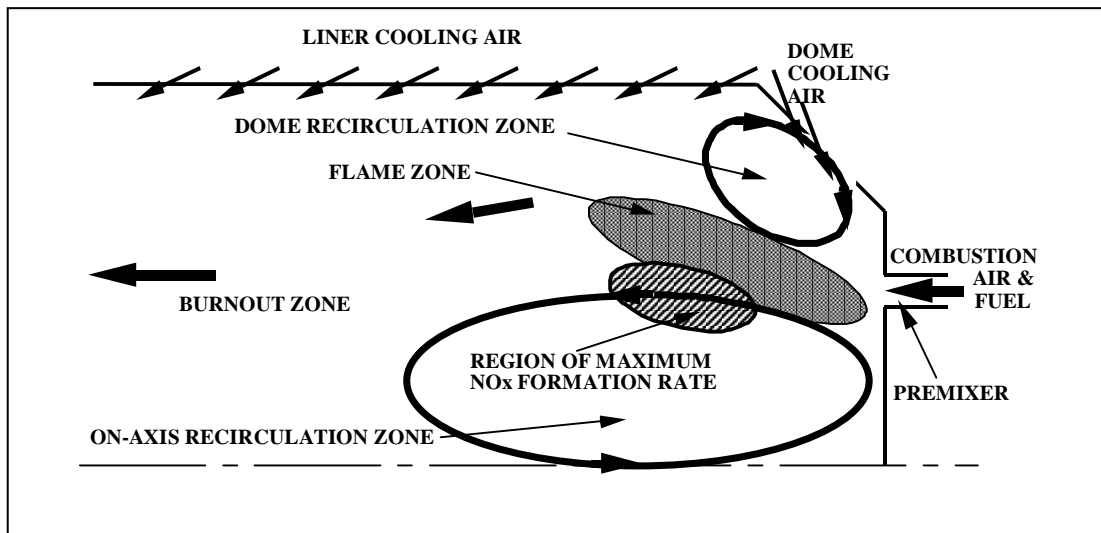


Figure 2.1 Schematic of a lean-premixed combustor can

The CFD work by Hamer and Roby (1997) shows that the highest rate of NO<sub>x</sub> formation is at the edge of the flame in a gas turbine lean-premixed combustor. The region of maximum NO<sub>x</sub> formation rate is indicated in Figure 2.1. NO<sub>x</sub> continues to form in the hot on-axis recirculation zone and in the burnout zone of the combustor. However, as the gas flows further from the flame, the rates of NO<sub>x</sub> formation decrease because the quantity of free radicals and the temperature are both decreasing.

The CFD modeling shows that the size and configuration of the characteristic combustion zones change with combustor type. These zones directly influence the NO<sub>x</sub> emission levels. Therefore, the NO<sub>x</sub> emissions are combustor dependent. An example of this dependence has been shown in field tests of General Electric's "F"-class engines. These engines have NO<sub>x</sub> emissions below 25 ppmv, dry (15% O<sub>2</sub>), when equipped with

DLN-2 combustors, and NO<sub>x</sub> emissions below 9 ppmv, dry (15% O<sub>2</sub>), when equipped with DLN-2.6 combustors (International Power Generation, May 1998).

Addition of air into the flame zone dilutes and cools the burning gases, reducing the NO<sub>x</sub> formation rate. When a cooling fluid penetrates deep into the flowing gas stream, it decreases the temperature of the flame and quenches the NO<sub>x</sub> chemistry. However, the addition of secondary air through ports in the liner for cooling is suspected to be the cause of high CO emissions (Lefebvre, 1983, p.468), which is also suggested by Nicol et al. (1997). The CO forms in the flame zone, and burns out towards the combustor exit, forming CO<sub>2</sub>. The gas that is close to the liner is leaner and colder than the rest of the flow, resulting in lower rates of CO oxidation. This is the cause of high concentrations of CO exiting the combustor. The move towards ceramic and convection-cooled combustor liners should eliminate much of the CO emission.

### ***2.5 Fuel/Air Equivalence Ratio***

Gas turbines currently sold are operated lean premixed because leaning out the fuel-air mixture at a uniform ratio reduces the flame temperature and therefore NO<sub>x</sub> formation. Heywood (1988, Fig. 11-2, p. 575) shows a variation of the NO<sub>x</sub> concentration with fuel-air equivalence ratio in the exhaust of a conventional spark-ignition engine. The NO<sub>x</sub> is low at fuel lean and fuel rich conditions, and sharply increases to reach a maximum at slightly fuel-lean conditions (i.e., a fuel-air equivalence ratio just below 1). The same behavior is characteristic for all hydrocarbon fuels, including methane. The major drawback for running a gas turbine engine significantly

fuel-lean is that the combustion becomes unstable, which results in flameout, increased flame oscillation and noise.

Fuel-air equivalence ratio,  $\phi$ , is not an actively varied parameter in this study. In this study, its value is between 0.61 and 0.8, and must be manually varied with changing residence time, pressure, and inlet temperature, to maintain a constant temperature in the reactor. The fuel-air equivalence ratio must be manually increased when increasing residence time and decreasing pressure in the reactor to compensate for increased heat loss. At the lowest residence times, the fuel-air equivalence ratio must be increased with decreasing residence time to compensate for the increasing amount of unreleased chemical energy. Finally,  $\phi$  is reduced at higher inlet temperatures, due to reduced amount of chemical energy required to achieve the desired combustion temperature.

## ***2.6 Combustion Temperature***

The need for more efficient energy conversion systems will drive the combustion temperatures higher in future designs of gas turbines. Currently, combustion temperatures are limited by material properties and cooling techniques of the turbine blades, which are, nevertheless, steadily improving. The Westinghouse 501G engine has the highest turbine inlet temperature of 1700 K and General Electric's "F"-class engine is advertised for firing temperatures of 1590 K, for both DLN-2 and DLN-2.6 combustors (International Power Generation, May 1998). Unfortunately, higher temperatures also produce higher NO<sub>x</sub>. Figure 2.2 (from Steele, 1995) shows NO<sub>x</sub> increase with combustion temperature for different experimental combustors. Original data are taken

from references indicated in Figure 2.2. The set of data points correspond to jet-stirred reactor data by Steele (1995). It is notable that these data are in good agreement with the laboratory combustor data of Leonard and Stegmaier (1993). The published data quantitatively differ considerably. For 1800 K, they range between 30 ppmv, dry, (15% O<sub>2</sub>) (Snyder et al., 1994) and 3 ppmv, dry, (15% O<sub>2</sub>) (Leonard and Stegmaier, 1993). Regardless of the differences, for any one combustor experiment, increasing temperature always causes an exponential increase in NO<sub>x</sub>.

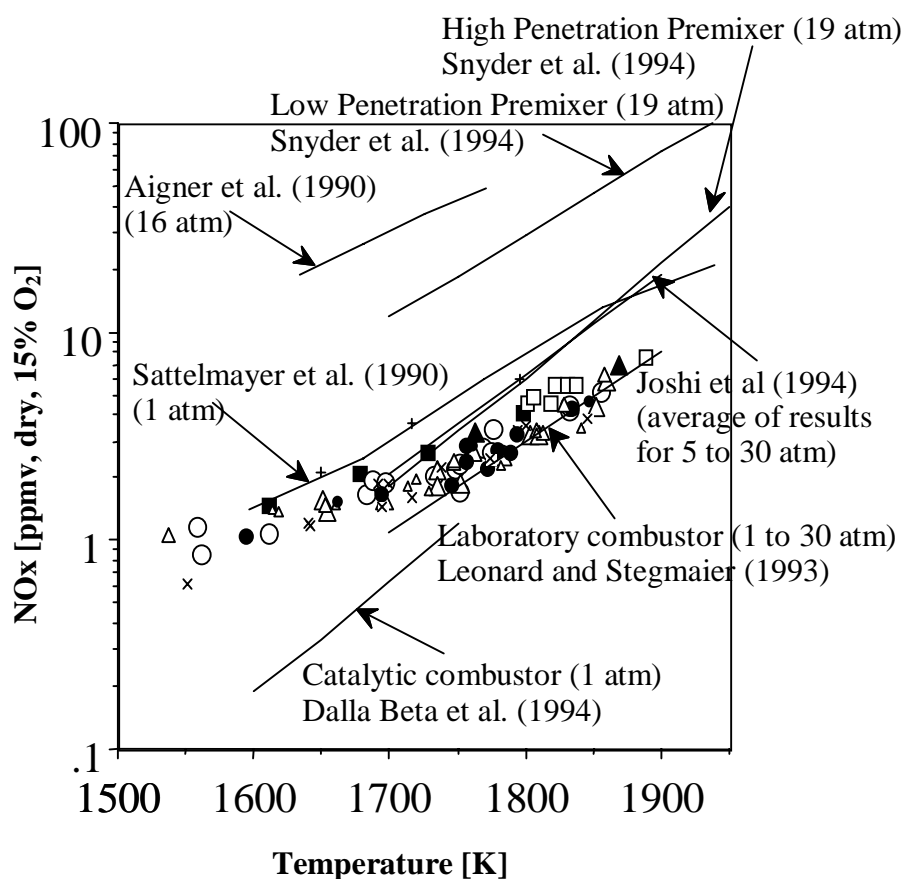


Figure 2.2 Published lean-premixed natural gas NO<sub>x</sub> experimental data

Since significant work has been done on NO<sub>x</sub> dependence on combustion temperature, and NO<sub>x</sub> behavior is empirically known, the present work does not explore the influence of the combustion temperature on NO<sub>x</sub> for lean-premixed combustion. Data obtained by Steele (1995), and shown in Figure 2.2, describe the trend of NO<sub>x</sub> versus temperature for jet-stirred reactor. The NO<sub>x</sub> temperature correlation for lean-premixed methane combustion developed by Steele (1995) is:

$$\text{NO}_x [\text{ppmv, dry, 15\% O}_2] = 1.724 \cdot 10^6 \exp(-23650/T) \quad (2.1)$$

### ***2.7 Combustor Residence Time***

Combustor residence time is the average time gases reside in the combustor. Residence time is one of the parameters varied in the HP-JSR experiments because it is thought to have value not only for laboratory combustors, but also for commercial gas turbine combustors. In both the HP-JSR and the commercial gas turbine combustor experiments, two distinctly different combustion zones can be identified: the flame and the post flame zone. The combustion reactions are significantly faster in the flame zone than in the post-flame zone (resulting in increased NO<sub>x</sub> and CO formation rates) because of the highly reactive species present in the flame. Therefore, both the size and the kinetics of the flame and the post-flame zone, which do change with mean reactor residence time, influence the formation of NO<sub>x</sub> and CO in the combustion system. Consequently, the study of the residence time effect incorporates the study of each of the two zones.

When temperature and free-radical concentrations are constant, and the NO concentration is sufficiently low for reverse reactions to be insignificant, NO<sub>x</sub> emissions will increase linearly with residence time (Heywood, 1988). This is a simple consequence of the increased time available for reaction. However, change in temperature, free-radical concentrations, and NO concentration could obscure the residence time effect. This phenomenon is seen in HP-JSR experiments by Bengtsson et al. (1998), in lean-premixed gas turbine combustors, and in the present experiments.

High-pressure jet-stirred reactor experiments by Bengtsson et al. (1998) show that NO<sub>x</sub> increases between 1.0 and 2.0 ms residence time for all pressures. However, this is pronounced only below 5 atm, with the difference being the largest at 1 atm, where measured NO<sub>x</sub> is 5.5 and 8.5 ppmv, wet for 1.0 and 2.0 ms, respectively. At pressure of 6 atm and above, the increase in NO<sub>x</sub> with residence time is small to negligible. The reactor temperature was 1783 K for measurements below 5 atm and 1823 K above 6 atm. Methane-air equivalence ratio was constant at 0.55, but the inlet temperatures were variable, and were not reported. The authors do not offer an explanation for the residence time behavior, but they do note that their reactor is not uniform.

In gas turbine combustors, the NO<sub>x</sub> dependency on residence time is further complicated by fluid mechanics within the combustor. The CFD solution of the flow within the swirl-stabilized lean-premixed combustor indicates the formation of recirculation zones in the primary combustor zone, such as ones shown in Figure 2.1. If these recirculation zones engulf a part of the flame zone, as found by Hamer and Roby (1997), then hot, free-radical rich gas resides there for extended periods of time, thus

locally forming NO<sub>x</sub>. Therefore, the lean-premixed combustor cannot be observed as a simple structure, such as a through-flow or a Bragg combustor (perfectly-stirred reactor to represent the flame zone, plug-flow reactor to represent the burn-up zone, and a non-reacting mixer for the dilution zone).

### ***2.8 Degree of Premixing***

Power generation gas turbines are operated in a lean premixed mode, as opposed to the previously used diffusion flame mode, because diffusion flames form at the stoichiometric fuel-air surface resulting in high local temperatures and one-to-two orders of magnitude higher NO<sub>x</sub> than with premixed flames. Premixed flames operate at a uniform stoichiometry which, if fuel-lean, will limit temperature and NO<sub>x</sub> formation. However, if the fuel and air enter the flame zone partially premixed, richer (hotter burning) and leaner (colder burning) pockets of reactants are formed. Since NO<sub>x</sub> formation is an exponential function of temperature, the fuel rich pockets form unproportionally more NO<sub>x</sub> than the fuel-lean pockets (Rutar et al., 1997). The result is an overall (average) lean flame with higher than expected NO<sub>x</sub> values. This is postulated to be one of the reasons why NO<sub>x</sub> measurements from industrial burner tests vary by a factor of 10, as shown in Figure 2.2 (from Steele, 1995).

In the present work, the fuel and air entering the HP-JSR are allowed sufficient time for premixing. Additionally, work by Nicol et al. (1997) suggests that any unmixedness in the inlet is removed soon upon entering a jet-stirred reactor. Therefore, the HP-JSR is

well suited for the study of NO<sub>x</sub> and CO emission for premixed combustion without a significant influence of unmixedness.

### ***2.9 Combustion Pressure***

The experimental data from the authors presented in Figure 2.2 show differing trends with respect to combustion pressure. Leonard and Stegmaier (1993) show no pressure dependency. Joshi et al. (1994) show NO<sub>x</sub> slightly decreasing when pressure is increased. Aigner et al. (1990) show NO<sub>x</sub> five times higher at 12 atm than at 1 atm. Snyder et al. (1994), with their high penetration premixer, show a 100% increase in NO<sub>x</sub> between 5 and 18 atm. In an attempt to determine the reason for such significant differences in the existing pressure data, works by Rutar et al. (1997) and Monghia et al. (1996) studied pressure trends versus unmixedness in the inlet fuel and air. They found that the NO<sub>x</sub> is independent of pressure for small levels of unmixedness, or essentially perfectly premixed cases, and that NO<sub>x</sub> becomes positively dependent on pressure with increasing unmixedness. This suggests that some of the aforementioned combustors could have been equipped with poor premixers.

The work of Steele (1995), for which a perfectly premixed reactor was assumed to have been used, has taken data at 1 atm, 4.7 atm, and 6.5 atm in a 2.0 cm<sup>3</sup> jet-stirred reactor at 4.0 ms and 2.0 ms residence times. He observed a slight decrease in NO<sub>x</sub> with combustion pressure. Bengtsson et al. (1998) have also seen that NO<sub>x</sub> decreases with pressure. This decrease was more pronounced at pressures up to 5 atm. Their data were taken for residence times of 1.0, 1.5 and 2.0 ms. Furthermore, the pressure effect was

most pronounced for the 2.0 ms data, for which the NO<sub>x</sub> varies between about 8.5 ppmv, wet, at 1.0 atm to about 5 ppmv, wet, at 5 atm. However, for the same pressure range, and for 1.0 ms residence time, the NO<sub>x</sub> decreases only from about 5.4 ppmv, wet, to about 4.5 ppmv, wet.

The pressure effect in the present work is studied for three elevated pressure levels, (3.0, 4.7 and 6.5 atm), and for a wide range of residence times, (0.5 to 4.0 ms), with an intent to explain how the pressure affects the NO<sub>x</sub> formation. The effect of increasing pressure is understood as a trade-off between two effects: (1) shorter time spent in fast NO<sub>x</sub> formation zone, and (2) generally faster formation kinetics.

### ***2.10 Inlet Air Temperature***

Experimental data on preheating of air show conflicting results for NO<sub>x</sub>. Researchers have observed zero, slight and extreme increases of NO<sub>x</sub> with increasing inlet temperature. Through work sponsored by AGTSR, the University of Washington was provided with experimental data taken in one of the industry's test combustors, termed Combustor A. The data show that increasing preheat temperature between 550 K and 650 K increases NO<sub>x</sub> 250% at a premixer fuel-air equivalence ratio of 0.57. Steele et al. (1997) found that NO<sub>x</sub> increases only slightly when inlet temperature is increased from 300 to 600 K for 1 atm ethylene combustion, with 3.5 ms residence time. Experimental data from the present work show a different trend: NO<sub>x</sub> decreases with increasing inlet temperature for the three pressures tested, and the decrease is most pronounced at low residence times, where the NO<sub>x</sub> formation approaches the well-stirred reactor condition.

The neutral inlet temperature effect observed at all pressures of the present work at longer residence times, should at least partially explain why Steele et al. (1997) have essentially not observed an inlet temperature effect at 3.5 ms. However, since the fuel and the nozzle configuration that they used were different than in the present work, final conclusion cannot be reached based on the available information.

Chapter 4 offers an explanation for the observed trends in the present work, which are summarized by the following. Higher inlet temperature cases inherently have lower fuel-air equivalence ratios, hence diminishing the effect of the prompt NO<sub>x</sub> pathway. This significantly affects the NO<sub>x</sub> at short residence times, where prompt NO<sub>x</sub> is the predominant pathway. At longer residence times, the free radical pool in the flame and temperature in the post-flame zone are rather similar between unheated and heated cases, yielding, therefore, similar NO<sub>x</sub>.

However, the Combustor A data trends still remain unexplained. Work by Rutal et al. (1997) offers a possible solution. It was found that with increasing unmixedness in the inlet fuel and air, the NO<sub>x</sub> becomes more positively dependent on inlet temperature. This suggests that Combustor A is equipped with a poor premixer. Only testing of the premixer with existing probes that measure unmixedness could confirm this postulate.

### ***2.11 Summary of Chapter 2***

Each section of Chapter 2 is summarized below:

1. Methane is the fuel used in this study because it is the main constituent of natural gas, which is the main fuel used in gas turbines for power generation. Natural gas has satisfactory supply sources, burns homogeneously, and gives low pollutant emissions.
2. The NO<sub>x</sub> in lean premixed combustion of methane and air is formed via Zeldovich, nitrous oxide, prompt and NNH chemical pathways.
3. In the gas turbine lean-premixed combustor, NO<sub>x</sub> forms at the edge of the flame at the highest rate, and then at a reduced rate in the post-flame zone. Cooling in the post flame zone quenches the NO<sub>x</sub> chemistry.
4. The CO forms in the flame zone, but the emissions are the consequence of incomplete burnout to CO<sub>2</sub>. Also, air addition for liner film-cooling can quench CO oxidation to CO<sub>2</sub> and cause high CO emissions.
5. NO<sub>x</sub> increases with fuel-air equivalence ratio in lean-premixed combustion. Therefore, manufacturers design gas turbine engines to run as lean as possible without incurring acoustic and combustion instability problems.
6. NO<sub>x</sub> increases with combustion temperature and this behavior is empirically known from previous work. Present work uses a relatively high temperature range, i.e., 1800 to 1940 K to satisfy prospective demands.
7. NO<sub>x</sub> increases linearly with residence time when temperature and free-radical concentrations are constant, because there is more time for it to form. However, in

- practical systems this is not necessarily the case due to complexity of factors influencing the NO<sub>x</sub> formation. Results from the HP-JSR support this theory.
8. Lean-premixed flames with poorly premixed reactants form higher NO<sub>x</sub> due to the existence of hot, richer-than-average pockets and make industrial burner test comparison difficult. Fuel and air in the present work are believed to be perfectly premixed. Therefore, unmixedness effect is not considered.
  9. Previous work shows NO<sub>x</sub> emissions increase or decrease with pressure, or are pressure neutral, depending on the combustor specifics. The pressure effect is studied in this work and data show negative to neutral pressure trends in the HP-JSR depending on the residence time in the reactor.
  10. Previous work shows NO<sub>x</sub> emissions increase with or are independent of the increase in the inlet temperature. The data obtained in this work show neutral behavior at residence times above 2.0 ms, and a decrease with increasing inlet temperature at lower residence times.

## CHAPTER 3

### HIGH-PRESSURE JET STIRRED REACTOR MEASUREMENTS: EXPERIMENTAL

#### METHODS AND RESULTS

##### *3.1 Introduction*

This chapter discusses the experimental method and details the experimental results and findings obtained under the present study with the purpose of satisfying the experimental objectives that were outlined in Section 1.4.1. The experiments study the NO<sub>x</sub> and CO formation in lean-premixed combustion within a jet-stirred reactor for a range of residence times from 0.5 to 4.0 ms, at three different pressure levels (3.0, 4.7, and 6.5 atm), and for preheated (to 573 K) and unheated inlet fuel and air. Section 3.2 describes the experimental hardware, including the test rig, data analyzers, gas sampling system and thermocouples. Due to the sensitivity of NO<sub>x</sub> to temperature, Section 3.3 is entirely devoted to temperature measurements and temperature corrections. Section 3.4 shows the NO<sub>x</sub> data for different residence times and pressures at unheated and preheated reactant experiments. This section contains measured NO<sub>x</sub> and CO reactor profiles for the studied conditions. Measured CO<sub>2</sub>, O<sub>2</sub>, C<sub>1</sub>-C<sub>2</sub> hydrocarbons and nitrous oxide are also shown for some conditions to assist discussion of the experimental results. The conceptual data interpretation is given in Section 3.5, and is used as a conceptual basis for the modeling of Chapter 4.

Data presented in Chapter 3 are accompanied by Appendices A and B. Appendix A contains the spreadsheets of all of the experimental data. Appendix B contains the

description of the gas temperature calculations, as well as results of the calculations in the accompanying spreadsheets.

### ***3.2 Experimental Setup***

The experiments are conducted in the high-pressure jet-stirred reactor (HP-JSR) facility at the University of Washington. The HP-JSR facility consists of a HP-JSR system, fuel and air supply lines, temperature and gas sampling lines, and instruments for measurements. The essential part of the facility is the HP-JSR system, which is illustrated in Figure 3.1. The pressure vessel, rated for 15 atm (Steele et al., 1997), houses the ceramic high-pressure jet-stirred reactor (HP-JSR), the nozzle, the fuel-air premixer, and the air heater. The combustion air, i.e., air that enters the HP-JSR, first passes through the preheater, then through the premixer, and finally through the nozzle before entering the HP-JSR. A second air stream, significantly larger in volume than the combustion air stream, is used to regulate the pressure in the vessel and does not pass through the HP-JSR. This is indicated as “pressure vessel air” in Figure 3.1.

The HP-JSR facility is fully described by Steele (1995). Minor modifications to the facility, necessary to achieve objectives of the present work, include: (1) smaller HP-JSR and larger nozzle to obtain lower residence times; (2) a ceramic probe to avoid the problem of fast deterioration of the former quartz probe; and (3) a smaller diameter wire in the thermocouple probe to decrease conduction losses. These modifications are described in detail later in the text.

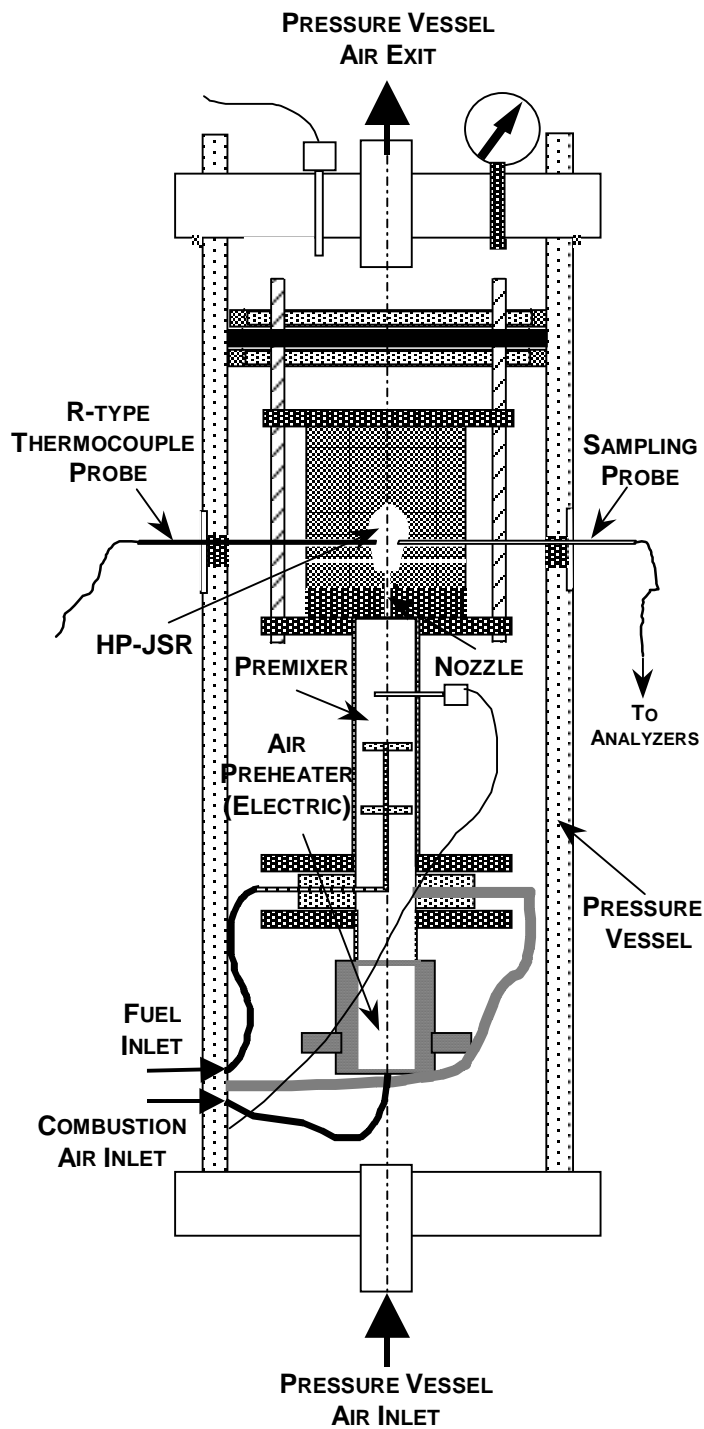


Figure 3.1 High-pressure jet-stirred reactor experimental system

Fuel (i.e., natural gas or pure methane) and air entering the HP-JSR are premixed in a chamber positioned below the jet nozzle and the HP-JSR. The residence time in the premixer exceeds 100 ms for all of the flow rates used in this study. The premixer residence time is two orders of magnitude greater than the eddy turnover times associated with the baffles in the premixer. This supports the assumption that the gases enter the HP-JSR fully premixed. Further, because of the mixing intensity within the HP-JSR, any unmixedness entering the reactor tends to be washed-out. Calculations with a partially stirred reactor model indicate that the effect of unmixedness on NO<sub>x</sub> formation in the HP-JSR is weak to negligible (Nicol et al., 1997). Therefore, combustion in the HP-JSR is treated in this work as perfectly premixed.

The HP-JSR system is equipped with a set of thermocouples for the measurement of both the premixer temperature and temperature of the top of the pressure vessel near the exhaust air port. The system is also equipped with a set of gages for pressure measurement in the sampling line, in the premixer, in the vessel, and across the nozzle (differential pressure drop). It should be noted that the pressure inside the HP-JSR is essentially the same as in the vessel because the flow-resistance through the exhaust ports of the reactor is small.

The maximum vessel operating pressure is determined by the maximum pressure available in the air supply line (called “shop air”) which is about  $7.5 \pm 0.4$  atm. Thus, for pressure stability, the maximum pressure at which the data can be taken is lower (i.e., 6.5 atm). The “shop air” is also used as combustion air in all experiments except for the

lowest residence times. The lowest residence times require bottled air to maintain high flow rates.

The schematic of the reactor cavity cross-section is shown in Figure 3.2. The diameter at the widest point is 11.5 mm, the height is 20.19 mm, and the inlet nozzle diameter is 1.4 mm, giving the height/jet-diameter ratio of 14.4. There are three differences between the present HP-JSR and previous reactors used in research by Steele (1995). The material used in the present reactor is cast alumina, versus cast zirconia used by Steele. Although geometrically similar, the volume of the present reactor is 1.5 cm<sup>3</sup>, versus a 2.0 cm<sup>3</sup> volume reactor used by Steele. Finally, the nozzle diameter is 40% larger than the nozzle diameter used by Steele. The smaller volume, combined with the larger jet diameter that permits higher mass flow rate, facilitates short residence time operation. With these differences it is possible to obtain 0.5 ms residence time operation.

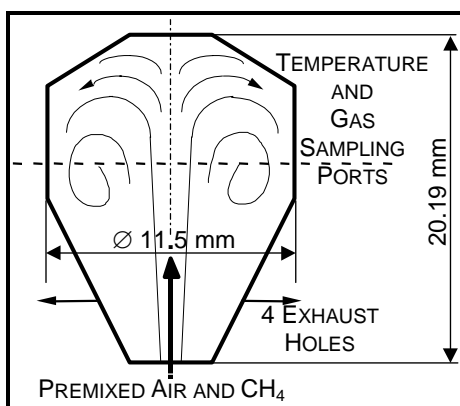


Figure 3.2 Schematic of the jet-stirred reactor cavity

The inlet jet diameter of 1.4 mm allows the HP-JSR to be run over a range of residence times from 0.5 to 4.0 ms. The large range in residence time results in an eight-fold range in the flow rate, thus, the pressure losses and jet velocity vary significantly. In order to account for these variations, pressure losses are measured and jet velocities are calculated. The jet velocity calculation is done using the following equation for isentropic discharge speed (Zucrow and Hoffman, 1976, p.124):

$$u_0 = \left\{ \frac{2\gamma RT}{\gamma - 1} \left[ 1 - \left( \frac{p'}{P} \right)^{\frac{\gamma-1}{\gamma}} \right] \right\}^{0.5} \quad (3.1)$$

where:

$u_0$  – inlet jet velocity

$\gamma$  - ratio of specific heats for methane and air mixture,

R - gas constant for methane and air mixture,

T - total temperature; i.e., the measured temperature in the top of the premixing chamber,

$p'$  - the pressure measured in the pressure vessel, which is assumed to be the pressure within the HP-JSR cavity, and

P - the total pressure, which is the pressure measured in the premixing chamber.

For 6.5 atm operation at 0.5 ms mean residence time, the measured pressure loss is 45% and the jet velocity is close to sonic. Whereas, for operation at 4.0 ms mean residence time, the pressure loss is about 3% and the velocity is about 80 m/s.

The gas sampling and temperature measurements are done at two-thirds of the height of the HP-JSR, which is the widest part of the reactor, as shown in Figure 3.2. The

position of the R-type thermocouple probe used for measuring HP-JSR gas temperature, and the HP-JSR gas sampling probe with respect to the pressure vessel is indicated in Figure 3.1. Gas sampling is done with a small ceramic probe, described by Horning (1996) and shown in Figure 3.3 below. The use of ceramic probes is favored in high-pressure environments over the previously used quartz probes, as described in Steele (1995), for two reasons. First, quartz suffers intense devitrification or crystallization at high temperatures, (of 1000 up to 1710°C), which is catalyzed by diffusion of water vapor and oxygen through the cristobalite to the glass-crystal interface. Second, nucleation on the external surfaces of fused silica is catalyzed by superficial condensed phase impurities (Ainslie et al., 1962). Practically, this means that probes need to be rebuilt after every run. Steele (1995) observed this problem in high pressure experiments at 2.0 and 4.0 ms residence times. It was anticipated that in the present work the problem would only be intensified at the short residence times, where high mass flow rates and free-radical concentrations can only exacerbate the problem.

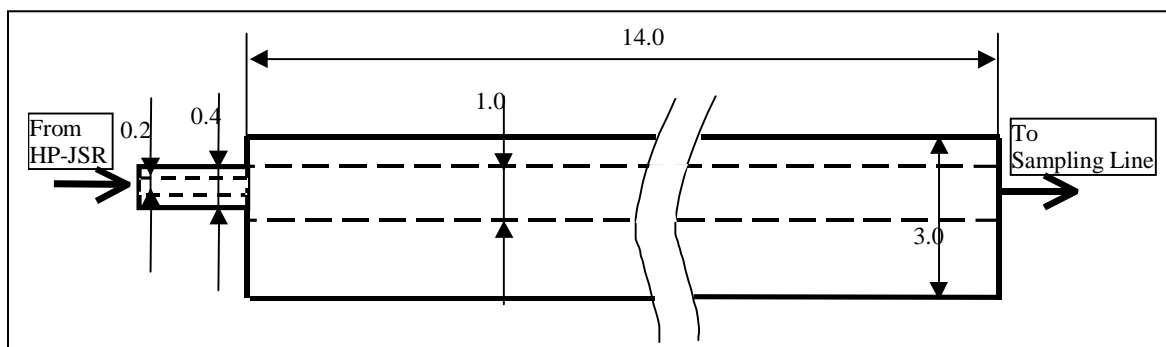


Figure 3.3 Schematic of the probe (units are mm)

The high pressure experiments have also increased the deterioration rate of the thermocouples. At short residence time runs, i.e., below 2.5 ms, and at 6.5 atm pressure, the thermocouple lifetime is about 5-6 run-hours. Upon that time, the thermocouples' accuracy rapidly decreases, and they soon break. At longer residence times and lower pressures, the thermocouple lifetime increases.

The R-type thermocouples are constructed in-house from Pt (platinum) and Pt/13%Rh (platinum/rhodium) wires welded together and placed in sheath. The sheath is a double-bore high-temperature alumina based ceramic with an outer diameter of 3/32 in ( $2.38 \times 10^{-3}$  m). The diameter of the wires, at 0.005 in ( $1.27 \times 10^{-4}$  m), is smaller than the wires used by Steele (1995), and is the smallest commercially available wire diameter that is practical for present application. The thermocouple junction, i.e., the welded bead joining the wires, is coated with Ceramabond 569, a high temperature ceramic paste consisting of at least 99% alumina. Burton et al. (1991) recommend this coating as opposed to toxic beryllium oxide/yttrium oxide coating or to silicon dioxide coating. The same authors also found that using a silicate thinner for Ceramabond 569 makes the coating less stable, which is also observed in the present work. If a tiny crack develops in the coating, the wires beneath deteriorate, and the thermocouple has to be replaced. Therefore, particular attention is devoted to building sturdy thermocouples with only alumina based coatings. To ensure that thermocouples, including the coatings, are properly manufactured, each thermocouple was calibrated to within a 15 K temperature variation (at 1800 K nominal temperature) at the standard operating conditions of the HP-JSR.

Gas samples are continuously withdrawn from the reactor, and are analyzed for NO, NO<sub>x</sub>, CO, CO<sub>2</sub>, and O<sub>2</sub> via process gas analyzers. The NO and NO<sub>x</sub> are measured by a chemiluminescent analyzer while the CO and CO<sub>2</sub> are measured by non-dispersive infrared analyzers, and the O<sub>2</sub> is measured by a paramagnetic analyzer. These four analyzers are zeroed and spanned (with customized span-bottles) approximately every two run-hours.

Additional (non-continuous) samples of gas are analyzed for C<sub>1</sub>-C<sub>3</sub> hydrocarbons and nitrous oxide by gas chromatography. The detector used for measuring C<sub>1</sub>-C<sub>3</sub> hydrocarbons is a flame ionization detector (FID), while N<sub>2</sub>O is measured with an electron capture detector (ECD). The FID is calibrated for each hydrocarbon by preparing the desired calibration gas mixtures in a Pyrex sample tank. The calibrations for methane, ethane, and ethylene are linear, extending over mole fractions between 0 and 11000 ppm (see Appendix A). The N<sub>2</sub>O is calibrated (using a span gas of 1 ppmv N<sub>2</sub>O) approximately every 2 run-hours to monitor small changes in the ECD sensitivity. A linear calibration is assumed since measured N<sub>2</sub>O levels did not exceed 2.5 ppm, and previous work by Steele (1995) found a linear correlation between the GC counts and the N<sub>2</sub>O mole fraction up to about 10 ppm. The gas chromatograph operation parameters are listed in Steele (1995).

Sample gas is continuously drawn from the HP-JSR with a sampling probe (sketched in Figure 3.3), as was mentioned above. After passing through the probe, the gases pass through the sampling line, which contains a water trap to dry the gas (because the analyzers require a dry sample), and a metal-bellows pump prior to entering the

analyzers. The pump maintains vacuum in the sample line of approximately 0.7 atm (0.3 atm absolute pressure). The high pressure difference across the probe from reactor pressure (6.5, 4.7 or 3.0 atm) to the vacuum pressure of 0.3 atm, causes high mass flow rates through the probe.

Reactions can continue within the probe, and some of those are relevant to this work, e.g.,  $\text{NO} + \text{HO}_2 \rightarrow \text{NO}_2 + \text{OH}$ , and  $\text{CO} + \text{OH} \rightarrow \text{CO}_2 + \text{H}$ . The NO conversion to  $\text{NO}_2$  reaction is important because: (1) the probe alters the  $\text{NO}_x$  composition from almost pure NO at the inlet to the probe, i.e., in the reactor, to almost pure  $\text{NO}_2$  measured at the analyzer; and, (2) the  $\text{NO}_2$  formed in the probe is soluble in water, thus it could be lost in the water condensed in the sampling line and cause a loss in total  $\text{NO}_x$  in the gas sample. The CO oxidation to  $\text{CO}_2$  reaction is important because it represents a loss of CO (while total carbon is conserved). Losses of  $\text{NO}_x$  and CO are not desired because they distort the apparent reactor concentrations of these species, leading to problems in data interpretation. The chemical kinetics in probes sampling gas from flames were studied by Kramlich and Malte (1978). The interaction between chemical kinetics and gas dynamics in the quartz probe was studied by Steele (1995), and in the ceramic probe was studied by Horning (1996).

The loss of CO in the probe, i.e., CO oxidation to  $\text{CO}_2$ , occurs because of the presence of the OH radical in the sampled gas. The concentration of OH radical is the highest at the probe entrance and it is reduced as the sampled gas cools along the probe. The cooling of the gas in the probe is induced by the cold pressure vessel air, surrounding the probe in the space between the HP-JSR and the pressure vessel (see Figure 3.1). The

portion of the probe in the pressure vessel wall and the sampling port is exposed to high rate of convective cooling caused by the high velocity of the pressure vessel air exiting the vessel through the narrow opening between the probe and the wall of the sampling port. The cooling of the probe induces the decrease in gas temperature, which, in turn, causes the rapid reduction of the OH, O, and H radicals to effectively zero, hence quenching the CO oxidation. Horning (1996) found that for initial CO mole fraction of 200 ppm only about 8% was lost due to reaction in the probe. Steele (1995), who used and modeled a different probe (as discussed above), has found that the fraction of the CO that oxidizes within the probe is proportional to the initial amount of CO. This is explained by the tendency of the OH concentration levels (and O-atom and H-atom levels) to correlate with the CO levels in lean-premixed combustion (Nicol, 1995). Therefore, high CO means high OH concentration, hence a high CO oxidation rate. The CO concentration in the reactor [% , wet] is calculated from the measured CO by the following equation (Equation 3.2), which accounts for the CO probe loss by a curve fit from the probe modeling results given by Steele (1995) and Horning (1996).

$$[\text{CO in reactor, \% wet}] = [\text{CO meas, \% wet}] / \{1.6327 - 0.1366 \ln[\text{CO meas, ppm wet}]\} \quad (3.2)$$

Equation 3.2 is used in the present work only in Section 3.3.4 for estimating the chemical energy retained in CO and thus not available to sensible energy. In the remainder of the dissertation, the experimental CO data are presented as measured, i.e., without the correction for the CO loss in the probe.

The conversion of NO to NO<sub>2</sub> in the probe occurs because of the presence of the transient HO<sub>2</sub>. Kramlich and Malte (1978) found that the HO<sub>2</sub> concentration in the sampled gas is negligibly small until the gas reaches a point of intense cooling, when the concentration rapidly increases, which was also verified by Horning (1996) and Steele (1995). At that point the concentrations of O, H, and OH radicals rapidly decrease, reducing the destruction rate of HO<sub>2</sub> via second-order reactions with the radicals. Consequently, the rapid HO<sub>2</sub> formation by three-body recombinations (induced by high radical concentrations immediately before the cooling begins) and the slow destruction in the rest of the probe, create a window of high HO<sub>2</sub> concentration. This transient HO<sub>2</sub> reacts with NO to form NO<sub>2</sub>. The mechanism of transient HO<sub>2</sub> formation in sample probes drawing gases from the flame zone is explained in Kramlich and Malte (1978).

It should be noted that the NO<sub>x</sub> in the HP-JSR is essentially only NO. However, due to formation of the HO<sub>2</sub> in the probe, the NO is converted to NO<sub>2</sub>, and is measured as such by the NO<sub>x</sub> analyzer. For the remainder of the dissertation, it is assumed that NO<sub>x</sub> (as the sum of NO and NO<sub>2</sub>) measured by the probe sampling is equivalent to the NO formed in the reactor.

The NO<sub>2</sub> presence in the sampled gas could cause the loss of total NO<sub>x</sub> in the gas sample only if the NO<sub>2</sub> is removed by water in the sampling line. To prevent this, the sampling line is kept above the condensation temperature for water at 0.3 atm via heating tape. In addition, checks are made to confirm that little if any of the NO<sub>2</sub> is lost. These checks are done with a NO<sub>x</sub>-to-NO converter placed at two different points in the sampling line, i.e., just downstream of the probe and just upstream from the water trap.

Because of the higher pressure in the probe of nominally 3 atm absolute pressure, caused by the flow-resistance of the NO<sub>x</sub>-to-NO converter, the residence time of the gas in the probe is increased, which inhibits existence of transient HO<sub>2</sub>, hence less NO is converted to NO<sub>2</sub> in the sample probe. Thus, two things are achieved by placing the NO<sub>x</sub>-to-NO converter in the sample line: (1) less NO<sub>2</sub> is formed in the probe, and (2) NO<sub>2</sub> is converted back to NO in the converter prior to the water trap. Therefore, the NO<sub>2</sub> loss in the sampling line is minimized. Tests showed no significant difference is measured between the NO<sub>x</sub> measurements for same conditions with and without the converter in the sample line. The in-line NO<sub>x</sub>-to-NO converter, however, promotes oxidation of CO in the sample probe due to the increased pressure. Thus, the in-line NO<sub>x</sub>-to-NO converter is only used periodically to verify the lack of NO<sub>2</sub> loss in the sample system.

### ***3.3 Gas Temperature***

Knowledge of gas temperature is important for the interpretation of NO<sub>x</sub> measurements. However, the true gas temperature cannot be directly measured due to heat-loss from the thermocouple, and thus, the measured temperature must be corrected. In order to assess the true gas temperature the following approach is taken: first, three types of temperature measurements are taken during production runs, and, second, the results are subjected to a detailed heat-transfer analysis. The three temperature measurements are:

1. Gas temperature inside the HP-JSR cavity measured by a R-type thermocouple,
2. Wall temperature measured by an optical pyrometer, and

3. Inlet gas temperature measured by a K-type thermocouple in the top part of the premixer.

### ***3.3.1 HP-JSR Gas Temperature Measurements Using R-Type Thermocouples***

Two main combustion zones are observed in HP-JSR – the jet zone and the recirculation zone. Steele (1995) and Steele et al. (1998) have shown typical temperature profiles across the HP-JSR. Temperature sharply increases from the jet centerline to the edge of the jet zone and then remains essentially uniform throughout the recirculation zone. The present work confirms this temperature profile by testing at a few conditions. For the majority of the experimental runs the thermocouple is positioned in the middle of the recirculation zone, measuring, and thus reporting, only one temperature - the essentially uniform temperature of the recirculation of the reactor. This position is chosen because it is in the region of the final stage of the combustion reaction and thus the maximum amount of chemical energy has been released. The measured uncorrected reactor temperature is held constant at  $1803 \pm 5$  K throughout the HP-JSR experiments.

During the experiments, enough time is allowed for the reactor to reach steady state temperature conditions. Depending on the starting temperature, this time is up to three hours in cases when the reactor is started cold, and as short as a few minutes when all of the parameters were constant, but the probe location is changed. Thermocouples are inspected daily for cracks in the alumina to assure minimal catalytic reaction at the surface of the thermocouple wires and bead, as well as to check the life of the thermocouple.

As stated previously, thermocouple measurements taken in the HP-JSR experiments do not represent the true gas temperature. This is mainly caused by radiation losses from the thermocouple to the reactor wall. Heat loss through the reactor wall increases with increasing residence time. This is manifested by decreasing wall temperature and results in increased radiation heat flux from the thermocouple to the walls as the residence time is increased. This flux cools the thermocouple, and is balanced by the convective heat transfer from the gases to the thermocouple. Minor cooling of the thermocouple also occurs by conduction through the wires and the thermocouple sheath. The thermocouple surface temperature is slightly higher than the bead temperature, since some heat is conducted to the environment through the thermocouple coating and through the thermocouple wires. A schematic of the heat flow is shown in Figure 3.4.

### ***3.3.2 Optical Pyrometer Wall Temperature Measurements***

The reactor wall temperature is measured with the optical pyrometer. Due to experimental constraints, the light emitted from the wall approaches the pyrometer through a window on the reactor pressure vessel and a safety screen outside of the vessel. See Figure 3.5.

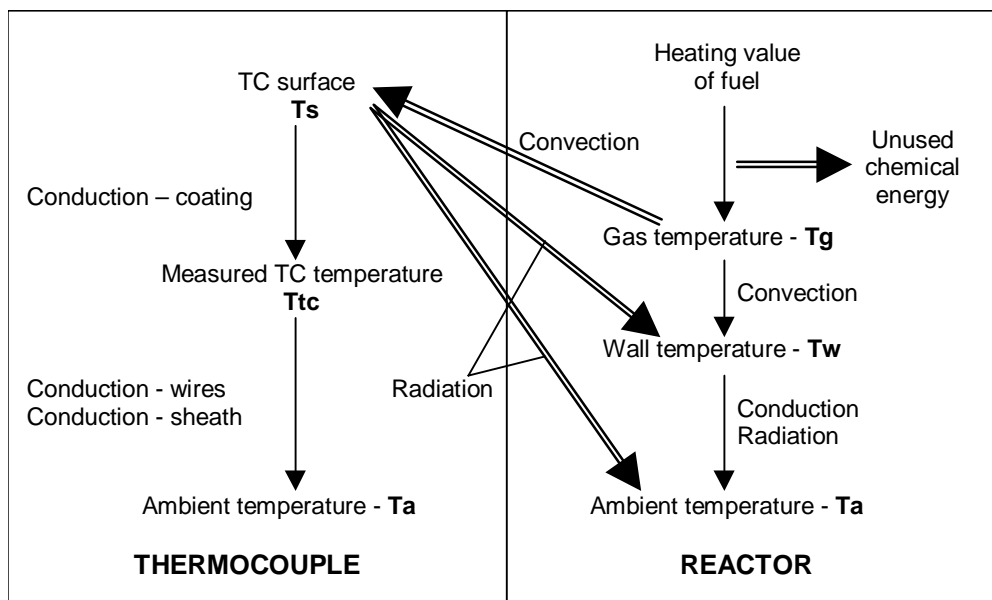


Figure 3.4 A schematic of the heat transfer within the HP-JSR

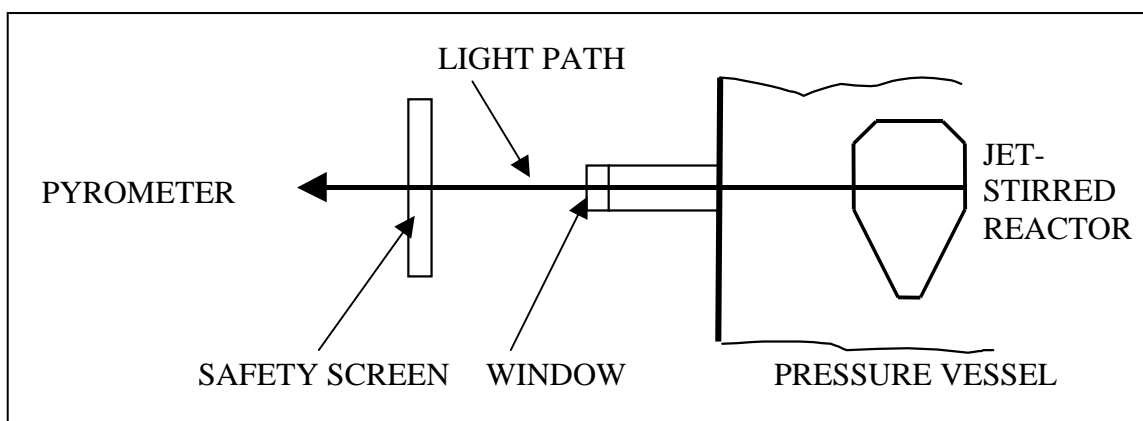


Figure 3.5 Light path during wall temperature measurements

In order to determine the effect of the window and the safety screen on the wall temperature reading, the pyrometer measurement technique is calibrated with the following four temperature readings:

- Case 1. Temperature reading with both the window and the safety screen,  
 Case 2. Temperature reading with the window and without the safety screen,  
 Case 3. Temperature reading without the window and with the safety screen, and  
 Case 4. Temperature reading without the window or safety screen, i.e., unobstructed.

The pyrometer temperature readings are summarized in Table 3.1. The overall reactor residence time is 1.1 ms, the thermocouple measured temperature is 1813 K, the fuel-air equivalence ratio is 0.8, and pressure is 1 atm. The wall emissivity is assumed to be unity ( $\epsilon_w = 1$ ), that is, it is assumed the reactor cavity behaves as a blackbody cavity for the purpose of estimating  $\epsilon_w$ .

Table 3.1 Measured pyrometer temperatures [ $^{\circ}\text{C}$ ]

	Case 1	Case 2	Case 3	Case 4
Experiment 1	1030	1110	1120	1220
Experiment 2	1030	1100	1210	1210
Experiment 3	1080	1095	1180	1220

The experimental results point out that the unobstructed temperature reading of 1210 to 1220  $^{\circ}\text{C}$  is diminished with the addition of the window and the screen by 150  $^{\circ}\text{C}$  to 200  $^{\circ}\text{C}$ . Addition of the window decreases the temperature 110  $^{\circ}\text{C}$  to 125  $^{\circ}\text{C}$ . Addition of the safety screen decreases the temperature between 0 and 100  $^{\circ}\text{C}$ . The significant difference between the readings observed in cases 1 and 3 are attributed to the safety screen. The safety screen is a clear plastic sheet and could have differences in transmissivity (due to scratches, thickness, etc.) depending on the location of the measurement.

Two other errors could influence the pyrometer measurements. First, the emissivity of the reactor wall varies due to varying surface roughness and due to wall deposits.

Thus, if the experimentalist does not take the measurements at exactly the same spot each time, variations in measured temperatures are possible. Second, the color of the filament in the optical pyrometer has to be matched to the color on the measured surface, which can be influenced by human error.

### ***3.3.3 Inlet Gas Temperature Measurements with a K-type Thermocouple***

Inlet gas temperature is measured inside the premixing chamber. The K-type thermocouple is placed just below the inlet nozzle (Steele, 1995), as sketched in Figure 3.1. These measurements are not corrected for heat loss. Measured inlet temperatures are plotted in Figure 3.6 versus HP-JSR residence time for the three pressure levels, i.e., 3.0, 4.7 and 6.5 atm. The residence time is calculated based on the following formula:

$$\tau = \frac{\rho V}{\dot{m}} \quad (3.3)$$

The numerator in the equation is the product of the reactor volume, i.e.,  $V = 1.5 \text{ cm}^3$ , and the gas density ( $\rho$ ), which is estimated for gas with a molecular weight of 28 kg/kmol, at reactor pressure, i.e., 3.0, 4.7 or 6.5 atm, and measured temperature ( $1803 \pm 5 \text{ K}$ ). The denominator represents the total (fuel and air) mass flow rate.

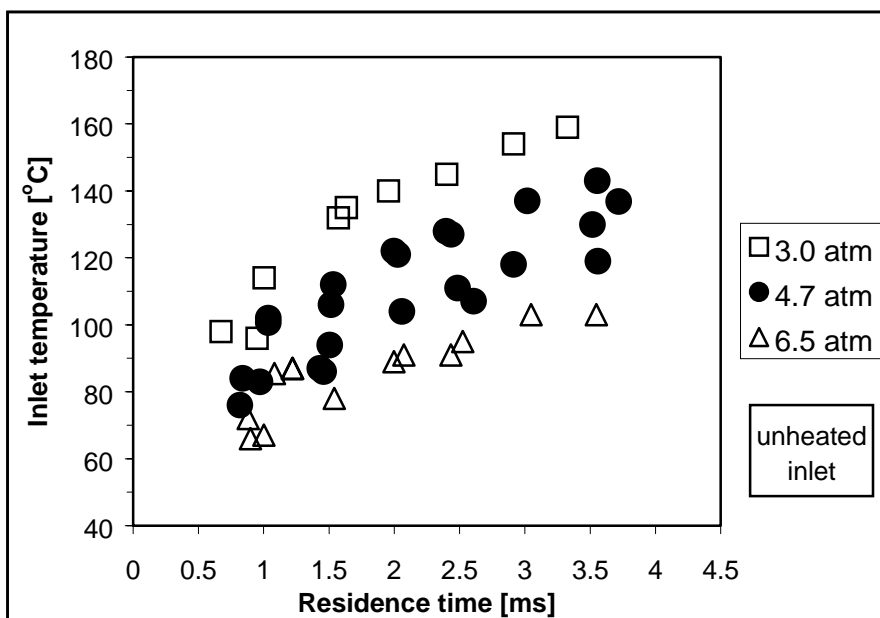


Figure 3.6 Measured inlet temperature versus residence time for 6.5, 4.7 and 3.0 atm runs in HP-JSR operated at 1800 K measured reactor gas temperature

Figure 3.6 shows that increasing residence time, i.e., decreasing mass flow rate, results in an inlet temperature increase for all the pressure levels considered. Two reasons are postulated to explain this increase: the increase in the true reactor temperature and the increase in time for heat transfer from the reactor to the premixing chamber. At high flow rates, the time gases spend in the reactor is insufficient for nearly complete combustion, and the unreleased chemical energy is evidenced by high CO and unburned hydrocarbon concentrations (discussed later in the text). To compensate for the unreleased chemical energy the fuel-air equivalence ratio is increased, thus maintaining thermocouple temperature at a constant value (i.e., 1803 K). Since the convective loading onto the thermocouple is high, the true gas temperature is close in value to the

thermocouple temperature. Consequently, the relatively low gas temperature in the reactor cavity and the short time available for heat transfer results in the reduced temperature of the premixer. As the overall residence time is increased, i.e., as the flow rates are decreased, more time is allowed for completing the combustion (evidenced by decreasing CO levels) and, there is more time for heat loss from the reactor. Also, under these low velocity conditions the convective loading onto the thermocouple decreases. This requires a higher true gas temperature to maintain the fixed thermocouple temperature of 1803 K. Heat transfer from the HP-JSR cavity to the premixer increases with increasing residence time because of higher gas temperature in the reactor cavity and greater time available for heat transfer, resulting in higher premixer temperature.

Data presented in Figure 3.6 also suggest that most of the measurements at 3.0 atm are obtained under conditions of increased heating of the premixer, compared to data taken at 4.7 and 6.5 atm. The inlet temperature variation at 6.5 atm is between 66 °C at 0.9 ms and 103 °C at 3.5 ms. At 3.0 atm, it increases between 98 °C at 0.7 ms and 159 °C at 3.3 ms, which is a considerably higher temperature than at 6.5 atm. Inlet temperatures at 4.7 atm fall between those at 6.5 atm and those at 3.0 atm. The increase in inlet temperature with decreasing pressure is caused by an increase in heat transfer from the HP-JSR cavity to the premixer.

### ***3.3.4 HP-JSR Gas Temperature Calculation***

Figure 3.7 shows the temperature measurements and calculations, including the calculated true gas temperature, for the HP-JSR operating at 6.5 atm. The measured

uncorrected reactor temperature is held constant at  $1803 \pm 5$  K throughout the HP-JSR experiments as shown by the dark circles in Figure 3.7. The HP-JSR inside wall temperature measurements, adjusted for finite transmissivity through the viewing ports of the high pressure housing and using  $\varepsilon_w=1$ , are shown in Figure 3.7 as dark triangles. The optical pyrometer measurement methods are described in Section 3.3.2 above.

As shown in Figure 3.7, the reactor inside wall temperature falls with increasing residence time. The increasing temperature difference between the reactor gas and the inside wall is indicative of increasing thermal resistance in the boundary layer as the reactor mass flow rate and velocity decrease with increasing residence time.

Although the HP-JSR measurements are conducted for constant measured uncorrected thermocouple temperature, the true gas temperature in the reactor increases with increasing residence time. The gas temperature in the recirculation zone is calculated by two methods. The first method is based on the heat balance for the thermocouple. Convective thermocouple heating is balanced by radiative loss to the walls and ports of the reactor. As the reactor residence time increases and velocity decreases, the convective heat transfer coefficient for the thermocouple surface decreases. Further, as shown in Figure 3.7, the wall temperature drops with increasing residence time. This increases the radiative heat transfer from the thermocouple to the wall, since the thermocouple views a surface of decreasing temperature. Both effects, i.e., the smaller convection coefficient and the greater radiative transfer, increase the temperature difference between the gas and thermocouple, and thus indicate an increasing true gas temperature.

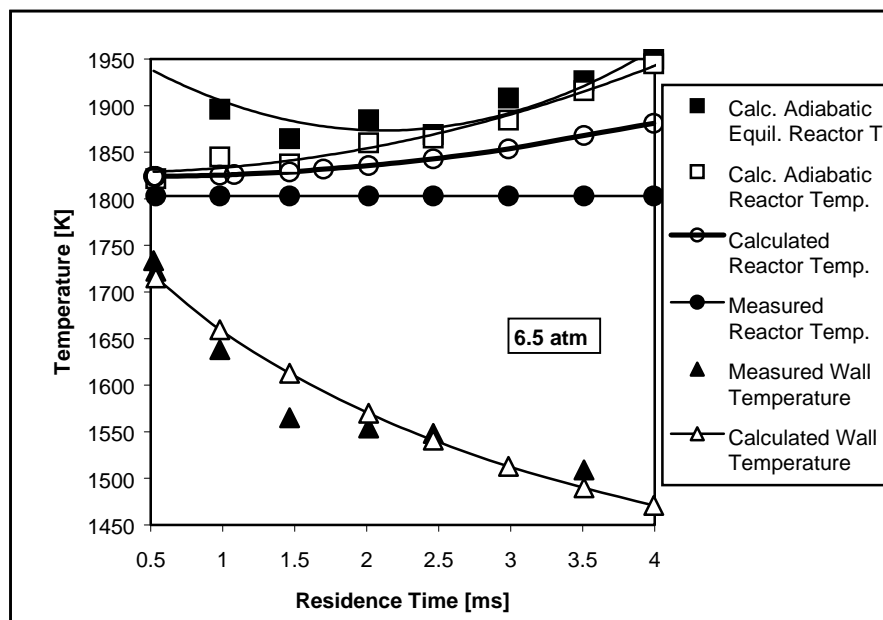


Figure 3.7 HP-JSR temperature measurements and calculations for 6.5 atm data

The second method for calculating the true gas temperature is based on a three step procedure that considers the chemical energy release in the reactor and the reactor heat loss. In the first step of the procedure, the adiabatic equilibrium temperature for the measured fuel-air equivalence ratio and measured mixture inlet temperature is computed. This is plotted in Figure 3.7 with dark squares. The fuel-air equivalence ratio is determined in two ways. It is based on the measurement of the sum of  $\text{CO}_2$  and  $\text{CO}$  in the recirculation zone of the reactor, i.e., on the total carbon, and on the measurement of the  $\text{O}_2$  concentration in this zone. The fuel-air equivalence ratio calculated with these two methods differs at most by 1.5%. For the present experiments, unburned hydrocarbons have a weak influence on the carbon balance. The measured

concentrations of unburned hydrocarbons show that the hydrocarbon levels in the recirculation zone do not exceed a few hundreds of parts per million carbon. Including unburned hydrocarbons into calculation of fuel-air equivalence ratio would change the calculated fuel-air equivalence ratio, based on measured CO and CO<sub>2</sub> concentrations, by less than 1%. Therefore, hydrocarbons are not included in calculations of the fuel-air equivalence ratio.

A minimum fuel-air equivalence ratio of 0.68 occurs in the 1.5 ms to 2.5 ms residence time range (at 6.5 atm). At longer residence times, the mixture is enriched to overcome heat loss, and reaches 0.73 at 4.0 ms. At shorter residence times, incomplete combustion occurs, i.e., CO is not oxidized to CO<sub>2</sub>, and the fuel-air equivalence ratio is enriched to overcome this. Consequently, at 0.5 ms, the fuel-air equivalence ratio is 0.75.

As the next step in this gas temperature calculation, the gas temperature is adjusted for the unburned CO. If this CO were burned, significant energy would be released. The estimate (using chemical equilibrium and chemical reactor modeling) shows that 1% CO, if oxidized forming CO<sub>2</sub>, increases the gas temperature about 80 K. The adiabatic equilibrium temperature is debited using this result, giving the adiabatic temperature plotted in Figure 3.7 as open squares. Detailed CO measurements are shown in Section 3.4 (see Figures 3.12 and 3.23). For the recirculation zone, i.e., for the  $(R/R_{\max})^2$  between 0.36 and 1.00 (where R is radius of the reactor circular cross section at the probe height, and R<sub>max</sub> is 5 mm, which is close to the wall radius of 5.75 mm), the measured CO (volume averaged) increases from about 0.05% (dry) at 4.0 ms residence time to about 0.81% (dry) at 0.5 ms. The CO measurements are adjusted for CO loss in the

sampling probe based on the chemical kinetic modeling of the probe reactions by Steele (1995) and Horning (1996), by using Equation 3.2. Thus, the measured CO of 0.81% (dry) at 0.5 ms becomes 1.61% adjusted CO in the reactor, leading to a temperature difference of  $1.61 \cdot 80 \cong 130$  K, as shown in Figure 3.7.

The third step in this calculation of the reactor temperature is the treatment of the reactor heat loss. This is conducted using engineering analysis to estimate the resistances for the convective, conductive, and radiative heat transfer processes. Comparison of the measured and calculated inside wall temperature serves as a check on the calculation. As shown in Figure 3.7, this agreement on the inside wall temperature is good, and provides confidence in the heat loss calculation for the reactor.

The loss in gas temperature predicted by the reactor heat loss, i.e., the second method, is about 0 K at 0.5 ms and about 62 K at 4.0 ms. Consequently, the difference between the predicted gas temperature and the measured uncorrected thermocouple temperature is 20 K at 0.5 ms, and 78 K at 4.0 ms. These values are in close agreement with the independent calculation of thermocouple heat loss via the first method, which gives a difference in temperature between the gas temperature and measured temperature of 13 K at 0.5 ms and 75 K at 4.0 ms. The solutions to the two methods, because of their close agreement, are averaged for the final result of the reactor true gas temperature. This average is plotted in Figure 3.7 as the open circles.

In the region from 0.5 to 2.0 ms, the reactor gas temperature (in the recirculation zone) is nearly constant at 1825 K, whereas in the region from 2.0 to 4.0 ms, the

temperature increases to 1880 K. The reactor gas temperature dependence on residence time  $[\tau]$  is shown in the Equation (3.4) below:

$$[\text{Reactor gas temperature at 6.5 atm, K}] = 4.4 [\tau, \text{ms}]^2 - 3.3 [\tau, \text{ms}] + 1824 \quad (3.4)$$

The same procedure is used in estimating the true gas temperature for the 4.7 and 3.0 atm data, and the results of the analysis are shown in Figures 3.8 and 3.9, respectively. The adiabatic equilibrium temperature for 4.7 atm, plotted in Figure 3.8, is quantitatively similar to the values at 6.5 atm, shown in Figure 3.7, because the equivalence ratios are similar. At 4.7 atm, the fuel-air equivalence ratio decreases from 0.72 at 0.9 ms, reaches a plateau of 0.68 in the vicinity of 2.0 ms, and then increases to 0.73 at 3.6 ms. However, at 3.0 atm, the equivalence ratio decreases from 0.71 at 0.7 ms, reaches a plateau of 0.69 for lower residence times of 1.0-1.5 ms, and then steadily increases from 0.69 at 1.5 ms to 0.8 at 3.3 ms. This increase, accompanied with lower CO levels (see Section 3.4.1), suggests that the reactor is operating in a high heat loss mode for the 3.0 atm cases with residence times between 1.0 and 3.3 ms. Unreleased chemical energy is noticed at lowest residence time, (i.e., at 1.0 ms and below), where CO levels in the recirculation zone are significantly higher than at the other residence times considered.

Heat transfer calculations for 4.7 atm show that the true reactor temperature increases from about 1820 K in the vicinity of 1.0 ms, to 1880 at 3.6 ms. These calculations show that the true gas temperature in the recirculation zone of the reactor at 4.7 atm is similar to that at 6.5 atm.

The true gas temperature in the recirculation zone of the reactor for data taken at 3.0 atm increases steadily between 1808 K at 0.7 ms and 1938 K at 3.3 ms. This increase is due to the heat transfer through the reactor walls, ports and the inlet jet nozzle. This dependence is plotted in Figure 3.9 and is given by equation (3.5).

$$[\text{Reactor gas temperature at 3.0 atm, K}] = 46.9 [\text{Residence time, ms}] + 1773 \quad (3.5)$$

The complete heat transfer analysis, with equations and assumptions, for the gas temperature calculations in the HP-JSR are shown in Appendix B. The spreadsheets containing the results of these calculations are shown in Appendix B. Appendix B also shows data spreadsheets and figures for preheated inlet cases, which are not discussed in this section.

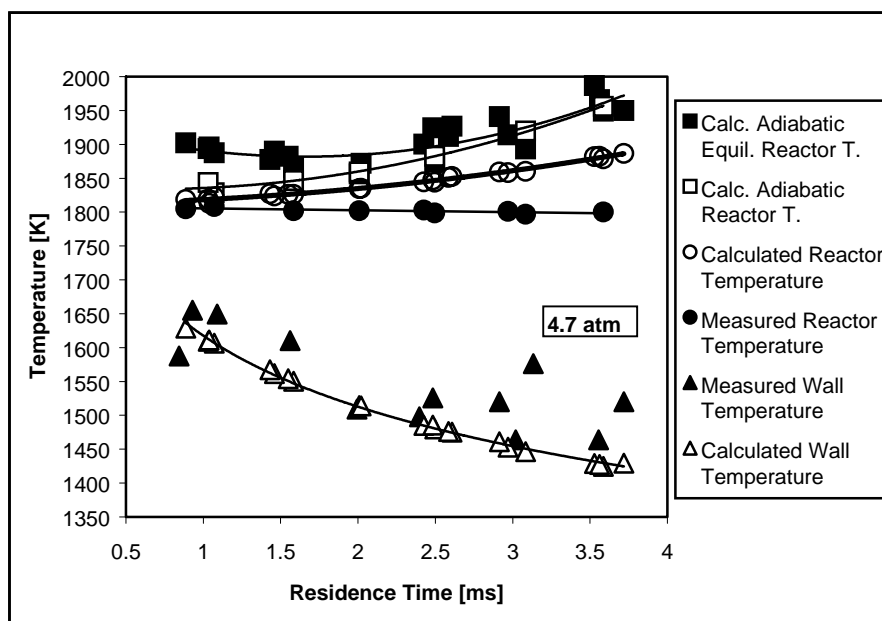


Figure 3.8 HP-JSR temperature measurements and calculations for 4.7 atm data

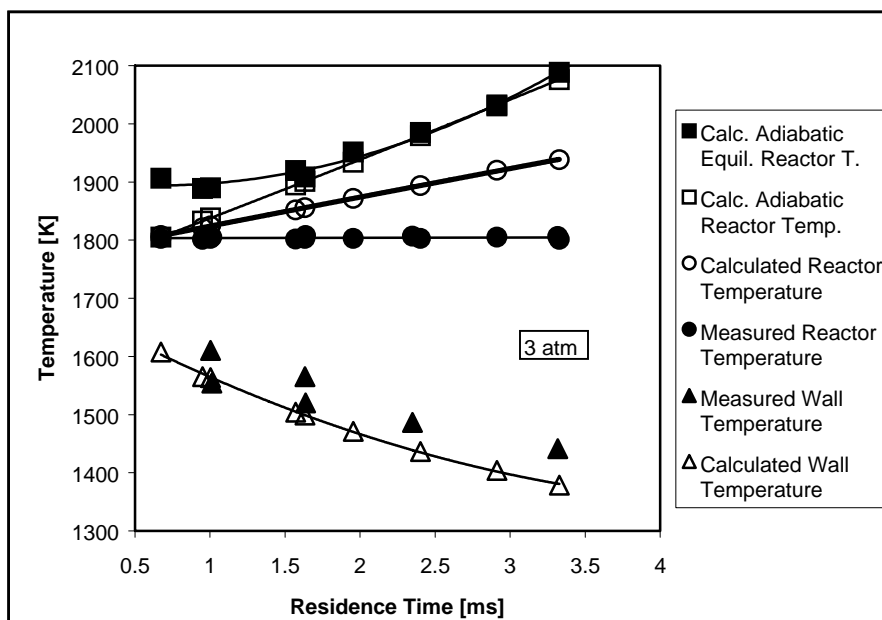


Figure 3.9 HP-JSR temperature measurements and calculations for 3.0 atm data.

### 3.4 Experimental Results and Discussion

#### 3.4.1 Residence Time and Pressure Effect on NO<sub>x</sub> Formation for Unheated Inlet Experiments

The effect of the residence time on measured NO<sub>x</sub> for the pressures of 6.5, 4.7 and 3.0 atm is shown in Figure 3.10. The combustion air is not electrically preheated, however, the measured air-fuel temperature at the exit of the premixer varies according to Figure 3.6, as discussed in Section 3.3.3. The recirculation zone in the HP-JSR is nearly uniform in NO<sub>x</sub> concentration and that NO<sub>x</sub> concentration is plotted in Figure 3.10. Furthermore, the NO<sub>x</sub> concentration in the recirculation zone is taken as the NO<sub>x</sub>

emission of the HP-JSR, since most of the exhaust draining from the reactor comes from this zone and the zone is nearly uniform in NO<sub>x</sub>.

Data for 6.5 atm show that over the mean residence time range covered, starting with 0.5 ms, the NO<sub>x</sub> concentration drops substantially with increasing residence time, attains a minimum in the vicinity of 2.5 ms, and then increases as the time is increased to 4.0 ms. This is shown in Figure 3.10. A similar behavior is observed for the two lower pressure levels, however, the minimum NO<sub>x</sub> is shifted towards shorter residence times. At 4.7 atm, the minimum is in the vicinity of 2.0 ms; whereas for 3.0 atm, it is between 1.0 and 1.5 ms. At residence times above about 2.0 ms, the NO<sub>x</sub> is clearly increasing with decreasing pressure. At lower residence times, NO<sub>x</sub> for 3.0 atm is clearly higher than at the other two pressures, while there is insignificant difference between NO<sub>x</sub> for 4.7 and 6.5 atm.

At 0.5 ms residence time and 6.5 atm, CO concentrations in the recirculation zone of the HP-JSR are in the range of about 0.5 to 1.2% (dry), indicating a significant amount of unreleased chemical energy. CO decreases to about 0.05% (dry) at 4.0 ms, indicating that sufficient time is allowed for chemical energy release. However, at those long residence times, more time is available for the heat loss from the reactor. Because the uncorrected thermocouple temperature is maintained constant at 1803 K (by adjusting the fuel flow rate of the reactor), the true gas temperature increases with increasing residence time, as described in the previous section.

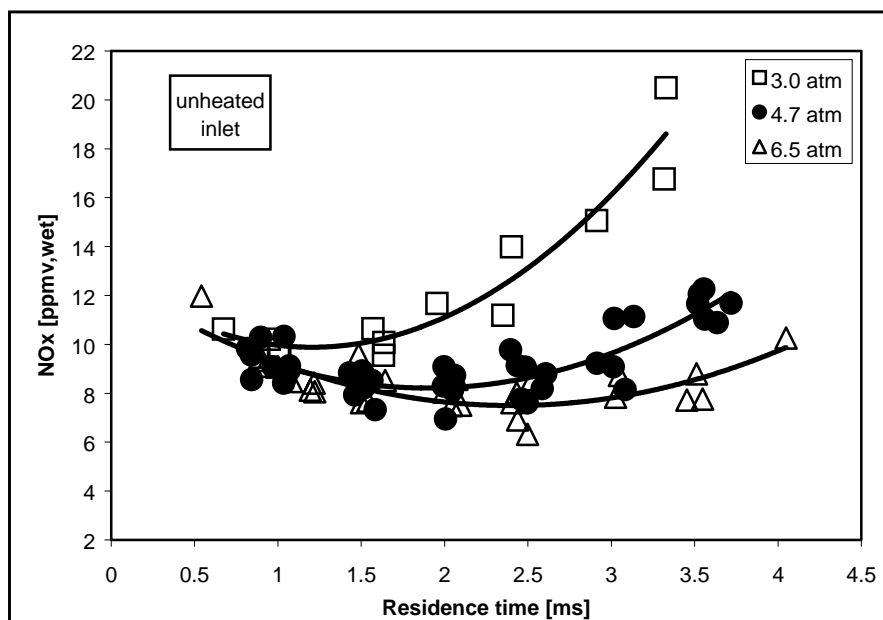


Figure 3.10 NO<sub>x</sub> versus residence time at 6.5, 4.7 and 3.0 atm for unheated inlet. Measured temperature is  $1803 \pm 5$  K

The increase in the NO<sub>x</sub> with increasing residence time (at the longer residence times) is caused, at least partially, by the increase in the true gas temperature. In order to avoid the effect of increasing reactor temperature on NO<sub>x</sub>, the NO<sub>x</sub> data for the 3.0 and 6.5 atm pressure levels are adjusted to a constant temperature of 1820 K, (i.e., the true temperature at lowest residence time levels), using the NO<sub>x</sub> versus temperature correlation developed by Steele (1995), (Equation 2.1). Since this correction is based on NO<sub>x</sub> at 15% O<sub>2</sub> dry, the data of Figure 3.10 are first adjusted to the 15% O<sub>2</sub> dry condition, and then are adjusted to 1820 K using the correlation of Steele (1995). Figure 3.11 shows the data corrected to the constant temperature of 1820 K. For the intermediate and short residence times, the corrected NO<sub>x</sub> increases with decreasing

residence time. The corrected NO<sub>x</sub>, as with uncorrected NO<sub>x</sub>, decreases with increasing pressure. The pressure effect on corrected NO<sub>x</sub> is small for residence times below 2.5 ms.

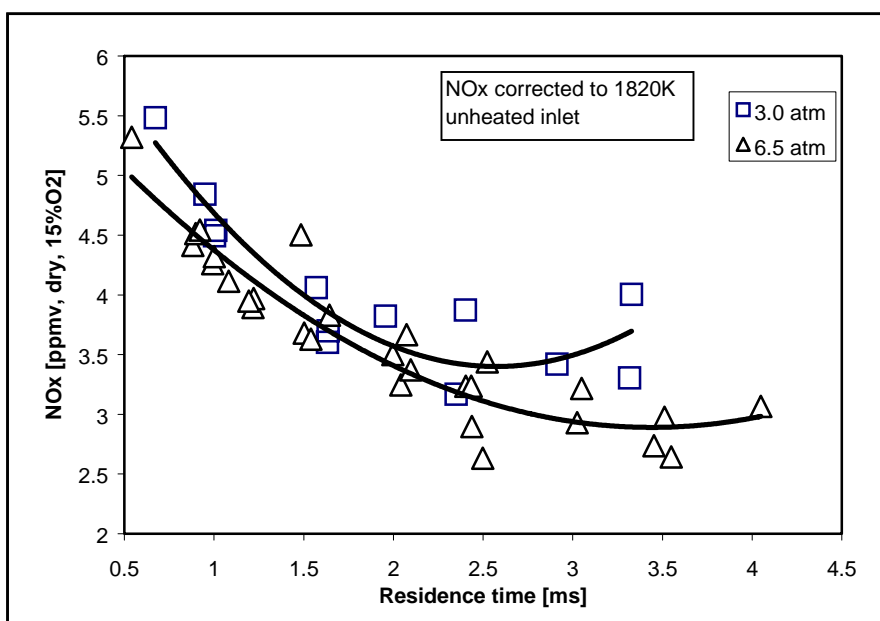


Figure 3.11 Corrected measured NO<sub>x</sub> data at 3.0 and 6.5 atm for unheated inlet. Corrected values correspond to a reactor temperature of 1820 K

### 3.4.1.1 NO<sub>x</sub>, CO and Hydrocarbon Profiles for Unheated Inlet Experiments

Profiles of CO and NO<sub>x</sub> concentrations at 6.5 atm for the unheated inlet, measured between the centerline and the wall of the HP-JSR, at two-thirds reactor height, are shown in Figures 3.12 and 3.13, respectively. The CO profiles clearly show that as the mean residence time of the reactor is decreased, the whole reactor becomes increasingly filled with high concentrations of CO. This implies a spreading of the free-radical rich

gas from the jet zone (i.e., the centerline region) into the recirculation zone (i.e., the bulk of the reactor). For lean-premixed combustion, NO<sub>x</sub> should form mainly in the free-radical rich (high CO) regions due to attack of super-equilibrium concentrations of O-atom, H-atom, and CH radical on N<sub>2</sub> through the Zeldovich, nitrous oxide, NNH, and prompt pathways (Section 2.3).

In Figure 3.13 one can note the decrease in the peak NO<sub>x</sub> as the residence time increases from 0.5 to 2.5 ms. For the data taken at 2.0, 2.5 and 3.5 ms residence time, an increase of the NO<sub>x</sub> in the jet zone is noted followed by a near flattening out of the profile in the recirculation zone. This behavior, which is thought to be linked with the sharp fall-off in the CO concentration at  $(R/R_{\max})^2 \cong 0.2$ , and indicative of a free-radical fall off, suggests that the NO<sub>x</sub> forms predominantly in the jet zone (or in the jet shear layer). On the other hand, for 0.5 ms residence time, the NO<sub>x</sub> profile, together with the CO profile, suggests additional NO<sub>x</sub> formation in the recirculation zone. Additional evidence for this is the inverse correlation between the NO<sub>x</sub> and CO concentrations in the recirculation zone. In the region of  $(R/R_{\max})^2 \cong 0.4$ , the NO<sub>x</sub> reaches its maximum and the CO reaches its minimum concentration. This region appears to be the *eye* of the recirculation zone. Here the NO<sub>x</sub> has greater time to form, and the CO has greater time to oxidize.

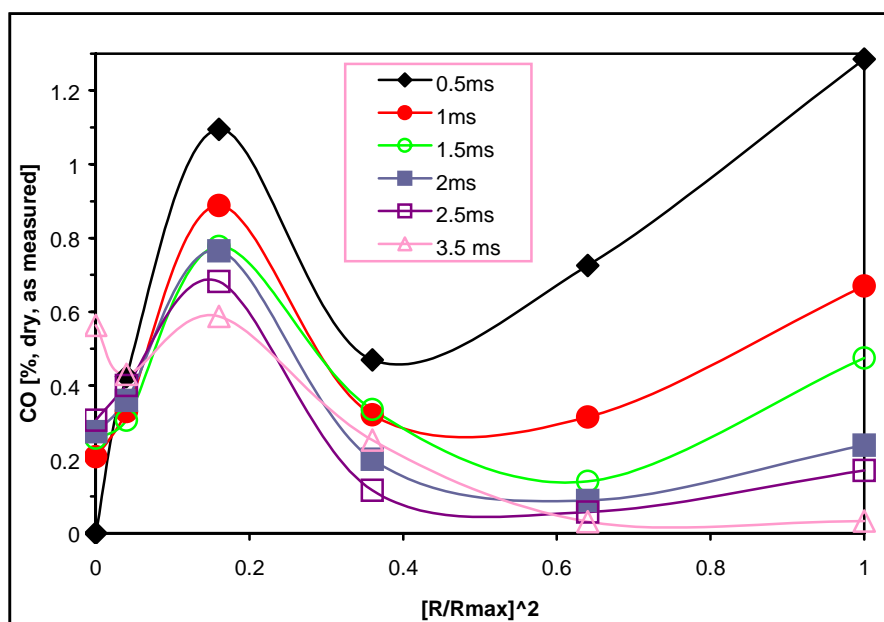


Figure 3.12 CO [%, dry, as measured] profiles in the HP-JSR at 6.5 atm, no preheat and 0.5, 1.0, 1.5, 2.0, 2.5 and 3.5 ms overall reactor residence times

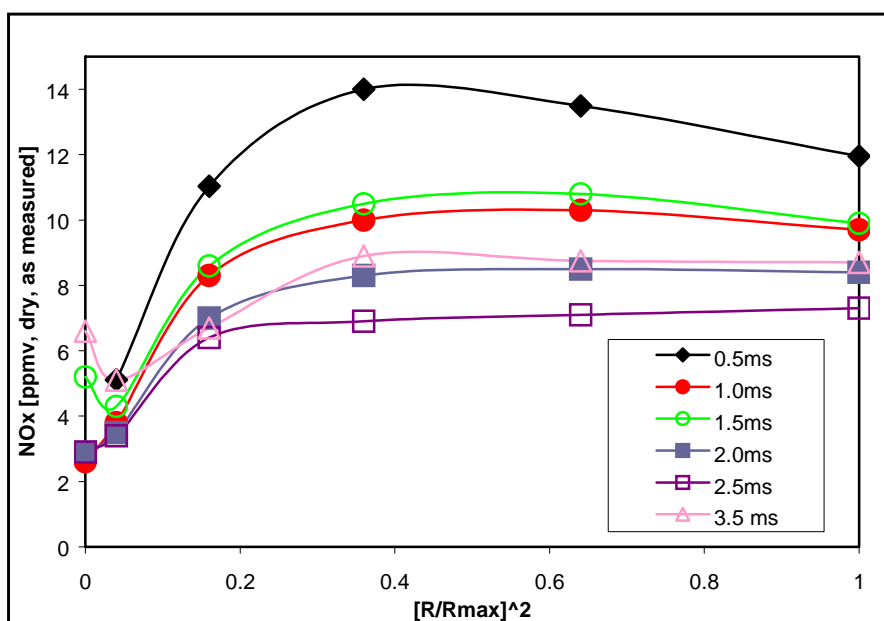


Figure 3.13 NO<sub>x</sub> [ppmv, dry, as measured] profiles in the HP-JSR at 6.5 atm, no preheat and 0.5, 1.0, 1.5, 2.0, 2.5 and 3.5 ms overall reactor residence times

The CO + CO<sub>2</sub> (total carbon), shown in Figure 3.14, is relatively constant throughout in the recirculation zone, but it significantly decreases towards the reactor centerline. Therefore, the total carbon profile shows that, outside of the flame zone, most of the hydrocarbons are reacted. Inside the flame zone, the decrease in CO + CO<sub>2</sub> is a consequence of the significant quantities of unburned hydrocarbons in the jet yet to react. This is further verified with the oxygen (O<sub>2</sub>) profile, shown in Figure 3.15, showing an increase in O<sub>2</sub>, and thus an increase in unreacted components, closer to the jet.

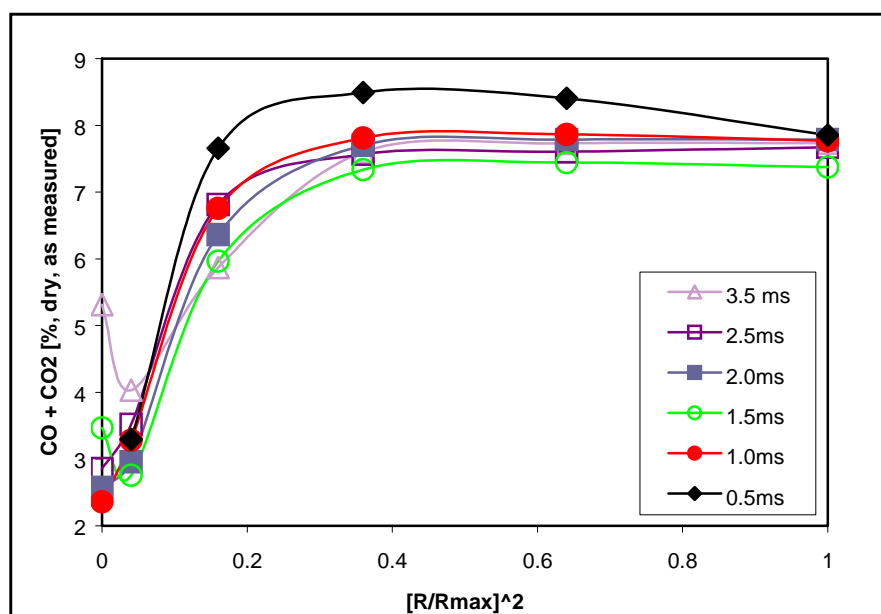


Figure 3.14 CO+CO<sub>2</sub> [% dry, as measured] profiles in the HP-JSR at 6.5 atm, no preheat and 0.5, 1.0, 1.5, 2.0, 2.5 and 3.5 ms overall reactor residence times

An increase in the fuel-air equivalence ratio is required at short residence times in order to compensate for the unreleased chemical energy. At long residence times the fuel-air equivalence ratio is increased to make up for the heat lost through the reactor

walls, as discussed earlier. The oxygen ( $O_2$ ) and ( $CO + CO_2$ ) profiles at 6.5 atm, discussed above and shown in Figures 3.15 and 3.14 respectively, verify that the total fuel-air equivalence ratio is high at low residence times, and is a minimum in the middle of the residence time range.

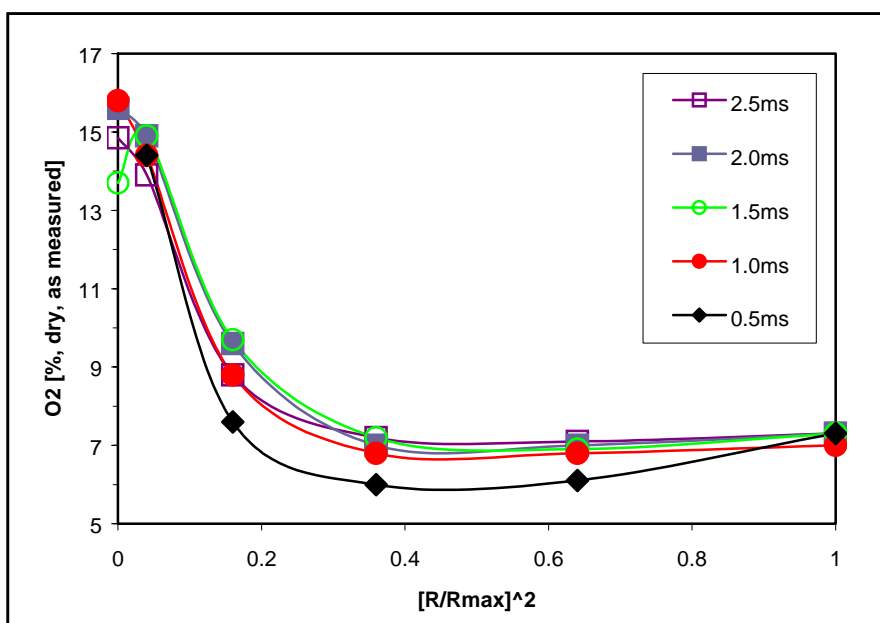


Figure 3.15  $O_2$  [% dry, as measured] profiles in the HP-JSR at 6.5 atm, no preheat and 0.5, 1.0, 1.5, 2.0, 2.5 and 3.5 ms overall reactor residence times

Profiles of CO and  $NO_x$  concentration, at 4.7 atm, measured between the centerline and the wall of the HP-JSR at two-thirds reactor height, are shown in Figures 3.16 and 3.17, respectively. They resemble those for 6.5 atm. Hydrocarbon profiles measured at residence time of 0.8 ms are shown in Figure 3.18. Methane is dominant, and its mole fraction is always one-to-two orders of magnitude higher than for ethane and ethylene. Ethane and ethylene form from the methane via one of the methane destruction pathways,

which is the following:  $\text{CH}_4 \rightarrow \text{CH}_3 \rightarrow \text{C}_2\text{H}_6 \rightarrow \text{C}_2\text{H}_5 \rightarrow \text{C}_2\text{H}_4$ . It should be noted that methane kinetics do not support significant  $\text{C}_3$  hydrocarbon formation, and this is reflected in the negligible concentrations measured in the present work. The methane profile shown in Figure 3.18 points to significant gradients in methane concentration in the reactor. The methane mole fraction on the centerline is 38000 ppm, whereas in the *eye* of the recirculation zone it is 250 ppm and 2050 ppm at the reactor wall. Ethane and ethylene profiles are qualitatively similar to those of methane, except that the concentrations are significantly smaller. In addition, the hydrocarbon profiles are qualitatively similar to that of CO, which is shown in Figure 3.16, in that they are high at the centerline and the wall, and low in the *eye* of the recirculation zone. The methane mole fraction in air, i.e., fraction of methane in the gas entering the HP-JSR at fuel-air equivalence ratio of 0.72, is approximately 7%, implying that almost half of the  $\text{CH}_4$  is destroyed by the time gases reach two-thirds of the reactor height where the sample is taken. If 3.8%  $\text{CH}_4$  is added to the measured 3.3%  $\text{CO}_2$  and 0.4% CO at the centerline, then the calculated total carbon is only 0.3% less than in the *eye* of the recirculation zone, where measured methane,  $\text{CO}_2$ , and CO are 0.025, 7.5, and 0.3%, respectively.

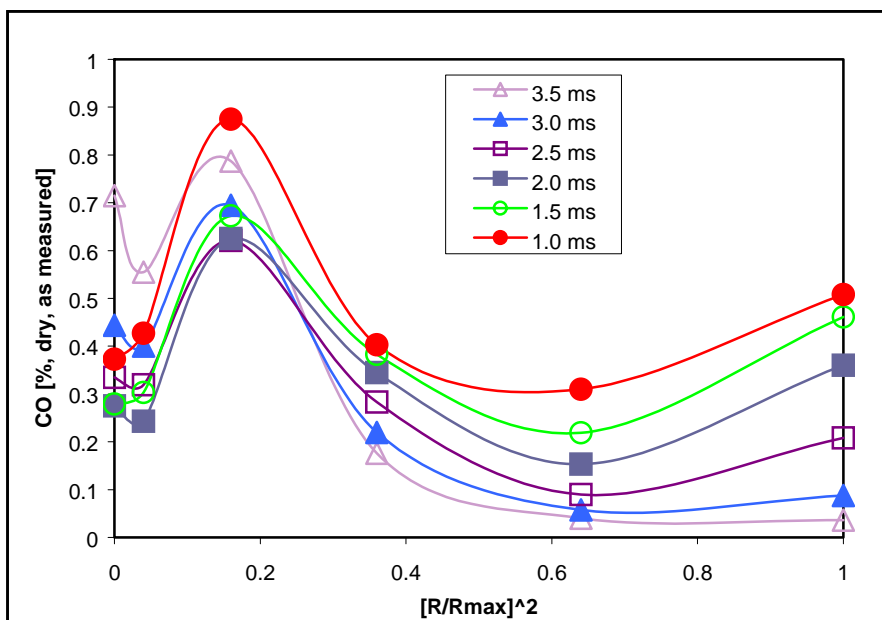


Figure 3.16 CO [% dry, as measured] profiles in the HP-JSR at 4.7 atm, no preheat and 1.0, 1.5, 2.0, 2.5, 3.0 and 3.5 ms overall reactor residence times

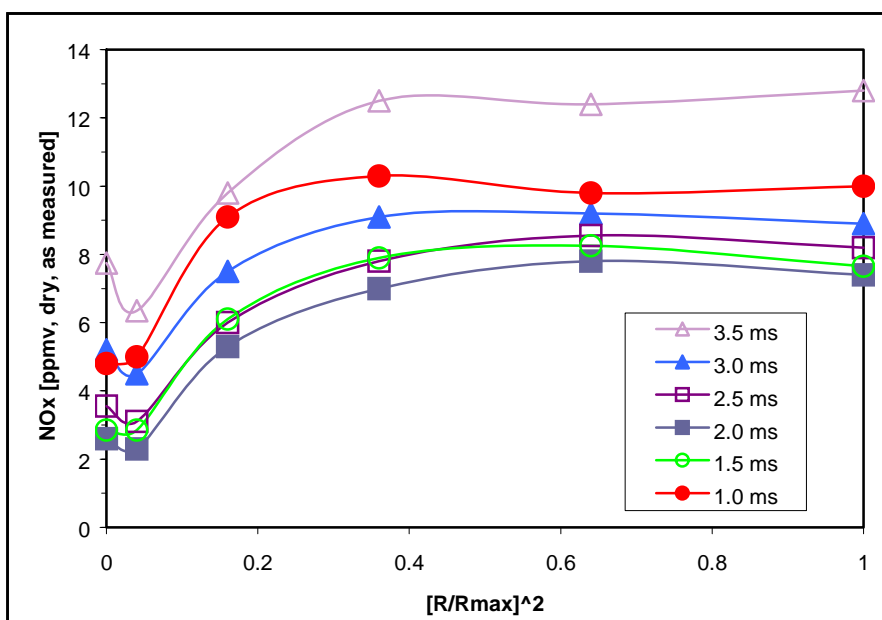


Figure 3.17 NOx [ppmv, dry, as measured] profiles in the HP-JSR at 4.7 atm, no preheat and 1.0, 1.5, 2.0, 2.5, 3.0 and 3.5 ms overall reactor residence times

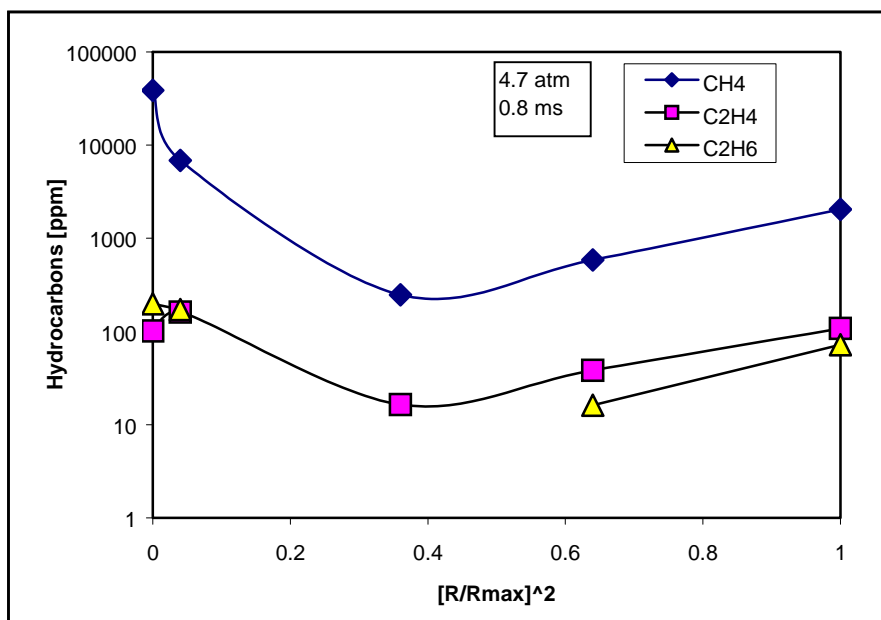


Figure 3.18 Hydrocarbon [ppmv, dry, as measured] profiles in the HP-JSR at 4.7 atm, no preheat and 0.8 ms overall reactor residence times

Profiles of CO concentration at 3.0 atm are shown in Figure 3.19. At residence times above 1.0 ms, the CO levels flatten in the recirculation zone, indicating low free-radical presence and little to no NO<sub>x</sub> formation. The CO profile at 1.0 ms differs from the profiles at other residence times. This profile is similar to the CO data at 4.7 and 6.5 atm at residence times below 2.0 ms due to the fact that the jet-stirred reactor is filled with the CO and the HP-JSR approaches a well-stirred reactor.

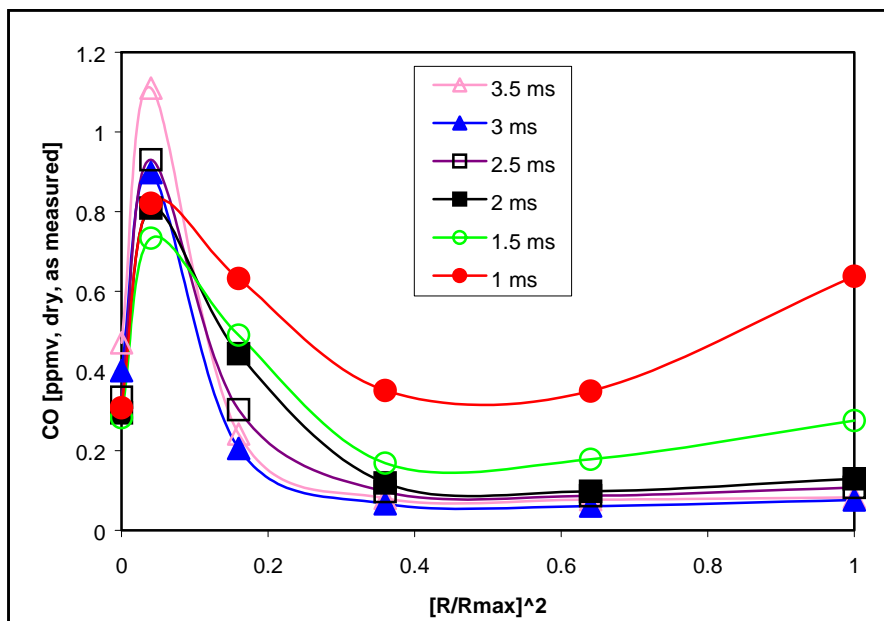


Figure 3.19 CO [% , dry, as measured] profiles in the HP-JSR at 3.0 atm, no preheat and 1.0, 1.5, 2.0, 2.5, 3.0 and 3.5 ms overall reactor residence times

The NO<sub>x</sub> concentration profiles, shown in Figure 3.20, indicate that the NO<sub>x</sub> remains constant in the recirculation zone. This behavior is true for all residence times, however, the NO<sub>x</sub> concentration increases with residence time.

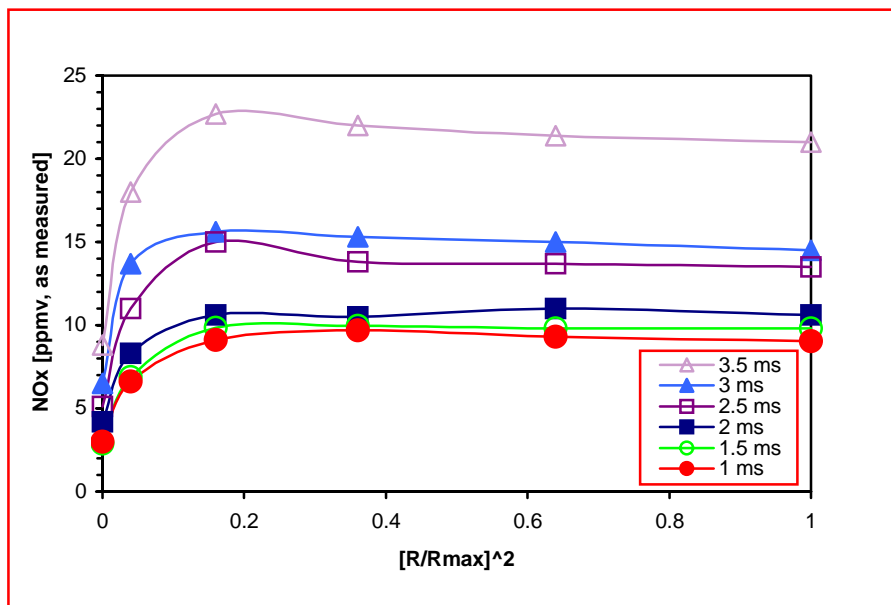


Figure 3.20 NO<sub>x</sub> [ppmv, dry, as measured] profiles in the HP-JSR at 3.0 atm, no preheat and 1.0, 1.5, 2.0, 2.5, 3.0 and 3.5 ms overall reactor residence times

### 3.4.2 Residence Time and Pressure Effect on NO<sub>x</sub> Formation for Preheated Inlet Experiments

The effect of the residence time on measured NO<sub>x</sub> is shown in Figure 3.21, for the pressures of 6.5, 4.7 and 3.0 atm. The conditions are the same as reported in Section 3.4.1 except the combustion air is electrically preheated, giving an inlet air-fuel mixture temperature of 573 K. As in the unheated experiments, measured (uncorrected) gas temperature is held constant at  $1803 \pm 5$  K. Also, NO<sub>x</sub> measurements are taken in the recirculation zone of the HP-JSR and assumed to be equivalent to the reactor emission.

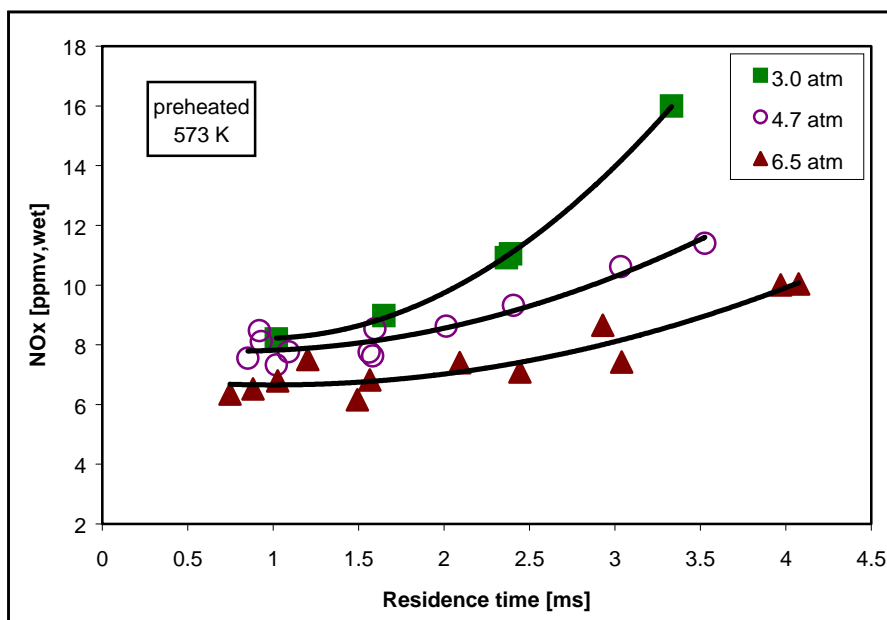


Figure 3.21 NO<sub>x</sub> versus residence time at 6.5, 4.7 and 3.0 atm for inlet preheated to 573 K. Measured temperature is  $1803 \pm 5$  K

Figure 3.21 shows that measured NO<sub>x</sub> increases with increasing residence time for the entire residence time range and for all three pressures. This differs from the NO<sub>x</sub> trends at unheated inlet cases (Figure 3.10) where, for increasing residence time, NO<sub>x</sub> concentrations decrease, reach a local minimum, and finally increase. This difference is due to the fact that, for the preheated experiments, less chemical energy is required to reach 1803 K during combustion. Less chemical energy required eliminates the need to increase the fuel-air equivalence ratio at low residence times and, therefore, eliminating the increase in NO<sub>x</sub> due to the increase in fuel-air equivalence ratio. Finally, Figure 3.21 also shows the NO<sub>x</sub> decreases with pressure, and, similar to the unheated cases, this pressure effect is more pronounced at longer residence times.

In order to eliminate the effect of true gas temperature, the NO<sub>x</sub>, from Figure 3.21, is corrected to a gas temperature of 1820 K and plotted versus residence time in Figure 3.22. The true gas temperatures for preheated inlet experiments are given in Appendix B (Figures B.2-4). The NO<sub>x</sub> behavior shown in Figure 3.22 is similar to that observed for the unheated inlet and shown in Figure 3.11. However, the short residence time concentrations in the two figures differ, where the NO<sub>x</sub> concentration is smaller for the preheated inlet experiments than for the unheated inlet experiments.

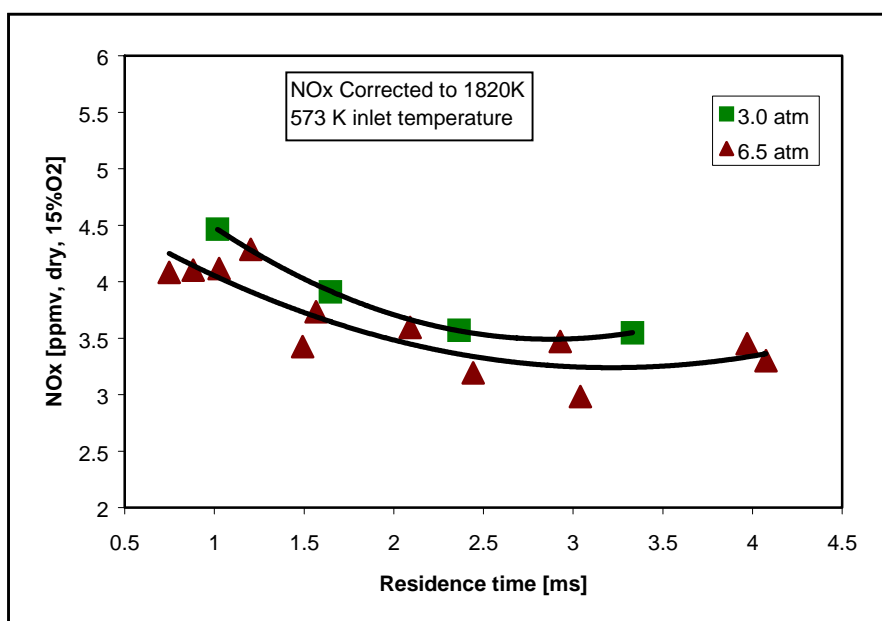


Figure 3.22 Corrected measured NO<sub>x</sub> data at 3.0 and 6.5 atm for inlet preheated to 573 K. Corrected values correspond to a reactor temperature of 1820 K

### ***3.4.2.1 NO<sub>x</sub> and CO Profiles for Preheated Inlet Experiments***

Profiles of CO and NO<sub>x</sub> concentrations at 6.5 atm, for the inlet preheated to 573 K, measured between the centerline and the wall of the HP-JSR, at the two-thirds reactor height, are shown in Figures 3.23 and 3.24, respectively. The CO and NO<sub>x</sub> behavior shown is similar to behavior shown for unheated inlet in Figures 3.12 and 3.13. The CO peak is at the edge of the jet, and the minimum is in the middle of the recirculation zone. At the wall, the CO concentrations are higher than in the recirculation zone only for the reactor residence time below 1.0 ms. The significant filling of the reactor with the CO, measured for preheated inlet at below 1.0 ms, also occurs for the unheated cases at below 2.0 ms (Figure 3.12). Therefore, the high CO concentrations in the HP-JSR occur for a narrower range of lower residence times for the preheated than for the unheated inlet cases. Another difference between the preheated and unheated inlet cases is at long residence times: the CO concentrations are lower for preheated inlet cases. The recirculation zone CO concentration at 4.0 ms is 0.02% by volume. Lower CO levels for preheated experiments are attributed to the lower fuel-air equivalence ratio of heated inlet experiments.

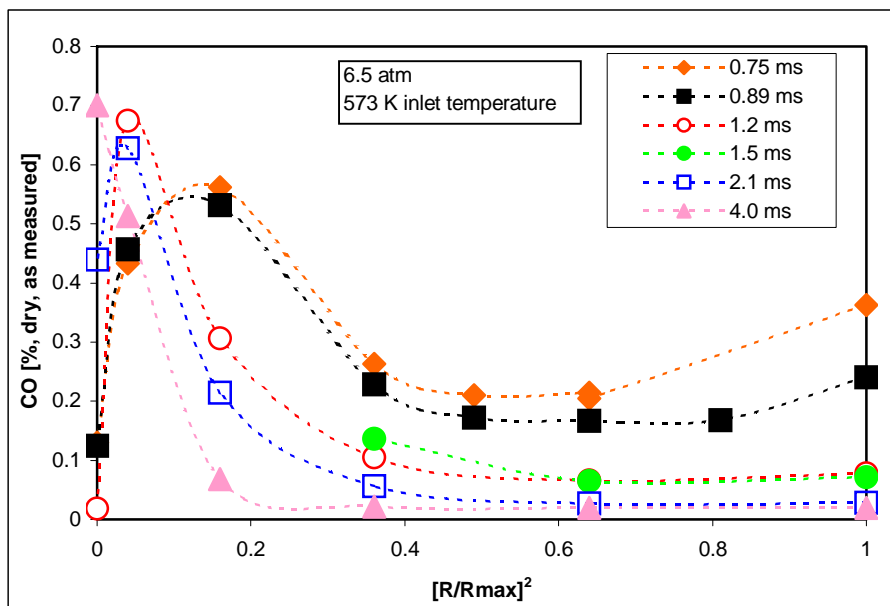


Figure 3.23 CO [% dry, as measured] profiles in the HP-JSR at 6.5 atm, 573 K preheat and 0.75, 0.9, 1.2, 1.5, 2.1 and 4.0 ms overall reactor residence times

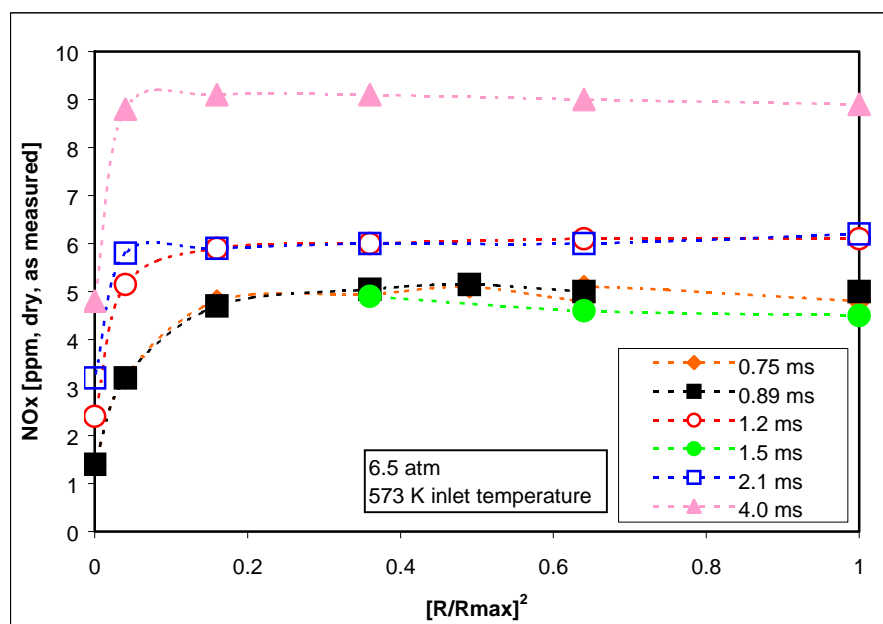


Figure 3.24 NO<sub>x</sub> [ppmv, dry, as measured] profiles in the HP-JSR at 6.5 atm, 573 K preheat and 0.75, 0.9, 1.2, 1.5, 2.1 and 4.0 ms overall reactor residence times

The measured CO peak appears to be located at two different positions in the reactor. On the run-day for which 0.75, 0.89, and 1.5 ms data were taken, it appears to be 2 mm away from the centerline, and on the run-day for which 1.2, 2.1, and 4.0 ms data were taken, it appears to be 1 mm away from the centerline for the 1.2 and 2.1 ms and on the centerline for the 4.0 ms. An explanation for the difference is that at long residence times, i.e., slower gas and shorter flame, the CO forms closer to the gas entrance. In general with a hot inlet, the combustion is expected to begin sooner in the jet than for cold inlet, resulting in more CO at the centerline.

The corresponding NO<sub>x</sub> reactor profiles, shown in Figure 3.24, depict the following trends: (1) NO<sub>x</sub> concentration increases from the reactor centerline to the edge of the jet zone; (2) NO<sub>x</sub> concentrations are constant throughout reactor recirculation zone; and (3) NO<sub>x</sub> concentrations increase with increasing residence time.

The CO and NO<sub>x</sub> concentration profiles at 4.7 atm for the inlet preheated to 573 K, are shown in Figures 3.25 and 3.26, respectively. The CO concentration peaks at the edge of the jet, and remains constant throughout the entire recirculation zone, even for residence times as low as 0.9 ms. The profile of CO indicates that the NO<sub>x</sub> formation is confined to the centerline region, which is evident in the NO<sub>x</sub> profiles shown in Figure 3.26. Although the NO<sub>x</sub> concentration does not significantly change with residence time between 0.9 and 1.5 ms, the CO concentration does. As in the CO profiles at other conditions, CO concentration decreases with residence time.

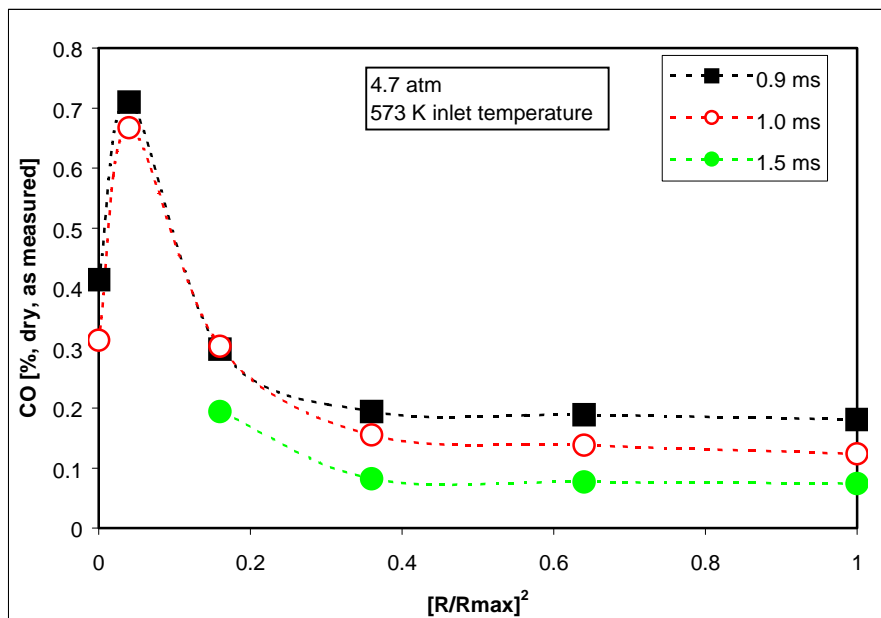


Figure 3.25 CO [% dry, as measured] profiles in the HP-JSR at 4.7 atm, 573 K preheat and 0.9, 1.0, and 1.5 ms overall reactor residence times

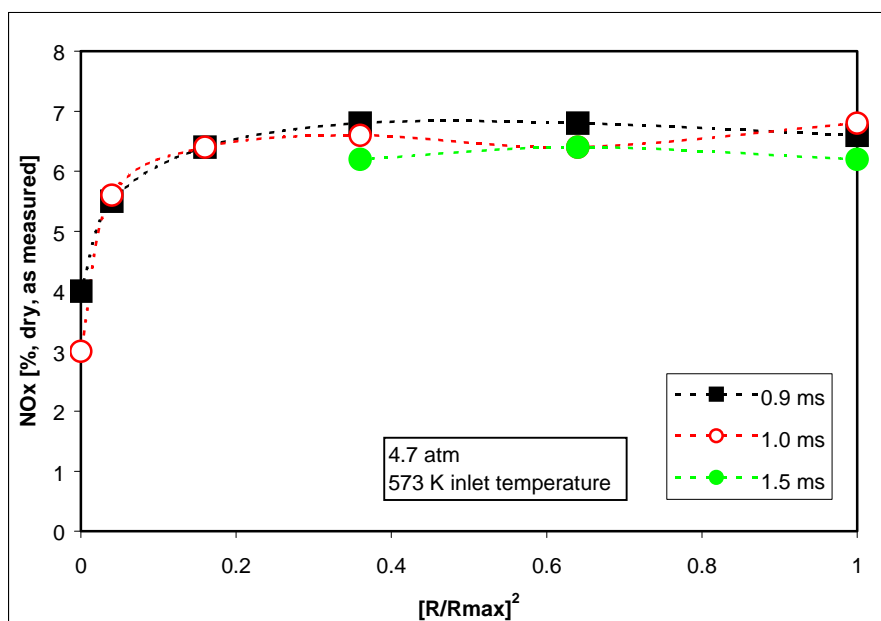


Figure 3.26 NOx [ppmv, dry, as measured] profiles in the HP-JSR at 4.7 atm, 573 K preheat and 0.9, 1.0, and 1.5 ms overall reactor residence times

### 3.4.3 Nitrous Oxide Measurements

Nitrous oxide measurements taken in the recirculation zone of the HP-JSR are plotted versus residence time for all three pressures and for both unheated and preheated cases (Figure 3.27). Although the measured values span a relatively narrow range, the following distinct trends are clearly identifiable:

1.  $N_2O$  decreases with residence time.
2.  $N_2O$  is insensitive to, or increases slightly with, pressure.
3.  $N_2O$  is insensitive to inlet temperature.

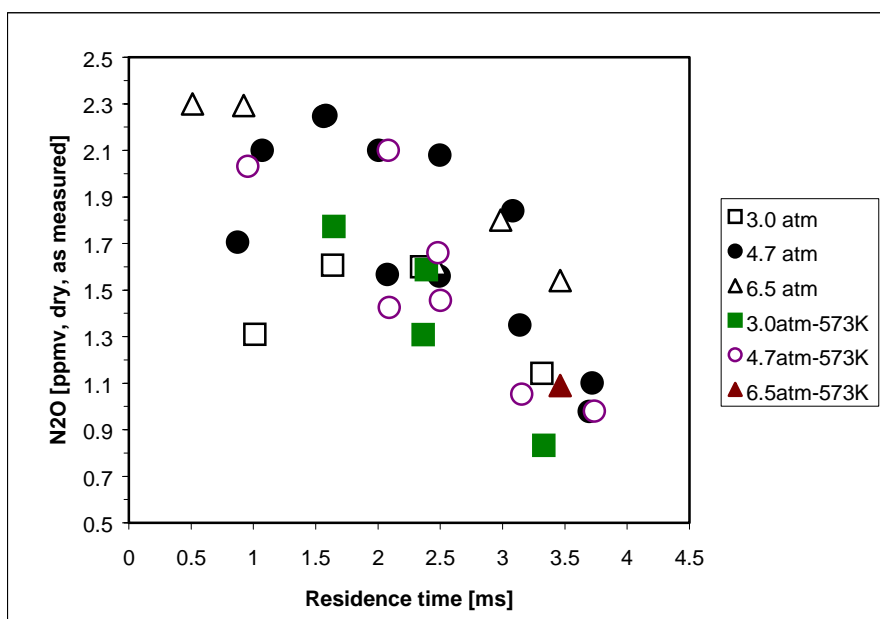


Figure 3.27  $N_2O$  versus residence time at 6.5, 4.7 and 3.0 atm for unheated inlet and inlet preheated to 573 K. Measured temperature is  $1803 \pm 5$  K

Steele (1995) thoroughly explored the  $N_2O$  formation in lean-premixed combustion in jet-stirred reactors. The results shown in Figure 3.27 are similar in value and trend to the

results Steele obtained at 1800 K, at elevated pressure and preheated inlet conditions. Steele (1995) found a small decrease in  $\text{N}_2\text{O}$  when residence time is increased between 1.9 and 3.8 ms, and essentially no pressure (for 4.7 and 7.1 atm) and inlet temperature (for 300 and 600 K) dependencies, confirming the trends observed in the present work and shown in Figure 3.27.

At the longest residence times, the measured  $\text{N}_2\text{O}$  decreases towards the equilibrium value of approximately 0.3 ppmv, wet.

### ***3.5 Conceptual Data Interpretation***

#### ***3.5.1 A Concept for Residence Time Effect on NO<sub>x</sub> Formation in the HP-JSR***

The results presented in Section 3.4 suggest a concept for NO<sub>x</sub> formation in the HP-JSR. This concept attempts to link the size of the NO<sub>x</sub> formation zone with the NO<sub>x</sub> formation rates, and explains how the size of the NO<sub>x</sub>-formation zone changes with residence time at 6.5 atm. This concept is the predecessor of the comprehensive model developed in Chapter 4.

In lean-premixed combustion there is tendency for O-atom levels to correlate with CO levels (Nicol, 1995). Since the CO profiles for 6.5 atm (Figure 3.12) show significantly higher CO concentrations at the short residence times than at the long residence times, it is expected that the O-atom levels are higher at short residence times. At the shortest mean residence times tested, there is insufficient time for the O-atom to relax to equilibrium concentration. [The characteristic O-atom relaxation time is about 1 to 2 ms for the 6.5 atm pressure tested in the HP-JSR, per Nicol (1995) and Steele et al.

(1998)]. Thus, there is an opportunity for the recirculation zone to maintain high O-atom concentration and to form NO<sub>x</sub> at a significant rate. Conversely, as the mean residence time is increased, it appears that the free-radical rich, high NO<sub>x</sub> production region exists mainly in the jet shear layer, and the overall rate of NO<sub>x</sub> production decreases. For the longest residence times tested, the increase in NO<sub>x</sub> with residence time noted in the data is probably caused by two factors, i.e., an increase in reactor gas temperature (as stated above) and an increase in the time available for the NO<sub>x</sub> to form.

The NO<sub>x</sub> production rate, calculated for a PSR operating at 6.5 atm pressure and at 0.5 ms residence time, is  $10.1 \pm 0.3$  ppmv, dry, (15% O<sub>2</sub>) per ms. If the NO<sub>x</sub> measured at 0.5 ms is assumed to have formed uniformly in the reactor, then the measured NO<sub>x</sub> production rate is found to be  $13.5 \pm 0.3$  ppmv, dry, (15% O<sub>2</sub>) per ms. The agreement between the measured and calculated rates at the minimum residence time tested is relatively good. However, for the longer residence time tested, the PSR model significantly overpredicts the measured NO<sub>x</sub>.

Much slower rates of NO<sub>x</sub> formation are calculated when the O-atom concentration is assumed to be at the equilibrium value. For conditions of 6.5 atm and 1820 K, the thermal NO<sub>x</sub> formation is only 0.05 ppmv, dry, (15% O<sub>2</sub>) per ms. The nitrous oxide pathway, assuming the nominal concentration of 2 ppmv, dry N<sub>2</sub>O measured for the reactor recirculation zone, and again using the equilibrium O-atom concentration (as well as the equilibrium H-atom concentration), forms NO<sub>x</sub> at about 0.15 ppmv, dry, (15% O<sub>2</sub>) per ms. Thus, the total NO<sub>x</sub> production rate for the recirculation zone under the

assumption of equilibrium free-radical concentrations is about 0.2 ppmv, dry, (15% O<sub>2</sub>) per ms.

In order to explain the NO<sub>x</sub> production by a two-zone model, the following expression is introduced:

$$\text{NO}_x = \tau[r_H * f + r_L * (1 - f)] \quad (3.6)$$

The terms  $r_H$  and  $r_L$  are the NO<sub>x</sub> production rates in the high- and low-NO<sub>x</sub> forming regions, respectively;  $\tau$  is the residence time of the reactor; and  $f$  is the fraction of the residence time associated with the high-NO<sub>x</sub> production rate.

The function  $f$  is determined in a two step process. First, the NO<sub>x</sub> data for 6.5 atm, adjusted to 1820 K, are curve-fitted. The data are fitted best with two linear equations, one for 0.5 to 2.5 ms and the other for residence times greater than 2.5 ms, as shown in Figure 3.28a. Then, the function  $f$  is determined from the fitted data, assuming  $r_H = 12$  ppm/ms and  $r_L = 0.2$  ppm/ms. (The term *ppm* denotes ppmv, dry, 15% O<sub>2</sub>.) The function  $f$  is plotted in Figure 3.28b. For mean residence times below 2 ms, the function  $f$  is well approximated as  $f = 0.415/\tau^{1.3}$ . Thus, as the overall residence time of the reactor decreases and the mixing intensity increases, NO<sub>x</sub> formation occurs predominately at the high production rate.

The high-NO<sub>x</sub> production rate used in the model, i.e.,  $r_H = 12$  ppm/ms, is a rounded off intermediate value between the measured NO<sub>x</sub> production rate of  $13.5 \pm 0.3$  ppm/ms and the calculated rate of  $10.1 \pm 0.3$  ppm/ms for the reactor operated at 0.5 ms residence

time. The value of the low-NO<sub>x</sub> production rate, i.e.,  $r_L = 0.2$  ppm/ms, is the value estimated above assuming equilibrium free-radical levels. By this interpretation of the data, the fraction of the reactor time used in high-NO<sub>x</sub> production varies from  $f = 0.96$  to 0.05. Under the minimum  $f$  condition, 75% of the NO<sub>x</sub> forms in the high-NO<sub>x</sub> production region. If, instead,  $r_L = 0$  is assumed, then the minimum value of  $f$  is 0.07, and the NO<sub>x</sub> forms exclusively in the high-NO<sub>x</sub> production region for all conditions. If  $r_L = 0.80$  ppm/ms is assumed, which is the maximum value possible based on the NO<sub>x</sub> data, (i.e., 3.2 ppm NO<sub>x</sub> formed at 4.0 ms), then the minimum value of  $f$  is 0, and all of the NO<sub>x</sub> forms in the low-NO<sub>x</sub> production region under minimum  $f$  conditions.

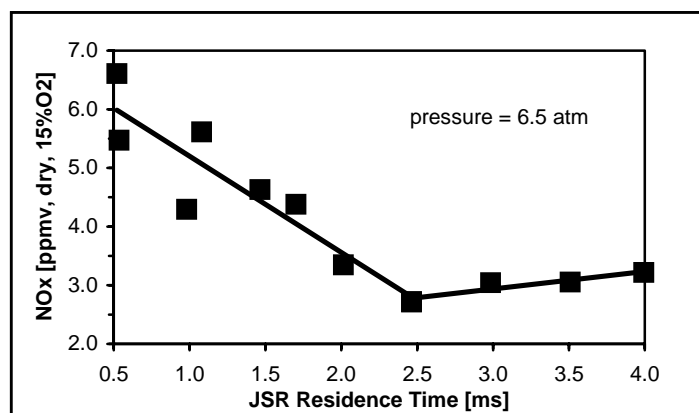


Figure 3.28a NO<sub>x</sub> data at 6.5 atm corrected to a constant temperature of 1820 K. Two linear curve-fits are used. One for data in the 0.5 to 2.5 ms range, and the other for the data in the 2.5 ms to 4.0 ms range

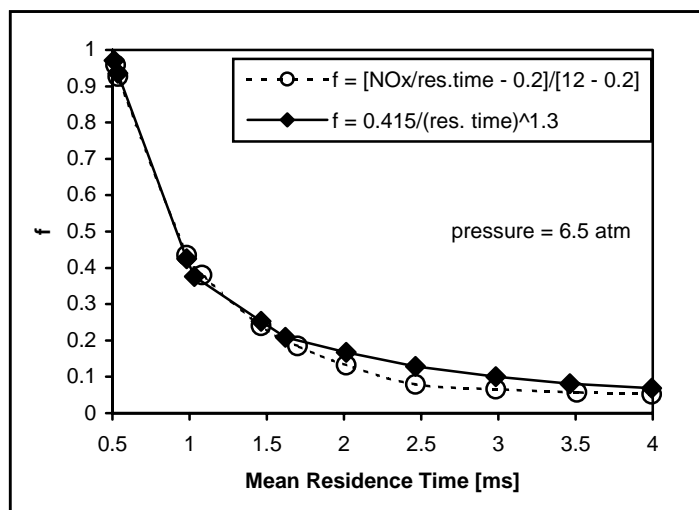


Figure 3.28b Function  $f$ , calculated using Eq. (3.6) and the power law, versus residence time

### ***3.5.2 Pressure Effect on NO<sub>x</sub> Formation in the HP-JSR***

The basic understanding of the NO<sub>x</sub> increase with decreasing pressure at long residence times, as shown in Figures 3.10 and 3.21, is as follows. As the pressure is decreased, the O-atom relaxation time increases until it reaches a value of about 17 ms for lean-premixed combustion at 1.0 atm (Nicol, 1995). In this case, the bulk of the reactor becomes rich in O-atom (as well as H-atom and OH), and NO<sub>x</sub> forms at a high rate throughout the reactor. Steele (1995) showed about a doubling of NO<sub>x</sub> as the reactor pressure was decreased from 7.1 to 1.0 atm. At short residence times, however, the reactor is free-radical rich throughout for both high and low pressure, that is, the reactor is nearly well stirred for NO<sub>x</sub>. Thus, changes in NO<sub>x</sub> with pressure are nearly exclusively caused by the chemical kinetic dependencies on pressure, which, by the results in Figure 3.10, appear to be weak.

### ***3.5.3 Inlet Temperature Effect in HP-JSR***

This section is intended to directly compare the data taken with the unheated inlet and data taken with the inlet preheated to 573 K, to thoroughly observe the inlet temperature effect. Two plots of NO<sub>x</sub> versus residence time are shown, one for 6.5 atm for both unheated and heated inlet (Figure 3.29) and the other for 3.0 atm for the unheated and heated inlet (Figure 3.30). Profiles of CO, also for unheated and preheated inlet conditions, are shown in Figure 3.31. These three figures are used to explain the effect of preheat, and to postulate that the NO<sub>x</sub> and CO formation in the HP-JSR are a function of

both the flame length, which varies with residence time and inlet temperature, and the reaction kinetics within the flame, which is confirmed by the models used in Chapter 4.

Figure 3.29 compares unheated and preheated data at 6.5 atm throughout the range of residence time. The measured NO<sub>x</sub> is lower when the inlet air is preheated than when the inlet is unheated for residence times below 2.0 ms. At residence times greater than 2.0 ms, the preheat does not influence the NO<sub>x</sub>. As discussed above, the unheated inlet air temperatures are not constant. Measured inlet temperatures are shown above in Figure 3.6 versus total flow rates for the three pressure levels, and are discussed in Section 3.3.3.

Table 3.2 contains NO<sub>x</sub> and fuel-air equivalence ratio data with unheated and preheated inlet for two sets of residence times: a long residence time of 3.0 ms, and a short residence time of 0.88 ms. As shown in Table 3.2, at 3.0 ms the NO<sub>x</sub> measured is 7.8 ppmv for the measured inlet temperature of 376 K and for the fuel-air equivalence of 0.71. The NO<sub>x</sub> is 7.4 ppmv for the inlet mixture temperature of 573 K and the fuel-air equivalence ratio of 0.63. At 0.88 ms, the measured NO<sub>x</sub> is 9.3 ppmv for the measured inlet temperature of 345 K and for the fuel-air equivalence ratio of 0.69. The measured NO<sub>x</sub> drops to 6.5 ppmv for the inlet mixture temperature of 573 K and the fuel-air equivalence ratio of 0.58. Consequently, at 0.88 ms, preheating the inlet to 573 K reduces the NO<sub>x</sub> formation by about 30% compared to the unheated inlet case. Thus, it appears that increasing the inlet temperature affects the NO<sub>x</sub> formation process at the short residence times. Table 3.2 also contains data for NO<sub>x</sub> in ppmv, dry, corrected for a common oxygen content in the products of 15% O<sub>2</sub> to assess effect of dilution. Dilution in preheated inlet cases is caused by a low fuel-air equivalence ratio. If the resultant

NO<sub>x</sub>, corrected to common oxygen content, is constant between cases of different fuel-air equivalence ratios, than dilution does affect NO<sub>x</sub> formation. Since the NO<sub>x</sub> values differ (4.6 and 3.8), dilution is not the only cause for lower measured NO<sub>x</sub> at preheated inlet and low residence times. The other cause is the chemical kinetics, which is explained at the end of this section.

Table 3.2 6.5 atm data at 3.0 and 0.88 ms. Unheated inlet and 573 K data are compared

Residence time [ms]	Measured inlet temperature [K]	Fuel-air equivalence ratio	NO <sub>x</sub> [ppmv, wet]	NO <sub>x</sub> [ppmv, dry, 15% O <sub>2</sub> ]
3.0	376	0.71	7.8	3.8
	573	0.63	7.4	4.0
0.88	345	0.69	9.3	4.6
	573	0.58	6.5	3.8

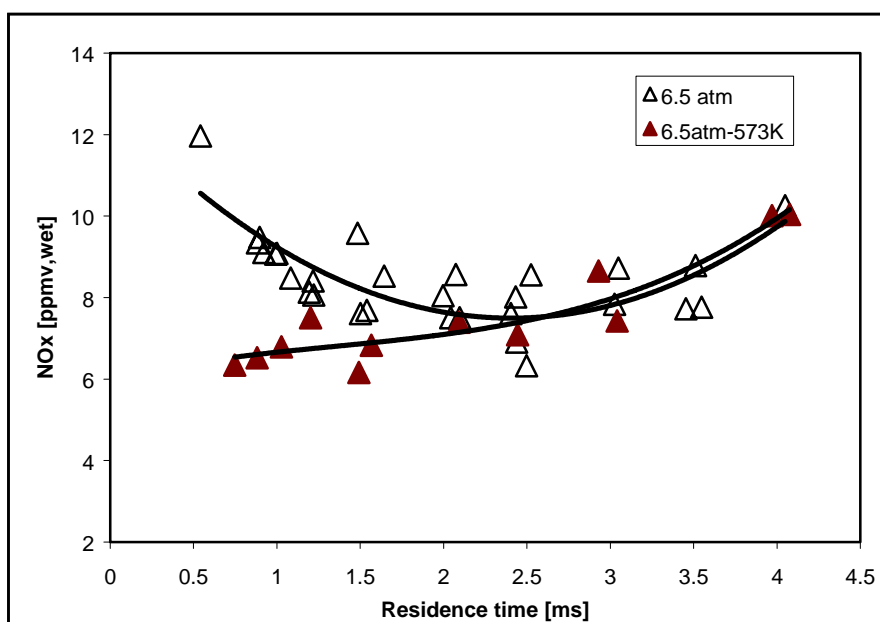


Figure 3.29 Effect of preheat on NO<sub>x</sub> [ppmv, wet] at 6.5 atm and 1800 K measured temperature in HP-JSR

Figure 3.30 compares unheated and preheated data at 3.0 atm throughout the range of residence times. The measured NO<sub>x</sub> is only slightly lower when the inlet air is preheated than when the inlet is unheated. Therefore, the inlet temperature effect is small at 3.0 atm.

The CO profiles for both the unheated and preheated inlet have shown (Sections 3.4.1.1 and 3.4.2.1) that at short residence times CO and free-radicals spread throughout the reactor. Thus, NO<sub>x</sub> forms in a larger portion of the reactor volume than at the long residence times when the formation appears to be confined mainly to the region of the reactor centerline. If the flame, i.e., high-CO concentration zone, is positioned in the jet shear layer, then the profiles can be interpreted in the following way. When the jet is longer than the reactor height, it hits the top of the reactor and sweeps the inner reactor wall while carrying the flame and the high CO. The jet may then partly exhaust through the exhaust ports and partly swirl around the recirculation zone. The CO profiles shown in Figures 3.12 and 3.23 suggest that the jet is longer than the reactor height for the short residence time runs, because high CO concentrations are measured near the reactor wall. It is hypothesized that the jet sweeps around so quickly that there is insufficient time for CO oxidation, thus resulting in high CO concentrations. However, for slower jets, i.e., for long residence time runs, the high CO concentrations are measured only near the reactor centerline suggesting that the jet does not reach the reactor wall. The confinement of CO is an indicator of a short reaction zone.

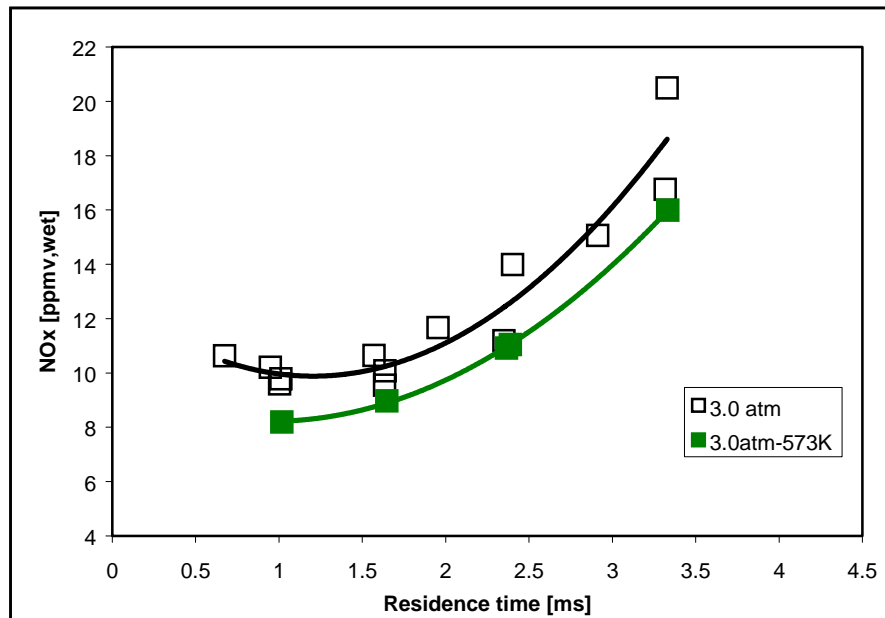


Figure 3.30 Effect of preheat on NOx [ppmv, wet] at 3.0 atm and 1800 K measured temperature in HP-JSR

Based on the previous discussion, it is postulated that the length of the jet varies with reactor conditions. For example, at short residence time, the jet is longer than at the long residence time. The application of the jet-entrainment formula (Equation 3.7) shows that the jet entrainment length decreases with increasing inlet temperature (Thornton et al., 1987):

$$L = b (\rho_{\text{inlet}}/\rho)^{0.5} d_{\text{inlet}} \quad (3.7)$$

where  $L$  is the jet entrainment length,  $b$  is a constant,  $\rho$  and  $\rho_{\text{inlet}}$  are reactor gas and inlet gas densities, respectively, and  $d_{\text{inlet}}$  is the inlet nozzle diameter.

The CO profile data shown in Figure 3.31 indicate that preheating the inlet decreases the CO levels that sweep around the walls of the reactor, confining the CO more to the centerline region of the HP-JSR. At short residence times, the preheat significantly changes the CO profile of the reactor, and thus NO<sub>x</sub> formation. At long residence times, there is sufficient time for CO to oxidize for both the preheated and the unheated inlet. Therefore, the effect of preheat on CO and NO<sub>x</sub> is reduced.

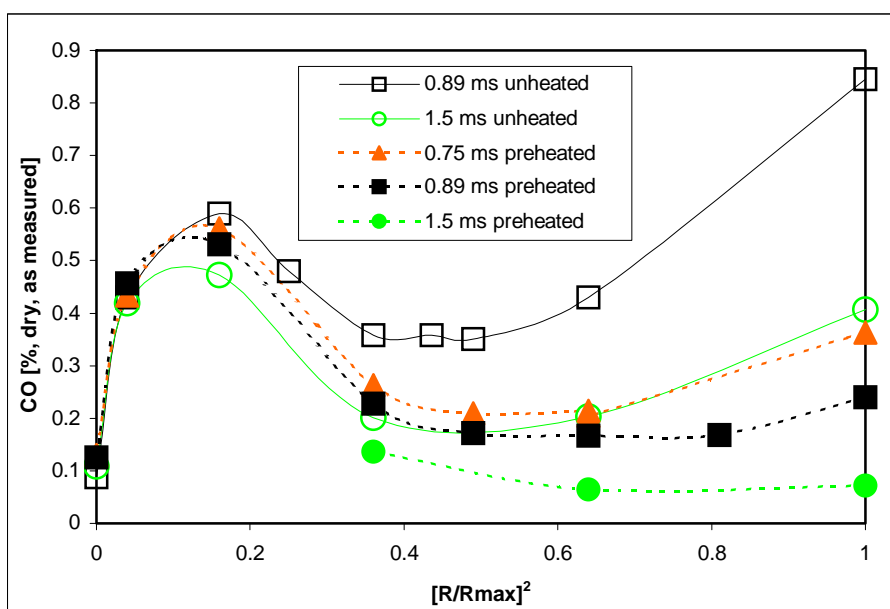


Figure 3.31 Comparison of CO [%, dry, as measured] profiles in the HP-JSR at 6.5 atm, for unpreheat cases at 0.89 and 1.5 ms and preheated cases at 0.75, 0.89 and 1.5 ms overall reactor residence times

The kinetics in the flame could also be affecting the overall decrease in NO<sub>x</sub> with increasing inlet temperature at short residence times. In these experiments, the increased

inlet temperature is associated with a leaner jet entering the reactor. For example, the fuel-air equivalence ratio is reduced by about 16% at 0.88 ms and about 11% at 3.0 ms. The leaning of the inlet jet means that the prompt pathway contributes less to the NO<sub>x</sub> formation when the inlet is heated.

### ***3.6 Summary of Major Experimental Findings***

The experimental findings for the laboratory high-pressure jet-stirred reactor with a single-jet nozzle indicate the following trends:

1. NO<sub>x</sub> versus residence time trend, for 0.5 to 4.0 ms residence time, at 3.0, 4.7 and 6.5 atm pressure, and 1800 to 1940 K reactor gas temperature. There appears to be an optimum residence time range for which NO<sub>x</sub> levels are at their minimum values. This range shifts towards shorter residence times at the lower pressures. At 6.5 atm, NO<sub>x</sub> decreases with increasing residence time below about 2-2.5 ms, and above that increases with residence time. At 3.0 atm, the NO<sub>x</sub> minimum is at about 1.0 ms residence time. The observed trends are believed to be a result of three competing effects: (1) the fraction of total residence time that the gases spend in the high-NO<sub>x</sub> formation zone (which is in the jet area) decreases with residence time; (2) the NO<sub>x</sub> increases when the time for its formation is increased; and (3) the NO<sub>x</sub> increases when the true reactor gas temperature increases.
2. NO<sub>x</sub> versus pressure, for 3.0, 4.7 and 6.5 atm pressure, at 1800 to 1940 K reactor gas temperature and variable residence time, between 0.5 and 4.0 ms. The NO<sub>x</sub> decreases with pressure because the time for O-atom relaxation to equilibrium

decreases with pressure, and because the NO<sub>x</sub> formation zone shrinks. The NO<sub>x</sub> is pressure neutral at low residence times and for the unheated inlet, because the chemical kinetic dependencies on pressure are weak and because the NO<sub>x</sub> formation zone spreads throughout the reactor for all pressure levels, i.e., the reactor is free-radical rich throughout for both high and low pressure (reactor is well-stirred).

3. NO<sub>x</sub> versus inlet air temperature, at 3.0, 4.7 and 6.5 atm pressure, variable residence time between 0.5 and 4.0 ms, and 1800 to 1940 K reactor gas temperature. Two temperature levels are studied: unheated inlet (approximately 373 K) and heated inlet (approximately at 573 K). Preheating the inlet combustion air has little effect at 3.0 atm, but it favors the reduction in NO<sub>x</sub> formation at 6.5 atm and residence times below 1.5 ms. Two possible reasons are postulated as explanation of the behavior: lower jet entrainment length, resulting in a smaller reaction zone, and a smaller influence of the prompt pathway due to leaning out of the flame.

## CHAPTER 4

### MODEL DEVELOPMENT, RESULTS AND DISCUSSION

#### *4.1 Introduction*

The data obtained using the high-pressure jet-stirred reactor indicate novel trends with respect to NO<sub>x</sub> dependency on pressure, residence times and inlet temperature during lean-premixed combustion of methane. The trends are the result of complicated chemical, fluid mechanical and heat transfer effects associated with combustion in a confined space.

The physical picture that emerges from discussion in Chapter 3 is of a turbulent premixed flame anchored over and around the inlet jet, all surrounded by a post-flame environment of recirculating gas. This dual reaction zone configuration lends itself to a two-zone chemical kinetic model in which the first zone represents the non-equilibrium turbulent flame and the second the post-flame gas, per discussion in Section 3.5.1. The size of the turbulent flame (*i.e.*, the fraction of the reactor volume occupied by the highly non-equilibrium gas) increases for low residence times and, at the lowest times, it may fill the entire reactor. The flame also fills more of the reactor volume at lower inlet temperatures than for a preheated inlet (Section 3.5.3). Therefore, the partitioning into the two zones depends on the turbulent premixed flame regime present in the reactor. Section 4.2.1 is dedicated to finding that regime by consolidating premixed turbulent flame correlations into a coherent representation of a confined flame. Section 4.2.2

develops a chemical reactor model to represent the flame and the post-flame zone, and finds the sizes of the zones to best match the data.

However, the chemical kinetics within the zones are also changing with varying combustion conditions. For example, the prompt mechanism has a smaller influence in the leaner preheated inlet gas cases compared to unheated inlet cases. In addition, there is an effect of pressure on NO<sub>x</sub>. The O-atom fills more of the reactor volume at low pressures, resulting in higher NO<sub>x</sub> than at high pressures. Section 4.3 analyzes the kinetics of the NO<sub>x</sub> formation based on the two-zone model developed in Section 4.2.2. In Section 4.3 the final link between the zone sizes and the kinetics in each zone is established for a broader understanding of the NO<sub>x</sub> formation in the HP-JSR.

The model is expected to have predictive capabilities for other jet-stirred reactor configurations and conditions, and may provide a conceptual method for modeling gas turbine combustors as well.

## ***4.2 Model Development***

### ***4.2.1 Calculation of Turbulent Flame Characteristics***

#### ***4.2.1.1 Defining the HP-JSR Operating Regime in Turbulent Combustion Terms***

The turbulent flame characteristics of interest for the present study are burning velocity and flame thickness. This section includes calculations of other characteristics, as well, because they are necessary to calculating the velocity and thickness. All calculations are done using some measured data, correlations from the literature, and

some assumptions, which will be clearly stated. The calculated values are used both in building the models and in verifying modeling results.

The first step is to define the regime of turbulent combustion in which the HP-JSR operates. There are three regimes of turbulent combustion (Turns, 2000):

1. Wrinkled laminar flames regime, where the laminar flame thickness ( $\delta_L$ ) is smaller than the smallest turbulent eddy, i.e., Kolmogorov scale,  $\eta$ :  $\delta_L < \eta$ . The small eddies curve the otherwise straight laminar flame. So, the flame is as thin as a laminar flame, but it is wrinkled due to turbulence.
2. Flamelets in eddies regime, where the laminar flame thickness is larger than the Kolmogorov scale but smaller than the integral turbulent length,  $l_0$ :  $\eta < \delta_L < l_0$ . Kobayashi et al. (1997) have visualized flamelets in eddies by instantaneous Schlieren photography and laser-tomography. They explain that the flames wrinkle significantly, and, consequently, parcels of unburned gas are engulfed into the flame. The experimental conditions are: Damköhler number is above 1.0, the ratio of turbulent intensity to the laminar burning velocity is below 10, and the turbulent Reynolds number is below 3000.
3. Distributed reaction regime, where laminar flame thickness is larger than the integral turbulent length,  $l_0$ :  $\delta_L > l_0$ . In this case flame thickness is so large that turbulence is embedded into the flame. Well-stirred reactors operate in this regime.

The above regimes are summarized in Figure 4.1, where Damköhler number is plotted versus turbulence Reynolds number. This plot was published by Abraham et al. (1985) and is reproduced herein.

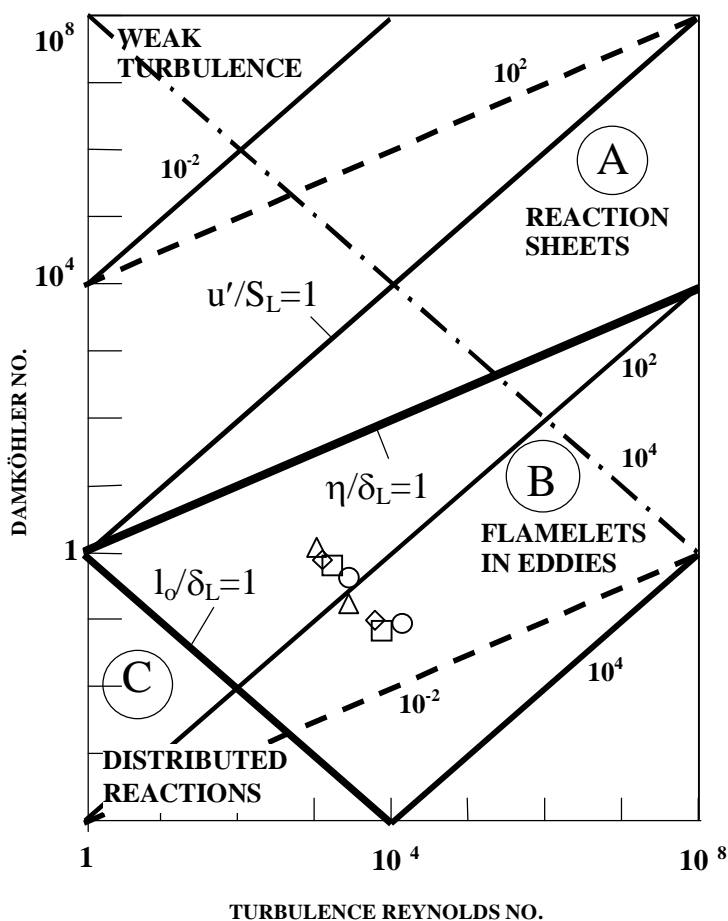


Figure 4.1 Important parameters characterizing turbulent premixed combustion. (Abraham et al., 1985.) Operation of the HP-JSR at the minimum and maximum residence times are identified for following conditions: 6.5 atm (circles), 3.0 atm (diamonds), 6.5 atm at 573 K inlet temperature (squares), and 3.0 atm at 573 K inlet temperature (triangles)

The two non-dimensional numbers, i.e., Damköhler and turbulence Reynolds, are calculated using the following procedure. The Damköhler number is defined as:  $Da = \text{mixing time}/\text{chemical time}$ . The turbulent Reynolds number is defined as:  $Re = u'd_o/v$ , where  $v$  is kinematic viscosity at the measured inlet temperature and reactor pressure. The nozzle diameter,  $d_o$ , is assumed to be integral turbulent scale ( $l_o = d_o$ ), i.e., it is comparable to the order of magnitude of the largest turbulent eddies. The nozzle

diameter in the present experiments is 0.0014 m. The time for mixing is calculated as the ratio of the jet nozzle diameter,  $d_o$ , to the turbulent intensity,  $u'$ , where  $u'$  is defined as 10% of inlet jet (cold) velocity,  $u_o$  (calculated by Equation 3.1 in Chapter 3), or

$$\tau_{\text{mix}} = d_o / u' = d_o / 0.1u_o$$

Turbulent intensity,  $u'$ , is plotted in Figure 4.2 versus residence time for the three pressures tested (3.0, 4.7 and 6.5 atm), with preheat (573 K) and without preheat. Turbulent intensity is not a function of pressure, and is only a weak function of the inlet temperature. It decreases 4-fold with the residence time increase between 0.5 and 4.0 ms. The decrease in  $u'$  is proportional to the decrease in the inlet velocity, which is caused by the 8-fold decrease in mass flow rate and the 2-fold decrease in the flow factor (caused by the increase in the ratio of reactor and total pressure) for the same residence time range. This decrease in  $u'$  causes a 4-fold increase in the mixing time over the range of residence times.

Appendix C contains the spreadsheet of the turbulent intensity and all other turbulence parameters discussed in this section and calculated for all conditions.

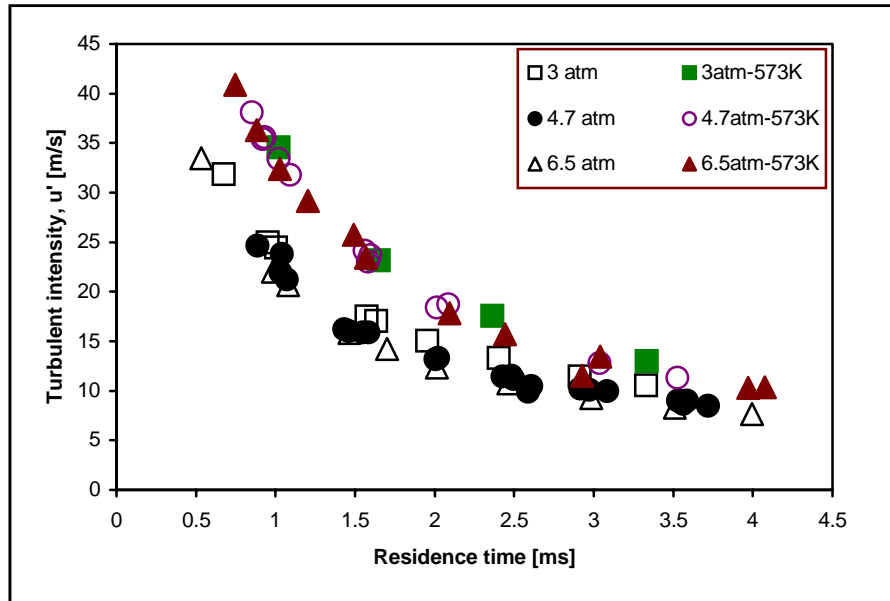


Figure 4.2 Turbulence intensity,  $u'$ , plotted versus residence time for three pressures and for unheated and heated (573 K) inlets

The chemical time is calculated as the ratio of laminar flame thickness to the laminar burning velocity:

$$\tau_{\text{chem}} = \delta_L / S_L$$

The burning velocity,  $S_L$ , is a function of fuel type, fuel-air equivalence ratio ( $\phi$ ), adiabatic flame temperature ( $T_b$ ), inlet temperature ( $T_u$ ), and pressure ( $p$ ). The equation used herein to calculate  $S_L$  for methane is taken from Göttgens et al. (1992):

$$S_L = 0.22167 \cdot \left( \frac{\dot{m}_f}{\dot{m}_f + \dot{m}_a} \right)^{0.565175} \cdot \exp\left( -\frac{6444.27}{T^0} \right) \cdot \left( \frac{T_u}{T^0} \right) \cdot \left( \frac{T_b - T^0}{T_b - T_u} \right)^{2.5158}$$

where for methane:

$$\frac{\dot{m}_f}{\dot{m}_f + \dot{m}_a} = \frac{1}{1 + \frac{1}{0.058 \cdot \phi}}$$

and

$$T^o = \frac{-23873}{\ln \frac{p(\text{bar})}{3.1557 \cdot 10^8}}$$

Göttgens et al. (1992) give a physical definition of  $T^o$  as the temperature at the point of transition between the chemically inert preheat zone and the energy release layer. Therefore, combustion chemistry only takes place at temperatures above  $T^o$ .

The dependence of burning velocity on inlet temperature and pressure in the Göttgens et al. (1992) equation for  $S_L$  is in excellent agreement with the comprehensive measurements by Andrews and Bradley (1972) at  $\phi=1.0$ . During methane combustion, at  $\phi=1.0$  with no preheat, pressure affects the burning velocity to the exponent of  $-0.5$ . This result was recently confirmed for  $\phi=0.9$ , 1.0, and 1.1 and for pressures between 0.1 and 1.0 MPa by Kobayashi et al. (1997). The dependence of the burning velocity on pressure at lean fuel-air equivalence ratios is also relatively close to the measured values presented in Andrews and Bradley (1972).

These points give confidence to the use of this equation for calculating burning velocity for the present experimental conditions. The calculated values for  $S_L$  versus the residence time of the HP-JSR are given in Figure 4.3.

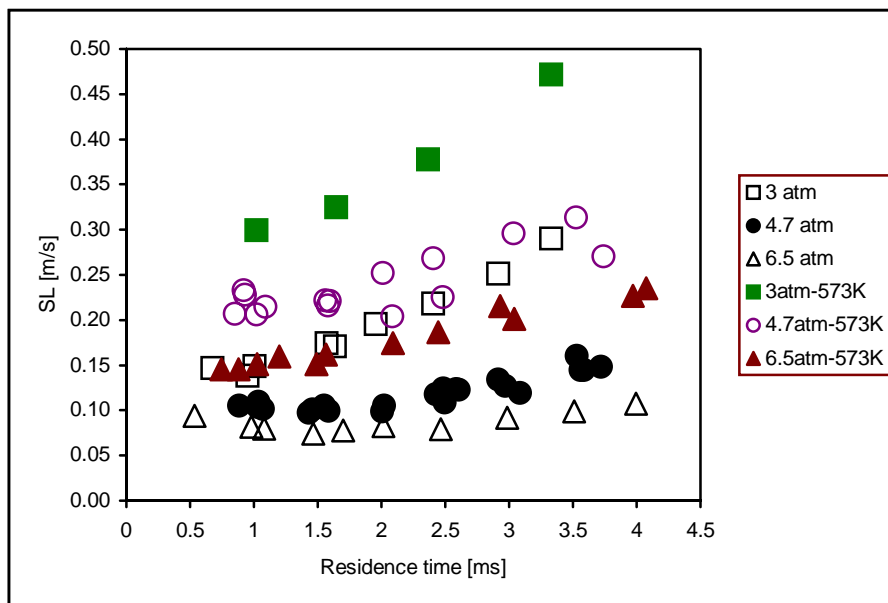


Figure 4.3 Laminar flame speed versus residence time for three pressures and for unheated and heated (573 K) inlets

The laminar flame thickness is calculated by  $\delta_L = \alpha / S_L$ , where  $\alpha$  is thermal diffusivity of air calculated using measured inlet temperature and reactor pressure. Abraham et al. (1985) suggested this equation, with  $\alpha$  based on inlet temperature, to be consistent with their approximations used to construct Figure 4.1.

Figure 4.4 shows how the calculated thermal diffusivity decreases with pressure and increases with inlet temperature. The slight increase with residence time, apparent at the unheated inlet cases is due to the increase of inlet temperature with residence time, which is concluded in Chapter 3 to be a result of increased reactor heat loss. The inlet temperature effect is most pronounced at 3 atm where the inlet temperature difference between low and high residence times is the highest.

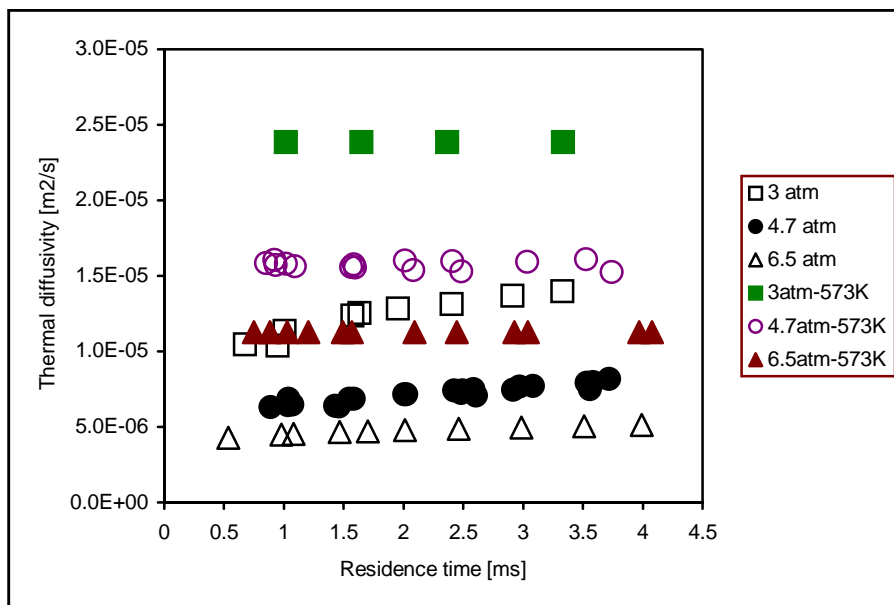


Figure 4.4 Calculated thermal diffusivity versus residence time for three pressures and for unheated and heated (573 K) inlets

The kinematic viscosity (not shown), used to calculate the turbulent Reynolds number, is similar in magnitude to the thermal diffusivity because the Prandtl number is about 0.7. Both the kinematic viscosity and thermal diffusivity are inversely proportional to pressure and increase with inlet temperature.

The calculated values for the laminar flame thickness are plotted versus residence time for the three pressures in Figure 4.5. The laminar flame thickness decreases with residence time, except at residence times below 1.5 ms, at 6.5 atm and 4.7 atm without preheat, where it increases with residence time. This behavior is a consequence of the decrease in laminar burning velocity at these conditions, caused by a minimum fuel-air equivalence ratio for residence times between 1.5 to 2 ms. For all calculated cases  $\delta_L$  is

between 0.046 and 0.080 mm. This is larger than the Kolmogorov scale, plotted in Figure 4.6, but smaller than the integral length scale, i.e., the nozzle diameter,  $d_0 = 1.4$  mm, indicating burning in the flamelets in eddies regime (Turns, 2000). The Kolmogorov scale is calculated using the following equation:

$$\eta = (v^3 / \epsilon_0)^{1/4}$$

where  $v$  is the kinematic viscosity at the inlet temperature and reactor pressure, and  $\epsilon_0$  is the dissipation rate, estimated by the following equation:

$$\epsilon_0 = 1.5 u'^3 / d_0$$

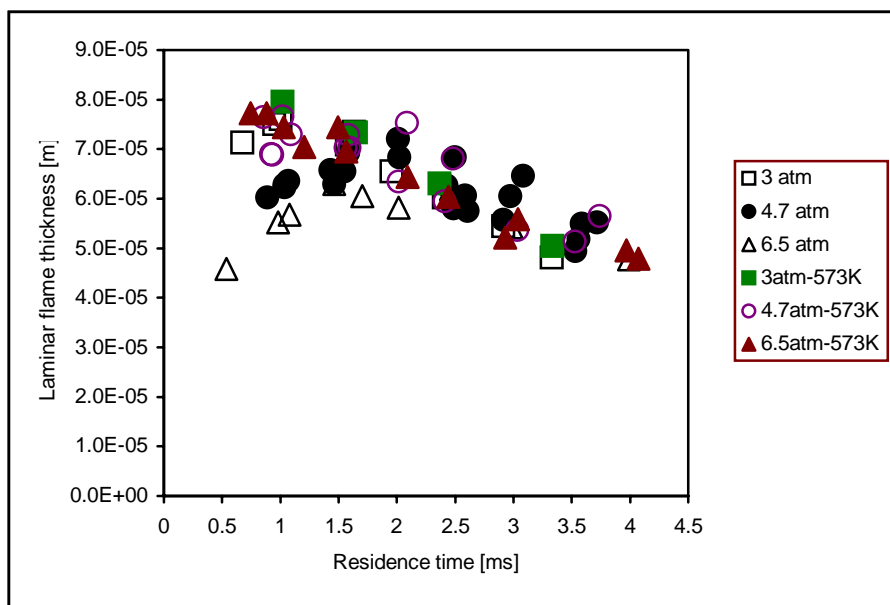


Figure 4.5 Laminar flame thickness versus residence time for three pressures and for unheated and heated (573 K) inlets

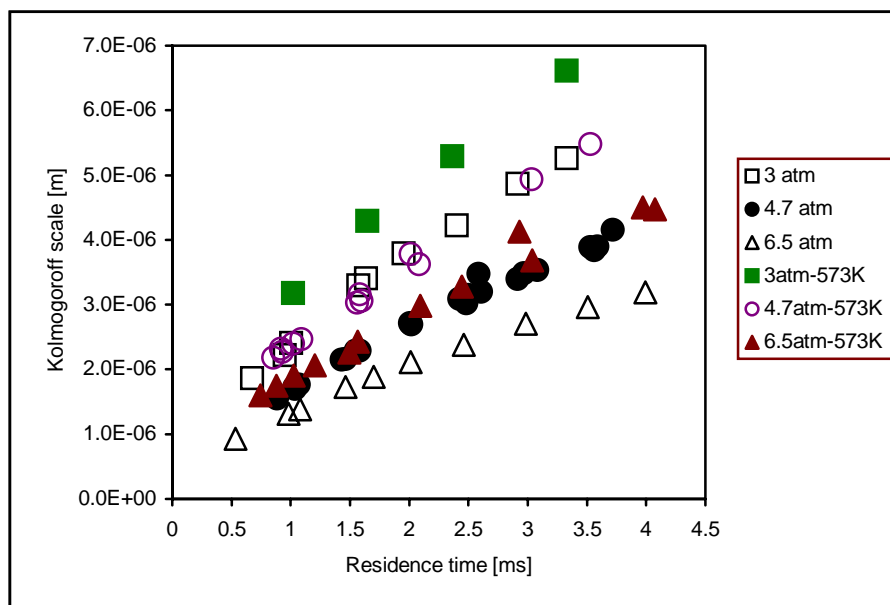


Figure 4.6 Kolmogorov scale versus residence time for three pressures and for unheated and heated (573 K) inlets

The parameters obtained to this point are sufficient to calculate  $Da$  and  $Re$  and determine the turbulent flame regime. The  $Da$  and  $Re$  numbers are shown for all calculated cases in Figures 4.7 and 4.8, respectively.

The calculated limiting cases for combustion in the HP-JSR, i.e., minimum and maximum residence times for the pressure levels of 6.5 atm and 3.0 atm for unheated and heated (573 K) inlets, are shown on Figure 4.1. For both pressures and both inlet temperatures, points higher in Figure 4.1 correspond to the largest residence time and the lower points to the smallest residence time. For example, at 6.5 atm without preheat,  $Da$  decreases from 0.41 at 4.0 ms (maximum residence time) to 0.09 at 0.5 ms (minimum residence time), and  $Re$  increases from 2917 to 15135 for the same change in residence time. The decrease in  $Da$  is primarily caused by the substantial increase in  $u'$ , which also

causes  $Re$  to increase.  $Da$  is also influenced by changes of the chemical time,  $\tau_{chem}$ , whereas  $Re$  is influenced by changes in kinematic viscosity for the unheated cases.

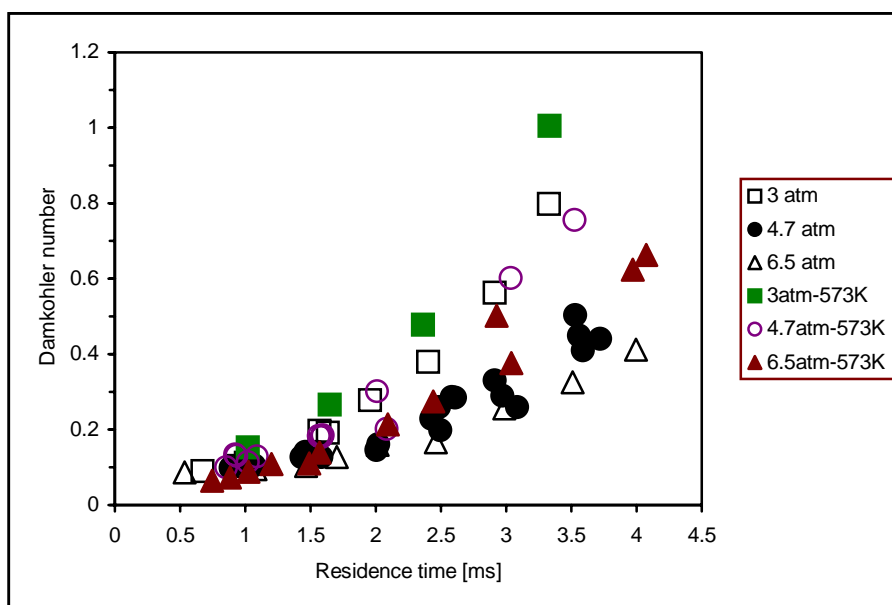


Figure 4.7 Damköhler number versus residence time

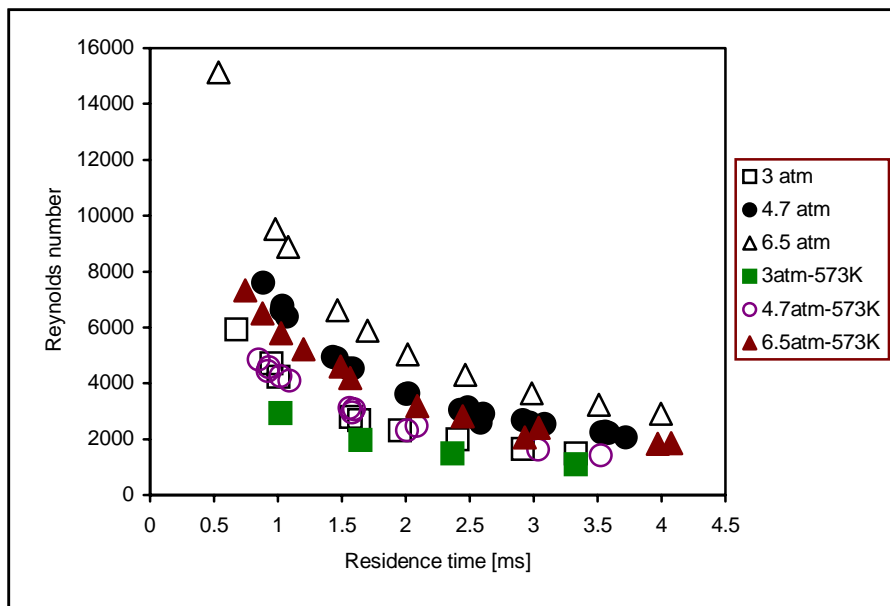


Figure 4.8 Turbulent Reynolds number versus residence time

The results shown in the  $Da$  versus  $Re$  plot of Figure 4.1 indicate the operation of the HP-JSR falls in the flamelets in eddies regime (Turns, 2000). A similar conclusion can be obtained if results are placed in the Borghi (1985) diagram, another non-dimensional diagram for which the axis are  $u'/S_L$  and  $l_o/\delta_L$ . The flamelets in eddies regime is fairly large with the criterion for the regime defined as:  $1 < l_o/\delta_L < \infty$  and  $\eta/\delta_L < 1$ .

The boundaries for the turbulent flame regimes suggested in the literature are rather arbitrary. Abraham et al. (1985) place the boundary between the flamelets in eddies regime and the distributed reaction regime at  $l_o = \delta_L$  but note that a sufficient condition for the presence of the distributed reaction regime is actually  $l_o \ll \delta_L$  (the necessary condition is not determined). Additionally, Kobayashi et al. (1997), based on Bray's diagram (Bray, 1980), and Chomiak (1990), call the regime of  $Da < 1$  the distributed

reaction regime. The  $Da < 1$  criterion suggests that combustion in the HP-JSR is in the distributed reaction regime because calculation of  $Da$  shows that it is always lower than unity, except for the highest residence time preheated case at 3.0 atm, for which it is 1.0.

The discussion in the previous paragraph suggests that the combustion regime in the HP-JSR is either the flamelets in eddies or the distributed reaction regime. The experimental evidence from the CO profiles is that reaction high in free-radical concentrations is spread through the reactor for operation at short residence times. This implies distributed reaction.

In the HP-JSR, mixing rate is faster than the chemical reaction rate. This is due to very high turbulence intensities which assure high turbulent Reynolds numbers ( $1100 < Re < 15135$ ). The ratio  $u'/S_L$  varies from 28 for 3 atm, at 573 K inlet temperature, and a residence time of 3.3 ms, to 356 for 0.5 atm, at no preheat, and a residence time of 0.535 ms. This ratio increases with increasing pressure and decreasing residence time and inlet temperature. The laminar flame thickness is only an order of magnitude smaller than the integral scale for all conditions, (i.e.,  $18 < d_0/\delta_L < 31$ ). In addition, for most cases,  $\eta/\delta_L$  has the order of magnitude of  $10^{-2}$ , characterizing a regime far from the thin reaction sheet regime of wrinkled laminar flames. This ratio increases with residence time, inlet temperature and decreases with pressure. The highest value of 0.13 is at 3.0 atm, 573 K preheat, and 3.3 ms.

#### 4.2.1.2 Calculation of Turbulent Burning Velocity

Glassman's (1996) general definition of turbulent burning velocity,  $S_T$ , is a mass consumption rate per unit area divided by the unburned gas density. In this analysis,  $S_T$  is taken from the non-dimensional modeling performed by Schmid et al. (1998). They found good agreement between calculated values for  $S_T$  and experimental results by the following equation:

$$S_T = S_L + u'(1 + Da^{-2})^{-1/4}$$

Although their comparisons were done for Damköhler number in the range of 0.2 to 2.8, the trend for  $S_T$  appears to be applicable outside of the range.

For  $Da > 3.2$ , i.e.,  $Da^2 > 10$ , the above formula for  $S_T$  reduces to  $S_T \cong S_L + u'$ . This solution is the same as the wrinkled laminar flame regime solution derived by Damköhler. Other theories that have been derived to describe the wrinkled laminar flame regime have resulted in similar solutions. Turns (2000) notes that in all theories the  $S_T$  is only a function of  $S_L$  and  $u'$  for this regime, and does not involve any other turbulence parameters, such as length scales. Since experimental conditions in HP-JSR are far from the wrinkled laminar flame regime, this will not be further discussed.

For  $Da < 0.31$ , i.e.,  $Da^2 < 0.1$ , the above formula for  $S_T$  reduces to:

$$S_T \cong S_L + u' Da^{0.5} = S_L + (u' S_L d_o / \delta_L)^{0.5}$$

Since  $u' d_o / \delta_L \gg S_L$ , the equation for turbulent burning velocity can be approximated by:

$$S_T \cong (u' S_L d_o / \delta_L)^{0.5} = (u' d_o / \tau_{chem})^{0.5} = (\alpha_T / \tau_{chem})^{0.5}$$

This is analogous to laminar flame theory with the turbulent diffusivity,  $\alpha_T$ , taken as  $u'd_o$ , and substituted for  $\alpha$ , the laminar thermal diffusivity. This means that  $S_T$  is proportional to the square root of the turbulent intensity and the integral scale, and inversely proportional to the square root of the chemical time ( $\tau_{chem} = S_L/\delta_L$ ). This is the distributed reaction regime solution presented in Chomiak (1990). The present work assumes that the integral scale is constant in all conditions, since large-scale turbulence is generated by flow through the nozzle of constant diameter  $d_o$ . This somewhat simplifies the analysis to a discussion of  $u'$  and  $\tau_{chem}$ . However, the significantly large range of inlet velocities in the experiments complicates the problem, because it causes turbulent intensities to vary substantially. This causes the increase in  $Re$  and is the primary cause of the decrease in  $Da$  at lower residence times. This change in  $Re$  and  $Da$  could mean a transition in combustion regimes occurring within the data range, which will be discussed later.

The calculated values of  $S_T$  for the pressures, residence times, and inlet temperatures of the HP-JSR are shown in Figure 4.9. Turbulent burning velocity decreases with residence time from 0.5 to 1.5 ms, and is constant or varies only slightly for residence times above 1.5 ms. This trend is explained by the following. Since the thermal diffusivity and the laminar burning velocity are fairly constant at low residence times, and  $u'$  is fairly large,  $S_T$  is effectively a function of  $u'^{0.5}$ . At residence times higher than 1.5 ms,  $S_T$  remains relatively constant because the increase of  $Da$  is compensated by the decrease of  $u'$ .

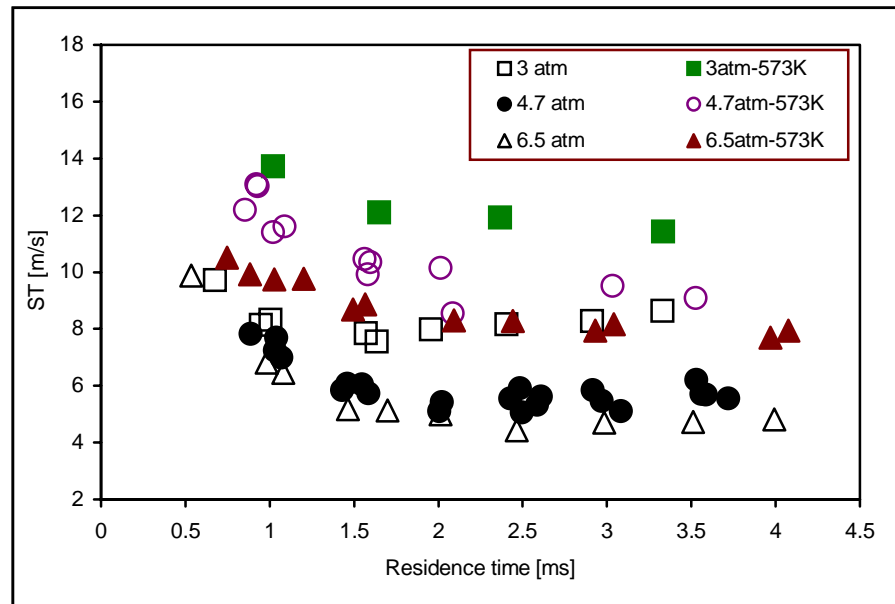


Figure 4.9 Turbulent burning velocity versus residence time for three pressures and for unheated and heated (573 K) inlets

Turbulent burning velocity decreases with pressure. This is a consequence of the decrease of Damköhler number with pressure. It increases with inlet temperature due to the increase in both the  $Da$  and the  $u'$  with increasing inlet temperature.

The non-dimensionalized burning velocity,  $S_T/S_L$ , is plotted versus  $u'Da^{0.5}/S_L$  in Figure 4.10. For most cases, the relationship can be approximated as linear and originating from the zero of the coordinate system, proving that the  $S_T = u'Da^{0.5}$  approximation is valid for most conditions in the present work. Only at highest residence times in preheated cases is a slight diversion from linearity observed, indicating that the above approximation begins to fail only for the largest Damköhler numbers encountered in this study.

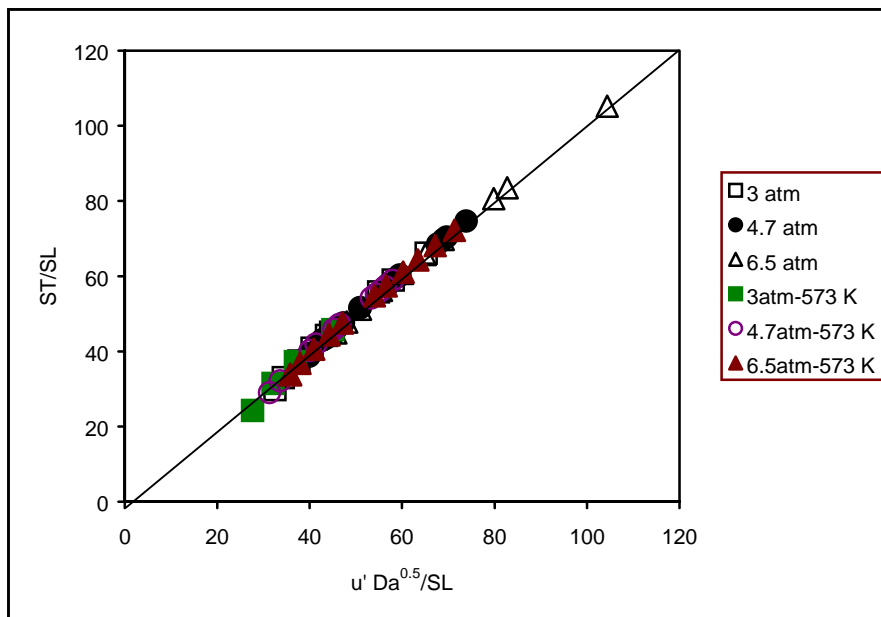


Figure 4.10 Non-dimensionalized burning velocity ( $S_T/S_L$ ) versus  $u' Da^{0.5}/S_L$

In Figure 4.11, a ratio of the turbulent and laminar burning velocities is plotted versus the ratio of the turbulent intensity and laminar burning velocity for all reactor conditions. If all the results are approximated by two linear functions, one to fit the lower data and the other the rest, then the change in the slope of the data, termed “bending”, occurs in the vicinity of  $u'/S_L = 60$  in all cases. The “bending” of the  $S_T/S_L$  curves for high  $u'/S_L$  ratios, and small  $Da$ , is suggested by Schmid et al. (1998) to be a result of reaching a point in which chemistry becomes so slow (relative to mixing) that it reduces the acceleration of the flame front by turbulence. The chemical time, defined as  $\tau_{chem} = \delta_L/S_L$ , is plotted versus residence time for all conditions in Figure 4.12. It decreases with

residence time for all conditions, except for 6.5 and 4.7 atm without preheat, where it first increases and then decreases with increase in residence time.

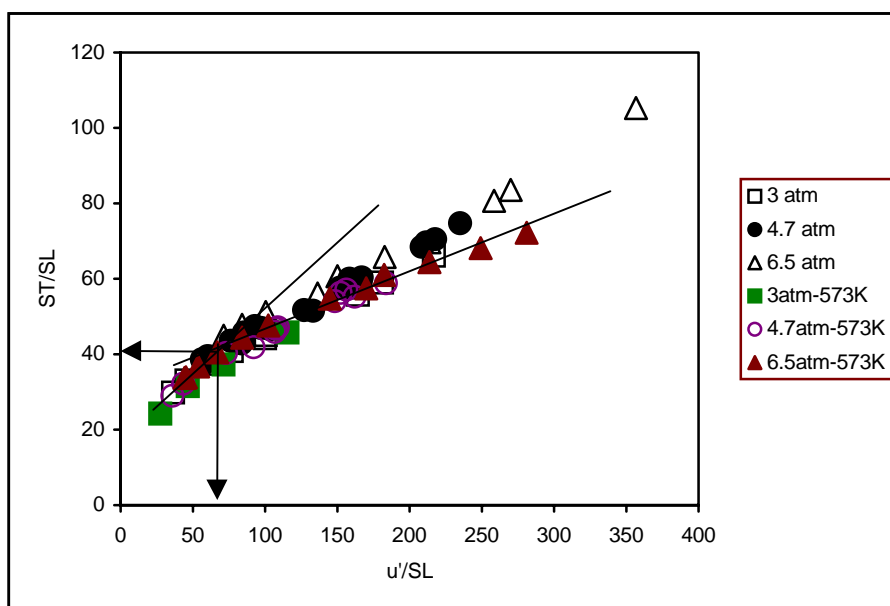


Figure 4.11 Ratio of turbulent and laminar burning velocities versus ratio of turbulent intensity and laminar burning velocity

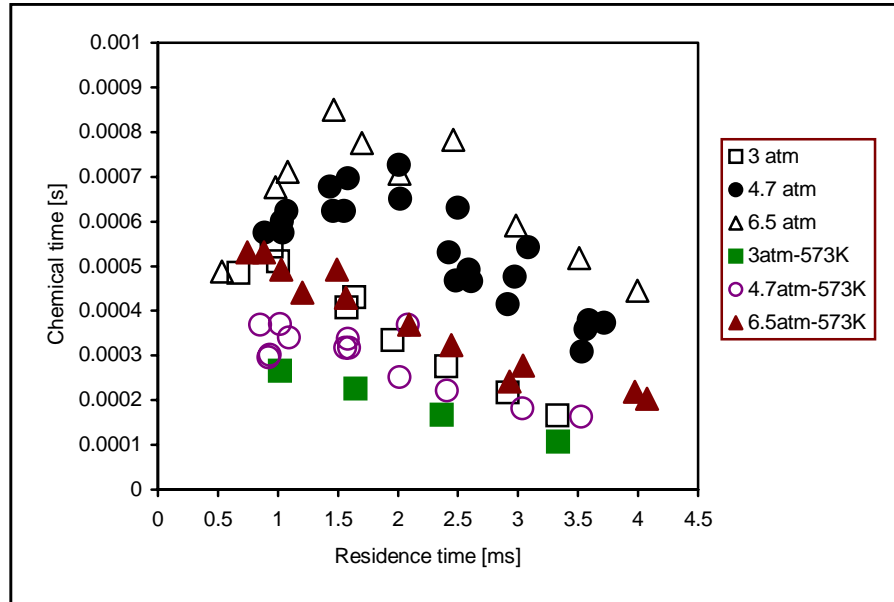


Figure 4.12 Chemical time versus residence time for three pressures and for unheated and heated (573 K) inlets

#### 4.2.1.3 Calculation of Turbulent Flame Thickness

The turbulent flame thickness is  $\delta_T$ . It is calculated by analogy with the laminar flame thickness,  $\delta_L$ , as ratio of the turbulent diffusivity to the turbulent burning velocity,  $S_T$ , as discussed above. Turbulent diffusivity in this work is estimated as a product of turbulent intensity,  $u'$ , and integral length scale,  $d_o$ , as suggested by Chomiak (1990).

Therefore, the values for turbulent flame thickness are calculated by the following formula:  $\delta_T = u' d_o / S_T$ . The relation between the flame thickness and the residence time for all three pressures and both heated and unheated inlets is depicted in Figure 4.13, which indicates that for a constant residence time the flame thickness decreases between

6.5 and 3.0 atm. This is a consequence of the turbulent flame speed's inverse dependence on pressure. For all three pressures and both heated and unheated inlets, the flame thickness increases with decreasing residence time. This is a consequence of the increase in inlet velocity with decreasing residence time. The increase in flame thickness at low residence times is counteracted by an increase in  $S_T$  with decreasing residence times, as shown in Figure 4.9. It is noted that the maximum thickness is 5.4 mm and it occurs at 0.75 ms and 6.5 atm, 573 K inlet temperature. This thickness is nearly identical to the radius of the HP-JSR at the widest point, which is 5.75 mm. This indicates that at this condition the flame spreads throughout the reactor. A flame thickness of the same order as the reactor radius is also calculated for the shortest residence times for the other pressures and for both heated and unheated cases.

Another factor that is important in the analysis of the physical parameters of the flame is how far the unreacted fuel and air reach into the reactor before being burned. Since the flame is assumed to form a cone positioned on top of the nozzle, then the height of the cone corresponds to the maximum length the unreacted gas reaches before being burned. This length, defined as the unreacted core length, increases with decreasing residence time. In fact, the core length increases in direct proportion to the flame thickness. The relation between the core length and the flame thickness is derived by the following procedure. The unreacted core length,  $h$ , is defined using the following geometric relation:

$$h = 0.5d_0/\tan\alpha$$

where  $\alpha = \text{asin}(S_T/U_o)$  is the half-angle of the unreacted jet core, defined in Figure 4.14. Figure 4.14 depicts the relation between flame angle, inlet velocity, and turbulent burning velocity at the flame front. The flame front is defined as the time and space average of the area at which fresh reactants begin to burn. It also depicts the unreacted core and its length.

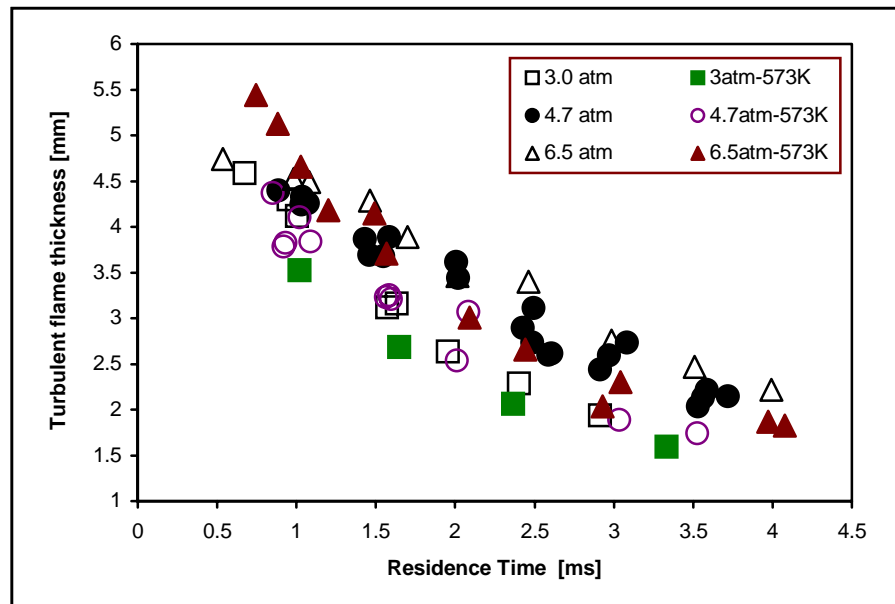


Figure 4.13 Turbulent flame thickness versus residence time for three pressures and for unheated and heated (573 K) inlets

For small angles,  $\tan\alpha \cong \sin\alpha$ , so  $d_o/2h \cong S_T/u_o \cong S_T/10u'$ . Consequently, one obtains  $h \cong 5\delta_T$ .

Assuming that the flame forms a cone positioned on the nozzle, as depicted in Figure 4.14, by neglecting the unreacted core, the volume of the flame can be approximated as  $V_{\text{flame}} \cong 5\pi\delta_T^3$ . The percent of the reactor volume filled by the flame is calculated as

$(V_{\text{flame}}/V_{\text{total}})100$ , where  $V_{\text{total}} = 1.5 \text{ cm}^3$ . When  $\delta_T \cong 3.6 \text{ mm}$ , the flame volume becomes  $V_{\text{flame}} \cong 0.75 \text{ cm}^3$ , which is one-half the reactor volume. This corresponds to  $h \cong 18 \text{ mm}$ , which is almost the reactor height of 20.19 mm. The calculated flame volume is shown in Section 4.3, where it is directly compared to the flame volume inferred from the chemical reactor modeling presented in Section 4.2.2.

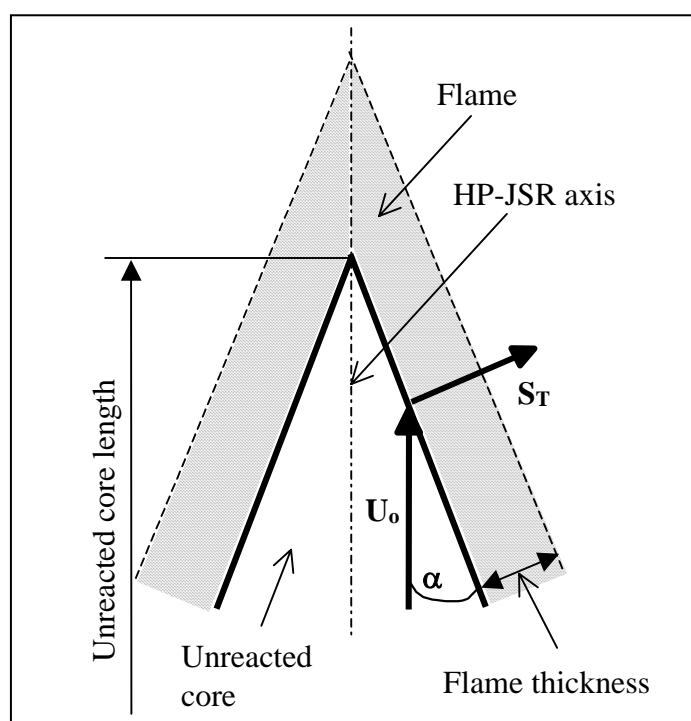


Figure 4.14 Sketch of flame geometry

The longest unreacted core length is at 6.5 atm, 0.75 ms and 573 K preheat, and it is 27.2 mm. This means that at this condition, premixed, unreacted fuel and air reach the top of the reactor and probably sweep along the top and sides of the reactor, before being burned. The shortest core length is 7.9 mm, for 3.0 atm, 3.33 ms and 573 K preheat. In this case, the unreacted gases reach at least 39% of reactor height.

At the low residence times, the core length and the flame thickness are large, so more of the reactor volume is filled by the unreacted mixture. The necessary criterion for the existence of a well-stirred reactor in combustion is that the flame spreads evenly throughout the whole volume, and it appears that combustion in the HP-JSR meets this criterion at low residence times. The sufficient criterion for the existence of a well-stirred reactor in combustion is that the chemical reaction species are time-mean homogeneous within the flame. The turbulent intensities are high in the HP-JSR at low residence times, implying it is approaching the sufficient criteria for a well-stirred reactor.

At large residence times, the flame thickness decreases, confining the flame to the region around the inlet jet. This effectively divides the reactor into two zones, i.e., the jet with surrounding flame brush (with a high NO production rate) and the recirculation zone or post-flame zone (with a low-NO production rate). This division into two zones has been postulated in Chapter 3 based on CO experimental measurements. It is important to define the transition point between the reactor volume being filled by the flame, and the flame being confined to a small part of the reactor volume. The Damköhler number is a convenient tool for assessing flames and is used to define this transition point.

Chomiak (1990) postulates that distributed reaction combustion occurs when  $l_o < \delta_T$ . If the equation for  $S_T = (u' l_o S_L / \delta_L)^{0.5}$ , derived in Section 4.2.1.2, is substituted into the equation for  $\delta_T = u' l_o / S_T$ , then  $\delta_T$  is expressed as:

$$\delta_T = u' l_o / S_T = u' l_o / (u' l_o S_L / \delta_L)^{0.5} = (u' l_o \delta_L / S_L)^{0.5}$$

After substituting the equation for  $\delta_T$  into  $l_o < \delta_T$ , the inequality becomes:

$$l_o < (u' l_o \delta_L / S_L)^{0.5},$$

which is equivalent to

$$l_o < u' \delta_L / S_L$$

This inequality is equivalent to  $Da < 1$ , the distributed reaction criterion of Chomiak (1990).

The HP-JSR approaches the well-stirred reactor for Damköhler numbers that satisfy the following inequality:

$$Da < C$$

where  $C$  is constant less than 1. The value of constant  $C$  is influenced by the fact that the flame in the HP-JSR is confined. Due to confinement, the flame bends, i.e., sweeps around the inner walls of the reactor cavity, and mixing within the flame is enhanced.

#### ***4.2.2 Two-PSR Model***

The two-PSR model is considered in this work. The model consists of two PSR's in series where fresh methane and air enter the first PSR, denoted PSR1, and all of the products exiting PSR1 enter the second PSR, denoted PSR2. This model was successfully used by Bengtsson et al. (1998) and Steele (1995) to model NO<sub>x</sub> data from high-pressure jet-stirred reactors. This model has the advantage of being very simple and easy to use. It is validated in thick turbulent flames with low Damköhler numbers if PSR1 and PSR2 represent the flame zone and the stirred post-flame zone respectively. Mixing of fuel and oxidizer in the distributed regime of turbulent flame is improved

compared to molecular diffusion, which is the only mechanism for mixing within thin laminar or wrinkled laminar flames. The flame zone is thicker than the smallest turbulent eddies, i.e., the Kolmogorov scale eddies roll within the flame, thus enhancing the mixing. The high mixing intensity at low  $Da$  warrants that the flame is reasonably well represented by the perfectly-stirred reactor. For the post-flame zone, the characteristic turbulence time is longer than in the flame zone because the characteristic length scale is the overall reactor dimension and not the inlet jet diameter. The chemical time is also longer than in the flame, since rate of chemistry slows considerably in the post flame zone. Therefore, the post-flame zone is also reasonably well represented by the perfectly-stirred reactor. Since conversion in PSR2 is highly dependent on the gas temperature, PSR2 is run at the measured temperature corrected by the heat transfer analysis presented in Section 3.3.4. Adiabatic conditions are assumed for PSR1 because the heat release rate in the flame is so high that any other heat transfer can be neglected. The volume of the PSR1 is an adjustable parameter. It is determined based on matching measured and modeled values for CO and NO<sub>x</sub>. The two-PSR model uses the GRI 3.0 (Smith et al., 1999) chemical kinetic mechanism.

The two-PSR model is illustrated, conceptually, in Figure 4.15, which represents the axi-symmetric cross sectional area of the HP-JSR. Figure 4.15 shows the jet zone and the recirculation zone. The flame is positioned on the edge of the jet zone in the form of a cone. The length of the unreacted core is depicted in Figure 4.15 with arbitrary height, because it varies with reactor conditions, i.e., it is shorter than the reactor height for the long residence times, and longer at the short residence times. The two-PSR model

consists of three reactors, as shown in the schematic given in Figure 4.16. A small PFR is added upstream of the two PSR's to represent the cold jet of premixed methane and air, i.e., the unreacted core. It's volume is determined assuming that it is a cone with a circular base of diameter  $d_0$  and with height  $h$ , which is the unreacted core length. (The means of calculating the unreacted core length were described in Section 4.2.1.3.) This volume is rather small, and for all cases does not exceed 1% of the total reactor volume. The sum of the volumes of the core-PFR, PSR1 and PSR2 is  $1.5 \text{ cm}^3$ , which is the total volume of the HP-JSR. Matching of the model to the measured  $\text{NO}_x$  and CO is performed by varying the volume of PSR1 starting from the blowout volume to the maximum volume. The blowout volume is determined based on the prescribed fuel-air equivalence ratio and mass flow rate. The maximum volume is determined as  $1.5 \text{ cm}^3$  minus the core-PFR volume.

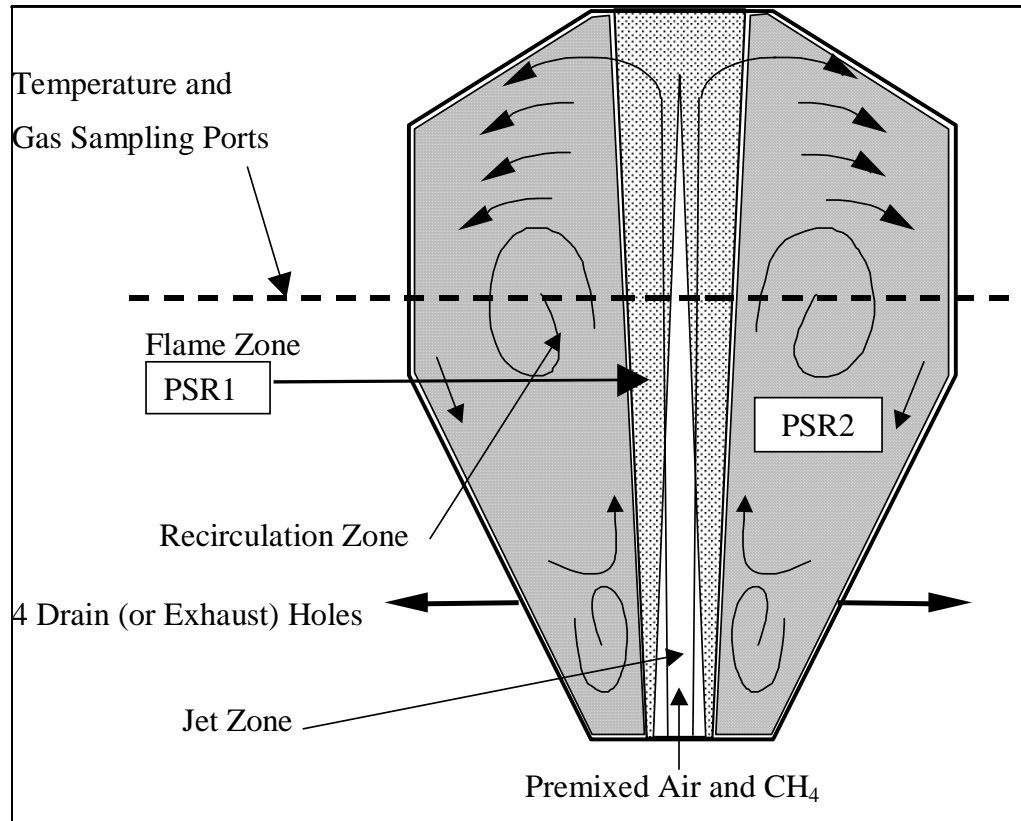


Figure 4.15 Conceptual model for two-PSR model

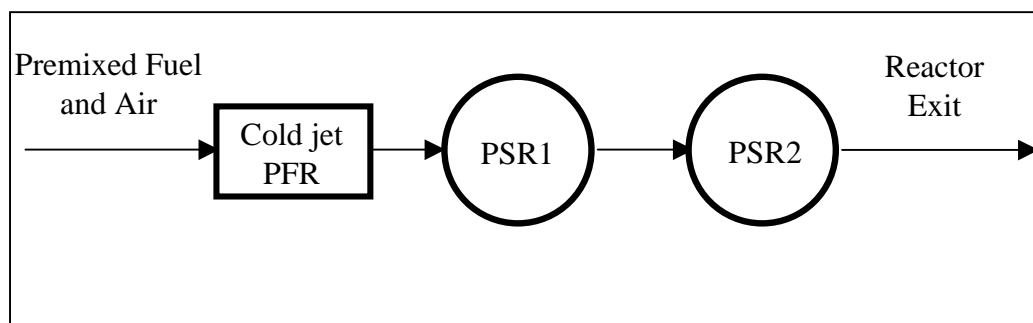


Figure 4.16 Schematic of the two-PSR model

As mentioned, the volume of PSR1 is determined as a result of analysis based on matching the measured and modeled values for CO and NO<sub>x</sub>. An example is given in Figure 4.17 below for 0.5 ms at 6.5 atm and no preheat. In this figure, both the NO<sub>x</sub> and the CO exiting the PSR2 are shown for volume partitions ranging from the PSR1 volume at blowout to the PSR1 volume equal to 100% of the reactor. The volume partition is defined as  $V_{\text{PSR1}}/V_{\text{total}}$ , where  $V_{\text{total}} = V_{\text{PSR1}} + V_{\text{PSR2}}$ . Two lines present the modeling results: the upper line corresponds to the modeled NO<sub>x</sub> and the lower one for modeled CO. The NO<sub>x</sub> and CO are for PSR2, which are the modeled reactor exit concentrations. The two circles indicate experimental measurements: the upper circle shows the measured CO and the lower circle shows the measured NO<sub>x</sub>. The measured NO<sub>x</sub> and CO are for the recirculation zone of the reactor, at the location of minimum CO (i.e., in the eye of the recirculation zone, as defined in Chapter 3). Assuming a nominal experimental error of 15% in measured concentrations, suggested by Steele (1995) for a similar system, the model can successfully predict the NO<sub>x</sub> for the volume ratios anywhere between about 17 and 100%. For CO, however, the model reaches the experimental value only around 97% volume ratio. Therefore, it is the CO level that determines the volume ratio for which the model successfully predicts the experimental emissions measurements at the conditions shown in Figure 4.17. In this case, the CO and NO<sub>x</sub> measurements suggest the reactor is operating close to a single PSR.

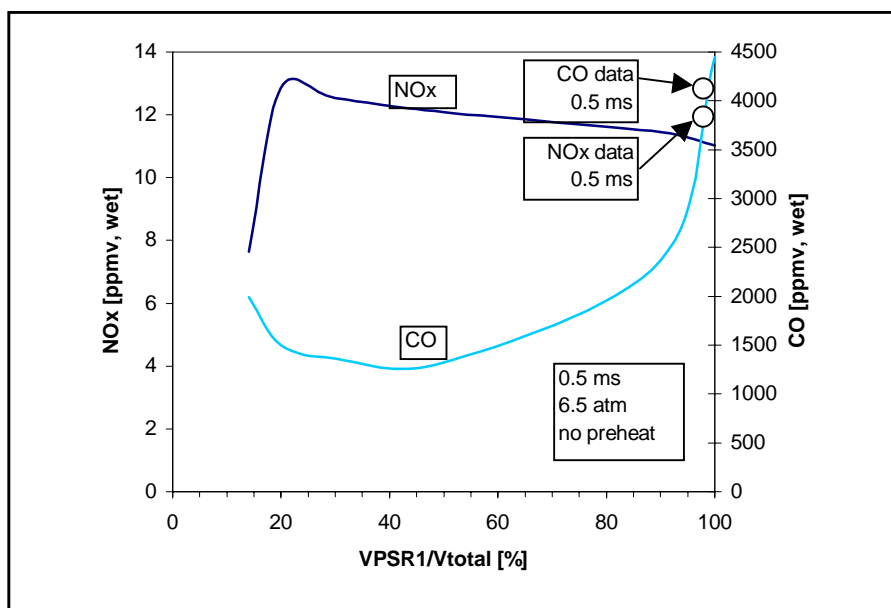


Figure 4.17 CO and NO exiting PSR2 in PFR+PSR1+PSR2 reactor setup, using GRI 3.0 Mech. at 0.5 ms, 6.5 atm and no preheat conditions. The two arrows indicate experimentally measured values of CO and NOx.

Figure 4.18 depicts the same modeling approach applied to conditions at 4.0 ms, 6.5 atm and no preheat. In this case the NOx, rather than CO, determines the volume ratio of  $V_{\text{PSR1}}/V_{\text{total}}$ . This is because the NOx modeling results are similar to measured values at the low volume ratios only, whereas the CO modeling remains within the experimental error for a wide range of volume ratios, from 0 to 95%. In this case, the NOx and CO data suggest the reactor is operating with two zones: a flame zone of small volume, followed by a large post-flame stirred zone.

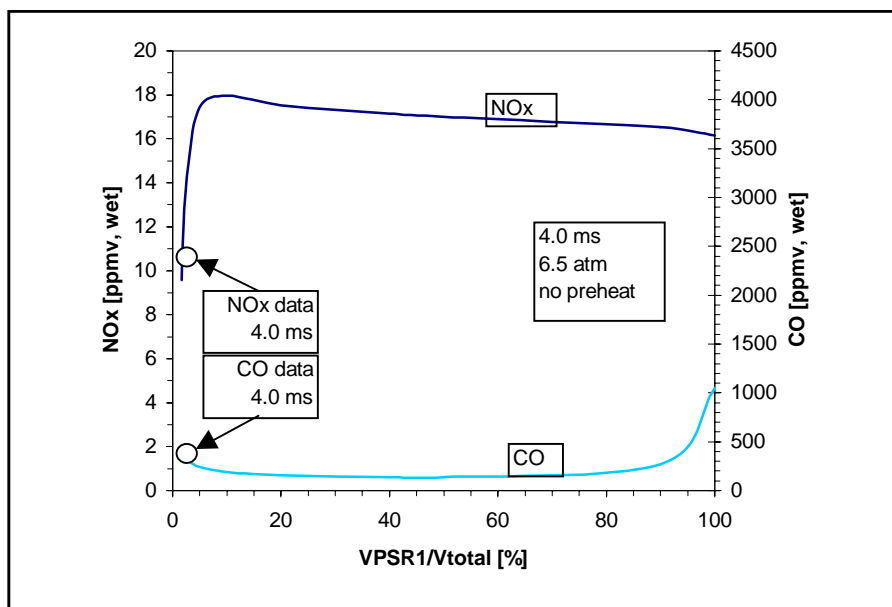


Figure 4.18 CO and NO exiting PSR2 in PFR+PSR1+PSR2 reactor setup, using GRI 3.0 Mech. at 4.0 ms, 6.5 atm and no preheat conditions. The two arrows indicate experimentally measured values of CO and NOx.

In order to further understand the two-PSR model, a plot of NOx formation rate versus volume ratio, for 0.5 and 4.0 ms cases at 6.5 atm and without preheat, is shown in Figure 4.19. Figure 4.19 is accompanied by Table 4.1, which contains concentrations of relevant species, for 0.5 ms case at 6.5 atm and no preheat. The O-atom, OH and CH are shown because they are indicators of the free-radical presence responsible for hydrocarbon destruction, CO oxidation, and finally NOx formation. The hydrocarbons are represented by CH<sub>4</sub>. The O-atom and CH radical have primary responsibility for NOx formation, per discussion in Sections 2.3 and 3.4. Figure 4.19 shows that the NOx formation rate is higher in PSR1 for both 0.5 and 4.0 ms cases and for all volume ratios.

With exception of near blowout, the NO<sub>x</sub> formation rate decreases with increasing volume ratio. The reduced NO<sub>x</sub> formation rates near blowout are probably caused by the reduced O-atom concentrations near blowout, which in turn, are caused by insufficient time for O-atom formation. The NO<sub>x</sub> formation rate decreases 5-fold in the PSR1 between volume ratios of 20% and 100%, whereas the O-atom decreases 56%. The CH radical is an order of magnitude different between 20% (and blowout, which occurs at 14%) and 100% volume ratio. Results in Figure 4.19 also suggest that the NO<sub>x</sub> formation rate in PSR2 decreases slightly for small volume ratios, and then increases slightly for most of the reactor volume ratios. At high ratios, it picks up and increases to reach single PSR conversion at 100%.

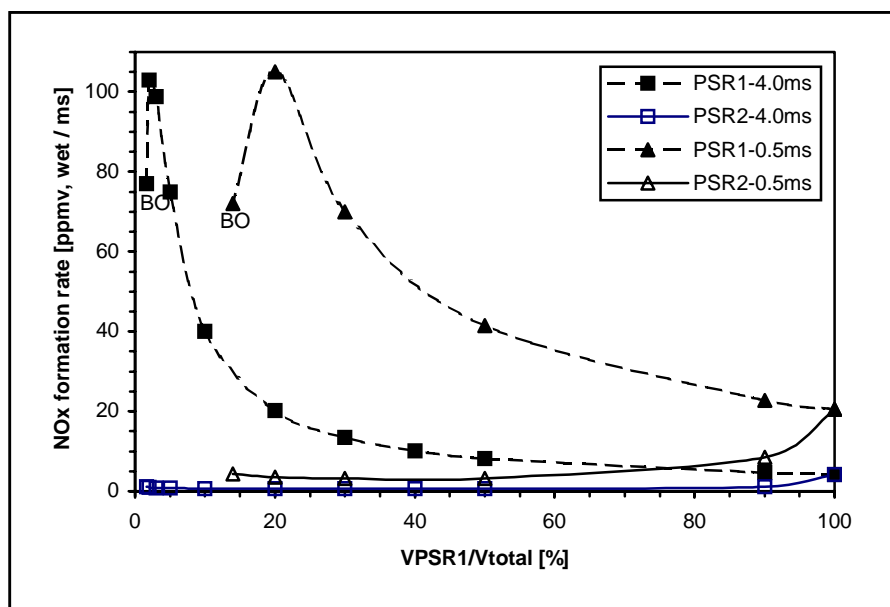


Figure 4.19 NO<sub>x</sub> conversion or formation rate versus volume ratio in two-PSR model

Table 4.1 Free radical concentrations [ppmv, wet] in PSR1 and PSR2 at 6.5 atm at 0.5 ms and no preheat conditions.

Volume ratio [%]		O	OH	CH <sub>4</sub>	CH	NO <sub>x</sub>	CO
14 (Blowout)	PSR1	528	1786	1348	0.1	5.64	18800
	PSR2	142	1299	7	0.0003	7.64	1993
20	PSR1	702	2594	645	0.12	11.33	12300
	PSR2	118	1191	4	0.00015	12.85	1497
30	PSR1	580	2391	486	0.07	11.32	9589
	PSR2	109	1146	4	0.0001	12.53	1360
90	PSR1	322	1842	233	0.02	11.04	4742
	PSR2	187	1487	10	0.00056	11.46	2364
100	PSR1	305	1797	219	0.02	11.02	4449

The high rate of NO<sub>x</sub> formation in PSR1 causes a sharp increase in NO<sub>x</sub> at low volume ratios shown in Figures 4.17 and 4.18. The maximum NO<sub>x</sub> occurs at a volume ratio of 20% for all residence times (shown in Figure 4.20 below) except 4.0 ms, where this maximum NO<sub>x</sub> occurs at volume ratio below 10%. NO<sub>x</sub> remains rather flat for higher volume ratios, because the rate is inversely proportional to residence time, i.e.,  $(\text{NO}_x \text{ rate}) \times (\text{VPSR1}/\text{Vtotal}) = \text{const.}$  For example (directly from the Figure 4.19):

$$[(\text{NO}_x \text{ rate}) \times (\text{VPSR1}/\text{Vtotal})] @30\% = [(\text{NO}_x \text{ rate}) \times (\text{VPSR1}/\text{Vtotal})] @50\% = [(\text{NO}_x \text{ rate}) \times (\text{VPSR1}/\text{Vtotal})] @90\%$$

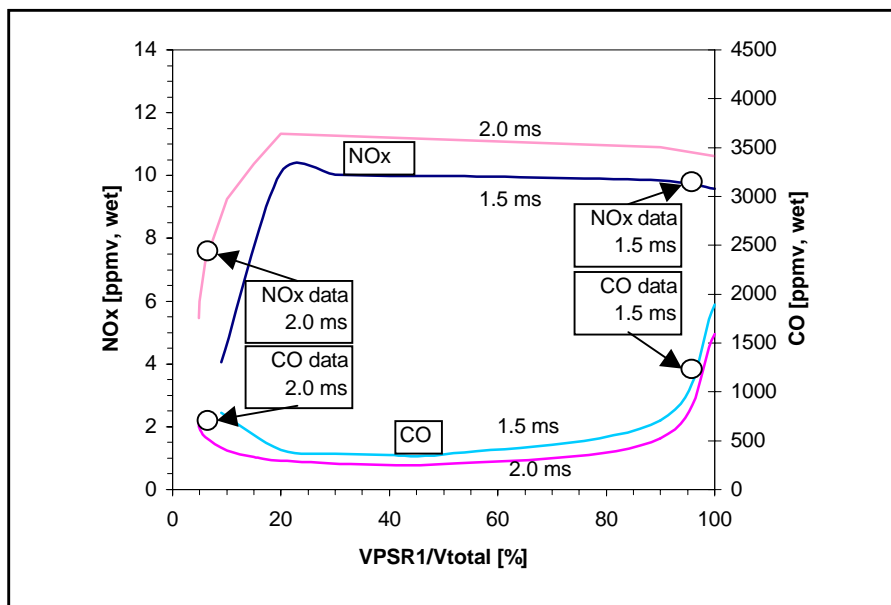


Figure 4.20 CO and NO exiting PSR2 in PFR+PSR1+PSR2 reactor setup, using GRI 3.0 Mech. at 1.5 and 2.0 ms, 6.5 atm and no preheat conditions. The arrows indicate experimentally measured values of CO and NO<sub>x</sub>

Figure 4.20 contains modeling and experimental results for 1.5 and 2.0 ms cases at 6.5 atm with no preheat. It can be noted that the best match between the model and the experiment is found at two distinctly different volume ratios. For 1.5 ms, the best match is found at 95%, and for 2.0 ms it is found at 6%. Therefore, the model suggests that transition between the HP-JSR operating as a single large flame and as a small flame zone followed by a large post-flame zone occurs somewhere between the two residence times shown in Figure 4.20. For low residence times, data are matched for volume ratios of about 100%, whereas at high residence times the match occurs closer to volume ratios of a few percent. This can be characterized as a two-mode behavior. Further, the

transition between the two modes appears to occur over a narrow range of residence times.

Similar plots to the ones shown in Figures 4.17, 4.18, and 4.20 have been created for other conditions. The best match with the experimental data is obtained for various levels of volume ratios. However, two-mode behavior is observed for all cases, with exception of the preheated 3.0 atm data, which will be discussed later. The best match volume ratio is plotted in Figures 4.21 and 4.22 for unheated and preheated (573 K) cases, respectively. It is apparent from these two figures that there are three distinguishable sets of data:

1. 6.5 atm with and without preheat, and 4.7 atm without preheat, which undergo transition between 1.5 and 2.0 ms
2. 4.7 atm with preheat, and 3.0 atm without preheat, which undergo transition between 1.0 and 1.5 ms, and
3. 3.0 atm with preheat, which remains in the small-flame-zone mode for residence times greater or equal to 1.0 ms.

The existence of the three distinguishable sets of data is related to the turbulent flame thickness, shown in Figure 4.13. The lowest values of  $\delta_T$  are noted for the 3.0 atm with preheat case, i.e., the third data set. The next highest values of  $\delta_T$  are noted for the 4.7 atm with preheat, and for 3.0 atm without preheat, i.e., the second data set. The highest values of  $\delta_T$  are noted for the first data set. In addition, for all three sets, all the cases for which  $\delta_T$  is above 3.6 mm correspond to the cases successfully modeled as a single PSR, and all the cases for which  $\delta_T$  is below 3.6 mm correspond to the cases successfully

modeled as a small PSR followed by a large PSR. The flame thickness of  $\delta_T = 3.6$  mm approximately corresponds to unreacted core gas striking the reactor top wall, and flame encompassing half of the reactor volume. The turbulent flame calculations indicate that the 3.6 mm flame thickness corresponds to a residence time of about 1.0 ms for the third data set, about 1.3 ms for the second data set, and about 1.8 ms for the first set. The varying residence time for the occurrence of the transition flame thickness is a result that is related to the discussion presented in Section 4.2.1.3. There, it is postulated that the HP-JSR approaches the well-stirred reactor for  $Da < C$ , where  $C$  is constant less than 1. Since transition occurs at  $\delta_T = 3.6$  mm, i.e.,  $l_o / \delta_T = 0.39$ , then  $Da = 0.15$  is a non-dimensionalized transition point. The value of constant  $C$  in the HP-JSR is determined to be 0.15.

Figures 4.23 through 4.26 give the comparisons of the two-PSR modeling for NO<sub>x</sub> and CO to the measured data at the point of minimum CO in the recirculation zone, to show how well the two-PSR model can fit both NO<sub>x</sub> and CO data.

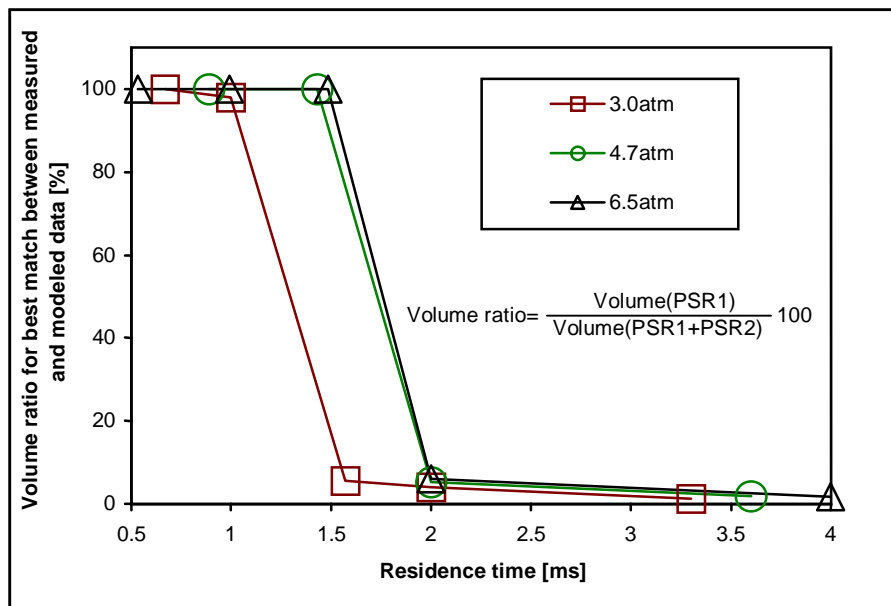


Figure 4.21 Volume ratio corresponding to the best match between the measured and modeled data versus reactor residence time for the three pressures and no preheat

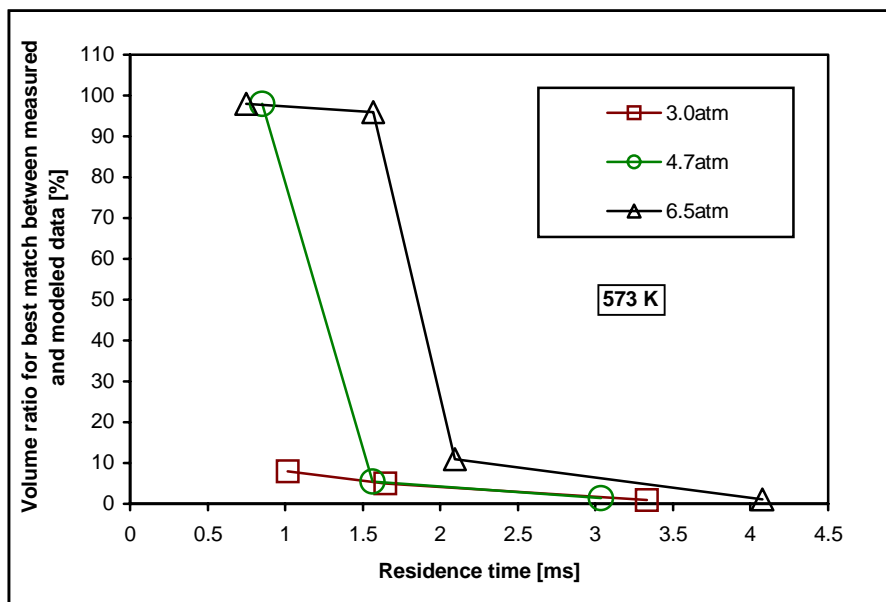


Figure 4.22 Volume ratio corresponding to the best match between the measured and modeled data versus reactor residence time for the three pressures and 573 K preheat

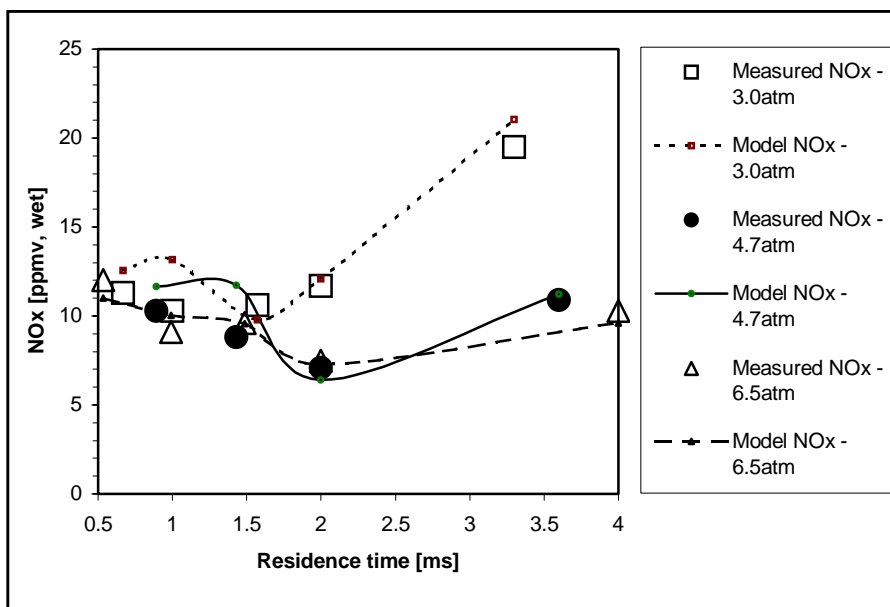


Figure 4.23 NOx data compared to the results obtained using two-PSR model for unheated cases

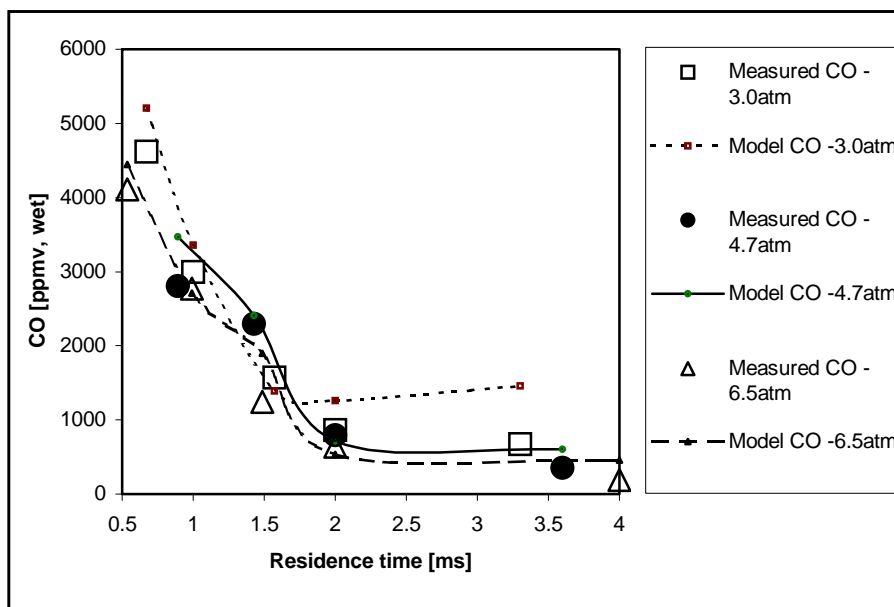


Figure 4.24 CO data compared to the results obtained using two-PSR model for unheated cases

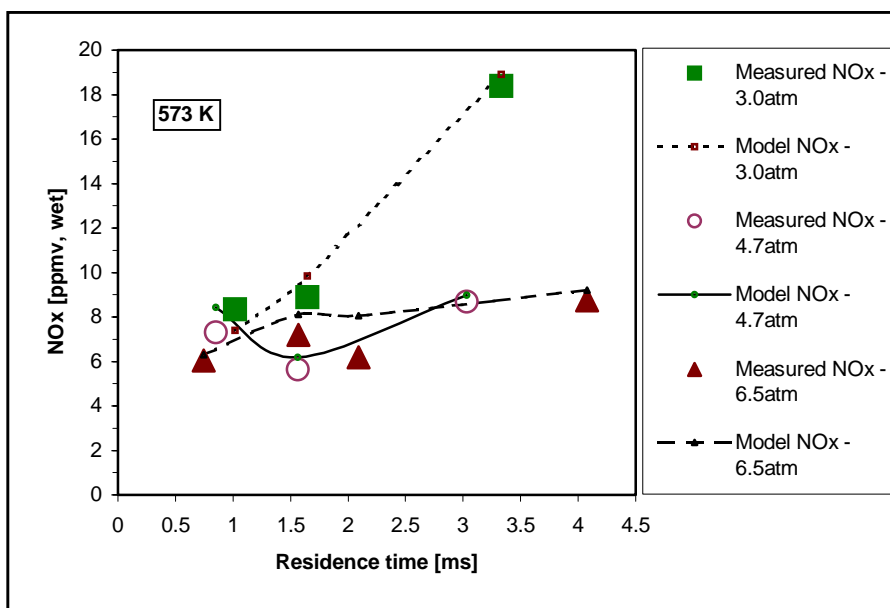


Figure 4.25 NOx data compared to the results obtained using two-PSR model for 573 K preheat cases

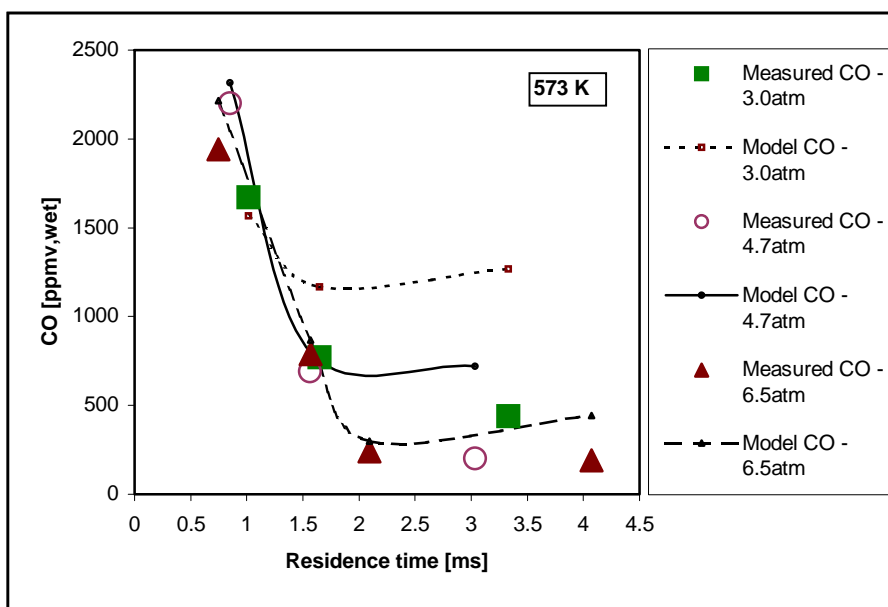


Figure 4.26 CO data compared to the results obtained using two-PSR model for 573 K preheat cases

The agreement between the modeled and measured NO<sub>x</sub> and CO is excellent for all cases at low residence times. However, at higher residence times, with the exception of 6.5 and 4.7 atm cases without preheat, the model overpredicts CO. The cases overpredicting CO are: 3.0 atm, no preheat, 3.3 ms; 3.0 atm, preheat, 1.6 and 3.3 ms; 4.7 atm, preheat, 3.0 ms; and, 6.5 atm, preheat, 4.1 ms. Since the model for these conditions is done assuming that PSR1 is at blowout (due to relatively low measured NO<sub>x</sub>), the predicted CO can not be any lower. It is postulated that, since in these cases mixing is the poorest, gases that reach close to the eye of the recirculation zone flow through a zone without any mixing, which could be represented by a PFR. The modeling suggests that the addition of a small PFR downstream of PSR2 could bring the CO levels within 20% of measured value, without significantly changing the NO<sub>x</sub>. The size of a PFR depends on the reactor conditions, as does the percent of the total volume pertaining to the eye of the recirculation zone. The PFR size increases with decreasing pressure, increasing residence time, and increased inlet temperature. At the highest residence time for 3.0 atm and 573 K preheat, a PFR with a volume of 5% of the total reactor volume is sufficient to lower the CO to level within 20% of the measured value.

It is important to note that although the reactor partition is done solely based on obtaining the best match between the measured and the modeled NO<sub>x</sub> and CO, the volume of PSR1 does appear to have physical significance. The residence time in PSR1 is of the same order of magnitude as the chemical time (shown in Figure 4.12). In addition, the high rate of formation of NO<sub>x</sub> in PSR1 is representative of the flame zone, whereas the slow burnout in PSR2 is representative of the post-flame zone. In cases for

which a single PSR models the data, the NO<sub>x</sub> formation rates are high in the entire reactor volume, simulating spreading of the flame and high concentrations of O-atom, CO, and other reacting species, throughout the HP-JSR.

The disadvantage of the two-PSR model is that it does not capture high CO levels that are measured at the reactor walls in the low residence time cases. Using a single PSR to model data at these conditions suggests homogeneous species concentrations, which is not the case according to the CO and NO<sub>x</sub> HP-JSR reactor profiles.

The HP-JSR researchers Steele (1995) and Bengtsson et al. (1998) have modeled the experimental data by using the chemical reactor model. Both have found that using two PSR's in series, first to represent the flame zone and the second the burnout zone, gives the best match to the experimental data. Steele has sized reactors to match the CO concentrations in the "high-CO" and "low-CO" zones. His work was done at high residence time (2-4 ms) with preheated inlet, so the reactor at these regimes was certainly experiencing a flame confined to the region around the inlet jet. In his work,  $V_{\text{PSR1}}/V_{\text{total}} \cong 5\text{-}10\%$ , which is consistent with the present findings that measured NO<sub>x</sub> and CO levels are best predicted using low volume ratios for  $V_{\text{PSR1}}/V_{\text{total}}$ .

Bengtsson et al. (1998) have added a PFR to the two PSR's to represent reactions in the flow that exits the reactor prior to entering the probe positioned in the exit pipe. The reactor sizes were determined by matching measured and predicted CO levels at all studied conditions and atmospheric extinction limits using the Bockhorn mechanism. The optimum volume partition in this work was 30% PSR1, 60% PSR2 and 10% PFR for residence times between 1.0 and 2.0 ms. The turbulent flow characteristics in the reactor

used by Bengtsson et al. (1998), i.e., the integral length scale, the multiple jets, the size of the reactor, were very different from the present work. In addition, Bengtsson et al. (1998) used a different chemical kinetic mechanism and measured species outside the reactor, where sufficient time was allowed for chemical conversion (namely CO oxidation to CO<sub>2</sub>), thus making it even more difficult to compare to the present work. Configurations other than PSR+PSR+PFR were explored in their work, as well, but without successful results. For example, they explored the addition of the recycle of the exit from the second PSR back into the first, which did not result in the significant reduction of high CO concentrations in the first PSR. Steele (1995) has independently arrived to the same conclusion regarding recycling. This is easily explained by the fact that the exhaust of the second PSR contains very little reactive species that could oxidize the CO. Bengtsson et al. (1998) have also explored the effect of different chemical kinetic mechanisms, and found that best match to the NO<sub>x</sub> data is not obtained by the GRI 2.11 mechanism – predecessor to the currently used GRI 3.0 (Smith et al., 1999), although this mechanism gives closest prediction of CO and N<sub>2</sub>O concentrations.

In summary, the two-PSR model was proven to give best results with respect to CO and NO<sub>x</sub> for both Steele (1995) and Bengtsson et al. (1998).

### ***4.3 Comparison of Turbulent Flame Thickness Model to Chemical Reactor Model***

This section is intended to combine the results obtained in Sections 4.2.1 and 4.2.2. The physical dimension of the flame, expressed as the flame thickness,  $\delta_T$ , calculated in Section 4.2.1.3, is related to the chemical kinetic solutions of the two-PSR model, i.e., to the sizes of the two PSR's, which are shown in section 4.2.2. The goal is to find a comprehensive model of NOx formation for the lean-premixed flame in the high-pressure jet-stirred reactor. This model is then used in Section 4.4 for the further explanation of the chemical kinetics of NOx formation as a function of reactor conditions, i.e., residence time, pressure, and inlet temperature.

#### ***4.3.1 Determination of the Size of the Flame***

The percent of the reactor volume filled by the flame, calculated as  $V_{\text{flame}}/V_{\text{total}}$ , where  $V_{\text{flame}} = 5\pi\delta_T^3$  and  $V_{\text{total}} = 1.5\text{e-}6 \text{ m}^3$  (section 4.2.1.3) varies with residence time, pressure, and inlet temperature. Figure 4.27 depicts  $V_{\text{flame}}/V_{\text{total}}$  applied to the 6.5 and the 3.0 atm cases without preheated inlet. The volume ratio  $V_{\text{PSR1}}/V_{\text{total}}$  is superimposed for the same conditions in Figure 4.21. By comparing Figures 4.21 and 4.27, it can be seen that the  $V_{\text{PSR1}}/V_{\text{total}}$  and  $V_{\text{flame}}/V_{\text{total}}$  curves are qualitatively similar. For all three pressures considered, and for both preheated and unheated cases, when height  $h$  of the unreacted core becomes approximately 18 mm, which is just below the height of the reactor cavity (20.2 mm), the turbulent flame thickness  $\delta_T$  is 3.6 mm and thus  $V_{\text{flame}} \cong 0.75 \text{ cm}^3$ . This is one-half the reactor volume. Comparison to the two PSR modeling shows this condition

closely corresponds to the sharp transition from  $V_{\text{PSR1}}/V_{\text{total}} = 100\%$  to  $V_{\text{PSR1}}/V_{\text{total}} < 10\%$  where the Damköhler number at transition is  $Da \cong 0.15$ .

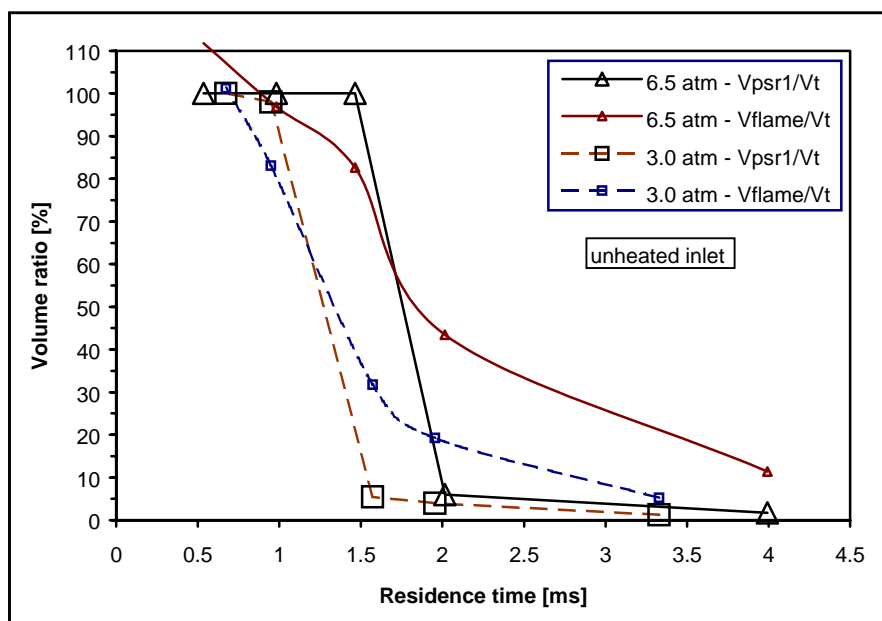


Figure 4.27 Ratio of PSR1 volume to the total volume ( $V_{\text{psr1}}/V_t$ ), corresponding to the best match between the measured and modeled data, and ratio of flame volume to the total volume ( $V_{\text{flame}}/V_t$ ), estimated by turbulent premix combustion correlations, plotted versus reactor residence time. The pressures are 6.5 and 3.0 atm and there is no preheat

The sharp decrease of  $V_{\text{flame}}/V_{\text{total}}$  at intermediate residence times, (i.e., 1 to 2 ms), is noted in Figure 4.27, and is caused by a decrease in  $\delta_T$ . The 3.0 atm case undergoes the transition at a smaller residence time than the 6.5 atm case. The 3.0 atm flame has a greater  $Da$  than the 6.5 atm flame, and hence, a smaller thickness. In order for the 3.0 atm flame to fill the reactor, the reactor must operate at a lower residence time than for the 6.5 atm case. Also, the 3.0 atm case shows closer agreement between the flame thickness modeling and the two PSR modeling, probably because its fuel-air equivalence

ratio, and hence  $Da$ , change significantly between low residence times ( $\phi=0.7$ ) and large residence times ( $\phi=0.8$ ).

Similar behavior to that shown in Figure 4.27 for the unheated cases is also noted for the preheated cases. The preheated results are shown in Figure 4.28 for all three pressure levels. The Damköhler number is higher for the preheated cases because the chemistry is faster than for the unheated cases. Thus, a lower residence time is required for transition. For the case of the preheated inlet and 3.0 atm, no transition to single PSR behavior occurs. That is, throughout the range of residence times studied, the reactor remains a small PSR for the flame zone and is followed by a large PSR for the stirred post-flame zone.

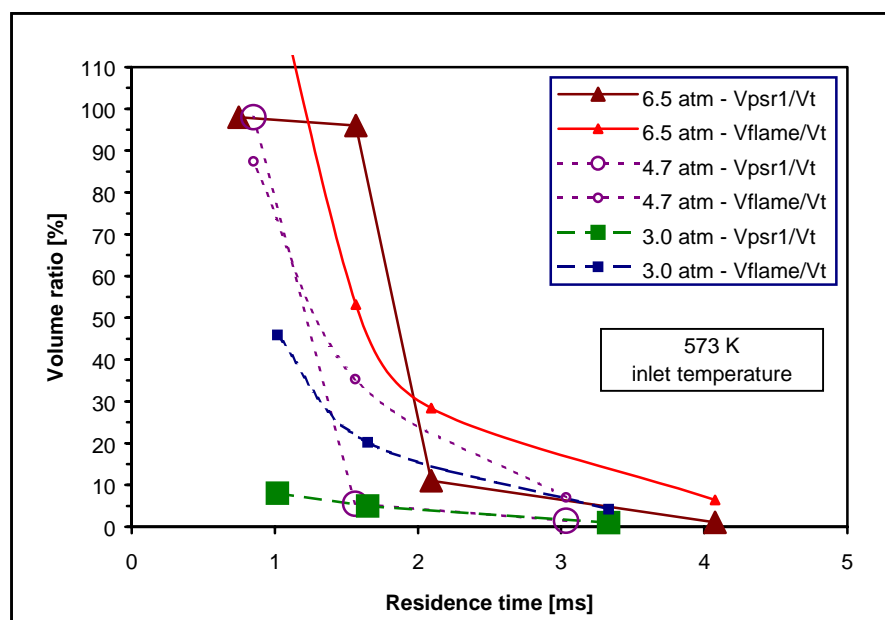


Figure 4.28 Ratio of PSR1 volume to the total volume ( $V_{psr1}/V_t$ ), corresponding to the best match between the measured and modeled data, and ratio of flame volume to the total volume ( $V_{flame}/V_t$ ), estimated by turbulent premix combustion correlations, plotted versus reactor residence time. The pressures are 6.5, 4.7 and 3.0 atm and reactants are preheated to 573 K

The model points to two-mode behavior in the reactor. At low residence times, the necessary and sufficient conditions for combustion in a well-stirred reactor, defined in Section 4.2.1.3, are reached, so the reactor is modeled as a single-PSR. At long times, the flame remains confined to a part of the reactor (less than 10% volume), so the reactor is modeled with a two-PSR model. The PSR is used because the Damköhler number is low ( $Da < 1$ ). The flame is modeled as PSR1 and the rest of the reactor, or post-flame zone, is modeled as PSR2. The NO<sub>x</sub> forms in both the flame and in the stirred post-flame zone, but the kinetics for its formation are significantly different in the two zones. Therefore, single- and two-PSR cases are analyzed separately in the following sections.

#### ***4.4 Chemical Kinetic Results***

The chemical kinetics of the NO<sub>x</sub> formation in the HP-JSR are analyzed for the single-PSR and the two-PSR cases separately. Section 4.4.1 analyzes kinetics of NO<sub>x</sub> formation for the single-PSR (low residence time) cases, whereas Section 4.4.2 analyzes kinetics of NO<sub>x</sub> formation for the two-PSR (long residence time) cases. At the end of each section, the kinetic analysis is applied to explain the experimental trends. In Section 4.4.2, the kinetics in PSR1 are analyzed separately from the PSR2, but at the end of the section, both are combined to explain the experimental trends.

#### 4.4.1 Kinetics of NO<sub>x</sub> Formation in Single-PSR (Short Residence Time) Cases

As shown above, the entire HP-JSR can be modeled as a single-PSR for several of the short residence time experiments. For these cases, chemical kinetic modeling can be conveniently used to assess the relative importance of the several pathways that can form NO<sub>x</sub>. These pathways are discussed in Chapter 2.

Each NO<sub>x</sub> formation pathway exchanges species that form NO<sub>x</sub> with two or more other pathways. For example, N-atom, which oxidizes into NO primarily through the second and third Zeldovich reactions, i.e., Equations 2.2 and 2.3, is formed via the first Zeldovich reaction (Equation 2.1), the prompt reaction (Equation 2.10), as well as through a series of reactions involving short-lived species such as NH and CN.

However, the maximum contribution of each pathway is easily estimated. The present work uses the following estimates based on the discussion by Nicol et al. (1994). The maximum contribution from the Zeldovich pathway is  $(dNO/dt)_{Zeld} = 2 k_{2.1} [O] [N_2]$ ; from the nitrous oxide pathway it is  $(dNO/dt)_{N_2O} = 2 k_{2.5} [O] [N_2O] + 2 k_{2.7} [H] [N_2O]$ ; from the prompt pathway it is  $(dNO/dt)_{prompt} = 2 k_{2.10} [CH] [N_2]$ ; and, from the NNH pathway it is  $(dNO/dt)_{NNH} = 2 k_{2.12} [O] [NNH]$ .

The NO computed using the above rate equations for each pathway and multiplied by the residence time in the PSR is plotted in Figures 4.29-4.32 as a percent of the total NO, or the sum of the four pathways shown. Table 4.2 contains the information used in the analysis for single-PSR cases, for the three pressures without preheat, and for 6.5 atm with 573 K preheat. The experimental conditions, i.e., the residence time, gas temperature, and fuel-air equivalence ratio, are presented first. The measured NO<sub>x</sub>

[ppmv, wet] is also included for comparison with the modeling results. The next section of Table 4.2 contains PSR output (with full mechanism) for O-atom, CH, H, NNH, N<sub>2</sub>O, N<sub>2</sub>, and NO, expressed in [ppmv, wet]. The next section of Table 4.2 contains the values of the NO in [ppmv, wet] that are formed via the Zeldovich, nitrous oxide, prompt and NNH pathways, as well as the sum of the NO formed by the four pathways. The sum of NO formed by the four pathways equals the NO formed by the full mechanism within  $\pm 5\%$ . The last row is the NO formation rate, which is calculated as the NO mole fraction in [ppmv, wet] from the PSR output divided by the reactor residence time in [ms]. The values in the table are taken from the spreadsheet shown in Appendix D. Appendix D also contains plots of O-atom and CH-radical concentration versus reactor overall residence time, which are not included in the text, but are nevertheless useful.

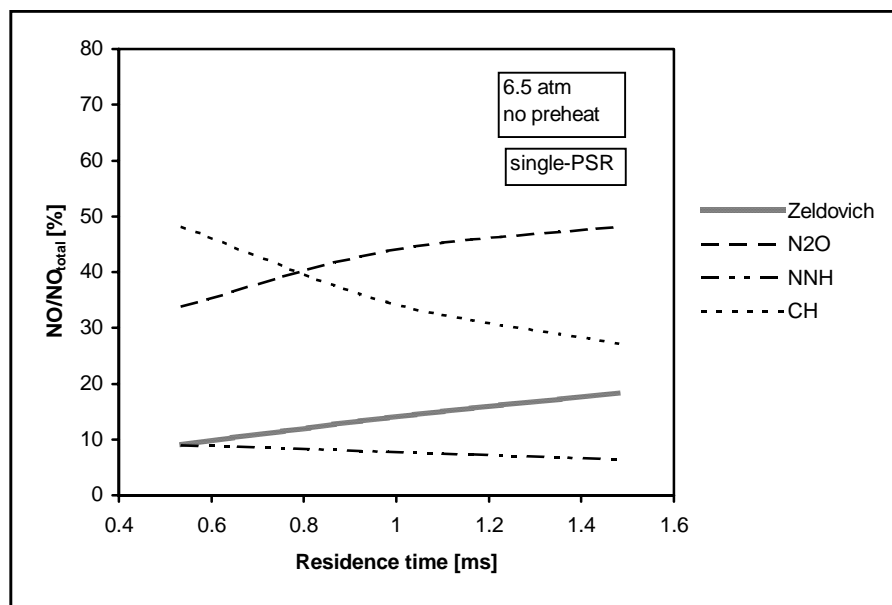


Figure 4.29 Percent of the NO formed by each of the four pathways in a single-PSR at 6.5 atm and without preheat

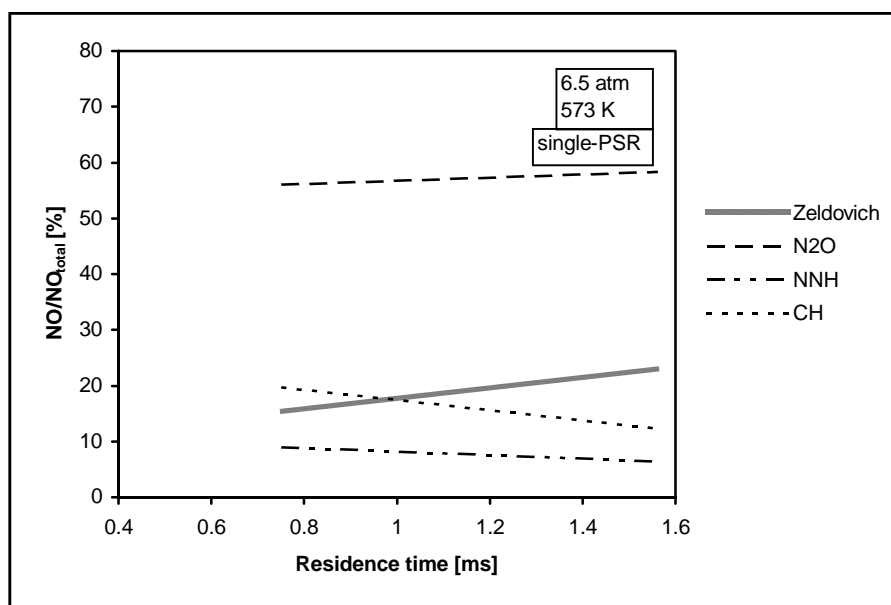


Figure 4.30 Percent of the NO formed by each of the four pathways in a single-PSR at 6.5 atm with 573K preheat

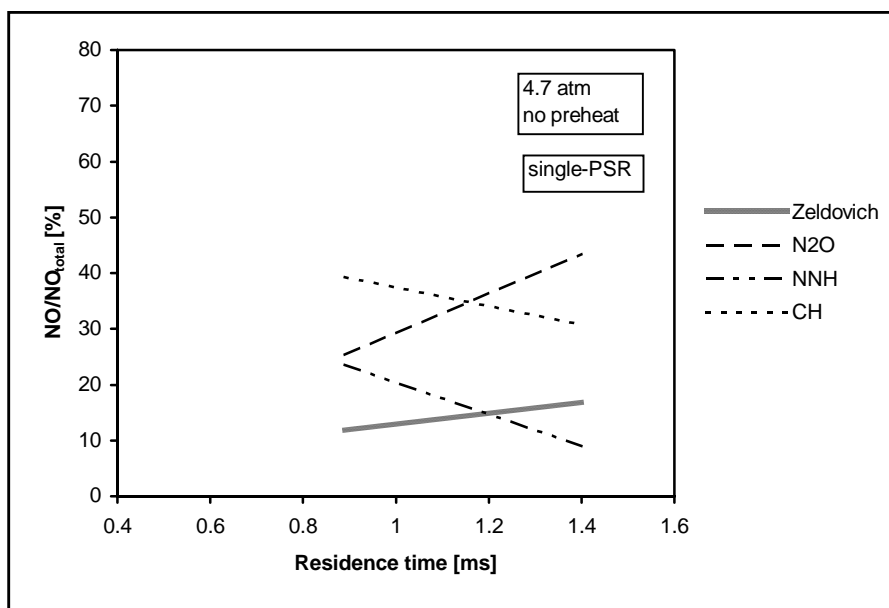


Figure 4.31 Percent of the NO formed by each of the four pathways in a single-PSR at 4.7 atm without preheat

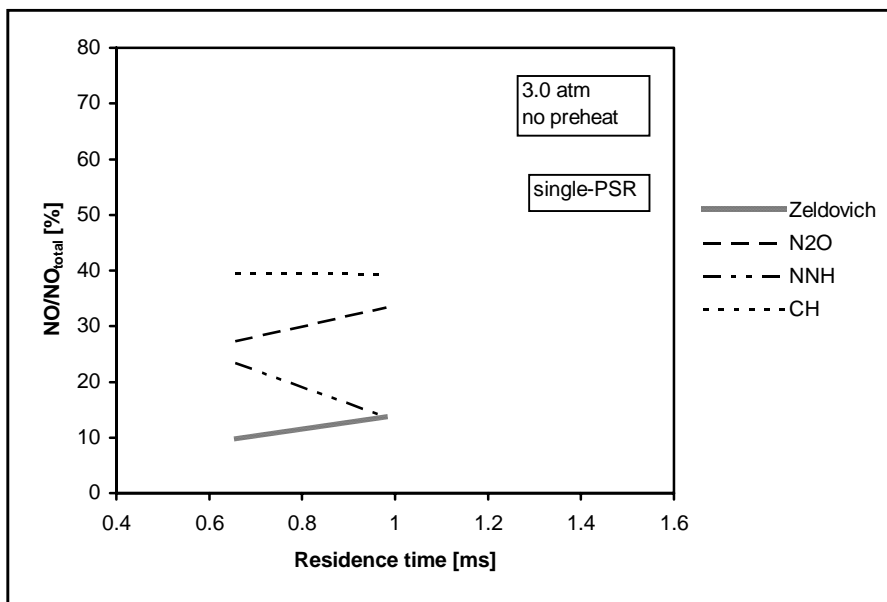


Figure 4.32 Percent of the NO formed by each of the four pathways in a single-PSR at 3.0 atm without preheat

Table 4.2 Numerical results for single-PSR model. ([ppmw] denotes [ppmv, wet].)

		6.5 atm unheated			6.5 atm preheated		4.7 atm unheated		3.0 atm unheated	
Experimental Data	Residence time [ms]	<b>0.54</b>	<b>0.98</b>	<b>1.48</b>	<b>0.74</b>	<b>1.56</b>	<b>0.89</b>	<b>1.40</b>	<b>0.66</b>	<b>0.98</b>
	Temperature [K]	1820	1825	1830	1805	1825	1819	1829	1804	1820
	Fuel-Air Equiv. Ratio	0.74	0.71	0.67	0.57	0.59	0.72	0.69	0.70	0.69
	Measured NO <sub>x</sub> [ppmw]	12.0	9.1	9.6	6.1	7.2	10.3	8.8	11.3	10.3
Mole fraction [ppmw]	O	305	221	178	252	173	369	288	789	652
	CH	0.017	0.006	0.003	0.003	0.001	0.013	0.006	0.03	0.02
	H	130	66	40	50	28	130	80	344	240
	NNH	0.001	0.0006	0.0004	0.0005	0.0003	0.002	0.0006	0.002	0.001
	N <sub>2</sub> O	1.64	1.82	1.87	2.33	2.07	1.07	1.61	1.07	1.18
	N <sub>2</sub>	730200	733700	73670	743700	743000	732700	734800	732300	734200
	NO	11	10	9.6	6.4	8	11.6	11.7	12.6	13
NO [ppmv, wet]	Zeldovich NO	1.00	1.41	1.82	1.00	1.78	1.44	1.98	1.24	1.82
	Nitrous NO	3.76	4.44	4.78	3.67	4.49	3.11	5.13	3.44	4.40
	Prompt NO	5.34	3.51	2.70	1.29	0.94	4.84	3.62	4.99	5.19
	NNH NO	1.00	0.79	0.64	0.58	0.49	2.89	1.06	2.95	1.80
	SUM NO	11.09	10.14	9.92	6.54	7.70	12.29	11.80	12.62	13.21
	NO formation rate [ppm/ms]	20.5	10.2	6.5	8.5	5.1	13.1	8.4	19.1	13.3

Figures 4.29-4.32 show that the dominant pathways for NO<sub>x</sub> formation in lean-premixed combustion without preheat, for residence times corresponding to the single-PSR solution, are the prompt (designated by “CH” in the figures) and the nitrous oxide pathways. The latter is dominant for preheated cases, and yields about 56-58% of the NO. The prompt pathway is, however, important for the cases with the unheated inlet. The prompt pathway’s maximum contribution of 48% of the NO occurs at 0.53 ms and

6.5 atm. The contribution from the Zeldovich pathway is secondary because of the relatively low temperature of the experiments. The NNH pathway's contribution is secondary, as well. The Zeldovich and NNH pathways add up to 33% of the total NO for all cases.

The NO formed by the prompt and NNH pathways decreases with increasing residence time, except for the 3.0 atm case, for which prompt NO is insensitive to the residence time. The prompt NO decreases because of a significant drop in [CH] with residence time. The NO formed by NNH decreases because both [NNH] and [O] decrease with increasing residence time.

The CH-radical is a short living species in flames, so the only way to capture it's existence in a PSR is if the PSR residence time is short. Figure 4.33 depicts [CH] versus PSR residence time for single-PSR cases. (Figure D.2 in Appendix D shows [CH] versus PSR residence time for all cases.) Figure 4.33 shows how the [CH] decreases an order of magnitude from 0.5 to 1.5 ms. The [CH] dependency on fuel-air equivalence ratio, pressure, temperature, and inlet temperature conditions is secondary to the strong decrease with residence time.

The NO formed by the nitrous oxide and Zeldovich pathways increases with residence time. The nitrous oxide NO and Zeldovich NO increase with residence time because the time available to form NO increases and overcomes decreases in [O] and [H]. Temperature is nearly constant at these low residence times. The decrease of O-atom with residence time is plotted in Figure 4.34 for the single-PSR cases. (Figure D.1 in Appendix D shows [O] versus PSR residence time for all cases.) It is apparent that the

decrease in O-atom with residence time is significantly weaker than the decrease in [CH], shown in Figure 4.33. O-atom also decreases with pressure, but the inlet temperature does not influence it.

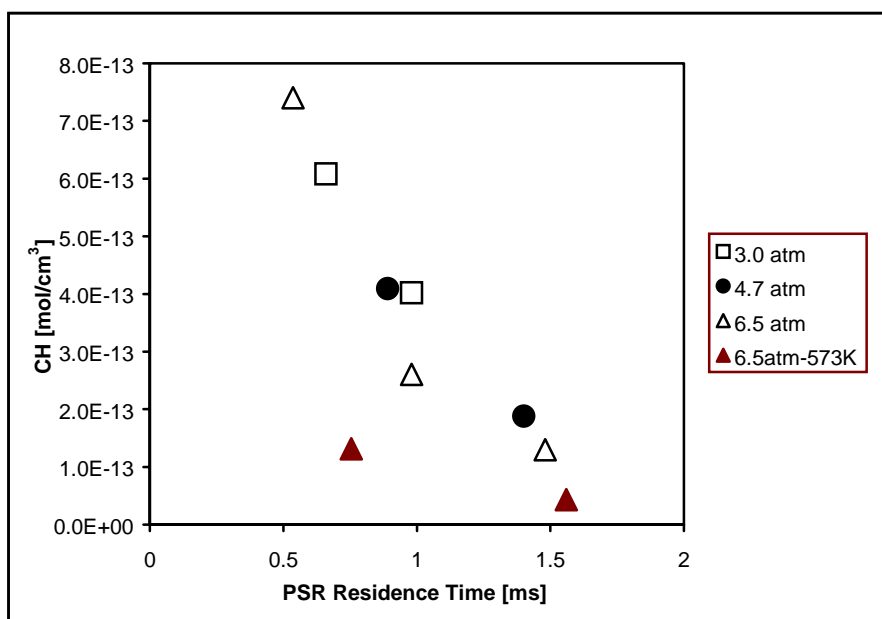


Figure 4.33 Concentration of CH radical versus reactor residence time for single-PSR cases

The absolute value of NO<sub>x</sub> formation from each of the four pathways, the sum of the NO<sub>x</sub> formed by all four pathways, the modeled NO and the experimentally measured NO<sub>x</sub>, are shown in Figures 4.35-4.38 at the end of the section.

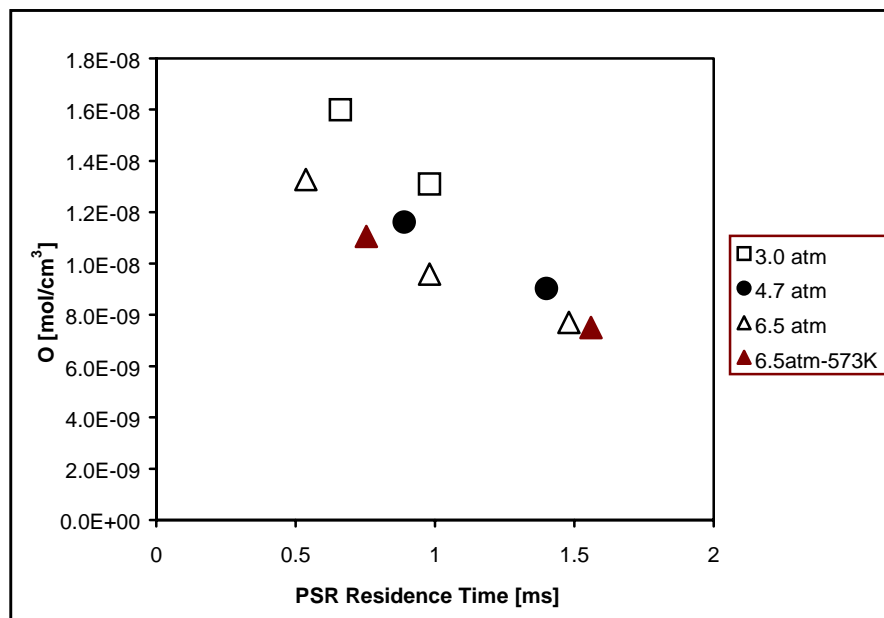


Figure 4.34 Concentration of O-atom versus reactor residence time for the single-PSR cases

Results from the chemical kinetic modeling explain the following experimental trends when the reactor is operating in single-PSR mode (residence time from 0.5 to 1.6 ms):

1. The fall-off in measured NO<sub>x</sub> with increasing residence time for unheated cases (Figure 3.10) is consistent with the decrease of the NO formed by the prompt and the NNH pathways at the lowest residence times. At 6.5 atm, the prompt contribution to NO formation decreases from 48% at 0.54 ms to 27% at 1.48 ms. This decrease is promoted by the sharp decrease (5.7 times) in [CH] (Figure 4.33). Furthermore, since [NNH] decreases 2.5 times and [O] decreases 1.7 times, the contribution of the NNH pathway to NO formation decreases from 9 to 6%. The Zeldovich contribution increases from 9 to 18% primarily due to the increase in

residence time. The NO yield by the nitrous oxide pathway increases from 34 to 48% between 0.54 and 1.48 ms residence time, but has little overall effect on total NO<sub>x</sub> yield. At 3.0 atm, the predominant pathway is the prompt, which remains constant at 40% NO yield between residence times of 0.66 and 0.98 ms. This behavior occurs because the decrease in [CH] by factor 1.5 through this residence time range is cancelled by the increase in time to form NO. In spite of the decrease in both the [O] and the [H] by factors 1.2 and 1.4, respectively, the NO-yield from the nitrous oxide pathway increases from 27 to 33% due to an increase in time and [N<sub>2</sub>O]. Zeldovich NO also slightly increases, whereas the NO yield from the NNH-pathway decreases from 23 to 14% primarily because of the 50% decrease in [NNH].

2. The decrease in NO<sub>x</sub> obtained by preheating the inlet air is consistent with a diminished influence of the prompt pathway, since the absolute yield of NO by the other three pathways is similar between the unheated and preheated cases (compare Figures 4.35 and 4.36). [O] is nearly insensitive to preheat, while [H] and [NNH] decrease slightly and [N<sub>2</sub>O] increases slightly. [CH] decreases significantly, because of the decrease in the fuel-air equivalence ratio, causing the prompt pathway to contribute only 12 to 20% of the NO. The nitrous oxide pathway is predominant, yielding 56-58% of the total NO. The Zeldovich pathway yields 15-23% of the NO, and the NNH pathway yields 6-9%. The measured increase in NO<sub>x</sub> of only 1.1 ppmv, wet between 0.74 and 1.56 ms at 6.5 atm (with the inlet preheated to 573 K) is explained by the small increase of only 2% in NO formed by the nitrous oxide pathway, as well as by the small increases in NO formed by the three other pathways.

3. The small increase in NO with decreasing pressure observed in the experiments is explained by the following. [O], [H], [NNH], and [CH] increase with decreasing pressure, while [N<sub>2</sub>O] decreases. Thus, the absolute yields of the NO formed by the prompt and the NNH pathways increase with decreasing pressure, whereas the absolute yields of NO formed by the nitrous oxide and Zeldovich pathways remain relatively constant with pressure. The increase of prompt NO from 3.5 to 5.2 ppmv, wet at 1.0 ms between 6.5 and 3.0 atm explains the measured small increase in NOx with decreasing pressure.

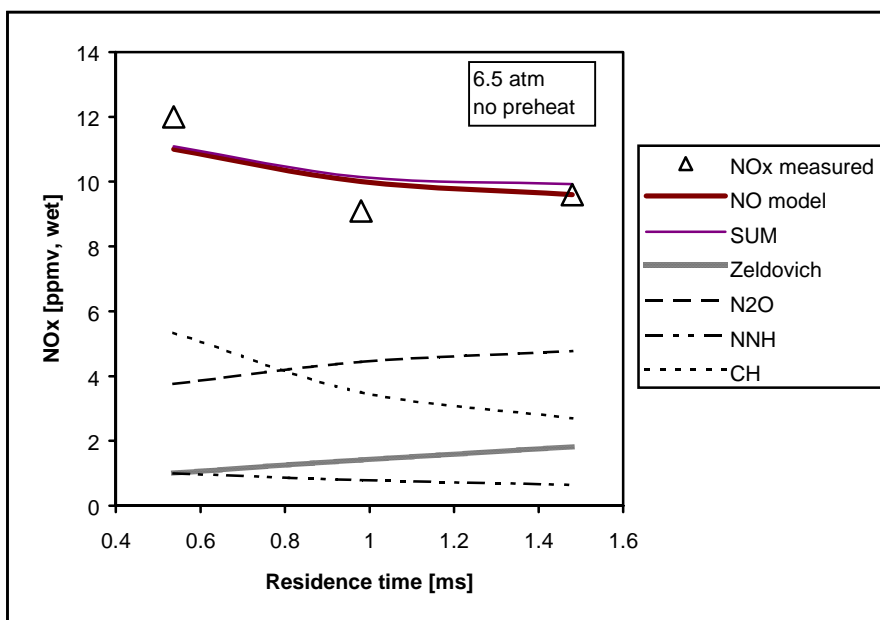


Figure 4.35 Absolute value of the NO formed by each of the four pathways in a single-PSR at 6.5 atm and without preheat. Also shown is the sum of the NOx formed by the four pathways, the NO from the PSR output (NO model) and the measured NOx

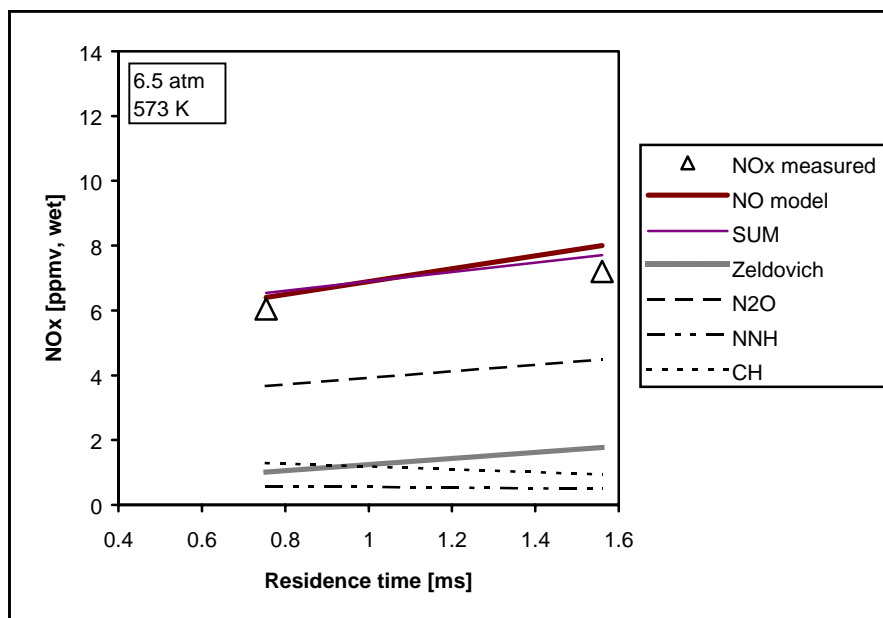


Figure 4.36 Absolute value of the NO formed by each of the four pathways in a single-PSR at 6.5 atm and 573 K preheat. Also shown is the sum of the NOx formed by the four pathways, the NO from the PSR output (NO model) and the measured NOx

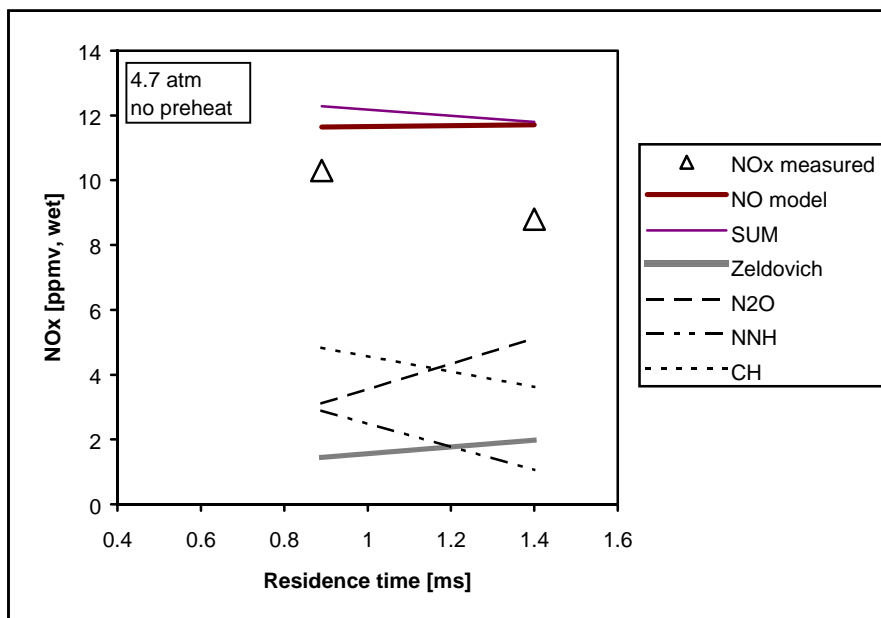


Figure 4.37 Absolute value of the NO formed by each of the four pathways in a single-PSR at 4.7 atm and without preheat. Also shown is the sum of the NOx formed by the four pathways, the NO from the PSR output (NO model) and the measured NOx

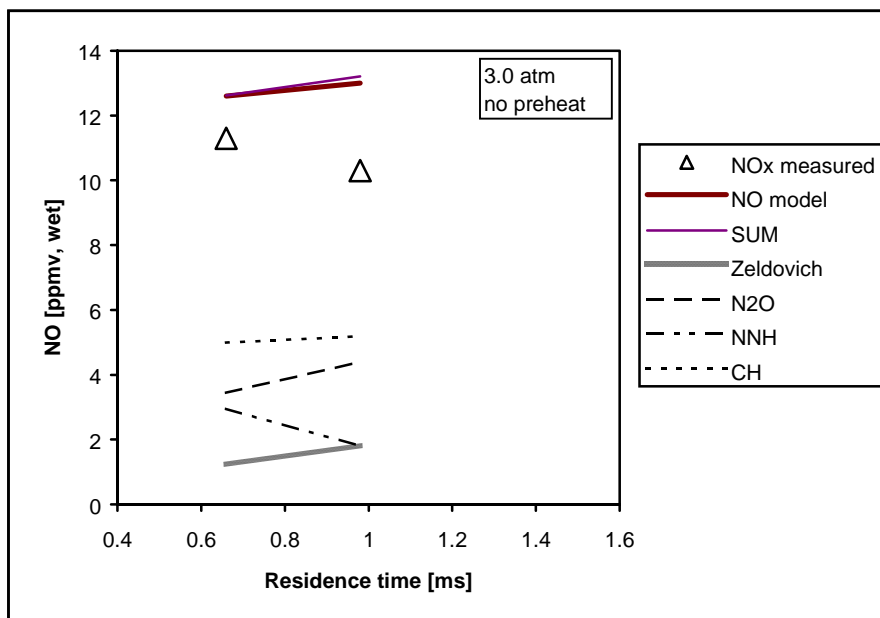


Figure 4.38 Absolute value of the NO formed by each of the four pathways in a single-PSR at 3.0 atm and without preheat. Also shown is the sum of the NOx formed by the four pathways, the NO from the PSR output (NO model) and the measured NOx

#### 4.4.2 Kinetics of NOx Formation in Two-PSR (Long Residence Time) Cases

Results from the chemical kinetic modeling applied to higher residence time cases, where the reactor is modeled as a small PSR1 followed by a large PSR2, indicate that (depending on conditions and overall residence times), 16 to 53% of NO forms in PSR2. This percentage increases with increasing overall residence time and with decreasing pressure. When the modeling results for all three pressures, with unheated and preheated inlets, are combined, the following conclusions can be made: at 2 ms,  $26 \pm 10$  % of the modeled NO forms in PSR2, whereas at 4 ms, the value is  $46 \pm 7$  %. The increase of the percentage of the NO formed in the PSR2 with increasing overall residence time is

caused by the increase in both overall time and temperature in PSR2. The increase of the percentage of NO formed in the PSR2 with decreasing pressure is a consequence of increasing O-atom levels in the PSR2 with decreasing pressure, as well as higher gas temperatures at the lower pressures. The predominant pathways for NO<sub>x</sub> formation in PSR2 are the Zeldovich and nitrous oxide pathways. The prompt and NNH pathways yield less than 5% NO each, due to low concentrations of CH and NNH. The Zeldovich contribution increases with residence time due to higher gas temperatures, offsetting contribution of the nitrous oxide pathway. The information used in the analysis of the two-PSR cases, for the three pressures without preheat, and for 6.5 atm with 573 K preheat is contained in Tables 4.3a and 4.3b below, as well as in the spreadsheet of Appendix D. The contributions of the four pathways that form the NO in PSR2 are plotted in Figures 4.39-4.42, for the case of unheated inlet at all pressures and the case of the heated inlet at 6.5 atm. The sum of the NO formed by the four pathways is up to 8.4% higher than the NO formed by the full mechanism in PSR1, whereas the difference between the sum and the full mechanism for NO in PSR2 is  $\pm 2.5\%$ .

The summary of the results for PSR2 follow:

1. For 2 ms overall residence time, about 25% of the NO<sub>x</sub> forms in PSR2. For the unheated inlet cases, and at all pressures, about 50% is from the nitrous oxide pathway and 50% from the Zeldovich pathway. For the preheated inlet case, the Zeldovich pathway is favored over the nitrous oxide pathway.

2. For 4 ms overall residence time, about 50% of the NO<sub>x</sub> forms in PSR2. Both the Zeldovich and nitrous oxide pathways contribute to NO<sub>x</sub>. However, the Zeldovich NO is favored.

Table 4.3a Numerical results for two-PSR model (for 6.5 atm). ([ppmw] denotes [ppmv, wet].)

		6.5 atm unheated				6.5 atm preheated			
Experimental Data	Overall residence time [ms]	2 ms		4 ms		2 ms		4 ms	
	PSR number	PSR1	PSR2	PSR1	PSR2	PSR1	PSR2	PSR1	PSR2
	Residence time in PSR <sub>x</sub> [ms]	<b>0.126</b>	<b>1.897</b>	<b>0.0695</b>	<b>3.833</b>	<b>0.231</b>	<b>1.847</b>	<b>0.045</b>	<b>3.892</b>
	Temperature [K]	1757	1836	1748	1880	1820	1840	1764	1884
	Fuel-Air Equivalence Ratio	0.7		0.73		0.6		0.66	
	Measured NO <sub>x</sub> [ppmv, wet]	7.5		10.3		6.2		8.8	
Mole fraction [ppmw]	O	518	53	569	53	516	44	750	60
	CH	0.05	5e-5	0.12	2e-5	0.016	5e-6	0.13	2e-5
	H	303	5.7	474	6.0	159	2.8	535.4	5.5
	NNH	0.003	6e-6	0.004	6e-5	0.002	3e-5	0.005	6e-5
	N <sub>2</sub> O	1.33	1	0.95	0.78	2.1	0.9	1	0.87
	N <sub>2</sub>	730400	735700	724800	733300	739800	742700	728900	738200
	NO	5.5	7.3	5.4	9.6	6.8	8.1	4.3	9.2
NO [ppmv, wet]	Zeldovich NO	0.20	0.74	0.11	2.36	0.74	0.63	0.11	2.85
	Nitrous NO	1.19	0.71	0.65	1.30	2.82	0.44	0.55	1.57
	Prompt NO	3.07	0.06	3.93	0.05	2.19	0.01	2.91	0.05
	NNH NO	1.24	0	1.00	0.07	1.45	0.01	1.06	0.08
	SUM NO	5.69	1.51	5.69	3.79	7.2	1.09	4.63	4.56
NO formation rate [ppmv, wet/ms]	43.7	3.8	77.7	2.5	29.4	4.4	95.6	2.4	

Table 4.3b Numerical results for two-PSR model (for 4.7 and 3.0 atm). ([ppmw] denotes [ppmv, wet].)

		4.7 atm unheated				3.0 atm unheated			
<b>Experimental Data</b>	<b>Overall residence time [ms]</b>	2.0 ms		3.6 ms		2.0 ms		3.3 ms	
	PSR number	<b>PSR1</b>	<b>PSR2</b>	<b>PSR1</b>	<b>PSR2</b>	<b>PSR1</b>	<b>PSR2</b>	<b>PSR1</b>	<b>PSR2</b>
	<b>Residence time in PSRx [ms]</b>	<b>0.126</b>	<b>1.84</b>	<b>0.0704</b>	<b>3.391</b>	<b>0.08</b>	<b>1.78</b>	<b>0.0432</b>	<b>2.994</b>
	Temperature [K]	1704	1836	1739	1879	1716	1865	1734	1928
	Fuel-Air Equivalence Ratio	0.68		0.72		0.71		0.79	
	Measured NOx [ppmv, wet]	7.1		10.9		11.7		19.5	
<b>Mole fraction [ppmw]</b>	O	683	91	948	84.2	1591	224	1613	222
	CH	0.07	1e-6	0.2	5e-5	0.35	0.0002	1	0.0004
	H	424.1	11.2	777.7	11.3	1354	44.8	2113	60.4
	NNH	0.003	8e-5	0.005	8e-5	0.006	0.00021	0.0087	0.0003
	N <sub>2</sub> O	1	1.1	0.8	0.83	0.57	1.02	0.37	0.76
	N <sub>2</sub>	730700	737000	724600	733700	724100	734000	713000	728100
	NO	4.28	6.4	6.8	11.2	7.7	12.1	10.1	21.1
<b>NO [ppmv, wet]</b>	Zeldovich NO	0.10	0.89	0.12	2.38	0.11	1.83	0.07	5.72
	Nitrous NO	0.71	0.99	0.64	1.52	0.51	1.92	0.29	3.57
	Prompt NO	2.60	0.00	4.59	0.08	5.32	0.11	8.56	0.42
	NNH NO	1.21	0.06	1.54	0.10	2.28	0.23	1.79	0.53
	SUM NO	4.62	1.94	6.88	4.08	8.22	4.09	10.7	10.24
	NO formation rate [ppmv, wet/ms]	33.8	3.5	96.6	3.3	96	6.8	233.8	7.0

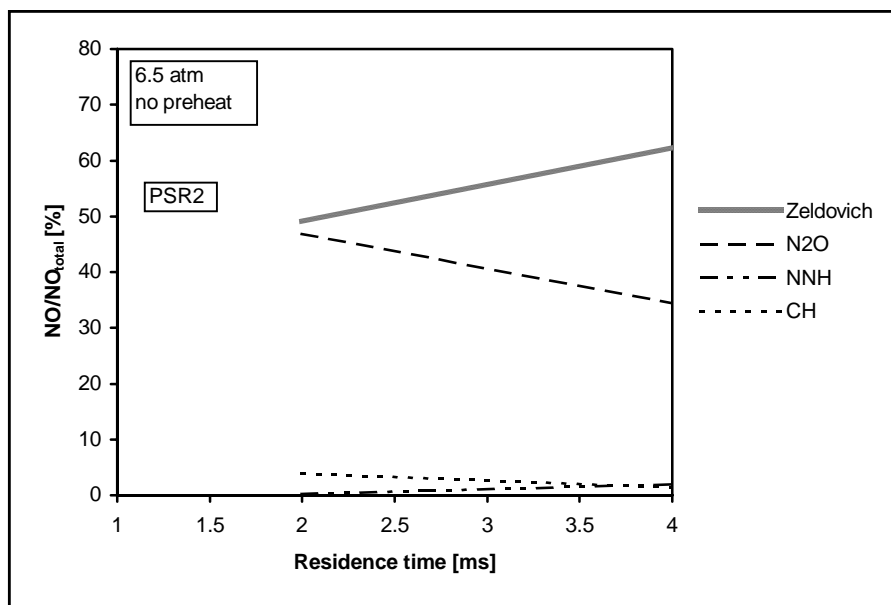


Figure 4.39 Percent of the NO formed by each of the four pathways in the PSR2 at 6.5 atm without preheat

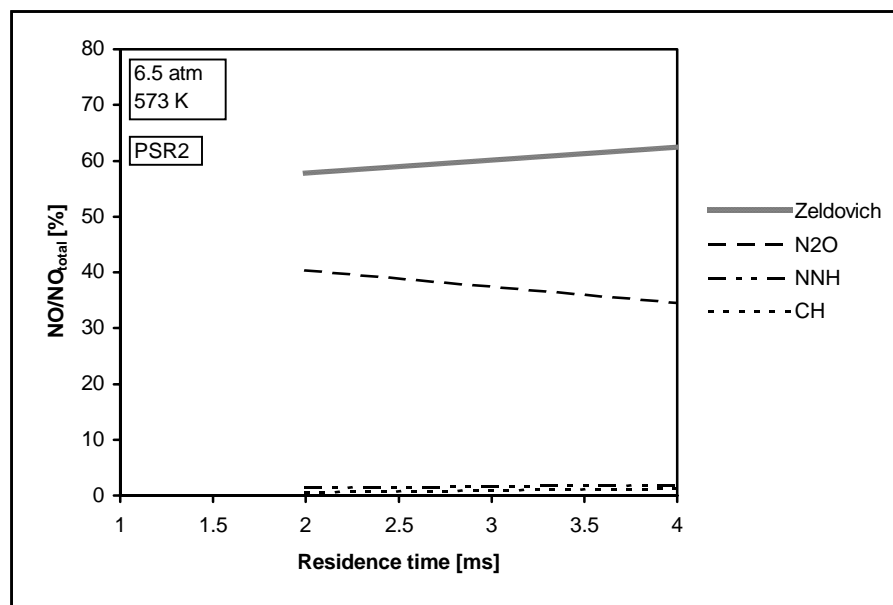


Figure 4.40 Percent of the NO formed by each of the four pathways in the PSR2 at 6.5 atm with 573 K preheat

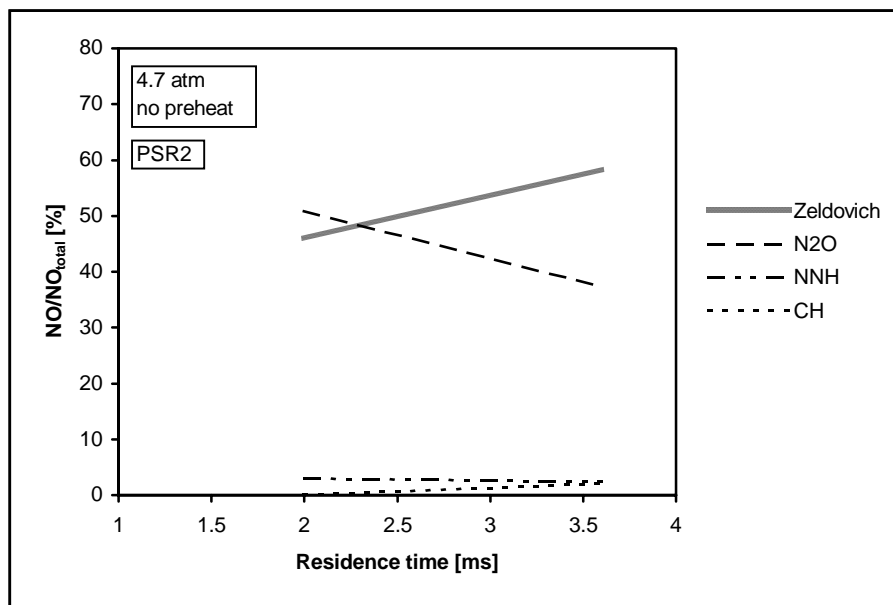


Figure 4.41 Percent of the NO formed by each of the four pathways in the PSR2 at 4.7 atm without preheat

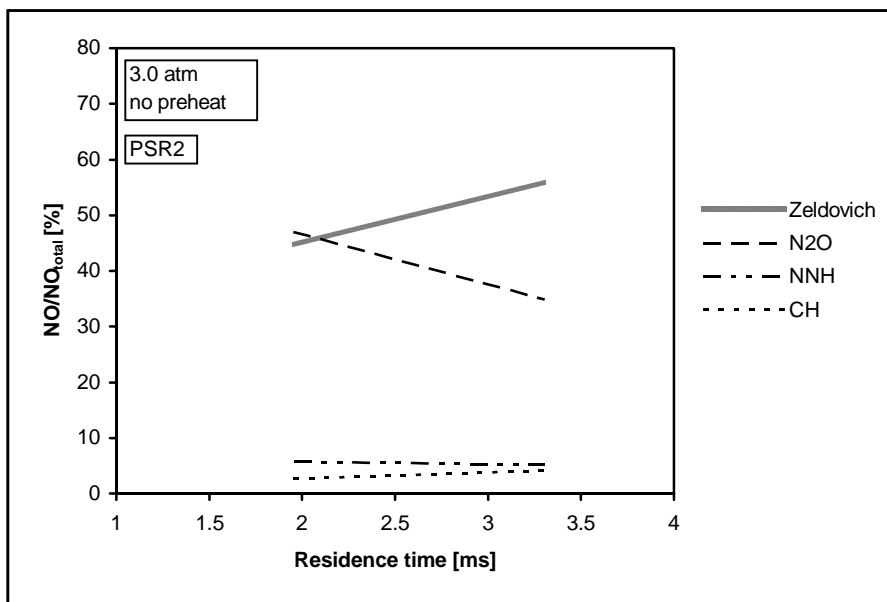


Figure 4.42 Percent of the NO formed by each of the four pathways in the PSR2 at 3.0 atm without preheat

For the residence time of 2 ms, the majority of the NO<sub>x</sub> forms in PSR1, whereas at 4 ms, the NO<sub>x</sub> split, about equally, between PSR1 and PSR2. For the cases considered herein, the O-atom is an order of magnitude higher in PSR1 compared to PSR2, [H] and [NNH] are two orders of magnitude higher, and [CH] is four to five orders higher. [N<sub>2</sub>O] decreases 15-30% between PSR1 and PSR2 at 6.5 atm (except for 2.0 ms with preheat where the decrease is 56%). However, at lower pressures [N<sub>2</sub>O] increases between PSR1 and PSR2. The highest increase in [N<sub>2</sub>O], which is 78%, is noted at 3.0 atm and 2.0 ms overall residence time. The rate of NO<sub>x</sub> formation is significantly higher in the PSR1, reaching a rate of 234 ppm/ms when the pressure is 3.0 atm and the overall residence time is 3.3 ms. The NO<sub>x</sub> formation rates in PSR1 and PSR2 are shown in Tables 4.3a and 4.3b. The rates in the PSR1 are compared to the rates in the single-PSR modeling in Figure 4.43. The PSR1 rates are plotted versus overall reactor residence time. It can be noted in Figure 4.43 that rates in PSR1 are larger than for the single-PSRs, in spite of lower temperatures. This is because the free-radical concentrations are significantly higher in PSR1, which is caused by the very short residence time of PSR1. (Note that PSR1 rates in Figure 4.43 are plotted versus overall reactor residence time and not PSR1 residence time.) As PSR residence time increases, there is more opportunity for free radical relaxation towards equilibrium.

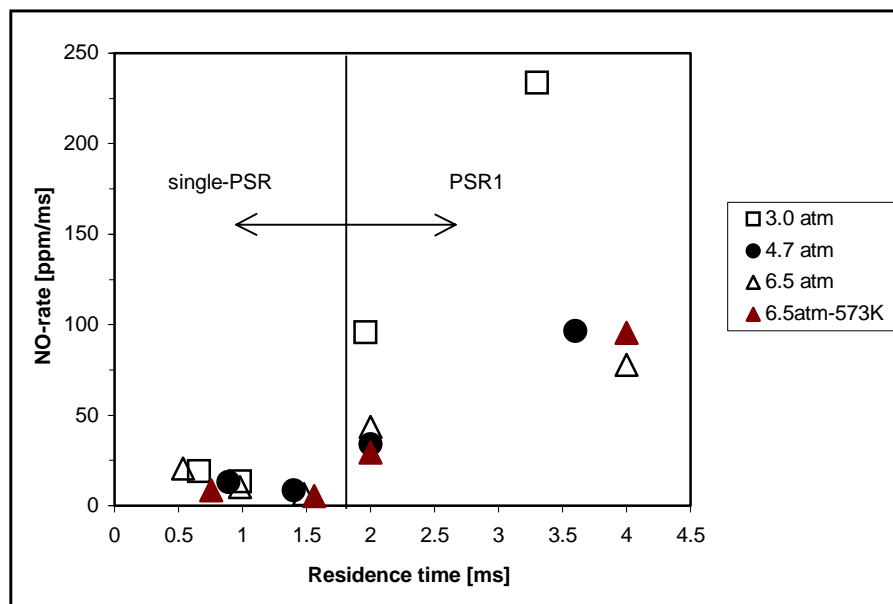


Figure 4.43 NO<sub>x</sub> formation rate versus overall residence time for three pressures with unheated inlet and for 6.5 atm and inlet preheated to 573 K. For residence times at 2.0 ms and above, the values correspond to the rates in corresponding PSR1

The contributions of the four pathways that form the NO in PSR1 are plotted in Figures 4.44-4.47, for the unheated inlet cases at all pressures and for the heated inlet case at 6.5 atm. The dominant pathway is the prompt pathway, responsible for the formation of up to 80% of the NO. The influence of the NNH-pathway is significantly increased compared to the single-PSR modeling and the PSR2 cases, contributing between 20 and 30% of the total NO. These effects occur because residence time in PSR1 is very short, causing high concentrations of short-living CH and NNH species. The influence of the nitrous oxide pathway is significantly diminished, and Zeldovich pathway contributes less than 10% of the NO in all cases.

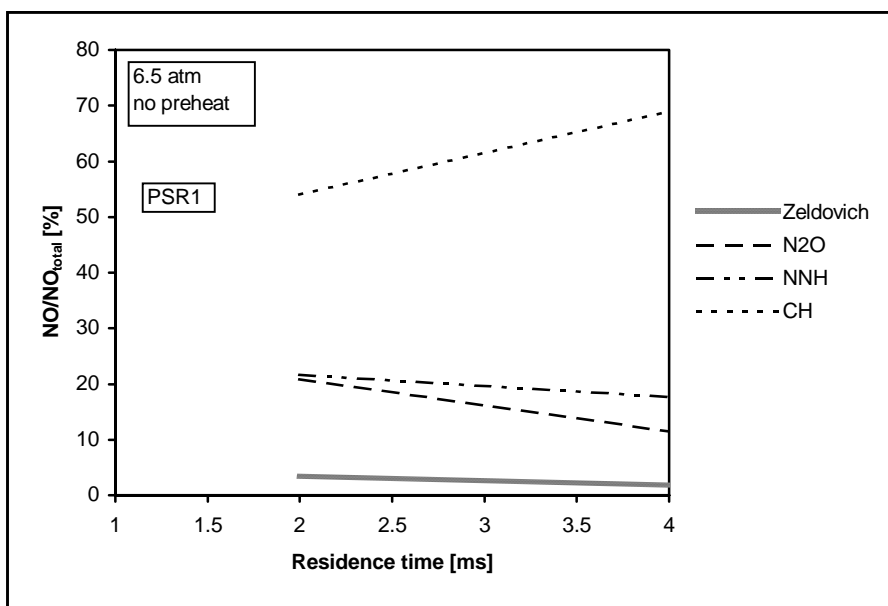


Figure 4.44 Percent of the NO formed by each of the four pathways in PSR1 at 6.5 atm without preheat

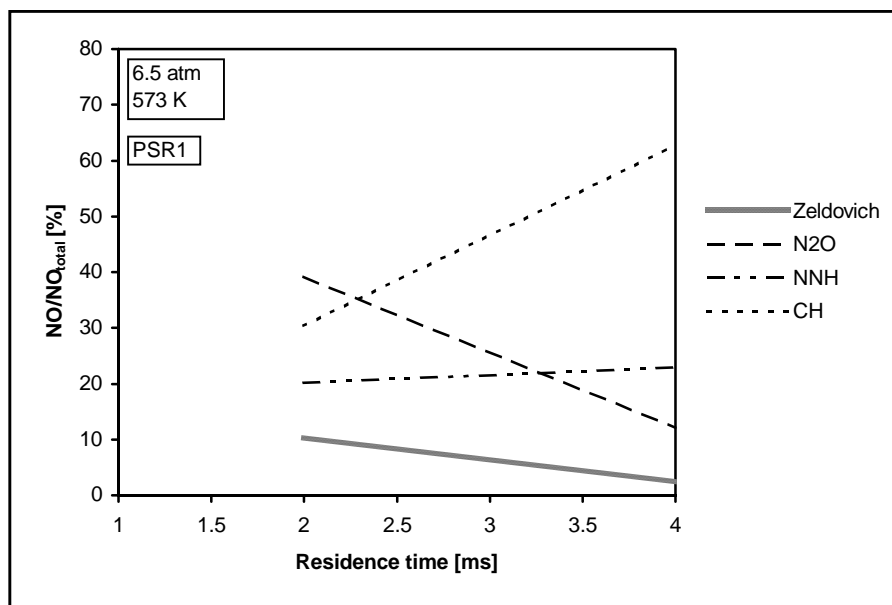


Figure 4.45 Percent of the NO formed by each of the four pathways in PSR1 at 6.5 atm with 573 K preheat

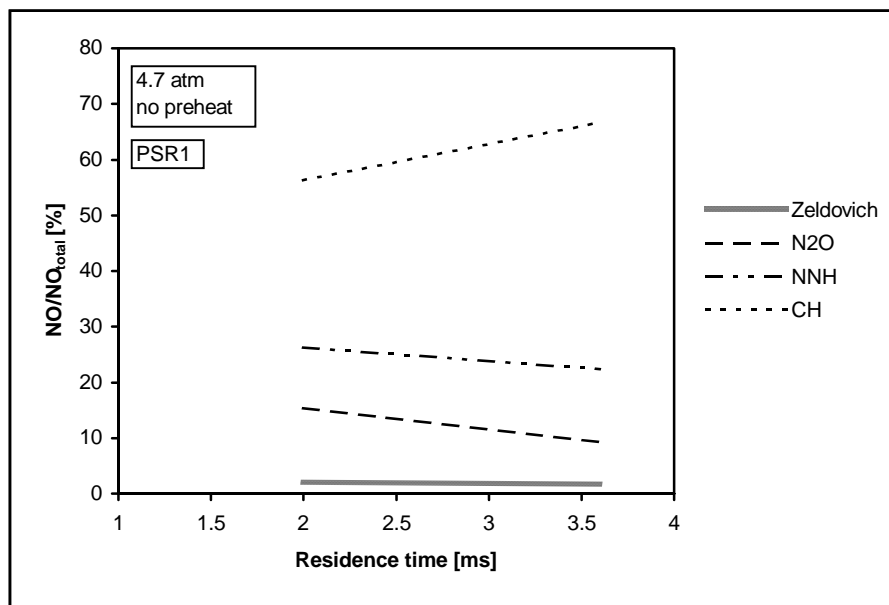


Figure 4.46 Percent of the NO formed by each of the four pathways in PSR1 at 4.0 atm without preheat

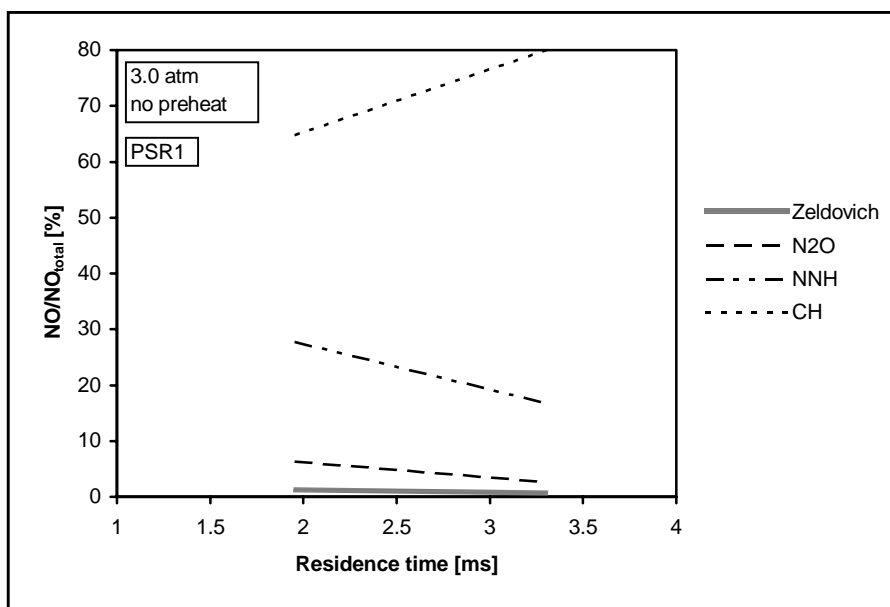


Figure 4.47 Percent of the NO formed by each of the four pathways in PSR1 at 3.0 atm without preheat

The prompt pathway yields increased amounts of NO formed in PSR1 for the long overall residence times. For example, the NO yield from prompt pathway for 6.5 atm at 2.0 ms overall time is 54% (3.1 ppm, wet), whereas, at 4.0 ms overall time the NO<sub>x</sub> yield is 69% (3.9 ppm, wet). This increase in prompt NO is caused by the increased CH-radical concentration in PSR1 from 2.25e-12 to 5.44e-12 mol/cm<sup>3</sup>. The increase in [CH] is caused by two factors: one is the increasing fuel-air equivalence ratio, and the other is shortening of PSR1 residence time from 0.13 to 0.07 ms for the overall residence time increase from 2.0 to 4.0 ms. The latter has a stronger effect, which can be evidenced in a few examples. The first example is for 6.5 atm with preheat and with residence times below 1.6 ms. The reactor is operating in the single-PSR mode. There, [CH] decreases with increasing residence time, in spite of the increase in fuel-air equivalence ratio. The second example is at 4.7 atm at a fuel-air equivalence ratio of 0.72 and the two residence times of 0.89 ms (single-PSR) and 0.0704 ms (PSR1). The CH radical concentrations are 4.1e-13 and 6.6e-12 mol/cm<sup>3</sup>, respectively, indicating a strong dependence on the reactor residence time.

Results from the chemical kinetic modeling explain the following experimental trends when the reactor is operating in two-PSR regime (residence times above 1.6 ms):

1. The increase in measured NO<sub>x</sub> with increasing overall residence time for unheated cases (Figure 3.10) is consistent with the increase of O-atom, H, CH, and NNH concentrations in PSR1, and with the increased time for the NO formation in PSR2. The former is, in effect, caused by decreasing residence times in PSR1. Since the

prompt pathway is predominant in PSR1, and its contribution to the total NO<sub>x</sub> increases with the overall residence times, it is most responsible for the increase in the NO<sub>x</sub> formed in the PSR1. The increased time available for the NO<sub>x</sub> formation in PSR2 (at the longer overall residence times) increases the percentage of the NO<sub>x</sub> that is formed in the PSR2. The reactive species concentrations are lower, but the overall residence time, and thus temperature, is significantly higher in PSR2, hence increasing the contribution of the Zeldovich pathway, which is the predominant NO<sub>x</sub> pathway in PSR2.

2. The decrease in measured NO<sub>x</sub> with preheating the reactants is relatively small at long residence times. The model is consistent with this observation. When PSR1 outputs listed in Table 4.3a are compared for unheated and preheated inlet cases, at 4 ms overall residence time, it is concluded that the mole fractions of O, CH, NNH, and N<sub>2</sub>O are relatively similar, thus resulting in similar NO<sub>x</sub> yields. The same is concluded when PSR1 outputs are compared for unheated and preheated cases for 2 ms cases, or when PSR2 cases are compared at both residence times. The contribution of each pathway is also rather similar in both PSR1 and PSR2.
3. The increase in NO<sub>x</sub> with decreasing pressure is caused by the increase in free-radical concentrations in both zones. In PSR1, between 6.5 and 3.0 atm, the O-atom concentration increases 3 times, the [CH] 7-8 times, the [H] 4.5 times, and the [NNH] 2-times, whereas the [N<sub>2</sub>O] decreases 2.5 times. Consequently, the NO<sub>x</sub> formation rates in PSR1 increase between the two pressure levels from 2.2 times at 2.0 ms to 3 times at 4.0 ms. The contribution of each pathway changes, however. In general, the

prompt contribution increases, nitrous oxide and Zeldovich are decreasing and the contribution of the NNH-pathway to the total NO<sub>x</sub> remains relatively constant. For example, at 2.0 ms, between 6.5 and 3.0 atm pressure levels, the prompt NO contribution increases from 54 to 65%, the NNH-NO contribution increases from 22 to 28%, the nitrous oxide NO contribution decreases from 21 to 6%, and Zeldovich NO decreases from 3 to 1%. The O-atom concentration in the PSR2 increases with decreasing pressure, and so does the gas temperature. This causes Zeldovich and nitrous oxide pathway NO rates to increase which, in turn, increase NO formation rates in the PSR2 from 1.8 times at 2.0 ms to 2.8 times at 4.0 ms. The prompt and NNH-pathways have little contribution to the overall NO production.

#### ***4.5 Summary of Modeling Results***

The experiments were modeled using two approaches: turbulent flame thickness estimation and chemical reactor modeling. The results are summarized below:

1. The turbulent flame thickness model shows the Damköhler numbers are low ( $0.06 \leq Da \leq 1$ ) and turbulent intensities are high (ratio of turbulent intensity to laminar burning velocity is  $28 \leq u'/S_L \leq 356$ ), indicating the combustion in the HP-JSR occurs in the high intensity, chemical rate limiting regime.
2. The chemical reactor model is developed to match the NO<sub>x</sub> and CO experimental data. The low residence time cases are modeled with a single PSR, indicating that the HP-JSR approaches a well-stirred reactor. The long residence time cases are modeled

with two PSR's in series, a small PSR to model the flame confined to the centerline region of the HP-JSR and a large PSR to model the remainder of the reactor.

3. The volume of the flame estimated by the turbulent flame thickness model,  $V_{\text{flame}} = 5\pi\delta_T^3$ , is comparable to the volume of PSR1, adding confidence to the validity of the chemical reactor model. This allows for the chemical kinetic interpretation of the experimental data by the chemical reactor model.
4. The low residence time data are modeled with a single-PSR chemical reactor model. The prompt pathway is the predominant pathway for NO formation in this regime. Both the decrease in NOx with residence time (found for unheated inlet experiments at short residence times) and with preheat are explained by the decrease of the NOx formed by the prompt mechanism.
5. The long residence time cases are modeled with a two-PSR chemical reactor model. The volume of the first PSR is up to 10% of the volume of the second PSR. The predominant pathway for NO formation in the first PSR (which represents the flame) is the prompt pathway. The predominant pathway in the second PSR (which represents the post-flame zone) is the Zeldovich pathway. The measured NOx increase with increasing residence time is consistent with the increased prompt NO in the first PSR and increased Zeldovich NO in the second PSR. The inlet temperature does not affect the measured NOx and this is consistent with the model. The decrease of NOx with pressure was measured only at long residence times and is consistent with the reduction of the prompt NO and NNH-NO in the first PSR, and with the reduction of the Zeldovich NO and nitrous oxide NO in the second PSR.

## CHAPTER 5

### CONCLUSIONS AND RECOMMENDATIONS

#### *5.1 Conclusions*

The NO<sub>x</sub> and CO formation in lean-premixed combustion have been studied at elevated pressures (6.5, 4.7 and 3.0 atm), for unheated inlet gas and for the inlet preheated to 573 K, and for a range of residence times (0.5 to 4.0 ms) - all at reactor gas temperatures between 1800 and 1940 K. The study has been conducted in two parts. First, an experimental database was created using a high-pressure jet-stirred reactor (HP-JSR). Second, data were modeled and interpreted using premixed turbulent combustion correlations and chemical reactor modeling.

The conclusions of this study are as follows:

1. The HP-JSR experiences significant heat loss at small flow rates, i.e., at large residence times. Consequently, although the measured temperature was held constant at  $1803 \pm 5$  K, the true gas temperature in the experiments varied from about 1800 to 1940 K.
2. The percent of the HP-JSR volume taken up by the flame varies with reactor residence time, pressure, and inlet temperature. This conclusion is made based on the measured CO reactor profiles and by the calculations of the flame volume. At short residence times, the highest CO concentrations are measured both at the centerline and at the wall. This CO behavior indicates the flame has extended all the way around the top and down the reactor wall. The turbulent flame thickness calculations

verify this behavior by showing a long and a thick flame at short residence times. Furthermore, at long residence times, the CO concentrations are low throughout the reactor, except near the centerline, where they are much higher. This CO behavior indicates that the flame is short and thin and confined to the centerline region of the reactor. The turbulent flame thickness calculations verify this observed CO behavior by showing a short and thin flame at long residence times. Additionally, a comparison of CO profiles for unheated and preheated cases shows that an increase in inlet temperature decreases the flame volume. Finally, calculations of the flame volume show that by increasing the pressure, the flame volume is decreased.

3. The NO<sub>x</sub> concentrations are dependent on the following: (a) the size of the flame and the post-flame zone, and (b) the NO<sub>x</sub> formation kinetics in each zone.
4. Experimental data and modeling of NO<sub>x</sub> formation show that the HP-JSR approaches a well-stirred reactor at lower residence times.
5. For unheated inlet combustion gas, the NO<sub>x</sub> decreases with increasing residence time, reaching a minimum at an intermediate residence time. This residence time is about 2.0 ms at 6.5 atm, 1.5 ms at 4.7 atm and 1.0 ms at 3.0 atm. At these residence times, the flame volume is approximately one-half of the reactor volume. The NO<sub>x</sub> behavior is consistent with a decrease in the contribution of NO<sub>x</sub> formation through the prompt pathway as residence time increases. The prompt NO decreases with residence time due to significant decrease in the CH radical concentration in the flame.

6. The measured NO<sub>x</sub> increases with increasing residence time above 2.0 ms at 6.5 atm, 1.5 ms at 4.7 atm and 1.0 ms at 3.0 atm. Two effects cause this increase. First, the NO<sub>x</sub> concentration in the flame zone increases with increasing residence time, primarily due to the increase in the NO<sub>x</sub> formed by the prompt pathway (caused by the increasing CH radical concentration in the flame). Second, the NO<sub>x</sub> concentration in the post-flame zone increases with increasing residence time due to the increase in the NO<sub>x</sub> formed by the Zeldovich pathway (caused by the increasing gas temperature).
7. At low residence times, the measured NO<sub>x</sub> concentrations for preheated inlet gas are somewhat lower than for the unheated inlet gas. This decrease in NO<sub>x</sub> is consistent with a decrease in the NO<sub>x</sub> formation through the prompt pathway, since the yield of NO by the other three pathways is similar between the unheated and preheated cases. At long residence times, the impact of the prompt NO is reduced since it only influences a small part of the reactor. Therefore, decrease in measured NO<sub>x</sub> with preheating the reactants is relatively small.
8. The measured increase in NO<sub>x</sub> with decreasing pressure is caused by: (1) the increase in free radicals in the flame and the post-flame zone, and (2) the increase in the true gas temperature with decreasing pressure. At the short residence times, the yields of the NO formed by the prompt and the NNH pathways increase with decreasing pressure, whereas the absolute yields of NO formed by the nitrous oxide and the Zeldovich pathways remain relatively constant with pressure. At the long residence times, the yields of the NO formed by the prompt pathway increase with decreasing

pressure in the flame, and the yields of the NO formed by of the Zeldovich and the nitrous oxide pathways increase with decreasing pressure in the post-flame zone.

## ***5.2 Recommendations***

The results obtained in this dissertation warrant the following recommendations for future research:

1. The model for predicting NO<sub>x</sub> and CO should be validated with data from other jet-stirred reactors and from industrial combustors.
2. The model for predicting NO<sub>x</sub> from gas turbine combustors should be applied to the design development of gas turbine combustors.
3. High pressure JSR experiments should be conducted with constant reactor temperature at higher pressures, higher inlet temperatures, and lower fuel-air equivalence ratios than used in this research, to better simulate the commercial gas turbine conditions.
4. A model should be developed that simulates distributed addition of fuel-air mixture to parcels of reacting gas as they flow through the reactor. This would be equivalent to distribution of fuel-air mixture throughout the reactor because of the intense jetting and mixing. However, the distribution would not be uniform (as assumed in the PSR theory). It would be skewed towards the jet zone in the reactor.
5. A model should be developed that simulates effect of residence time distribution on NO<sub>x</sub> formation and CO. Interpretation of the present NO<sub>x</sub> measurements is based on NO<sub>x</sub> formation in the jet zone as a means of explaining the NO<sub>x</sub> uniformity in the

recirculation zone. However, the NO<sub>x</sub> uniformity could also arise as the recirculation zone being a PSR-NO<sub>x</sub> producer. It could be that NO<sub>x</sub> forms two ways: 1) by fast, free-radical chemistry in the jet zone (and jet shear layer), and 2) by slow, free-radical deficient chemistry in the eye of the recirculation zone. The latter could yield significant NO<sub>x</sub> if gas is trapped in the eye for a long time. As a first approximation, NO<sub>x</sub> formation could assume a PSR residence time distribution, or a PSR distribution with a short PFR added up front (effectively requiring each gas particle to remain within the reactor for at least the PFR time). The young particles in the reactor would form NO<sub>x</sub> at a fast rate, and the old particles would form NO<sub>x</sub> at a slow rate. Most likely, only the “limit” particles, i.e., the very young (through free-radical driven NO<sub>x</sub>) and the very old (through a large amount of time) would yield significant NO<sub>x</sub>.

## CHAPTER 6

### DESIGN CONCEPT FOR A LEAN-PREMIXED COMBUSTOR WITH A TIME- OPTIMIZED FLAME CAVITY

#### *6.1 Background*

Growing environmental concerns, discussed in Chapter 1, are driving the industry towards reducing greenhouse gases, ozone layer depleting chemicals and pollutant emissions. As concluded, natural gas fired gas turbines present an important source of pollutant emissions, and their impact on the environment will increase in the future due to their increased utilization in the US and international electric power generation markets.

Over the past ten years, the lean-premixed combustor has been developed and is now the accepted technology for burning natural gas in gas turbine engines. In lean-premixed combustors, fuel and air are premixed prior to entering the combustor. This technology is popular, due to its relatively low cost, reliability and acceptable levels of pollutant emissions. However, NO<sub>x</sub> emissions are still two digit parts-per-million by volume, corrected to 15% O<sub>2</sub> (ppmv, dry, 15% O<sub>2</sub>), while new emissions regulations are pushing towards single-digit NO<sub>x</sub> emissions. One approach to addressing this issue is the use of catalytic combustors, guaranteeing NO<sub>x</sub> emissions of a few parts-per-million from gas turbine engines. However, these devices still have several technological difficulties, such as material and structural integrity of the catalyst under high temperature and thermal cycling conditions, which have to be resolved in practical operation. Also, the use of

catalytic combustion may increase the capital, operating and maintenance costs of the gas turbines.

The results presented in Chapter 3 lead to a conclusion that if flames in the gas turbine combustor were confined to a small, enclosed volume, the emissions from these devices could be significantly reduced. This is the basis of the Time-Optimized Flame Cavity (TOFC) concept in the lean-premixed combustor of a gas turbine engine. The Time-Optimized Flame Cavity (TOFC) is essentially a jet-stirred reactor embedded into a primary combustion zone of combustion systems that involve burning of gaseous and prevaporized liquid fuels. This device significantly reduces pollutant emissions by intensely mixing the gases and by controlling their residence time.

The TOFC is a relatively small cavity that contains a stabilized flame. Fuel and air enter the TOFC through a single jet or multiple jets. (The fuel and air may be premixed or partially premixed.) Mixing of the colder inlet gases with the hot combustion products in the TOFC results in combustion of the inlet gas and consequently in a distribution of temperature and species concentrations from the colder jet core(s) of combustion reactants to the hot combustion products within the cavity. An optimal distribution of species concentrations and temperature, leading to the maximum reduction in pollutant emission, can be obtained by optimizing the residence time of the cavity. It is expected that this utilization of the TOFC will reduce the NO<sub>x</sub> emissions levels by an order of magnitude from the levels measured in the currently operating lean-premixed gas turbine engines, with a potential of significant CO reduction as well. In addition, the application of the TOFC can be extended to many other industrial combustors and furnaces.

The addition of the TOFC to lean-premixed combustors can lead to single-digit NO<sub>x</sub> emissions (in ppmv) with natural gas fuel, which is comparable to the levels expected from the catalytic combustor technology. However, the TOFC in lean-premixed gas turbine combustors has a significant advantage over the use of catalytic combustion technology. This device presents only a modification of the existing designs of lean-premixed gas turbine combustors that have run successfully for thousands of field hours, and have proven to be reliable and marketable. The TOFC can be implemented into existing designs with only minor modifications; it does not require developing additional new technologies, which could be very expensive. In addition, the TOFC has advantages over the existing designs of lean-premixed gas turbine combustors since single-digit NO<sub>x</sub> emissions are feasible with natural gas fuel at current firing temperature conditions, and the potential for low emissions still exist even if these temperatures are increased.

The central idea of the TOFC is to use a residence time, or a range of residence times, that minimizes pollutant formation. If the residence time is too short, fuel and intermediates of combustion, such as CO, will be emitted, and free radicals, such as O-atom, H-atom, OH-radical, and CH-radical, will fill the combustion cavity and cause a high formation rate of oxides of nitrogen (NO<sub>x</sub>). If the residence time is too long, NO<sub>x</sub> emission will increase simply by virtue of the long time during which it can form. Thus, there is an optimal residence time, or residence time range, for each cavity geometry and jet design, which leads to maximum pollutant reduction.

The decrease in the CO<sub>2</sub> emitted to the atmosphere per every kilowatt of power produced is achieved by increasing the overall thermodynamic efficiency of the process.

One way of increasing this efficiency is by increasing the firing temperature, but that generally results in increasing the NO<sub>x</sub> formation. The TOFC, by reducing the residence time in the flame, can be effective in achieving low overall NO<sub>x</sub> formation in spite of the increased firing temperature, and therefore creates a potential for future gas turbine engine development.

### ***6.2 Application to Lean-Premixed Gas Turbine Combustors***

The TOFC's are positioned inside the gas turbine combustor. The fuel and air enter the combustor through several fuel/air injectors. The TOFC's should be placed as an inverted cup, or cap, on each injector. Two design options are proposed:

1. TOFC is a cap detached from the housing but secured in the combustor, and
2. TOFC is a cap attached to the combustor housing.

In the first option, the TOFC's need to be securely positioned due to high intensity of the fuel/air jet exiting the injector nozzle. The specifics of the positioning will depend on the actual combustor in which the cavity is placed. In the case of the example design shown in Figure 6.1, the fuel/air jet is hitting the opposite side of the TOFC, with a consequence being that the TOFC would move away from the injector. A solution for securing the TOFC in place could be a rod secured on one end in the combustor housing, and reaching with the other end to the outside walls of the TOFC. This rod will prevent it from moving axially, i.e., in the direction of the jet(s), while a cap, or a ring would prevent it from moving radially. Both the rod and the cap, or the ring, should be made of temperature resistant materials.

In the second design option, the use of the rod and the cap might not be necessary since the TOFC is an integral part of the housing. This means that the TOFC and the housing are cast in the same mold. This second design is believed to be the optimal solution, because the vibrations and the fatal errors of the system will be minimized.

Figure 6.1 shows an example of the TOFC positioned on a single inlet premixed fuel/air jet nozzle where back mixing is used to stabilize the flame. This example was conceptualized based on the current design of the HP-JSR, but it can be modified in other applications. Arrows in Figure 6.1 indicate the back-mixing pattern. The gases exit on the bottom, underneath the cavity. Any further chemical reaction, and possible pollutant formation, is quenched by injecting air, denoted secondary air in Figure 6.1, into the exiting gases immediately upon leaving the cavity. The use of the TOFC opens another possibility in LP combustion, which is staged lean-lean combustion for ultra low NO<sub>x</sub>. The flame in TOFC is very lean, so little NO<sub>x</sub> is formed, and if a second flame downstream of the TOFC is also lean, then it would not form much additional NO<sub>x</sub> since burning would be under highly diluted conditions.

The cavity should be constructed with temperature resistant material. Various ceramic materials that are designed to operate in highly oxidizing and high temperature environments are recommended for this application.

The fabrication of the ceramic TOFC is proposed as a three-step process. In the first step, a mold is constructed out of a high temperature resistant material. In the second step, the ceramic is poured into the mold. Then, the mold with the ceramic is placed in a high temperature oven, in which the ceramic is cured, i.e., hardened. This mold should

be re-usable for mass production and it should include the outer shell, and the inner piece. The outer shell should define the outside dimensions of the device. The inner piece defines the shape of the cavity. For example, for the design of the example TOFC shown in Figure 6.1, the outer shell should be made as a cylinder with half-spherical bottom. The inner mold has the same shape in this case. This design has the advantage that the inner mold can be pulled out after curing. If, however, the inlet to the cavity is smaller than the cavity, as in the case of stirred reactor described in Chapter 3, then the mold cannot be pulled out after curing. Then the inner mold has to be constructed from a material, such as wax, that would melt in the oven during curing. The ceramic properties are such that the inner mold will serve its purpose, during the poring and hardening of the ceramic, by giving the shape to the cavity. But, once the ceramic is hardened the inner mold can be melted out.

The placing of TOFC's as caps on single or smaller groups of fuel/air injectors adds another advantage to the implementation of this design to lean-premixed gas turbine combustors which is low emissions during start-up, shut-down, and low-power operation. This can be accomplished by the regulation of mass flow rates into each fuel/air injector. During reduced-power operation the overall mass flow rates are reduced. This can be regulated in two ways: 1) by reducing the flow into all the injectors, and 2) by shutting down flows into some fuel injectors, while the rest work with optimum mass flow rates. Since the TOFC's are designed for a particular range of residence times, which are defined by the optimum range of mass flow rates entering the TOFC, the latter regulation

option is preferred since it will ensure the low emission formation operating conditions within the TOFC's.

The dimensions and shapes of the TOFC depend on the flow rates and composition of the jet(s) gas, jet(s) diameter, conditions in the reactor, and the optimal residence time or residence time range for which the pollutant formation will be minimized.

Results obtained in Chapter 3 lead to the conclusion that the application of the TOFC can yield the NO<sub>x</sub> levels of as low as 3 ppmv, dry, (15% O<sub>2</sub>). In order to terminate all post-flame NO<sub>x</sub> formation, a relatively small amount of secondary air could be injected at the exit of the TOFC, as indicated in Figure 6.1. Reducing the gas temperature in the TOFC can further decrease the low NO<sub>x</sub> levels. However, higher temperatures increase the thermal efficiency of the cycle, which ultimately results in lower CO<sub>2</sub> emissions per kW power produced. CO is also expected to be low. Measured levels in the HP-JSR are, on average, a few hundreds ppmv. Allowing enough time, this level should significantly decrease due to CO oxidation into CO<sub>2</sub>. Work by Nicol et al. (1997) suggests that most of the CO in the exhaust from the gas turbine engines originates from liner cooling with air addition into the flow, as discussed in Section 2.4. This air addition leans out the gas near the liner, so that the CO oxidation process is slowed down. Therefore, secondary air addition into the gas stream exiting the TOFC has two functions: it cools the gases and quenches the NO<sub>x</sub> chemistry, and it eliminates the necessity for liner cooling because the flame is confined and the exiting gases are cool. The remainder of the combustor should be designed to provide enough time for the CO oxidation to CO<sub>2</sub>. CO should oxidize to low levels of the order 10 ppmv, dry (15% O<sub>2</sub>). The unburned hydrocarbons measured in

the HP-JSR are approximately 100 ppm, dry at lowest NO<sub>x</sub> levels, and should oxidize in the remainder of the combustor to levels of the order 10 ppmv, dry (15% O<sub>2</sub>).

As shown in Figure 6.1, the jet entering the TOFC delivers premixed fuel and air, feeding the flame located inside the TOFC.

The modeling by Nicol et al. (1997) supports the theory that intense mixing in closed cavities washes out the tendency of fuel-air unmixedness to increase NO<sub>x</sub> levels. Fuel-air unmixedness means that the fuel and air entering the cavity through the jet are not perfectly premixed. This allows an advantage for gas turbine manufacturers that have poor premixers.

Use of the Time-Optimized Flame Cavity is not limited only to gas turbine combustors. It can be utilized in furnaces and any industrial combustors.

This device can be used with other gaseous fuels, (such as alternative gaseous or gasified coal, biomass or liquid fuels), and prevaporized liquid fuels, (such as liquid petroleum distillates, naphtha, diesel fuels, kerosene, and JP fuels).

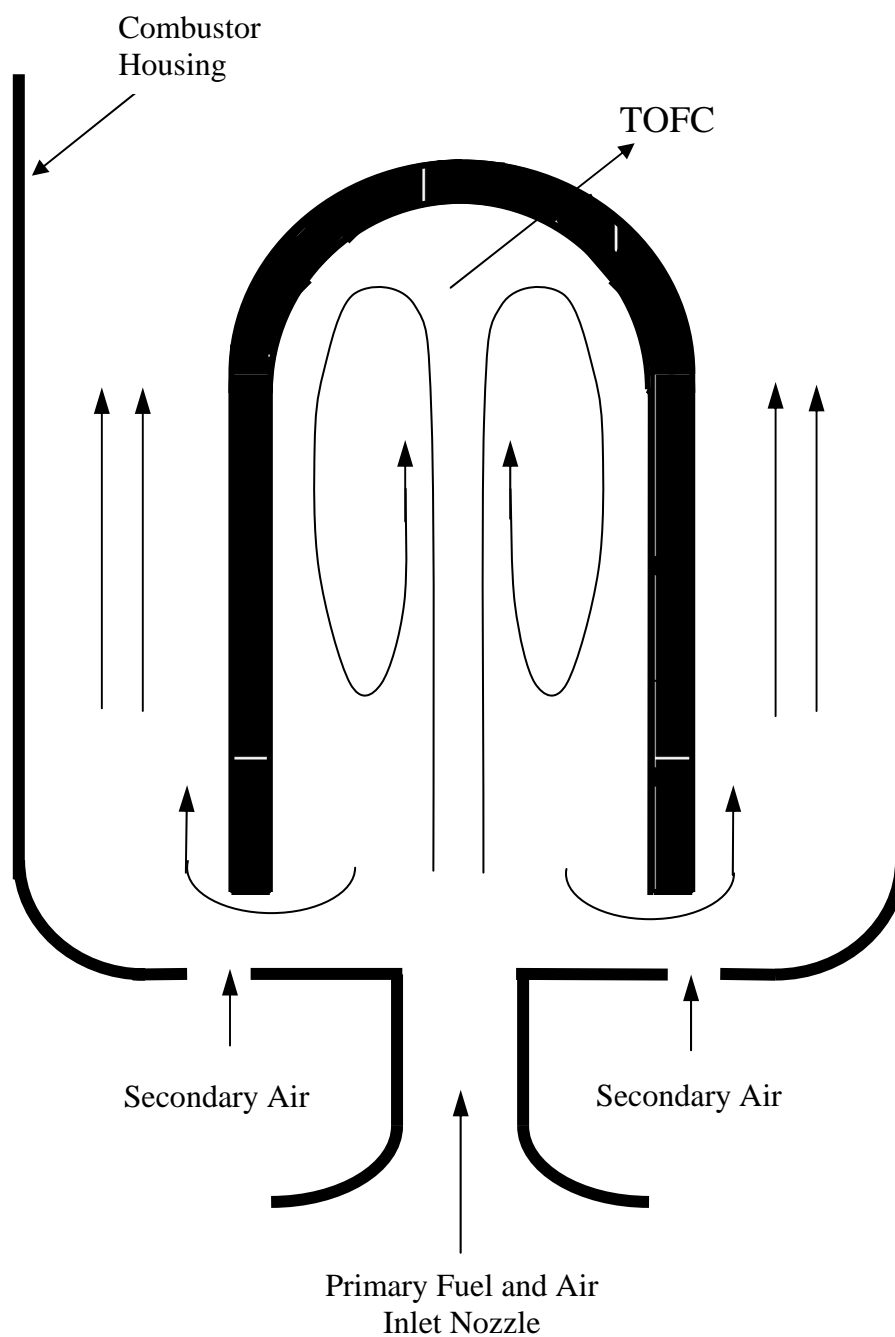


Figure 6.1 Conceptual design of the circular Time-Optimized Flame Cavity (TOFC) positioned above single premixed fuel-air nozzle in a lean-premixed combustor primary zone

**LIST OF REFERENCES**

- Abraham, J., Williams, F. A., and Bracco, F. V. "A Discussion of Turbulent Flame Structure in Premixed Charges." SAE paper 850345, in *Engine Combustion Analysis: New Approaches*, P-156, (1985): 27-43.
- Ainslie, N. G., Morelock, C. R., and Turnbull, D. "Devitrification Kinetics of Fused Silica." Nucleation and Crystallization Symposium, American Chemical Society, 1962.
- Alzueta, M. U., Bilbao, R., Millera, A., Glarborg, P., Østberg, M., and Dam-Johansen, K. "Low Temperature Gas Reburning. NO<sub>x</sub> Reduction Potential and Effects of Mixing." *Energy & Fuels* 12, (1998): 329-338.
- Andrews, G. E., and Bradley, D. "The Burning Velocity of Methane-Air Mixtures." *Comb. Flame*. 19, (1972): 275-288.
- Bengtsson, K. U. M., Benz P., Schaeren, R., and Frouzakis, C. E. "NyO<sub>x</sub> Formation in Lean Premixed Combustion of Methane in a High-Pressure Jet-Stirred Reactor." *Twenty-Seventh Symposium (International) on Combustion*, The Combustion Institute, (1998): 1393-1401.
- Borghi, R., in *Recent Advances in Aeronautical Science*, Pergamon, London, (1985): 117-134.
- Bozzelli, J. W., Chang, A. Y., and Dean, A. M. "Analysis of the Reactions H + N<sub>2</sub>O and NH + NO: Pathways and Rate Constants Over a Wide Range of Temperature and

- Pressure.” *Twenty-Fifth Symposium (International) on Combustion*, The Combustion Institute, (1994): 965-974.
- Breidenthal, R. E., Buonadonna, V. R. and Weisbach, M. F. “Molecular mixing via jets in confined volumes.” *J. Fluid Mech.* 219, (1990): 531-544.
- Bray, K. N. C. “Turbulent Flows with Premixed Reactants,” in *Turbulent Reacting Flows*, (P. A. Libby and F. A. Williams, eds.), Springer-Verlag, New York, (1980): 115-183.
- Burton, K. A., Ladouceur, H. D., and Fleming, J. W. “An Improved Noncatalytic Coating for Thermocouples.” Short communication, *Combust. Sci. and Tech.*, 81 (1992): 141-145.
- Capehart, S.A., Lee, J.C.Y., Williams, J.T., and Malte, P.C. “Effect of fuel composition on NO<sub>x</sub> formation in lean premixed prevaporized combustion.” ASME Paper No. 97-GT-336, ASME, New York, NY, 1997.
- Chomiak, J. *Combustion: A Study in Theory, Fact and Application*, Gordon and Breach Science Publishers, 1990.
- Combustion Engineering. *Combustion-Fossil Power Systems*, Combustion Engineering, Inc., Windsor, CT, (1981): 2-35, 36.
- Farmer, R. "Reheat GTs boost 250 and 365 MW combined cycle efficiency to 58%." *Gas Turbine World*, September-October 1993.
- Glassman, I. *Combustion*, Academic Press, 1996.
- Göttgens, J., Mauss, F., and Peters, N. “Analytic Approximations of Burning Velocities and Flame Thicknesses of Lean Hydrogen, Methane, Ethylene, Ethane, Acetylene,

- and Propane Flames.” *Twenty-Fourth Symposium (International) on Combustion*, The Combustion Institute, (1992): 129-135.
- Smith, G. P., Golden, D. M., Frenklach, M., Moriarty, N. W., Eiteneer, B., Goldenberg, M., Bowman, C. T., Hanson, R., Song, S., Gardiner, W. C. Jr., Lissianski, V., and Qin, Z., [http://www.me.berkeley.edu/gri\\_mech/](http://www.me.berkeley.edu/gri_mech/), 1999.
- Hamer, A. J. and Roby, R. J. “CFD Modeling of a Gas Turbine Combustor Using Reduced Chemical Kinetic Mechanisms.” AIAA 97-3242, presented at the 33<sup>rd</sup> AIAA/ASME.SAE/ASEE Joint Propulsion Conference & Exhibit, Seattle, WA, 1997.
- Harrington, J. E., Smith, G. P., Berg, P. A., Noble, A. R., Jeffries, J.B., and Crosley, D. R. “Evidence for a New NO Production Mechanism in Flames.” *Twenty-Sixth Symposium (International) on Combustion*, The Combustion Institute, (1996): 2133-2138.
- Heywood, J. B. *Internal Combustion Engine Fundamentals*, McGraw-Hill, USA, 1988.
- Horning, D. C. “Pollutant Formation by Lean-Premixed Combustion in a High Pressure Jet-Stirred Reactor.” *M.S. Thesis*, University of Washington, Seattle, WA, 1996.
- International Power Generation, “Low NO<sub>x</sub> Gives a Winning Edge”, May 1998: 15-16.
- Jarrett, A. C. “NO<sub>x</sub> Formation in Lean-Premixed Combustion.” *M.S. Thesis*, University of Washington, Seattle, WA, 1995.
- Joshi, N.D., Epstein, M.J., Durlak, S., Marakovits, S., and Sabla, P.E. "Development of a Fuel Air Premixer for Aero-Derivative Dry Low Emissions Combustors." ASME Paper 94-GT-253, ASME, New York, NY, 1994.

- Kobayashi, H., Nakashima, T., Tamura, T., Maruta, K., and Niioka, T. "Turbulence Measurements and Observations of Turbulent Premixed Flames at Elevated Pressures up to 3.0 MPa." *Comb. Flame*. 108 (1997): 104-117.
- Kramlich, J. C. and Malte, P. C. "Modeling and Measurement of Sample Probe Effects on Pollutant Gases Drawn from Flame Zones." *Comb. Sci. and Tech.* 18 (1978): 91-104.
- Kuehn, S. E. "Advancing gas turbine technology: evolution and revolution." *Power Engineering*, May 1995.
- Lefebvre, A. H. *Gas Turbine Combustion*, Hemisphere Publishing Corporation, USA, 1983.
- Leonard, G. and Stegmaier, J. "Development of an Aeroderivative Gas Turbine Dry Low Emissions Combustion System." ASME Paper 93-GT-288, ASME, New York, NY, 1993.
- Miller, J. A. and Bowman, C. T. "Mechanism And Modeling of Nitrogen Chemistry in Combustion." *Prog. In Energy and Combust. Science* 15, (1989): 287-338.
- Mills, A. F. *Heat Transfer*, Richard D. Irwin, Inc., USA, 1992.
- Mongia, R. K., Tomita, E., Hsu, F. K., Talbot, L., and Dibble, R. W. "Use of an Optical Probe for Time-Resolved *In-Situ* Measurement of Local Air-to-Fuel Ratio and Extent of Fuel Mixing with Application to Low NO<sub>x</sub> Emissions in Premixed Gas Turbines." *Twenty-Sixth Symposium (International) on Combustion*, The Combustion Institute, (1996): 2749-2757.

- Nicol, D.G., Malte, P.C., Hamer, A. J., Roby, R. J., and Steele, R.C., "Development of a Five-Step Global Methane Oxidation – NO Formation Mechanism for Lean-Premixed Gas Turbine Combustion." *Transactions of the ASME, Journal of Engineering for Gas Turbines and Power* 121 (1999): 272-280.
- Nicol, D. G., Rutar, T., Martin, S. M., Malte, P. C. and Pratt, D. T. "Chemical Reactor Modeling Applied to the Prediction of Pollutant Emissions from an LP Combustor." Presented at the 33<sup>rd</sup> AIAA/ASME/SAE/ASEE Joint Propulsion Conference and Exhibit in Seattle, Washington, July 7-9, 1997.
- Nicol, D.G. "A Chemical and Numerical Study of NO<sub>x</sub> and Pollutant Formation in Low-Emission Combustion." *Ph.D. Thesis*, University of Washington, Seattle, WA, 1995.
- Nicol, D.G., Steele, R.C., Marinov, N. M., Malte, P.C. "The importance of the nitrous oxide pathway to NO<sub>x</sub> in lean-premixed combustion." *Transactions of the ASME, Journal of Engineering for Gas Turbines and Power* 117 (1995): 100-111.
- Nicol, D.G., Malte, P.C., and Steele, R.C., "Simplified Models for NO<sub>x</sub> Production Rates in Lean-Premixed Combustion." ASME Paper 94-GT-432, ASME, New York, NY, 1994.
- Rutar, T., Horning, D. C., Lee, J. C. Y., and Malte, P.C. "NO<sub>x</sub> Dependency on Residence Time and Inlet Temperature for Lean-Premixed Combustion in Jet-Stirred Reactors." ASME Paper No. 98-GT-433, ASME, New York, NY, 1998.
- Rutar, T., Martin, S.M., Nicol, D.G., Malte, P.C., and Pratt, D.T. "Effects of incomplete premixing on NO<sub>x</sub> formation at temperature and pressure conditions of LP combustion turbines." ASME Paper No. 97-GT-335, ASME, New York, NY, 1997.

- Sattelmayer, T., Felchine., M. P., Haumann, J., Hellet, J., and Styner, D. "Second-Generation Low-Emission Combustors for ABB Gas Turbines: Burner Development and Tests at Atmospheric Pressure." *Transactions of the ASME, Journal of Engineering for Gas Turbines and Power* 114, (1992): 118-125.
- Schmid, H-P, Habisreuther, P., and Leuckel, W. "A Model for Calculating Heat Release in Premixed Turbulent Flames." *Comb. Flame.* 113 (1998): 79-91.
- Sloss, L.L. et al. *Nitrogen Oxides Control Technology Fact Book*, Noyes Data Corporation, USA, 1992.
- Snyder, T. S., Rosfjord, T. J., McVey, J. B., Hu, A. S., and Schlein, B. C. "Emission and Performance of a Lean-Premixed Gas Fuel Injection System for Aero-derivative Gas Turbine Engines." ASME Paper 94-GT-234, ASME, New York, NY, (1994).
- Southall, L. and McQuiggan, G. "New 200 MW class 501G combustion turbine." ASME 95-GT-215, ASME, New York, NY, 1995.
- Steele, R. C. "NO<sub>x</sub> and N<sub>2</sub>O Formation in Lean-Premixed Jet-Stirred Reactors Operated from 1 to 7 atm." Ph.D. Thesis, University of Washington, Seattle, WA, 1995.
- Steele, R.C., Jarrett, A.C., Malte, P.C., Tonouchi, J.H., and Nicol, D.G. "Variables affecting NO<sub>x</sub> formation in lean-premixed combustion." *Transactions of the ASME, Journal of Engineering for Gas Turbines and Power* 119 (1997): 102-107.
- Steele, R.C., Tonouchi, J.H., Nicol, D.G., Horning, D.C., Malte, P.C., and Pratt, D.T. "Characterization of NO<sub>x</sub>, N<sub>2</sub>O, and CO for lean-premixed combustion in a high-pressure jet-stirred reactor," *Transactions of the ASME, Journal of Engineering for Gas Turbines and Power* 120 (1998): 303-310.

- Sturgess, G. J. and Shouse, D. T. "A Hybrid Model for Calculating Lean Blow-outs in Practical Combustors." Presented at the 32<sup>nd</sup> AIAA/ASME/SAE/ASEE Joint Propulsion Conference in Lake Buena Vista, FL, July 1-3, 1996.
- Thornton, M.M., Malte, P.C., and Crittenden, A.L. "A Well-Stirred Reactor for the Study of Pyrolysis and Oxidation Kinetics: Carbon Monoxide and n-Pentane Oxidation." *Combust. Sci. and Tech.* 54 (1987): 275-297.
- Tonouchi, J. H. "Macromixing and Micromixing in Lean Premixed Combustion." Ph.D. Thesis, University of Washington, Seattle, WA, 1996.
- Touchstone, G. "Gas Turbines: Leading Technology for Competitive Markets." *Global Gas Turbine News* 36, (1996): 10.
- Turns, S. T. *An Introduction to Combustion*, McGraw-Hill, USA, 2000.
- Zucrow, M. J. and Hoffman, J. D., *Gas Dynamics*, John Wiley & Sons, USA, 1976.

**APPENDIX A**  
**EXPERIMENTAL DATA**

**APPENDIX A****EXPERIMENTAL DATA**

The following explanations are accompanying data presented in Appendix A:

1. All experimental data are taken at measured temperature of  $1803 \pm 5$  K.
2. Residence time is calculated based on equation 3.2 in Chapter 3.
3. The fuel-air equivalence ratio ( $\phi$ ) is calculated based on measured total carbon (%CO + %CO<sub>2</sub>), using the following formula:

$$\phi = ((\%CO + \%CO_2) 9.546/100)/(1 + (\%CO + \%CO_2)/100)$$

4. The inlet temperature is measured with a “K” type thermocouple positioned in the premixer, 0.025 m below the nozzle.
5. The reactor wall temperature is measured with an optical pyrometer through 6 mm holes for optical access.
6. The measured mole fractions of O<sub>2</sub>, CO<sub>2</sub>, CO, NO<sub>x</sub>, and N<sub>2</sub>O are in volume percent or ppm by volume of dry gas, and are referred to “as measured” (See the tables of the reactor profiles). The “as measured” data are corrected for the estimated 2.2% of water remaining in the sampling line downstream of the water trap and for air leaks into the sampling line (expressed as %O<sub>2</sub>) to obtain true dry data. The air leaks are small and measured as 0.1% O<sub>2</sub> or below. The wet corrected data are obtained by dividing the dry data by the ratio of wet to dry combustion product gas, calculated based on the calculated fuel-air equivalence ratio. The CO data listed are not

corrected for CO oxidation in the probe. The following formulas show the exact method for calculation:

[wet data] = [as measured data]  $[1.022/((100-\%O_2/0.21)/100)]/[wet/dry]$ , where

$$[wet/dry] = [(9.546 + \phi)]/[9.546 - \phi]$$

7. The NO<sub>x</sub> conversion to 15% O<sub>2</sub> is done based on the dry NO<sub>x</sub> mole fraction and the O<sub>2</sub> calculated for complete combustion. That is:

$$[NO_x, \text{ppmv, dry, 15\% O}_2] = [NO_x, \text{ppmv, dry}] [5.95/(20.95 - 100(2-2\phi)/(9.546-\phi))]$$

8. The pressure difference across the nozzle,  $\Delta p$ , is measured by a differential pressure gage.

***** 6.5 atm EXPERIMENTAL DATA *****														
	RESIDENCE	FUEL-AIR	INLET	WALL	AIR	CH4	TOTAL	WET CORRECTED DATA					NOx	NOZZLE
	TIME	EQUIVALENCE	TEMP	TEMP	flow	flow	flow	O2	CO2	CO	NOx	N2O	[ppmv,dry]	ΔP
	[ms]	RATIO	[degC]	[K]	[g/s]	[g/s]	[g/s]	[%]	[%]	[%]	[ppm]	[ppm]	15% O2]	[psi]
*** 4.0 ms Jan 1997***	4.05	0.73			0.433	0.018	0.451		7.11	0.019	10.3		4.8	<3
*** 3.5 ms Jan 1997***	3.51	0.72			0.500	0.020	0.520		6.99	0.020	8.8	1.35	4.2	3
*** 3 ms Jan 1997***	3.03	0.71			0.581	0.023	0.603	5.7	6.89	0.025	7.8	1.59	3.8	3.75
*** 2.5 ms Jan 1997***	2.50	0.69		1378	0.704	0.026	0.730	6.3	6.66	0.053	6.3	1.42	3.1	5.2
*** 2 ms Jan 1997***	2.04	0.70		1383	0.860	0.033	0.893	6.1	6.75	0.064	7.5		3.7	7.0
*** 1.5 ms Jan 1997***	1.48	0.67		1393	1.185	0.037	1.222	6.1	6.48	0.124	9.6		4.8	12.0
*** 1 ms Jan 1997***	0.99	0.71		1458	1.775	0.059	1.833	6.0	6.65	0.277	9.1		4.4	
*** 0.5 ms Jan 1997***	0.54	0.75		1533	3.238	0.120	3.358	5.2	6.85	0.411	12.0		5.5	77.0
** 3.5 ms July 29, 1997**	3.45	0.70		1230	0.509	0.020	0.530	6.3	6.80	0.027	7.7		3.8	3.1
** 2.5 ms July 29, 1997**	2.40	0.69		1245	0.732	0.028	0.760	6.5	6.64	0.069	7.6		3.8	5.2
** 1.5 ms July 29, 1997**	1.64	0.69	54	1310	1.068	0.001	1.068	6.4	6.67	0.117	8.5		4.2	10.2
** 3.5 ms Jan 15, 1998**	3.55	0.70	103	1343	0.495	0.021	0.515	5.6	6.82	0.035	7.8		3.8	
** 2.5 ms Jan 15, 1998**	2.44	0.68		1383	0.721	0.028	0.749	6.0	6.58	0.073	6.9		3.5	
*** 1 ms May 4, 1998***	1.22	0.68	87		1.440	0.054	1.494	6.1	6.44	0.256	8.4		4.2	19.8
*** 1 ms May 4, 1998***	1.22	0.68	87		1.449	0.054	1.503	6.2	6.38	0.292	8.1		4.0	19.8
*** 1 ms May 4, 1998***	1.08	0.67	86	1030	1.627	0.060	1.687	6.1	6.22	0.345	8.5		4.3	26
** 2.5 ms July 15, 1998**	2.43	0.71	91	1105	0.721	0.028	0.749	5.8	6.83	0.058	8.0		3.9	5.6
*** 2 ms July 15, 1998***	2.00	0.69	89	1170	0.879	0.034	0.913	5.8	6.63	0.096	8.0		4.0	7.6
*** 3 ms July 17, 1998***	3.05	0.71	103	1165	0.575	0.024	0.599	5.6	6.87	0.025	8.7		4.2	3.8
** 2.5 ms July 17, 1998**	2.52	0.70	95		0.695	0.028	0.723	5.7	6.80	0.040	8.6		4.2	
*** 2 ms July 17, 1998***	2.07	0.69	91	1180	0.846	0.034	0.880	5.7	6.71	0.072	8.6		4.2	6.9
** 2.5 ms July 17, 1998**	2.44	0.62	300	1210	0.721	0.026	0.747	7.4	6.06	0.028	7.1		3.9	7.2
*** 3 ms July 17, 1998***	3.04	0.63	300	1160	0.579	0.022	0.601	7.3	6.21	0.021	7.4		4.0	5.2
*** 3 ms July 17, 1998***	2.93	0.65	300	1160	0.601	0.019	0.619	6.8	6.33	0.019	8.7		4.5	3.8
*** 4 ms July 17, 1998***	4.08	0.67	300	1155	0.431	0.016	0.448	6.5	6.51	0.019	10.0		5.1	3.05
** 4.0 ms Sept. 10, 1998**	3.97	0.66	300	1160	0.444	0.016	0.460	6.8	6.44	0.018	10.0		5.1	3
** 2.1 ms Sept. 10, 1998**	2.09	0.61	303	1180	0.843	0.027	0.871	7.6	5.96	0.024	7.4		4.1	9.4
** 1.2 ms Sept. 10, 1998**	1.20	0.59	301	1260	1.468	0.044	1.512	7.9	5.78	0.060	7.5		4.3	28
** 1.2 ms Sept. 10, 1998**	1.19	0.67		1220	1.474	0.051	1.526	6.4	6.26	0.269	8.1		4.1	21
** 2.1 ms Sept. 10, 1998**	2.10	0.67		1140	0.839	0.030	0.869	6.3	6.47	0.061	7.5		3.8	7.2
* 0.89 ms Sept. 16, 1998*	0.88	0.69		1320	1.990	0.053	2.043	6.2	6.33	0.381	9.3		4.6	34
* 0.89 ms Sept. 16, 1998*	0.88	0.58	300	1300	2.009	0.058	2.067	8.2	5.55	0.151	6.5		3.8	48
* 0.75 ms Sept. 16, 1998*	0.75	0.58	297	1300	2.371	0.069	2.440	8.3	5.51	0.194	6.3		3.7	66
** 1.5 ms Sept. 16, 1998**	1.49	0.58	301	1250	1.184	0.035	1.219	8.1	5.70	0.059	6.2		3.6	21
** 1.5 ms Sept. 16, 1998**	1.50	0.66	64	1250	1.173	0.040	1.214	6.7	6.25	0.181	7.6		3.9	14
** 1.5 ms Dec.17, 1998**	1.54	0.67	78	1160	1.143	0.040	1.183	6.5	6.33	0.198	7.7		3.9	12
** 1.0 ms Dec.17, 1998**	1.00	0.68	67	1210	1.758	0.063	1.821	6.0	6.36	0.328	9.1		4.5	26
** 0.9 ms Dec.17, 1998**	0.90	0.69	66	1225	1.959	0.071	2.030	5.9	6.36	0.354	9.5		4.7	32
** 1.6 ms Dec.21, 1998**	1.57	0.59	300	1195	1.129	0.034	1.164	7.9	5.78	0.079	6.8		3.9	17
** 1.0 ms Dec.21, 1998**	1.03	0.58	300	1230	1.724	0.051	1.775	8.0	5.59	0.170	6.8		3.9	36
*** 0.9 ms Feb11, 1999***	0.92	0.67	50	1210	1.917	0.069	1.986	6.0	6.18	0.354	9.1	2.0	4.6	32

***** 4.7 atm EXPERIMENTAL DATA *****														
	RESIDENCE	FUEL-AIR	INLET	WALL	AIR	CH4	TOTAL	WET CORRECTED DATA					NOx	NOZZLE
	TIME	EQUIVALENCE	TEMP	TEMP	flow	flow	flow	O2	CO2	CO	NOx	N2O	[ppmv,dry	ΔP
	[ms]	RATIO	[degC]	[K]	[g/s]	[g/s]	[g/s]	[%]	[%]	[%]	[ppm]	[ppm]	15% O2]	[psi]
*** 3 ms May 1997***	3.08	0.69			0.418	0.017	0.435	5.9	6.73	0.051	8.1	1.6	4.0	3
*** 2.5 ms May 1997***	2.50	0.69			0.516	0.021	0.537	6.1	6.62	0.080	7.6	1.8	3.8	3.9
*** 2 ms May 1997***	2.01	0.68			0.641	0.025	0.666	6.2	6.50	0.136	6.9	1.9	3.5	5.6
*** 1.5 ms May 1997***	1.58	0.69		1210	0.812	0.031	0.843	6.2	6.53	0.195	7.3	2.0	3.6	8.5
*** 1 ms May 1997***	1.07	0.71		1245	1.196	0.047	1.243	5.8	6.57	0.314	9.1	1.9	4.4	
*** 3.5 ms July29, 1997***	3.64	0.72		1210	0.353	0.015	0.368	5.5	7.02	0.035	10.9		5.1	2.4
*** 3 ms July29, 1997***	3.01	0.71		1220	0.427	0.017	0.444	6.0	6.85	0.045	9.1		4.4	3.1
*** 2.5 ms July29, 1997***	2.46	0.70		1200	0.522	0.021	0.543	6.3	6.79	0.059	7.8		3.8	4.1
*** 2 ms July29, 1997***	2.05	0.69		1260	0.627	0.024	0.652	6.4	6.63	0.088	8.1		4.0	5.7
*** 1.5 ms July29, 1997***	1.57	0.70		1350	0.820	0.032	0.852	6.3	6.66	0.152	8.5		4.2	8.5
*** 1 ms July29, 1997***	1.05	0.71		1350	1.226	0.048	1.275	6.1	6.65	0.273	8.6		4.1	18
** 0.89 ms July29, 1997**	0.90	0.72			1.428	0.056	1.484	5.8	6.71	0.281	10.3		4.9	24
*** 3.5 ms Jan.15, 1998***	3.56	0.74	119	1110	0.359	0.016	0.375	4.9	7.09	0.070	11.0		5.1	2.3
*** 2.5 ms Jan.15, 1998***	2.59	0.71		1250	0.495	0.020	0.516	5.6	6.83	0.073	8.2		3.9	3
*** 1.5 ms Jan.15, 1998***	1.43	0.70	87	1120	0.896	0.035	0.931	5.7	6.56	0.230	8.8		4.3	9.2
*** 3.5 ms Jan.8, 1998***	3.53	0.75		1180	0.362	0.016	0.378	4.9	7.25	0.028	12.1		5.5	<2.5
*** 2.6 ms Jan.8, 1998***	2.61	0.72	107	1220	0.491	0.020	0.511	5.6	6.88	0.113	8.8		4.2	3.5
*** 1.5 ms Jan.8, 1998***	1.46	0.70	86	1360	0.880	0.035	0.915	6.0	6.70	0.173	7.9		3.8	9
*** 1 ms April 1998***	1.04	0.70	101	1160	1.251	0.049	1.300	5.7	6.53	0.312	10.3		5.0	21
*** 1 ms May 4, 1998***	1.07	0.69		1120	1.208	0.047	1.255	6.0	6.45	0.327	8.9		4.4	19.5
*** 3.5 ms May 11, 1998***	3.72	0.72	137	1080	0.347	0.016	0.363	5.1	6.97	0.027	11.7	1.0	5.6	
*** 3.5 ms May 11, 1998***	3.74	0.66	307	1110	0.347	0.014	0.362	6.4	6.40	0.022	9.4	0.9	4.9	
*** 2.5 ms May 11, 1998***	2.48	0.62	304	1110	0.524	0.019	0.543	7.4	6.02	0.040	6.3	1.5	3.4	
*** 2 ms May 11, 1998***	2.08	0.60	306		0.625	0.022	0.647	7.6	5.83	0.056	5.5	1.9	3.1	7.7
*** 2 ms July 15, 1998***	2.06	0.70	104		0.622	0.025	0.647	5.6	6.75	0.099	8.7		4.2	5.6
*** 2.5 ms July 15, 1998***	2.48	0.71	111	1085	0.516	0.021	0.537	5.5	6.90	0.061	9.1		4.3	4.2
*** 3 ms July 15, 1998***	2.91	0.72	118	1080	0.439	0.019	0.458	5.3	6.98	0.044	9.2		4.4	3.2
*** 1.5 ms July 17, 1998***	1.59	0.61	301	1240	0.808	0.029	0.837	7.6	5.93	0.074	8.5		4.7	12.7
*** 1.5 ms Sept.4, 1998***	1.56	0.61	298	1230	0.826	0.027	0.852	7.5	5.94	0.069	7.8		4.3	13.2
*** 1 ms Sept.4, 1998***	1.09	0.60	304	1290	1.184	0.037	1.220	7.8	5.82	0.124	7.8		4.3	25
*** 0.9 ms Sept.4, 1998***	0.93	0.61	302	1315	1.385	0.042	1.427	7.6	5.88	0.170	8.1		4.5	33
*** 3.1 ms Sept.10, 1998**	3.13	0.72	74	1130	0.409	0.016	0.426	5.4	6.98	0.031	11.1		5.3	3
** 1.6 ms Dec.17, 1998 **	1.51	0.67	106	1160	0.849	0.029	0.878	6.3	6.38	0.158	8.2		4.2	9.2
*** 1.0 ms Dec.17, 1998***	0.97	0.68	83	1195	1.324	0.045	1.369	5.9	6.38	0.298	9.1		4.5	20
** 0.85 ms Dec.17, 1998**	0.82	0.69	76	1200	1.570	0.054	1.625	5.8	6.35	0.358	9.8		4.9	27
*** 1.6 ms Dec. 21, 1998***	1.58	0.60	300	1175	0.816	0.026	0.842	7.7	5.87	0.073	7.6		4.3	11.8
*** 1.0 ms Dec. 21, 1998**	1.02	0.59	300	1210	1.269	0.038	1.308	7.9	5.68	0.170	7.3		4.2	28
** 0.85 ms Dec. 21, 1998**	0.85	0.59	300	1225	1.515	0.046	1.561	7.8	5.64	0.220	7.5		4.3	39
*** 2 ms Jan. 1999***	1.99	0.67	68.5	1070	0.645	0.022	0.667	6.3	6.44	0.142	8.3		4.2	5.45
** 0.84 ms Jan. 1999***	0.84	0.68	57	1140	1.525	0.052	1.578	6.4	5.96	0.647	8.6		4.3	26
*** 3.5 ms Feb. 2, 1999***	3.56	0.73	143	1030	0.361	0.014	0.375	5.0	7.08	0.025	12.3	0.9	5.7	2.35
*** 3 ms Feb. 2, 1999***	3.02	0.72	137	1030	0.425	0.016	0.441	5.4	6.96	0.026	11.1	1.2	5.3	2.75
*** 2.5 ms Feb. 2, 1999***	2.40	0.70	128	1060	0.536	0.019	0.556	5.7	6.76	0.044	9.8	1.4	4.8	3.8
*** 2 ms Feb. 2, 1999***	2.00	0.69	122	1075	0.644	0.023	0.667	5.8	6.62	0.079	9.1	1.4	4.5	5.4
*** 1.5 ms Feb. 2, 1999***	1.51	0.68	94	1155	0.852	0.030	0.881	6.0	6.49	0.174	8.9	2.0	4.4	9.4
** 0.88 ms Feb. 2, 1999**	0.84	0.69	84	1190	1.529	0.053	1.582	5.9	6.28	0.460	9.6	1.5	4.7	26
*** 3 ms Feb. 2, 1999***	3.03	0.67	300	1100	0.423	0.015	0.438	6.4	6.52	0.020	10.6	0.9	5.4	3.4
*** 2.5 ms Feb. 2, 1999***	2.41	0.64	300	1140	0.537	0.018	0.554	6.7	6.29	0.027	9.3	1.3	4.9	
*** 2 ms Feb. 2, 1999***	2.01	0.63	300	1140	0.642	0.021	0.663	7.1	6.15	0.034	8.6	1.3	4.6	7.2
*** 1 ms Feb. 2, 1999***	0.92	0.61	300	1190	1.401	0.042	1.443	7.5	5.91	0.117	8.5	1.8	4.7	32
*** 3.5 ms Feb. 11, 1999**	3.52	0.72	130	1090	0.365	0.016	0.380	5.2	7.01	0.025	11.7		5.5	2.4
*** 3.5 ms Feb. 11, 1999**	3.53	0.68	300	1100	0.365	0.015	0.379	5.8	6.62	0.023	11.4		5.7	2.6
** 0.89 ms Feb. 11, 1999**	0.86	0.68			1.500	0.052	1.552	6.0	6.30	0.387	9.8		4.9	25.5
** 2.5 ms March 2, 1999**	2.44	0.68	127		0.527	0.020	0.548	6.0	6.61	0.079	9.1		4.5	4
** 1.5 ms March 2, 1999**	1.53	0.67	112		0.840	0.031	0.871	6.4	6.20	0.327	8.6		4.4	8.6
*** 1 ms March 2, 1999***	1.04	0.66	102	1150	1.243	0.046	1.288	6.7	5.85	0.658	8.4		4.3	18
*** 2 ms March 2, 1999***	2.03	0.67	121	1085	0.634	0.024	0.658	6.3	6.35	0.166	8.3		4.2	5.5

***** 3.0 atm EXPERIMENTAL DATA *****														
	RESIDENCE	FUEL-AIR	INLET	WALL	AIR	CH4	TOTAL	WET CORRECTED DATA					NOx	NOZZLE
	TIME	EQUIVALENCE	TEMP	TEMP	flow	flow	flow	O2	CO2	CO	NOx	N2O	ppmv.dry	ΔP
	[ms]	RATIO	[degC]	[K]	[g/s]	[g/s]	[g/s]	[%]	[%]	[%]	[ppm]	[ppm]	15% O2]	[psi]
*** 3 ms Sept. 98***	2.91	0.76	154	1140	0.283	0.013	0.297	4.79	7.34	0.053	15.1		6.8	2.4
*** 2 ms Sept. 98***	1.96	0.72	140	1200	0.424	0.018	0.442	5.362	6.91	0.086	11.7		5.5	4.4
*** 1 ms Sept. 98***	0.95	0.70	96	1240	0.875	0.035	0.910	6.1	6.51	0.308	10.2		5.0	15.5
*** 3.5 ms Sept. 98***	3.33	0.80	159	1110	0.248	0.012	0.260	3.9	7.65	0.067	20.5		8.8	2.0
*** 2.5' ms Sept. 98***	2.40	0.74	145	1150	0.344	0.016	0.360	5.1	7.09	0.076	14.0		6.5	3.4
*** 1.5 ms Sept. 98***	1.57	0.70	132	1185	0.528	0.022	0.550	5.8	6.69	0.157	10.6		5.2	6.2
** 1.6 ms Dec. 17, 1998**	1.63	0.69	135	1120	0.508	0.018	0.526	6.1	6.63	0.150	9.6		4.7	5.8
** 1.0 ms Dec. 17, 1998**	1.00	0.69	114	1160	0.827	0.030	0.857	6.0	6.46	0.300	9.6		4.7	13.9
* 0.67 ms Dec. 17, 1998*	0.67	0.71	98		1.231	0.045	1.277	5.6	6.45	0.462	10.6		5.1	28.5
*** 2.5 ms Feb.9, 1999***	2.35	0.72	81	1050	0.352	0.015	0.367	5.4	6.92	0.076	11.2	1.4	5.3	3.15
*** 3.5 ms Feb.9, 1999***	3.32	0.78		1010	0.249	0.012	0.260	4.0	7.47	0.059	16.8	1.0	7.4	<2
*** 1.5 ms Feb.9, 1999***	1.64	0.69	76	1080	0.506	0.020	0.526	5.7	6.64	0.142	10.1	1.4	4.9	5.6
*** 1 ms Feb.9, 1999***	1.01	0.69	68	1110	0.820	0.032	0.852	5.8	6.39	0.340	9.8	1.2	4.8	13.9
*** 1 ms Feb.9, 1999***	1.02	0.62	300	1160	0.818	0.029	0.846	7.5	5.92	0.167	8.2		4.5	20
*** 1.5 ms Feb.9, 1999***	1.65	0.64	300	1130	0.506	0.018	0.523	7.0	6.17	0.077	9.0	1.6	4.8	7.85
*** 2.5 ms Feb.9, 1999***	2.36	0.67	300	1075	0.351	0.014	0.366	6.1	6.55	0.051	10.9	1.2	5.5	4.3
*** 3.5 ms Feb.9, 1999***	3.33	0.74	300	1045	0.248	0.011	0.259	4.8	7.16	0.044	16.0	0.7	7.4	2.3
** 2.5 ms Feb.18, 1999**	2.38	0.72	89		0.348	0.015	0.363	5.3	6.94	0.079	11.7		5.5	
** 2.5 ms Feb.18, 1999**	2.39	0.68	300		0.348	0.014	0.362	6.1	6.56	0.056	11.0	1.4	5.5	



\*\*\*\*\* 4.7 atm PROFILES as measured\*\*\*\*\*

\*\*\*3.0 ms May 97\*\*\*

x	% CO2	% CO	ppm NOx	ppm N2O	% O2	TC Temp (°C)	PHI
5	7.70	0.088	8.9	3.05	6.7	1470	0.69
4	7.60	0.098	9.2	1.84	6.75		0.68
3	7.45	0.220	9.1	1.86	6.9	1516	0.68
2	5.65	0.695	7.5	1.39	9.3	1526	0.57
1	3.10	0.400	4.5	0.78	14	1517	0.32
0	3.50	0.444	5.2	0.86	13.2	1315	0.36

\*\*\*2.5 ms May 97\*\*\*

x	% CO2	% CO	ppm NOx	ppm N2O	% O2	TC Temp (°C)	PHI
5	7.32	0.208	8.2	2.32	7.05		0.67
4	7.45	0.090	8.55	2.08	7		0.67
3	7.18	0.283	7.8	2	7.2		0.66
2	5.35	0.621	6	1.45	9.85		0.54
1	2.8	0.319	3.1	0.76	14.3		0.29
0	3.2	0.335	3.55	0.77	13.7		0.33

\*\*\*2.0 ms May 97\*\*\*

x	% CO2	% CO	ppm NOx	ppm N2O	% O2	TC Temp (°C)	PHI
5	7.08	0.36	7.4	2.5	7.4		0.66
4	7.30	0.15	7.8	2.1	7.1		0.66
3	7.00	0.35	7.0		7.4		0.65
2	5.20	0.63	5.3		9.9		0.53
1	2.40	0.24	2.3	0.7	15.0		0.25
0	2.81	0.28	2.6	0.7	14.3		0.29

\*\*\*1.5 ms May 97\*\*\*

x	% CO2	% CO	ppm NOx	ppm N2O	% O2	TC Temp (°C)	Pyro Temp (°C)	PHI
5	7.05	0.46	7.65	2.2	7.35	1482		0.67
4	7.35	0.22	8.25	2.25	7.1	1500		0.67
3	7.06	0.38	7.9		7.35	1510		0.66
2	5.47	0.67	6.1	1.62	9.7	1525		0.55
1	2.75	0.30	2.85		14.6	1507		0.28
0	2.78	0.28	2.85		14.6	1270		0.28

\*\*\*1.0 ms May 97\*\*\*

x	% CO2	% CO	ppm NOx	ppm N2O	% O2	TC Temp (°C)	Pyro Temp (°C)	PHI
5	6.9	0.71	9.05	1.93	7.2			0.67
4	7.42	0.36	10.3	2.1	6.7			0.67
3	7.05	0.51	8.95	1.47	7.15			0.67
2	5.04	0.71	6.75		10.3			0.67
1	2.86	0.34	3.85		14.3			0.67
0	2.58	0.29	3.65		14.8			0.67

\*\*\*1.0 ms July29, 1997\*\*\*

x	% CO2	% CO	ppm NOx	ppm N2O	% O2	TC Temp (°C)	PHI
5	7.27	0.508	10		7.05		0.69
4	7.55	0.310	9.8		6.9		0.70
3	7.40	0.403	10.3				0.69
2	5.90	0.875	9.1		9.1		0.61
1	3.30	0.427	5				0.34
0	3.10	0.373	4.8		14.1		0.32

\*\*\*3.5 ms July29, 1997\*\*\*

x	% CO2	% CO	ppm NOx	ppm N2O	% O2	TC Temp (°C)	PHI
5	8.2	0.036	12.8				0.73
4	8	0.040	12.4		6.3		0.71
3	7.85	0.176	12.5				0.71
2	6.17	0.787	9.8		8.6		0.62
1	3.67	0.555	6.35				0.39
0	4.3	0.715	7.75		11.8		0.46

\*\*\*1.5 ms Jan. 15, 1998\*\*\*

x	% CO2	% CO	ppm NOx	ppm N2O	% O2	TC Temp (°C)	Pyro Temp (°C)	PHI
5	7.25	0.410	9.8	2	6.6	1532		0.68
4	7.43	0.260	10	4.5	6.5	1535		0.68
3	7	0.494	8.7	0	-	1525		0.67
2								
1								
0								

\*\*\*2.5 ms Jan. 15, 1998\*\*\*

x	% CO2	% CO	ppm NOx	ppm N2O	% O2	TC Temp (°C)	Pyro Temp (°C)	PHI
5	7.69	0.083	9	-	6.4	1530		0.69
4	7.75	0.083	9.3	2.3	6.4	1534		0.69
3	7.28	0.431	8.55	0	6.8	1529		0.68
2								
1								
0								

\*\*\*3.5 ms Jan. 15, 1998\*\*\*

x	% CO2	% CO	ppm NOx	ppm N2O	% O2	TC Temp (°C)	Pyro Temp (°C)	PHI
5	8.13	0.048	11.3	4	5.4	1523		0.72
4	8.1	0.080	12.6	5.5	5.55	1534		0.72
3	7.75	0.352	11.5	0.5	6	1530		0.72
2								
1								
0								

\*\*\*1 ms Sept.4, 1998\*\*\*preheated

x	% CO2	% CO	ppm NOx	ppm N2O	% O2	TC Temp (°C)	PHI
5	6.56	0.124	6.8	0	8.5	1535	0.598
4	6.46	0.138	6.4	0	8.7	1532	0.591
3	6.48	0.155	6.6	0	8.8	1532	0.594
2	6.22	0.303	6.4	0	8.8	1533	0.585
1	5.10	0.667	5.6	0	10.2	1528	0.521
0	2.66	0.313	3	0	14.6	1530	0.276

\*\*\*0.9 ms Sept.4, 1998\*\*\*preheated

x	% CO2	% CO	ppm NOx	ppm N2O	% O2	TC Temp (°C)	PHI
5	6.55	0.181	6.6	0	8.5	1533	0.602
4	6.54	0.189	6.8	0.1	8.5	1533	0.602
3	6.45	0.194	6.8	0.1	8.6	1533	0.595
2	6.26	0.298	6.4	0.1	8.9	1531	0.587
1	5.08	0.710	5.5	0.2	10.2	1531	0.522
0	4.08	0.414	4	-	13.8		0.411

\*\*\*1.5 ms Sept.4, 1998\*\*\* preheated

x	% CO2	% CO	ppm NOx	ppm N2O	% O2	TC Temp (°C)	PHI
5	6.65	0.074	6.2	0	8.3	1533	0.60
4	6.60	0.077	6.4	0	8.3	1531	0.60
3	6.63	0.082	6.2	0.1	8.3	1532	0.60
2		0.194					
1							
0							

\*\*\*3.1 ms Sept 10, 1998\*\*\*

x	% CO2	% CO	ppm NOx	ppm N2O	% O2	TC Temp (°C)	PHI
5	7.95	0.035	10.4	3.4	6.1	1528	0.706
4	7.92	0.033	10.5	4	6.1	1529	0.703
3	7.92	0.037	10	3.5	6.1	1526	0.704
2	7.85	0.179	11.5	1.5	6.1	1533	0.709
1	6.45	0.845	10	0.2	7.7	1532	0.649
0	2.62	0.470	4.2	0.2	14.4	1527	0.266

\*\*\*1.6 ms Dec. 17, 1998\*\*\*

x	% CO2	% CO	ppm NOx	ppm N2O	% O2	TC Temp (°C)	PHI
5	0.300					5	0.569
4	0.178					4	0.337
3	0.270					3	0.435
2	0.548					2	0.763
1	0.363					1	0.462
0	0.089					0	0.088

\*\*\*1.0 ms Dec. 17, 1998\*\*\*

x	% CO2	% CO	ppm NOx	ppm N2O	% O2	TC Temp (°C)	PHI
5	0.57					5	0.10
4	0.41					4	0.08
3	0.53					3	0.15
2	0.83					2	0.38
1	0.42					1	0.59
0	0.09					0	0.19

\*\*\*0.85 ms Dec. 17, 1998\*\*\*

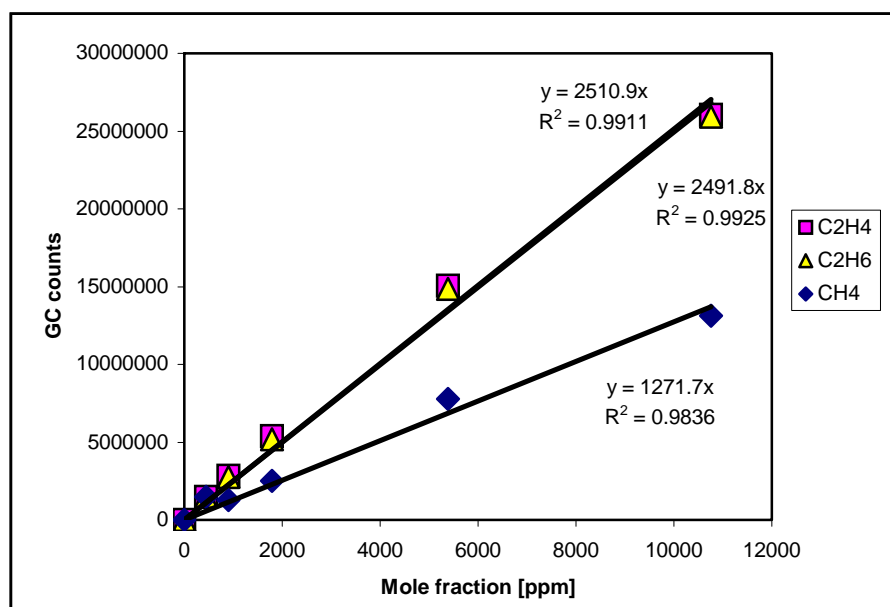
x	% CO2	% CO	ppm NOx	ppm N2O	% O2	TC Temp (°C)	PHI
5	0.57					5	0.10
4	0.41					4	0.08
3	0.53					3	0.15
2	0.83					2	0.38
1	0.42					1	0.59
0	0.09					0	0.19

\*\*\*1.6 ms Dec. 21, 1998\*\*\*

x	% CO2	% CO	ppm NOx	ppm N2O	% O2	TC Temp (°C)	PHI
5	0.27					5	0.36
4	0.19					4	0.24
3	0.24					3	0.27
2	0.44					2	0.48
1	0.60					1	0.66
0	0.17					0	0.16

***** 3.0 atm PROFILES as measured*****																															
*** 3 ms Sept. 98***						TC		Pyro		*** 2 ms Sept. 98***						TC		Pyro		*** 1 ms Sept. 98***						TC		Pyro			
x	%	%	ppm	ppm	%	Temp	Temp	1140	(°C)	x	%	%	ppm	ppm	%	Temp	Temp	1200	(°C)	x	%	%	ppm	ppm	%	Temp	Temp	1240	(°C)		
	CO2	CO	NOx	NO	O2	(°C)	PHI				CO2	CO	NOx	NO	O2	(°C)	PHI				CO2	CO	NOx	NO	O2	(°C)	PHI				
5	8.37	0.076	14.5	9.4	5.4	1528	0.74			5	7.87	0.129	10.6	5.9	6.1	1534	0.71			5	7.08	0.638	9.05	2.35	7.1	1529	0.68				
4	8.43	0.061	15	10	5.5	1532	0.75			4	7.86	0.098	11	6.5	6.1	1530	0.70			4	7.38	0.349	9.3	3.5	6.9	1528	0.68				
3	8.43	0.067	15.3	10.2	5.3	1530	0.75			3	7.80	0.119	10.5	5.9	6.2	1526	0.70			3	7.37	0.351	9.7	4.1	6.8	1532	0.68				
2	8.28	0.206	15.6	9.6	5.3	1530	0.75			2	7.40	0.443	10.6	2.8	6.4	1527	0.69			2	6.93	0.632	9.1	0.8	7.2	1532	0.67				
1	6.96	0.898	13.7	0	6.7	1533	0.70			1	6.01	0.809	8.3	0	8.3	1525	0.61			1	5.18	0.821	6.6	0.1	9.9	1525	0.54				
0	3.48	0.401	6.5	0.1	12.9	1520	0.36			0	3.05	0.295	4.2	0	13.8	1527	0.31			0	2.47	0.308	3	0	14.9	1528	0.26				
*** 3.5 ms Sept. 98***						TC		Pyro		*** 2.5 ms Sept. 98***						TC		Pyro		*** 1.5 ms Sept. 98***						TC		Pyro			
x	%	%	ppm	ppm	%	Temp	Temp	1110	(°C)	x	%	%	ppm	ppm	%	Temp	Temp	1150	(°C)	x	%	%	ppm	ppm	%	Temp	Temp	1185	(°C)		
	CO2	CO	NOx	NO	O2	(°C)	PHI				CO2	CO	NOx	NO	O2	(°C)	PHI				CO2	CO	NOx	NO	O2	(°C)	PHI				
5	8.84	0.083	21	14.4	4.6	1528	0.78			5	8.08	0.108	13.5	7.6	6	1532	0.72			5	7.54	0.276	9.8	3.6	6.6	1534	0.69				
4	8.85	0.077	21.4	15	4.5	1528	0.78			4	8.10	0.087	13.7	8.2	5.85	1530	0.72			4	7.59	0.178	9.8	4	6.6	1529	0.69				
3	8.86	0.080	22	15.4	4.4	1527	0.78			3	8.10	0.097	13.8	8.4	5.8	1529	0.72			3	7.63	0.169	9.95	4.45	6.6	1532	0.69				
2	8.73	0.242	22.7	14.8	4.5	1528	0.79			2	7.95	0.303	15	7.5	5.8	1532	0.73			2	7.20	0.490	9.85	4.45	6.6	1532	0.68				
1	6.99	1.110	18	0.15	6.3	1525	0.72			1	5.87	0.930	11	0.2	8.6	1527	0.61			1	4.96	0.733	6.9	0.15	10.3	1528	0.51				
0	3.15	0.471	8.8	0.1	13.4	1525	0.33			0	2.66	0.334	5.1	0.15	14.5	1532	0.28			0	2.26	0.283	2.9	0.1	15.3	1525	0.24				
*** 1.6 ms Dec.17, 98***						*** 1.0 ms Dec.17, 98***		*** 0.67 ms Dec.17, 98***																							
x	%	CO				x	%	CO		x	%	CO																			
5	0.280					5	0.574			5	0.640																				
4	0.170					4	0.340			4	0.525																				
3	0.235					3	0.440			3	0.655																				
2	0.598					2	0.842			2	1.030																				
1	0.627					1	0.646			1	0.670																				
0	0.128					0	0.100			0																					

## HYDROCARBON MEASUREMENTS

Figure A.1 GC calibration data and best-fit functions for C<sub>2</sub>H<sub>4</sub>, C<sub>2</sub>H<sub>6</sub>, and CH<sub>4</sub>.

**HP-JSR DATA - HYDROCARBON MEASUREMENTS****1.0 ms run at 4.7 atm on May 4, 1998**

4 mm	176224	17269	11082	2	277.1	13.8	8.9
4 mm	194734	19660	12198	2	306.3	15.7	9.8
4 mm	131274	13883	7902	2	206.5	11.1	6.3
					<b>263.3</b>	<b>13.5</b>	<b>8.3</b>

**1.2 ms run at 6.5 atm on May 4, 1998**

4 mm	119153	12801	6642	2	187.4	10.2	5.3
4 mm	125198	13309	7601	2	196.9	10.6	6.1
4 mm	140336	15147	8084	2	220.7	12.1	6.5
					<b>201.7</b>	<b>11.0</b>	<b>6.0</b>

**1.2 ms run, preheated, at 6.5 atm on May 4, 1998**

4 mm	88228	8209	4946	2	138.8	6.5	4.0
4 mm	79726	6649	4558	2	125.4	5.3	3.7
					<b>132.1</b>	<b>5.9</b>	<b>3.8</b>
6 mm	16046	1825	-	2	25.2	1.5	-
6 mm	15430	2517	-	2	24.3	2.0	-
					<b>24.8</b>	<b>1.7</b>	<b>-</b>

**1.0 ms run at 6.5 atm on May 4, 1998**

4 mm	122953	15638	6231	2	193.4	12.5	5.0
4 mm	107760	14293	5155	2	169.5	11.4	4.1
					<b>181.4</b>	<b>11.9</b>	<b>4.6</b>

**0.8 ms run at 4.7 atm on January 28, 1999**

PROFILE	CH4 counts	C2H4 counts	C2H6 counts	Attenuation	CH4 PPM	C2H4 PPM	C2H6 PPM
POINT	154771	16194	10758	16	1947.3	103.2	69.1
5 mm	170314	17704	11731	16	2142.8	112.8	75.3
AVERAGE					<b>2045.0</b>	<b>108.0</b>	<b>72.2</b>
4 mm	36160	4855	1798	16	455.0	30.9	11.5
4 mm	49108	6241	2489	16	617.9	39.8	16.0
4 mm	52822	6910	2924	16	664.6	44.0	18.8
4 mm	380999	48318	23050	2	599.2	38.5	18.5
					<b>584.1</b>	<b>38.3</b>	<b>16.2</b>
3 mm	17612	2367	0	16	221.6	15.1	0
3 mm	21629	2777	0	16	272.1	17.7	0
					<b>246.9</b>	<b>16.4</b>	<b>0</b>
1 mm	517195	24962	26023	16	6507.1	159.1	167.1
1 mm	570237	25732	27518	16	7174.5	164.0	176.7
					<b>6840.8</b>	<b>161.5</b>	<b>171.9</b>
CL	1558176	8126	15789	32	39208.6	103.6	202.8
CL	3029063	15653	30262	16	38110.4	99.7	194.3
					<b>38659.5</b>	<b>101.7</b>	<b>198.5</b>

**0.9 ms run at 6.5 atm on February 11, 1999**

4 mm	7794	0	0	16	98.1	0	0
4 mm	5345	0	0	16	67.2	0	0
4 mm	66752	10462	3564	2	105.0	8.3	2.9
4 mm	120288	18870	6627	1	94.6	7.5	2.7
					<b>99.2</b>	<b>7.9</b>	<b>2.8</b>

**0.9 ms run at 4.7 atm on February 18, 1999**

4 mm	34679	4278	0	8	218.2	13.6	0
4 mm	59599	17021	2005	1	46.9	6.8	0.8
4 mm	59910	13774	1763	1	47.1	5.5	0.7
4 mm	63040	14100	1686	1	49.6	5.6	0.7
					<b>47.8</b>	<b>6.0</b>	<b>0.7</b>

**2.5 ms run at 4.7 atm on March 2, 1999**

4 mm	80038	0	0	1	62.9	0	0
4 mm	8375	0	0	1	6.6	0	0
4 mm	6850	0	0	1	5.4	0	0
4 mm	57597	0	0	1	45.3	0	0
4 mm	5188	0	0	1	4.1	0	0
					<b>24.9</b>	<b>0</b>	<b>0</b>

**APPENDIX B**

**HP-JSR GAS TEMPERATURE CALCULATIONS**

## APPENDIX B

### HP-JSR GAS TEMPERATURE CALCULATIONS

The HP-JSR true gas temperature is calculated using two approaches. The first approach is based on the heat balance for the thermocouple, and the second approach is based on the reactor heat loss. The two approaches are explained in Section 3.3.4 with the schematic of heat transfer within the HP-JSR (Figure 3.4) showing the heat fluxes (denoted by arrows in the figure) for both the thermocouple and the reactor heat balance.

The heat balance for the thermocouple surface is the following:

$$Q_{\text{conv}} = Q_{\text{rad}} + Q_{\text{condcer}}$$

where  $Q_{\text{conv}}$ ,  $Q_{\text{rad}}$ , and  $Q_{\text{condcer}}$  are net heat fluxes due to convection from gases to the thermocouple, radiation from the thermocouple to the reactor wall, and conduction through thermocouple alumina coating. They are calculated by the following formulas, which are eventually solved for the true gas temperature,  $T_g$ :

$$Q_{\text{conv}} = h (\pi DL/2) (T_g - T_s)$$

$$Q_{\text{rad}} = \epsilon_s (\pi DL/2) 5.67e-8 (T_s^4 - T_w^4)$$

$$Q_{\text{condcer}} = (T_s - T_{tc}) k_{s69} (D^2 \pi / 4) / l$$

For the convection formula, the convective heat transfer coefficient is calculated by:  $h = \text{Nu } k_{\text{air}} / D$ , where Nu is the Nusselt number for forced convection over a cylinder. For  $\text{Re}_D < 10^4$ ,  $\text{Nu} = 0.3 + (0.62 \text{Re}_D^{0.5} \text{Pr}^{0.33}) / (1 + (0.4/\text{Pr})^{2/3})^{0.25}$  (Mills, 1992, eq.4.71a / p.287);  $k_{\text{air}}$  is the thermal conductivity at the gas temperature,  $D = 0.00238$  m (3/32 in) is thermocouple probe diameter;  $L = 0.00577$  m is the radius of the widest part of the HP-

JSR cavity; factor of  $\frac{1}{2}$  is used because thermocouple reaches up to about half of reactor radius; Prandtl number is  $Pr=0.7$ ;  $Re_D = u D/\nu$ , where  $\nu$  is the kinematic viscosity at the gas temperature and pressure and  $u$  is the average velocity in the reactor. The velocity is calculated as  $u = 2 H N / (\text{reactor residence time})$  (Thornton, 1987), where the reactor height is  $H = 0.02019$  m, and  $N$  is the average number of cycles which a gas particle makes in a jet-stirred reactor. Thornton (1987) estimated:  $N = \rho_a/\rho_o D_1^2/d_o^2 (0.5+4.5 (\rho_o/\rho_a)^{0.5} d_o/H)/4$ , where  $\rho_a$  and  $\rho_o$  are the densities of the reactor and inlet gas respectively;  $D_1$  is diameter of a cylinder with height equal to  $H$  and volume equal to the reactor volume ( $V = 1.5 \text{ cm}^3$ ); and  $d_o = 0.0014$  m is the nozzle diameter. Finally,  $T_s$  is the thermocouple surface temperature.

The radiation formula was derived from the following basic formula for thermocouple radiation

$$Q_{tc} = \varepsilon_s(\pi DL/2)/(1-\varepsilon_s)(Eb_s - J_s)$$

where  $Eb_s = 5.67e-8 \cdot T_s^4$  is the blackbody emissive power of the thermocouple surface,  $J_s$  is the radiosity of the thermocouple surface, estimated based on the radiation resistance network shown in Figure B.1 as the following:  $J_s = \varepsilon_s Eb_s + (1 - \varepsilon_s)(J_w F_{sw} + J_a F_{sa} + J_s F_{ss})$ .

The radiosity of the wall,  $J_w = [\varepsilon_w Eb_w + (1 - \varepsilon_w) J_a F_{wa}] / [1 - (1 - \varepsilon_w) F_{ww}]$ , is simplified to

$J_w = Eb_w = 5.67e-8 \cdot T_w^4$ , using the assumption that the wall emissivity is  $\varepsilon_w = 1$  (assuming

black body cavity). The radiosity of the ambient,  $J_a = [\varepsilon_a Eb_a + (1 - \varepsilon_a) J_w F_{aw}] / [1 - (1 - \varepsilon_a) F_{aa}]$ , is simplified to  $J_a = \varepsilon_a Eb_a + \varepsilon_w (1 - \varepsilon_a) Eb_w$ , (where  $Eb_a = 5.67e-8 \cdot T_a^4$ ) using the

assumption that the view factors from ambient to wall and ambient to ambient are  $F_{aw} = 1$

and  $F_{aa} = 0$  respectively. The thermocouple surface emissivity is estimated as  $\varepsilon_s = 0.2$

(for alumina at elevated temperature), and the emissivity of the ambient is  $\epsilon_a = 1$  (assuming pressure vessel is a black body cavity). When formulas for  $J_a$  and  $J_w$  are substituted into the formula for  $J_s$ , and  $E_b_s$  and  $J_s$  are substituted into the equation for  $Q_{tc}$ , then after some manipulation, and with the assumption that  $F_{sw} = 1$ ,  $F_{sa} = 0$ , and  $F_{ss} = 0$ , the  $Q_{rad}$  equation is derived. Essentially, with the aforementioned assumptions, the three-body radiation problem of Figure B.1 is reduced to a two body problem.

For the conduction formula, the thermocouple junction (thermocouple bead) temperature is  $T_{tc}$ ; and the conductivity of the thermocouple coating (Ceramabond 569),  $k_{569}$  is 5.4 W/mK. The thickness of the alumina coating,  $l$ , is estimated as 0.0005 m.  $T_{tc}$  is lower than the thermocouple surface temperature,  $T_s$ , because of conduction losses.

$T_s$  is calculated from the heat balance for the thermocouple junction, which is:

$$Q_{condcer} = Q_{condwire} + Q_{condsheath}$$

where  $Q_{condcer}$ ,  $Q_{condwire}$ , and  $Q_{condsheath}$  are net heat fluxes due to conduction through the ceramic coating, through thermocouple wires, and through the thermocouple sheath. The  $Q_{condwire}$  and  $Q_{condsheath}$  are calculated by the following formulas:

$$Q_{condwire} = 2(T_{tc} - T_a) k_{wire} (d_{wire}^2 \pi/4)/(L_{wire})$$

$$Q_{condsheath} = (k_c (D^2 \pi/4) h' (D\pi))^{0.5} (T_g' - T_B) \tanh((h' (D\pi)/(k_c (D^2 \pi/4)))^{0.5} L_{wire})$$

The thermocouple wire conductivity is  $k_{wire} = 76$  W/mK; the wire diameter is  $d_{wire} = 0.000127$  m (0.005 in); the wire length is  $L_{wire} = 0.23$  m; and, the ambient temperature is  $T_a = 300$  K. The equation listed above for  $Q_{condsheath}$  is derived from equation for heat flux through a fin, with the following assumptions. The thermocouple sheath conductivity is  $k_c = 11$  W/mK; the base temperature is  $T_B = 300$  K; the temperature of the

bulk of the surrounding gas is  $T_g' = 500$  K (estimated average temperature of reactor gas and of the pressure vessel air); and the convective heat transfer coefficient is calculated as  $h = Nu k_{air}/L'$ , where Nusselt number is estimated as  $Nu = 3.66$  (Mills, 1992, eq.4.40 / p.269), and characteristic reactor length  $L' = 0.074285$  m.

The second approach for calculating the true gas temperature in the HP-JSR is based on calculating the heat loss of the reactor. That is, the heat released by combustion per unit time ( $mc_p (T_A - T_a)$ ) equals the sensible energy flow per unit time ( $mc_p(T_g - T_a)$ ) and the heat lost from the reactor per unit time ( $UA(T_g - T_a)$ ). This is represented by the equation:

$$mc_p (T_A - T_a) = (mc_p + UA) (T_g - T_a)$$

where  $m$  and  $c_p$  are the mass flow rate and the heat capacity of the gas; the  $T_A$ ,  $T_a$ , and  $T_g$  are the adiabatic, the ambient, and the true gas temperatures, respectively.  $T_A$  is estimated as  $T_A = T_{Aeq} - 80[\text{CO in reactor, \% wet}]$ , where  $T_{Aeq}$  is the adiabatic equilibrium temperature, 80 is the increase in temperature in [K] per every 1% CO in the reactor, and [CO in reactor, % wet] is the average CO volume percent in the reactor recirculation zone, defined by Equation 3.2.  $U$  is the overall heat transfer through the reactor wall, with  $UA$  estimated as 0.025 W/K.

The reactor cavity wall temperature,  $T_w$ , is calculated by setting the convective heat flux from the hot reactor gas to the reactor cavity wall equal to the conductive and radiative heat flux from the reactor cavity wall to the ambient environment. Figure 3.4 identifies these two heat fluxes by arrows in the lower right side. Therefore, the wall temperature is calculated from the following equality:

$$2LH\pi h_w(T_g - T_w) = (T_w - 450)/R$$

The convective heat flux from the hot reactor gas to the wall is  $2LH\pi h_w(T_g - T_w)$ , where  $h_w = Nu_w k_{air}/H$ , and  $Nu_w = 0.023 Re_w^{0.8} Pr^{0.4}$ . The Nusselt number formula is for thermally fully developed flow in a tube with  $Pr > 0.5$  and  $Re_w > 10^4$  (Mills, 1992, eq.4.44 / p.270).  $Re_w = uH/2\nu$ . The  $u$ ,  $H$ ,  $k_{air}$  and  $\nu$  were defined above as the average reactor velocity, the reactor height, the conductivity and the kinematic viscosity at the reactor temperature and pressure.

The conductive and radiative heat flux from the reactor cavity wall to the ambient is approximated as  $(T_w - 450)/R$ , where  $R = 30 \text{ K/W}$  is the estimated reactor heat-flux resistance, and 450 K is the estimated temperature outside the HP-JSR insulation. The radiative heat flux is negligibly small, so the estimated  $R$  value is essentially only for conduction through the reactor wall.

This calculated wall temperature,  $T_w$ , is compared to the measured wall temperature, which is corrected for the finite transmissivity through the viewing ports of the high pressure housing. That is, the measured corrected wall temperature in [K] is the measured wall temperature in [K] divided by 0.89.

The HP-JSR temperature measurements and calculations at inlet gas temperature preheated to 573 K, for 6.5, 4.7 and 3.0 atm pressures are shown in Figures B.2-4. Figures B.2-4 and Figures 3.6-8 represent a complete set of HP-JSR gas temperature calculations. In all cases, the “calculated reactor temperature” is the average of the values estimated by the thermocouple and the reactor heat loss modeling.

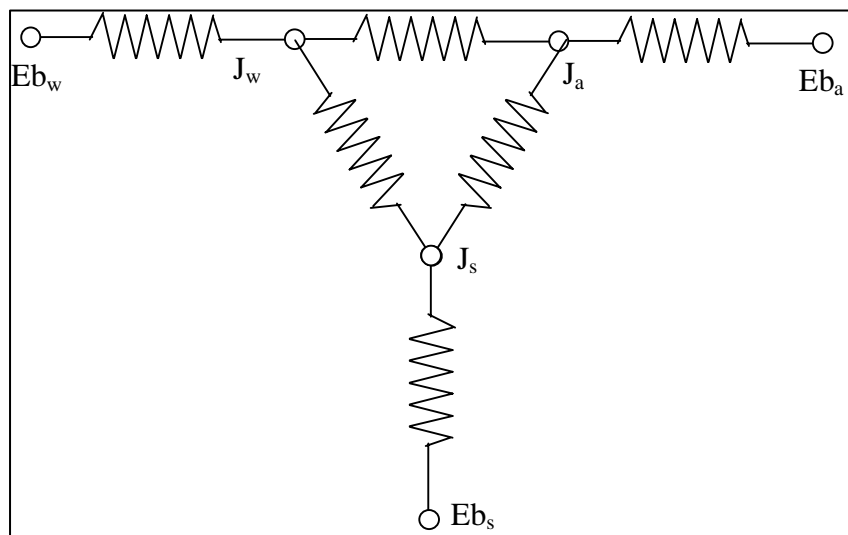


Figure B.1 Radiation resistance network

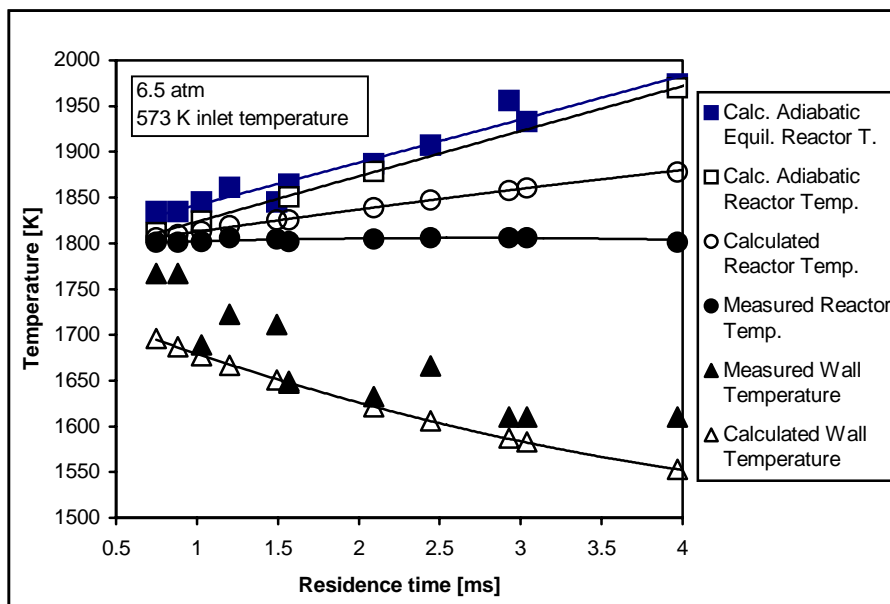


Figure B.2 HP-JSR temperature measurements and calculations for 6.5 atm data and inlet gases preheated to 573 K

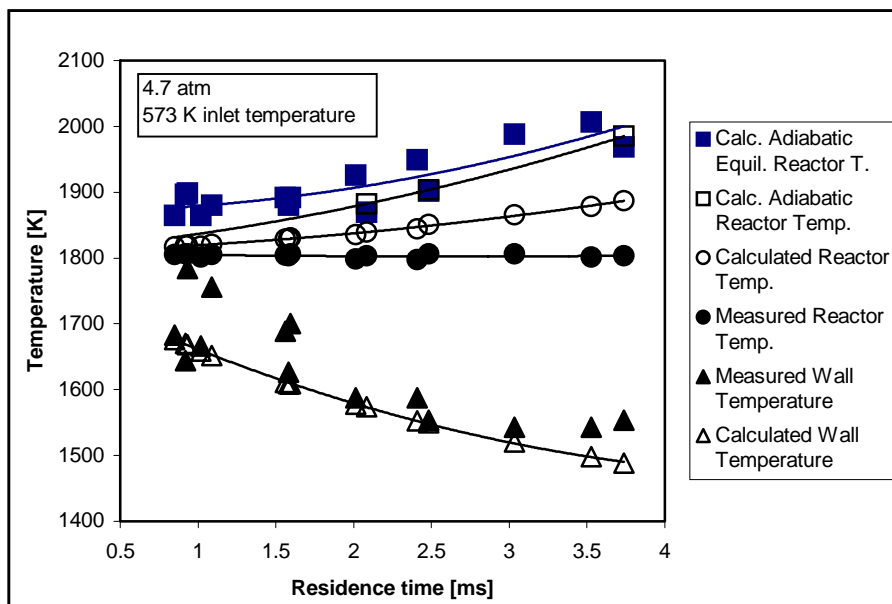


Figure B.3 HP-JSR temperature measurements and calculations for 4.7 atm data and inlet gases preheated to 573 K

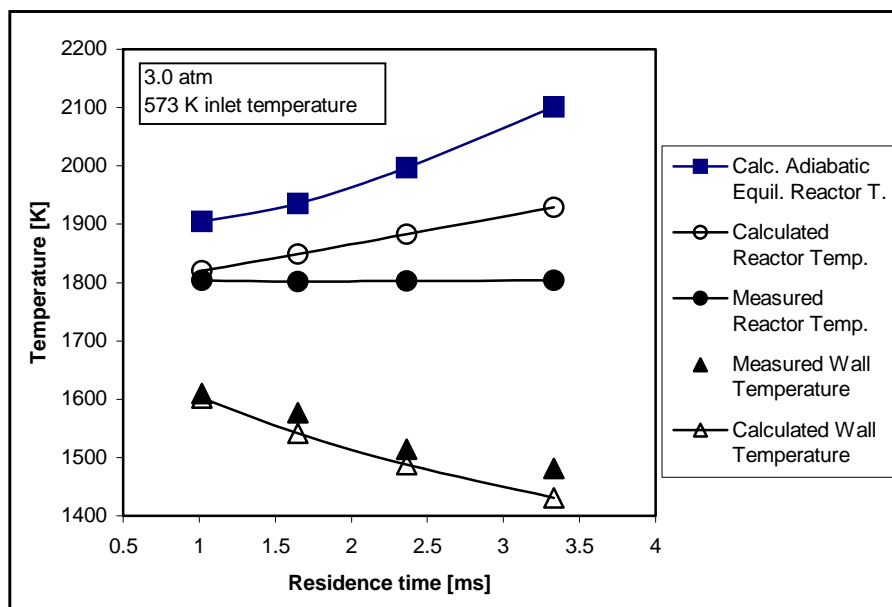


Figure B.4 HP-JSR temperature measurements and calculations for 3.0 atm data and inlet gases preheated to 573 K

GAS TEMPERATURE CALCULATION - THE THERMOCOUPLE HEAT BALANCE														THE REACTOR HEAT BALANCE											
pressure atm	res. time calc [ms]	inlet T C	average reactor		ReD	Nu	Kair W/mK	h W/m2K	Q	Q	Ts K	Q	Q	Tg	Q	Tad K	Tad-CO K	Re wall	Nu wall	h wall W/m2K	Measured	Tw [K] Estimate	UA/Cp	Tg	Tg
			condsheath W	condwire W					radiation W	gas temp K		convect W	corrected Tw [K]	gas temp K	average K										
3.0	3.33	159	3.1	37.6	878	15	0.106	654	0.114	0.013	1804	0.13	1.41	1912.3	1.53	2088	2078	3726	14	76	1554	1378.7	0.018	1963.8	1938.1
3.0	2.91	154	3.1	43.0	1003	16	0.107	699	0.114	0.013	1808	0.13	1.37	1906.9	1.50	2031	2031	4253	16	84	1588	1404.1	0.018	1933.4	1920.2
3.0	2.40	145	3.1	52.1	1216	17	0.106	768	0.114	0.013	1806	0.13	1.29	1891.0	1.41	1985	1976	5157	19	98	1599	1436.3	0.019	1896.8	1893.9
3.0	1.96	140	3.1	64.2	1500	19	0.106	851	0.114	0.013	1806	0.13	1.20	1877.9	1.33	1951	1936	6361	22	116	1655	1471.0	0.019	1865.3	1871.6
3.0	1.57	132	3.1	79.6	1861	21	0.106	946	0.114	0.013	1805	0.13	1.11	1865.1	1.23	1920	1898	7893	26	138	1638	1503.9	0.020	1839.0	1852.0
3.0	0.95	96	2.9	125.4	2932	26	0.106	1184	0.114	0.013	1804	0.13	0.92	1844.8	1.05	1888	1831	12437	38	198	1700	1565.2	0.021	1797.8	1821.3
3.0	1.63	135	3.1	76.9	1795	21	0.106	930	0.114	0.013	1806	0.13	1.13	1868.1	1.25	1909	1902	7613	25	134	1565	1499.0	0.020	1842.9	1855.5
3.0	1.00	114	3.0	122.4	2859	26	0.106	1170	0.114	0.013	1806	0.13	0.94	1847.9	1.07	1890	1838	12126	37	194	1610	1563.7	0.021	1801.1	1824.5
3.0	0.67	98	2.9	178.7	4172	32	0.106	1411	0.114	0.013	1806	0.13	0.80	1836.0	0.92	1906	1790	17694	50	263	307	1607.6	0.022	1779.9	1808.0
3.0	2.35	145	3.1	53.4	1242	17	0.107	777	0.114	0.013	1810	0.13	1.29	1894.3	1.42			5266	19	100	1487	1441.8	0.019	1892.9	1893.6
3.0	3.32	163	3.1	37.9	884	15	0.107	657	0.114	0.013	1809	0.13	1.42	1917.9	1.55			3748	14	76	1442	1382.4	0.018	1962.7	1940.3
3.0	1.64	129	3.1	75.9	1765	21	0.107	924	0.114	0.013	1811	0.13	1.15	1874.8	1.28			7484	25	132	1520	1498.6	0.020	1843.3	1859.0
3.0	1.01	110	3.0	120.6	2811	26	0.107	1161	0.114	0.013	1808	0.13	0.95	1850.7	1.08			11924	36	192	1554	1562.4	0.021	1801.7	1826.2
4.7	3.08	113	2.9	38.6	1403	18	0.106	822	0.114	0.012	1800	0.13	1.23	1876.4	1.36	1893	1920	5949	21	110		1446.5	0.019	1843.5	1860.0
4.7	2.50	105	2.9	47.1	1709	20	0.106	906	0.114	0.013	1802	0.13	1.16	1867.4	1.29	1874	1883	7249	24	129		1479.7	0.020	1821.0	1844.2
4.7	2.01	97	2.9	57.9	2094	22	0.106	1003	0.114	0.013	1805	0.13	1.08	1860.3	1.21	1856	1859	8883	29	152		1514.6	0.021	1808.6	1834.5
4.7	1.58	89	2.8	72.6	2626	25	0.106	1122	0.114	0.013	1805	0.13	0.97	1850.1	1.10	1866	1847	11140	34	182	1666	1550.5	0.021	1802.6	1826.4
4.7	1.07	78	2.8	105.4	3791	30	0.107	1348	0.114	0.013	1811	0.13	0.82	1843.4	0.95	1888	1828	16078	46	244	1706	1606.7	0.022	1801.3	1822.3
4.7	3.59	120	3.0	33.5	1213	17	0.106	766	0.114	0.013	1803	0.13	1.30	1889.0	1.43	1949	1956	5146	19	98	1666	1424.7	0.019	1867.8	1878.4
4.7	2.97	112	2.9	40.0	1448	19	0.106	836	0.114	0.013	1804	0.13	1.24	1879.2	1.36	1914		6140	21	113	1678	1453.1	0.019	1837.4	1858.3
4.7	2.42	104	2.9	48.4	1749	21	0.106	918	0.114	0.013	1806	0.13	1.16	1870.8	1.29	1900		7420	25	131	1655	1485.3	0.020	1817.9	1844.4
4.7	2.02	98	2.9	57.6	2081	22	0.106	1000	0.114	0.013	1806	0.13	1.09	1861.8	1.21	1872		8828	29	151	1722	1513.8	0.021	1808.1	1835.0
4.7	1.55	89	2.8	74.2	2681	25	0.106	1134	0.114	0.013	1806	0.13	0.97	1850.4	1.09	1882		11374	35	185	1824	1554.0	0.021	1801.9	1826.2
4.7	1.03	77	2.8	109.4	3953	31	0.106	1374	0.114	0.013	1806	0.13	0.79	1836.6	0.92	1894	1844	16769	48	252	1824	1609.5	0.022	1801.2	1818.9
4.7	0.89	73	2.8	126.3	4558	33	0.107	1475	0.114	0.013	1808	0.13	0.73	1834.7	0.86	1902		19332	54	283		1628.7	0.022	1802.3	1818.5
4.7	3.53	119	3.0	33.8	1217	17	0.107	770	0.114	0.013	1811	0.13	1.33	1898.2	1.45	1987		5164	19	98	1554	1428.9	0.019	1865.2	1881.7
4.7	2.61	107	2.9	45.1	1621	20	0.107	886	0.114	0.013	1811	0.13	1.21	1890.7	1.34	1927		6876	23	124	1711	1475.3	0.020	1824.2	1852.5
4.7	1.46	86	2.8	78.4	2838	26	0.106	1165	0.114	0.013	1804	0.13	0.94	1845.9	1.06	1890		12036	37	193	1565	1561.7	0.021	1801.8	1823.8
4.7	3.56	119	3.0	33.6	1209	17	0.107	767	0.114	0.013	1810	0.13	1.33	1897.5	1.45	1966	1949	5126	19	98	1633	1427.4	0.019	1867.1	1882.3
4.7	2.59	106	2.9	45.4	1636	20	0.107	890	0.114	0.013	1810	0.13	1.21	1879.1	1.33	1911	1887	6937	24	125	1678	1476.3	0.020	1823.6	1851.3
4.7	1.43	87	2.8	79.9	2875	26	0.107	1176	0.114	0.013	1811	0.13	0.95	1853.1	1.08	1877	1843	12197	37	196	1835	1567.4	0.021	1801.4	1827.3
4.7	1.04	101	2.9	114.3	4169	32	0.106	1404	0.114	0.012	1796	0.13	0.74	1824.2	0.87	1896		17683	50	262	1610	1611.1	0.022	1801.8	1813.0
4.7	3.72	137	3.1	33.4	1205	17	0.107	765	0.114	0.013	1809	0.13	1.32	1896.1	1.44	1950		5109	18	98	1520	1429.2	0.019	1876.7	1886.4
4.7	2.48	111	3.0	48.0	1729	20	0.107	914	0.114	0.013	1809	0.13	1.18	1874.8	1.30	1925		7333	25	130	1526	1485.4	0.020	1820.3	1847.5
4.7	2.91	118	3.0	41.3	1490	19	0.107	850	0.114	0.013	1809	0.13	1.24	1883.2	1.37	1941		6321	22	116	1520	1461.2	0.020	1835.6	1859.4
6.5	3.99	111	2.9	29.7	1441	19	0.107	841	0.114	0.013	1806	0.13	1.20	1878.8	1.33	1950	1945	6113	21	113	1509	1470.9	0.019	1883.3	1881.0
6.5	3.51	106	2.9	33.6	1630	20	0.107	895	0.114	0.013	1808	0.13	1.16	1874.3	1.29	1927	1916	6912	24	125	1509	1489.8	0.020	1861.8	1868.1
6.5	2.98	101	2.9	39.4	1912	21	0.107	967	0.114	0.013	1806	0.13	1.09	1863.9	1.21	1908	1884	8109	27	142	1509	1512.9	0.020	1843.2	1853.5
6.5	2.46	96	2.9	47.3	2298	23	0.107	1059	0.114	0.013	1806	0.13	1.01	1855.3	1.13	1869	1865	9748	31	165	1548	1541.1	0.021	1830.4	1842.8
6.5	2.01	89	2.9	57.3	2785	26	0.107	1165	0.114	0.013	1806	0.13	0.92	1847.3	1.05	1885	1860	11814	36	192	1554	1569.9	0.021	1823.7	1835.5
6.5	1.70	84	2.8	67.4	3272	28	0.107	1261	0.114	0.013	1806	0.13	0.84	1841.3	0.97			13878	41	218	1560	1593.4	0.021	1822.1	1831.7
6.5	1.46	80	2.8	77.7	3776	30	0.107	1354	0.114	0.013	1806	0.13	0.78	1836.7	0.91	1864	1837	16016	46	245	1565	1612.7	0.022	1821.0	1828.8
6.5	1.08	72	2.8	103.8	5039	35	0.107	1562	0.114	0.013	1806	0.13	0.65	1828.8	0.78			21375	58	309	1599	1649.1	0.022	1823.3	1826.1
6.5	0.98	70	2.8	113.8	5529	36	0.107	1635	0.114	0.013	1806	0.13	0.61	1826.6	0.74	1896	1845	23453	63	332	1638	1659.6	0.022	1824.0	1825.3
6.5	0.54	57	2.7	203.4	9878	48	0.107	2181	0.114	0.013	1806	0.13	0.40	1816.8	0.53	1950	1822	41899	99	529	1722	1715.0	0.023	1831.1	1824.0
6.5	0.52	57		209.3	10166	49	0.107	2213	0.114	0.013	1806	0.13	0.39	1816.5	0.52			43119	102	541	1734	1717.2	0.023	1831.2	1823.8
6.5	1.54	78		73.8	3585	29	0.107	1319	0.114	0.013	1806	0.13	0.80	1838.3	0.93			15207	44	235	1610	1605.9	0.022	1821.5	1829.9
6.5	1.00	67		111.1	5395	36	0.107	1616	0.114	0.013	1806	0.13	0.62	1827.2	0.75			22884	61	326	1666	1657.0	0.022	1824.1	1825.6
6.5	0.90	66		123.6	6003	38	0.107	1703	0.114	0.013	1806	0.13	0.58	1824.9	0.71			25461	67	355	1683	1668.7	0.022	1825.2	1825.1

GAS TEMPERATURE CALCULATION - THE THERMOCOUPLE HEAT BALANCE														THE REACTOR HEAT BALANCE													
pressure atm	res. time calc [ms]	inlet T C	average reactor				ReD	Nu	Kair W/mK	h W/m2K	Q	Q	Ts K	Q	Q	Tg	Q	Tad K	Tad-CO K	Re wall	Nu wall	h wall W/m2K	Measured	Tw [K] Estimate	UA/Cp	Tg	Tg
			condsheath W	condwire W	radiation W	gas temp K					convect W	corrected Tw [K]		gas temp K	average K												
3.0	1.02	300	4.0	159.2	3714	30	1.1E-01	1332	0.114	0.013	1807	0.13	0.82	1839.6	0.95	1905		15751	45	240	1610	1601.7	0.022	1801.1	<b>1820.4</b>		
3.0	1.65	300	4.0	97.3	2274	23	1.1E-01	1045	0.114	0.013	1805	0.13	1.00	1854.7	1.13	1935		9645	31	162	1576	1541.4	0.020	1842.1	<b>1848.4</b>		
3.0	2.36	300	3.9	66.9	1562	19	1.1E-01	868	0.114	0.013	1806	0.13	1.16	1874.1	1.28	1997		6624	23	120	1515	1488.2	0.019	1891.0	<b>1882.6</b>		
3.0	3.33	300	3.8	46.6	1088	16	1.1E-01	727	0.114	0.013	1807	0.13	1.30	1897.8	1.43	2102		4614	17	90	1481	1431.1	0.018	1959.5	<b>1928.6</b>		
4.7	3.74	300	3.9	42.2	1540	19	1.1E-01	862	0.114	0.013	1806	0.13	1.16	1874.6	1.28	1969		6531	22	119	1554	1488.1	0.019	1899.2	<b>1886.9</b>		
4.7	2.48	301	4.0	64.6	2349	24	1.1E-01	1063	0.114	0.013	1809	0.13	0.99	1857.5	1.12	1902		9964	32	166	1554	1550.2	0.021	1844.9	<b>1851.2</b>		
4.7	2.08	302	4.0	77.4	2821	26	1.1E-01	1162	0.114	0.013	1806	0.13	0.91	1846.9	1.03	1870		11965	36	192		1573.8	0.021	1832.7	<b>1839.8</b>		
4.7	1.59	303	4.0	101.6	3662	30	1.1E-01	1324	0.114	0.013	1809	0.13	0.81	1841.4	0.93	1892		15533	45	237	1700	1608.7	0.022	1820.5	<b>1830.9</b>		
4.7	1.56	304	4.0	103.9	3754	30	1.1E-01	1339	0.114	0.013	1807	0.13	0.79	1838.4	0.92	1892		15921	46	242	1689	1610.6	0.022	1819.8	<b>1829.1</b>		
4.7	1.09	305	4.0	149.7	5400	36	1.1E-01	1604	0.114	0.013	1808	0.13	0.65	1830.1	0.78	1880		22906	61	324	1756	1652.1	0.022	1812.2	<b>1821.2</b>		
4.7	0.93	306	4.0	175.7	6333	39	1.1E-01	1737	0.114	0.013	1809	0.13	0.60	1827.9	0.72	1899		26862	70	368	1784	1668.4	0.022	1810.5	<b>1819.2</b>		
4.7	1.58	307	4.0	103.1	3725	30	1.1E-01	1334	0.114	0.013	1806	0.13	0.79	1837.6	0.92	1880	1985	15800	46	240	1627	1609.2	0.022	1820.1	<b>1828.8</b>		
4.7	1.02	308	4.1	161.0	5824	37	1.1E-01	1664	0.114	0.013	1805	0.13	0.61	1825.3	0.74	1864	1903	24701	65	343	1666	1658.2	0.022	1811.4	<b>1818.4</b>		
4.7	0.85	309	4.1	192.8	6955	41	1.1E-01	1819	0.114	0.013	1808	0.13	0.56	1825.1	0.69	1864	1882	29500	75	396	1683	1676.6	0.023	1809.8	<b>1817.5</b>		
4.7	3.03	310	4.0	53.1	1915	21	1.1E-01	961	0.114	0.013	1809	0.13	1.08	1866.8	1.21	1989		8123	27	141	1543	1520.8	0.020	1865.0	<b>1865.9</b>		
4.7	2.41	311	4.0	67.6	2456	24	1.1E-01	1083	0.114	0.012	1801	0.13	0.95	1846.7	1.08	1949		10417	33	172	1588	1552.2	0.021	1841.9	<b>1844.3</b>		
4.7	2.01	312	4.1	81.3	2949	27	1.1E-01	1186	0.114	0.013	1802	0.13	0.88	1840.8	1.00	1926		12510	38	199	1588	1577.6	0.021	1830.2	<b>1835.5</b>		
4.7	0.92	313	4.1	179.3	6463	39	1.1E-01	1755	0.114	0.013	1809	0.13	0.59	1827.5	0.72	1897		27412	71	374	1644	1670.3	0.023	1810.4	<b>1819.0</b>		
4.7	3.53	314	4.0	45.7	1654	20	1.1E-01	893	0.114	0.013	1805	0.13	1.12	1869.6	1.25	2006		7015	24	125	1543	1498.2	0.020	1887.6	<b>1878.6</b>		
6.5	2.44	300	4.0	65.6	3237	28	1.1E-01	1246	0.114	0.013	1809	0.13	0.82	1843.7	0.94	1907		13731	41	215	1666	1606.3	0.021	1851.1	<b>1847.4</b>		
6.5	3.04	300	4.0	52.5	2588	25	1.1E-01	1115	0.114	0.013	1809	0.13	0.89	1851.0	1.02	1933		10978	34	180	1610	1583.3	0.021	1870.3	<b>1860.6</b>		
6.5	2.93	300	4.0	54.5	2689	25	1.1E-01	1137	0.114	0.013	1809	0.13	0.88	1849.7	1.01	1956		11406	35	185	1610	1587.1	0.021	1866.4	<b>1858.0</b>		
6.5	4.08	300	3.9	38.8	1914	21	1.1E-01	961	0.114	0.013	1809	0.13	1.00	1862.8	1.12	1988		8117	27	141	1604	1549.3	0.020	1903.7	<b>1883.3</b>		
6.5	3.97	300	3.9	39.9	1977	22	1.1E-01	975	0.114	0.013	1804	0.13	0.96	1855.4	1.09	1974	1970	8388	27	145	1610	1553.1	0.020	1900.3	<b>1877.9</b>		
6.5	2.09	300	4.0	76.9	3797	30	1.1E-01	1347	0.114	0.013	1808	0.13	0.76	1838.2	0.89	1887	1879	16104	46	244	1633	1621.3	0.022	1839.7	<b>1838.9</b>		
6.5	1.20	300	4.0	134.9	6654	40	1.1E-01	1780	0.114	0.013	1809	0.13	0.60	1827.6	0.73	1861		28222	72	383	1722	1666.5	0.023	1811.2	<b>1819.4</b>		
6.5	0.88	300	4.0	184.7	9152	47	1.1E-01	2081	0.114	0.013	1804	0.13	0.50	1817.6	0.63	1835		38818	94	493	1767	1686.9	0.023	1801.1	<b>1809.4</b>		
6.5	0.75	300	4.0	218.2	10812	51	1.1E-01	2261	0.114	0.013	1804	0.13	0.47	1815.8	0.59	1835	1812	45861	107	563	1767	1696.1	0.023	1796.9	<b>1806.3</b>		
6.5	1.49	300	4.0	108.4	5352	36	1.1E-01	1597	0.114	0.013	1808	0.13	0.66	1830.4	0.78	1845		22701	61	321	1711	1650.4	0.022	1820.5	<b>1825.4</b>		
6.5	1.57	300	4.0	103.3	5114	35	1.1E-01	1560	0.114	0.013	1805	0.13	0.66	1827.9	0.78	1865	1851	21690	59	310	1649	1646.8	0.022	1822.9	<b>1825.4</b>		
6.5	1.03	300	4.0	158.4	7840	43	1.1E-01	1928	0.114	0.013	1805	0.13	0.54	1820.7	0.67	1845	1824	33255	83	436	1689	1677.4	0.023	1805.7	<b>1813.2</b>		

**APPENDIX C****PREMIXED TURBULENT COMBUSTION CALCULATIONS**

\*\*\*UNHEATED INLET CONDITIONS\*\*\*

pressure [atm]	residence time [ms]	inlet T [degC]	PHI	kinetic viscosity [m2/s]	thermal diffusiv. [m2/s]	turbulent intensity [m/s]	laminar burning vel [m/s]	lam. flame thickness [m]	chemical time [s]	mixing time [s]	Damkohler number	Reynolds number	Kolmogorov scale [m]	turbulent burning vel [m/s]	turb.flame thickness [mm]
3.0	3.33	159	0.80	9.90E-06	1.40E-05	10.56	0.29	4.81E-05	1.66E-04	1.3E-04	0.80	1494	5.27E-06	8.64	1.71
3.0	2.91	154	0.76	9.69E-06	1.37E-05	11.47	0.25	5.44E-05	2.17E-04	1.2E-04	0.56	1657	4.87E-06	8.29	1.94
3.0	2.40	145	0.74	9.33E-06	1.31E-05	13.32	0.22	6.03E-05	2.76E-04	1.1E-04	0.38	2000	4.23E-06	8.16	2.29
3.0	1.96	140	0.72	9.12E-06	1.28E-05	15.07	0.20	6.55E-05	3.34E-04	9.3E-05	0.28	2313	3.79E-06	8.00	2.64
3.0	1.63	135	0.69	8.92E-06	1.25E-05	17.04	0.17	7.34E-05	4.30E-04	8.2E-05	0.19	2674	3.40E-06	7.56	3.16
3.0	1.57	132	0.70	8.80E-06	1.24E-05	17.51	0.17	7.1E-05	4.07E-04	8.0E-05	0.20	2784	3.30E-06	7.86	3.12
3.0	1.00	114	0.69	8.11E-06	1.14E-05	24.47	0.15	7.61E-05	5.10E-04	5.7E-05	0.11	4227	2.41E-06	8.32	4.12
3.0	0.95	96	0.70	7.43E-06	1.04E-05	25.01	0.14	7.5E-05	5.43E-04	5.6E-05	0.10	4710	2.22E-06	8.15	4.30
3.0	0.67	98	0.71	7.51E-06	1.05E-05	31.84	0.15	7.13E-05	4.85E-04	4.4E-05	0.09	5938	1.87E-06	9.71	4.59
4.7	3.72	137	0.72	5.82E-06	8.18E-06	8.51	0.15	5.52E-05	3.73E-04	1.6E-04	0.44	2049	4.15E-06	5.55	2.15
4.7	3.59	131	0.72	5.67E-06	7.96E-06	9.02	0.15	5.49E-05	3.79E-04	1.6E-04	0.41	2229	3.90E-06	5.70	2.22
4.7	3.56	119	0.74	5.36E-06	7.51E-06	8.70	0.14	5.19E-05	3.58E-04	1.6E-04	0.45	2274	3.84E-06	5.72	2.13
4.7	3.53	130	0.75	5.64E-06	7.92E-06	9.01	0.16	4.94E-05	3.08E-04	1.6E-04	0.50	2237	3.89E-06	6.21	2.03
4.7	3.08	125	0.69	5.50E-06	7.72E-06	9.98	0.12	6.46E-05	5.42E-04	1.4E-04	0.26	2541	3.53E-06	5.12	2.73
4.7	2.97	124	0.71	5.48E-06	7.69E-06	10.13	0.13	6.05E-05	4.77E-04	1.4E-04	0.29	2589	3.49E-06	5.47	2.59
4.7	2.91	118	0.72	5.33E-06	7.48E-06	10.21	0.13	5.57E-05	4.15E-04	1.4E-04	0.33	2680	3.40E-06	5.86	2.44
4.7	2.61	107	0.72	5.06E-06	7.09E-06	10.51	0.12	5.75E-05	4.66E-04	1.3E-04	0.29	2907	3.20E-06	5.63	2.61
4.7	2.59	118	0.71	5.34E-06	7.48E-06	9.90	0.12	6.07E-05	4.92E-04	1.4E-04	0.29	2596	3.48E-06	5.33	2.60
4.7	2.50	117	0.69	5.30E-06	7.43E-06	11.22	0.11	6.84E-05	6.30E-04	1.2E-04	0.20	2963	3.15E-06	5.05	3.11
4.7	2.48	111	0.71	5.16E-06	7.23E-06	11.54	0.12	5.81E-05	4.67E-04	1.2E-04	0.26	3130	3.02E-06	5.91	2.73
4.7	2.42	116	0.70	5.29E-06	7.41E-06	11.49	0.12	6.27E-05	5.31E-04	1.2E-04	0.23	3040	3.09E-06	5.55	2.90
4.7	2.02	110	0.69	5.13E-06	7.18E-06	13.34	0.11	6.84E-05	6.51E-04	1.0E-04	0.16	3639	2.70E-06	5.43	3.44
4.7	2.01	109	0.68	5.11E-06	7.16E-06	13.21	0.10	7.21E-05	7.27E-04	1.1E-04	0.15	3618	2.71E-06	5.12	3.61
4.7	1.58	101	0.69	4.93E-06	6.88E-06	15.91	0.10	6.92E-05	6.96E-04	8.8E-05	0.13	4524	2.29E-06	5.74	3.88
4.7	1.55	101	0.70	4.92E-06	6.87E-06	15.91	0.10	6.54E-05	6.23E-04	8.8E-05	0.14	4529	2.29E-06	6.05	3.68
4.7	1.46	86	0.70	4.57E-06	6.37E-06	16.01	0.10	6.3E-05	6.23E-04	8.7E-05	0.14	4903	2.16E-06	6.07	3.69
4.7	1.43	87	0.70	4.59E-06	6.40E-06	16.19	0.10	6.58E-05	6.77E-04	8.6E-05	0.13	4938	2.15E-06	5.86	3.87
4.7	1.07	90	0.71	4.65E-06	6.49E-06	21.25	0.10	6.36E-05	6.23E-04	6.6E-05	0.11	6396	1.77E-06	6.99	4.25
4.7	1.04	101	0.70	4.92E-06	6.88E-06	23.81	0.11	6.29E-05	5.75E-04	5.9E-05	0.10	6775	1.69E-06	7.70	4.33
4.7	1.03	89	0.71	4.63E-06	6.46E-06	21.93	0.10	6.23E-05	6.00E-04	6.4E-05	0.11	6624	1.72E-06	7.24	4.24
4.7	0.89	85	0.72	4.54E-06	6.32E-06	24.63	0.10	6.02E-05	5.74E-04	5.7E-05	0.10	7597	1.55E-06	7.84	4.40
6.5	3.99	105	0.73	3.66E-06	5.12E-06	7.63	0.11	4.77E-05	4.45E-04	1.8E-04	0.41	2917	3.19E-06	4.82	2.22
6.5	3.51	102	0.72	3.62E-06	5.05E-06	8.32	0.10	5.12E-05	5.18E-04	1.7E-04	0.33	3220	2.96E-06	4.72	2.47
6.5	2.98	99	0.71	3.56E-06	4.98E-06	9.24	0.09	5.42E-05	5.90E-04	1.5E-04	0.26	3630	2.71E-06	4.70	2.75
6.5	2.46	96	0.69	3.50E-06	4.89E-06	10.78	0.08	6.18E-05	7.83E-04	1.3E-04	0.17	4309	2.38E-06	4.44	3.40
6.5	2.01	92	0.70	3.44E-06	4.80E-06	12.37	0.08	5.82E-05	7.07E-04	1.1E-04	0.16	5035	2.12E-06	5.00	3.46
6.5	1.70	89	0.69	3.38E-06	4.72E-06	14.23	0.08	6.05E-05	7.75E-04	9.8E-05	0.13	5890	1.88E-06	5.13	3.89
6.5	1.46	87	0.67	3.35E-06	4.67E-06	15.83	0.07	6.3E-05	8.50E-04	8.8E-05	0.10	6618	1.72E-06	5.17	4.29
6.5	1.08	81	0.70	3.26E-06	4.54E-06	20.66	0.08	5.68E-05	7.10E-04	6.8E-05	0.10	8871	1.38E-06	6.45	4.49
6.5	0.98	80	0.71	3.24E-06	4.51E-06	22.02	0.08	5.52E-05	6.77E-04	6.4E-05	0.09	9518	1.31E-06	6.82	4.52
6.5	0.54	71	0.75	3.09E-06	4.30E-06	33.45	0.09	4.58E-05	4.88E-04	4.2E-05	0.09	15135	9.27E-07	9.88	4.74

\*\*\*PREHEATED INLET (573 K) CONDITIONS\*\*\*

pressure [atm]	residence time [ms]	inlet T [degC]	PHI	kinetic viscosity [m2/s]	thermal diffusiv. [m2/s]	turbulent intensity [m/s]	laminar burning vel [m/s]	lam. flame thickness [m]	chemical time [s]	mixing time [s]	Damkohler number	Reynolds number	Kolmogorov scale [m]	turbulent burning vel [m/s]	turb.flame thickness [mm]
3.0	3.33	300	0.74	1.66E-05	2.38E-05	13.02	0.47	5.048E-05	1.07E-04	1.1E-04	1.01	1101	6.62E-06	11.44	1.59
3.0	2.36	300	0.67	1.66E-05	2.38E-05	17.56	0.38	6.302E-05	1.67E-04	8.0E-05	0.48	1485	5.29E-06	11.92	2.06
3.0	1.65	300	0.64	1.66E-05	2.38E-05	23.20	0.32	7.34E-05	2.26E-04	6.0E-05	0.27	1961	4.29E-06	12.11	2.68
3.0	1.02	300	0.62	1.66E-05	2.38E-05	34.56	0.30	7.956E-05	2.66E-04	4.1E-05	0.15	2922	3.18E-06	13.72	3.53
4.7	3.74	300	0.66	1.06E-05	1.53E-05		0.27	5.645E-05	2.09E-04						
4.7	3.53	314	0.68	1.12E-05	1.61E-05	11.31	0.31	5.133E-05	1.63E-04	1.2E-04	0.76	1417	5.48E-06	9.10	1.74
4.7	3.03	310	0.67	1.10E-05	1.59E-05	12.84	0.30	5.37E-05	1.81E-04	1.1E-04	0.60	1629	4.93E-06	9.52	1.89
4.7	2.48	301	0.62	1.06E-05	1.53E-05		0.23	6.806E-05	3.02E-04						
4.7	2.41	311	0.64	1.11E-05	1.60E-05		0.27	5.949E-05	2.22E-04						
4.7	2.08	302	0.60	1.07E-05	1.54E-05	18.76	0.20	7.526E-05	3.69E-04	7.5E-05	0.20	2462	3.62E-06	8.56	3.07
4.7	2.01	312	0.63	1.11E-05	1.60E-05	18.41	0.25	6.348E-05	2.52E-04	7.6E-05	0.30	2321	3.78E-06	10.16	2.54
4.7	1.59	303	0.61	1.08E-05	1.56E-05	23.72	0.22	7.032E-05	3.18E-04	5.9E-05	0.19	3076	3.06E-06	10.36	3.21
4.7	1.58	307	0.60	1.09E-05	1.58E-05	23.03	0.22	7.286E-05	3.37E-04	6.1E-05	0.18	2948	3.16E-06	9.92	3.25
4.7	1.56	304	0.61	1.08E-05	1.56E-05	24.16	0.22	7.032E-05	3.17E-04	5.8E-05	0.18	3122	3.03E-06	10.47	3.23
4.7	1.09	305	0.60	1.09E-05	1.57E-05	31.83	0.21	7.293E-05	3.40E-04	4.4E-05	0.13	4101	2.47E-06	11.62	3.84
4.7	1.02	308	0.59	1.10E-05	1.58E-05	33.42	0.21	7.656E-05	3.71E-04	4.2E-05	0.11	4266	2.40E-06	11.41	4.10
4.7	0.93	306	0.61	1.09E-05	1.57E-05	35.62	0.23	6.88E-05	3.01E-04	3.9E-05	0.13	4575	2.27E-06	13.04	3.82
4.7	0.92	313	0.61	1.11E-05	1.61E-05	35.40	0.23	6.9E-05	2.96E-04	4.0E-05	0.13	4449	2.32E-06	13.11	3.78
4.7	0.85	309	0.59	1.10E-05	1.59E-05	38.08	0.21	7.649E-05	3.69E-04	3.7E-05	0.10	4846	2.18E-06	12.20	4.37
6.5	4.08	300	0.67	7.82E-06	1.13E-05	10.36	0.24	4.786E-05	2.04E-04	1.4E-04	0.66	1856	4.47E-06	7.94	1.83
6.5	3.97	300	0.66	7.82E-06	1.13E-05	10.28	0.23	4.957E-05	2.18E-04	1.4E-04	0.62	1841	4.50E-06	7.70	1.87
6.5	3.04	300	0.63	7.82E-06	1.13E-05	13.44	0.20	5.581E-05	2.77E-04	1.0E-04	0.38	2407	3.68E-06	8.18	2.30
6.5	2.93	300	0.65	7.82E-06	1.13E-05	11.54	0.22	5.218E-05	2.42E-04	1.2E-04	0.50	2067	4.13E-06	7.94	2.03
6.5	2.44	300	0.62	7.82E-06	1.13E-05	15.71	0.19	6.033E-05	3.23E-04	8.9E-05	0.28	2814	3.27E-06	8.28	2.66
6.5	2.09	300	0.61	7.82E-06	1.13E-05	17.82	0.17	6.441E-05	3.69E-04	7.9E-05	0.21	3193	2.98E-06	8.31	3.00
6.5	1.57	300	0.59	7.82E-06	1.13E-05	23.43	0.16	6.951E-05	4.29E-04	6.0E-05	0.14	4196	2.43E-06	8.86	3.70
6.5	1.49	300	0.58	7.82E-06	1.13E-05	25.74	0.15	7.435E-05	4.91E-04	5.4E-05	0.11	4610	2.26E-06	8.69	4.15
6.5	1.20	300	0.59	7.82E-06	1.13E-05	29.15	0.16	7.034E-05	4.40E-04	4.8E-05	0.11	5221	2.06E-06	9.77	4.18
6.5	1.03	300	0.58	7.82E-06	1.13E-05	32.36	0.15	7.433E-05	4.91E-04	4.3E-05	0.09	5797	1.90E-06	9.74	4.65
6.5	0.88	300	0.58	7.82E-06	1.13E-05	36.29	0.15	7.726E-05	5.30E-04	3.9E-05	0.07	6500	1.75E-06	9.92	5.12
6.5	0.75	300	0.58	7.82E-06	1.13E-05	40.87	0.15	7.728E-05	5.31E-04	3.4E-05	0.06	7321	1.60E-06	10.52	5.44

**APPENDIX D**  
**CHEMICAL KINETIC MODELING DATA**

***CHEMICAL KINETIC MODELING DATA***																								
	HP-JSR	PSR																						
	residence	time	temperature		V <sub>psr1</sub> /V <sub>t</sub>	NOx	NOx	NOx rate																
	[ms]	[ms]	[K]	PHI	[%]	[ppmv, wet]	[ppmv, wet]	[ppm/ms]	O	CH	H	NNH	N2O	N2	N									
unheated			meas.						[ppmv, wet]															
6.5 atm	0.536	0.536	1820	0.74	100	11	12	20.5	305	0.017	130	0.001	1.64	730200	0.0009	1.00	3.76	1.00	5.34	11.09	9.04	33.87	8.99	48.11
	0.98	0.98	1825	0.71	100	10	9.1	10.2	221	0.006	66	0.0006	1.82	733700	0.0004	1.41	4.44	0.79	3.51	10.14	13.88	43.77	7.78	34.56
	1.48	1.48	1830	0.67	100	9.6	9.6	6.5	178	0.003	40	0.0004	1.87	736700	0.0002	1.82	4.78	0.64	2.70	9.92	18.29	48.12	6.43	27.16
PSR1	2	0.126	1757	0.7	6	5.5		43.7	518	0.05	303	0.003	1.327	730400	0.002	0.20	1.19	1.24	3.07	5.69	3.43	20.85	21.71	54.00
PSR1	4	0.0695	1748	0.73	1.67	5.4		77.7	569	0.12	474	0.004	0.95	724600	0.004	0.11	0.65	1.00	3.93	5.69	1.85	11.47	17.63	69.05
PSR2	2	1.897	1836	0.7		7.3	7.5	3.8	53	5E-05	5.7	6E-06	1	735700	3E-05	0.74	0.71	0.00	0.06	1.51	49.02	46.85	0.24	3.88
PSR2	4	3.833	1860	0.73		9.6	10.3	2.5	53	2E-05	6	6E-05	0.776	733300	4E-05	2.36	1.30	0.07	0.05	3.79	62.30	34.40	1.90	1.40
preheated	0.754	0.754	1805	0.57	100	6.4	6.05	8.5	252	0.003	50	0.0005	2.33	743700	0.0002	1.00	3.67	0.58	1.29	6.54	15.34	56.01	8.92	19.74
6.5 atm	1.56	1.56	1825	0.59	100	8	7.2	5.1	173	0.001	28	0.0003	2.07	743000	0.0001	1.78	4.49	0.49	0.94	7.70	23.07	58.32	6.39	12.23
PSR1	2	0.231	1820	0.6	11	6.8		29.4	516	0.016	159	0.002	2.1	739800	0.0007	0.74	2.82	1.45	2.19	7.20	10.27	39.17	20.16	30.41
PSR1	4	0.045	1764	0.66	1.08	4.3		95.6	750	0.13	535.4	0.005	1	728900	0.004	0.11	0.55	1.06	2.91	4.63	2.36	11.98	22.90	62.76
PSR2	2	1.847	1840	0.6		8.1	6.2	4.4	44	5E-06	2.8	3E-05	0.9	742700	2E-05	0.63	0.44	0.01	0.01	1.09	57.74	40.38	1.35	0.53
PSR2	4	3.892	1864	0.66		9.2	8.8	2.4	60	2E-05	5.5	6E-05	0.87	738200	4E-05	2.85	1.57	0.08	0.05	4.56	62.49	34.50	1.81	1.20
unheated	0.89	0.89	1819	0.72	100	11.64	10.3	13.1	369	0.013	130	0.002	1.07	732700	0.0007	1.44	3.11	2.89	4.84	12.29	11.75	25.33	23.56	39.36
4.7 atm	1.4	1.4	1829	0.69	100	11.71	8.8	8.4	288	0.006	80	0.0006	1.61	734600	0.0004	1.98	5.13	1.06	3.62	11.80	16.81	43.49	8.99	30.71
PSR1	2	0.126	1704	0.677	6	4.26		33.8	683	0.07	424.1	0.003	1	730700	0.002	0.10	0.71	1.21	2.60	4.62	2.12	15.35	26.30	56.23
PSR1	3.6	0.0704	1739	0.72	1.9	6.8		96.6	948	0.2	777.7	0.005	0.8	724600	0.006	0.12	0.64	1.54	4.59	6.88	1.68	9.26	22.36	66.69
PSR2	2	1.84	1836	0.677		6.41	7.1	3.5	91	1E-06	11.2	8E-05	1.1	737000	4E-05	0.89	0.99	0.06	0.00	1.94	46.02	50.92	3.02	0.04
PSR2	3.6	3.391	1879	0.72		11.23	10.9	3.3	84.2	5E-05	11.3	8E-05	0.83	733700	6E-05	2.38	1.52	0.10	0.08	4.08	58.31	37.24	2.39	2.06
unheated	0.66	0.66	1804	0.7	100	12.6	11.3	19.1	789	0.03	344	0.002	1.07	732300	0.002	1.24	3.44	2.95	4.99	12.62	9.80	27.25	23.41	39.55
3.0 atm	0.98	0.98	1820	0.69	100	13	10.3	13.3	652	0.02	240	0.001	1.18	734200	0.001	1.82	4.40	1.80	5.19	13.21	13.75	33.34	13.60	39.31
PSR1	2	0.08	1716	0.71	4	7.68		96.0	1591	0.35	1354	0.006	0.57	724100	0.009	0.11	0.51	2.28	5.32	8.22	1.29	6.26	27.72	64.73
PSR1	3.3	0.0432	1734	0.79	1.3	10.1		233.8	1613	1	2113	0.0087	0.3719	713000	0.0279	0.07	0.29	1.79	8.56	10.70	0.67	2.67	16.71	79.95
PSR2	1.96	1.775	1865	0.71		12.1	11.7	6.8	224	0.0002	44.75	0.0002	1.019	734000	0.0001	1.83	1.92	0.23	0.11	4.09	44.70	46.98	5.71	2.61
PSR2	3.3	2.994	1928	0.79		21.1	19.5	7.0	222	0.0004	60.44	0.0003	0.7643	728100	0.0003	5.72	3.57	0.53	0.42	10.24	55.88	34.82	5.17	4.14
* - model NOx/PSR res. Time																								

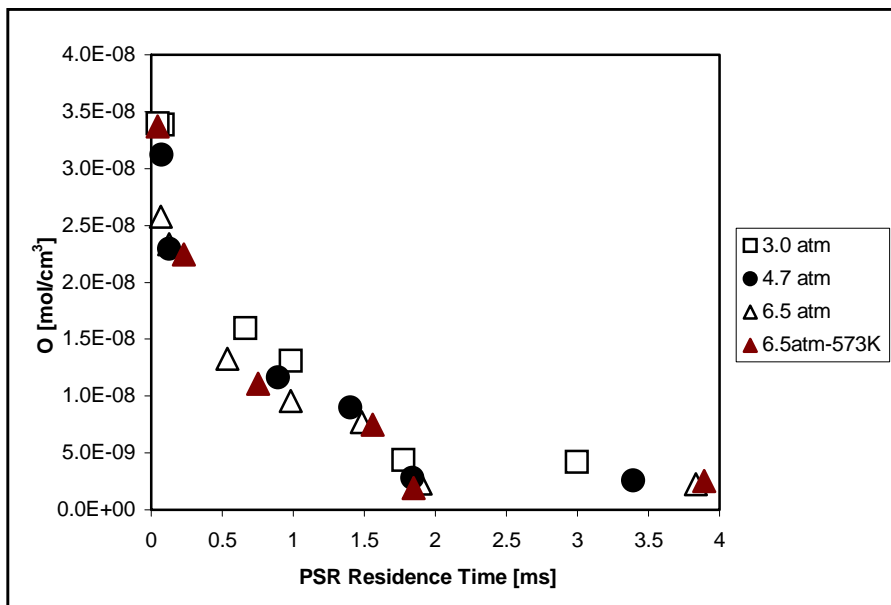


Figure D.1 O-atom concentration versus PSR residence time

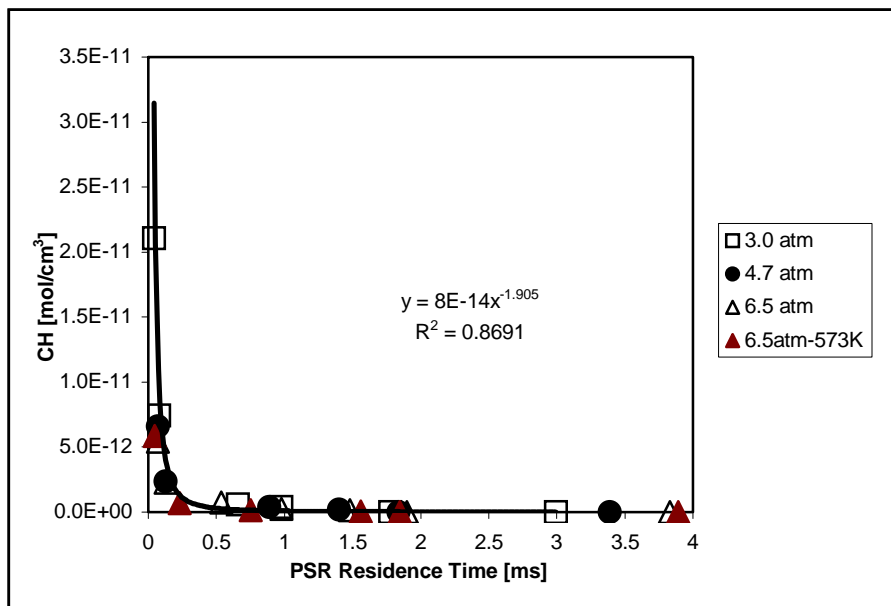


Figure D.2 CH-radical concentration versus PSR residence time

## VITA

### EDUCATION

**Doctor of Philosophy, Mechanical Engineering** **2000**  
**University of Washington, Seattle, Washington**

*Dissertation:* “NO<sub>x</sub> and CO Formation for Lean-Premixed Methane-Air  
 Combustion in a Jet-Stirred Reactor Operated at Elevated Pressure”

**Master of Science, Mechanical Engineering** **1994**  
**University of Washington, Seattle, Washington**

*Thesis:* “N<sub>2</sub>O Destruction by Reburning”

*Published:* *Combustion and Flame*, Vol. 107, p. 453-463, 1996

**Bachelor of Science, Mechanical Engineering** **1992**  
**University of Belgrade, Belgrade, Yugoslavia**

*Thesis:* “Thermal Power Plant Design”

### EMPLOYMENT

Assistant Professor, Seattle University, Seattle, WA commences March 2000

Class Instructor, University of Washington, Seattle, WA 1997—1999

Teaching and Research Assistant, University of Washington, Seattle, WA 1992—1997

### HONORS

Dean’s Outstanding Teaching Award for Teaching Assistant for 1998

College of Engineering, University of Washington 1998